Preparation of Monolayer-Protected Gold and Silver Nanoclusters and their Optical, Chiroptical and Photochemical Properties

Mostafa Farrag Mostafa Farrag

TECHNISCHE UNIVERSITÄT MÜNCHEN
Lehrstuhl für Physikalische Chemie

Preparation of Monolayer-Protected Gold and Silver Nanoclusters and their Optical, Chiroptical and Photochemical Properties

Mostafa Farrag Mostafa Farrag

Vollständiger Abdruck der von der Fakultät für Chemie der Technischen Universität
München zur Erlangung des akademischen Grades eines

Doktors der Naturwissenschaften

genehmigten Dissertation.

Vorsitzender: Univ.-Prof. Dr. S. Günther

Prüfer der Dissertation:

1. Univ.-Prof. Dr. U. K. Heiz

2. Univ.-Prof. Dr. K. Köhler

Die Dissertation wurde am 27.06.2013 bei der Technischen Universität München eingereicht und durch die Fakultät für Chemie am 11.07.2013 angenommen.

To

My Country Egypt, My Parents, My Wife and My Children

For the Deep Love They Give to Me

TABLE OF CONTENTS

Table of contents

ABSTRACT

Abstract

This work focuses on the preparation and characterization of ultrasmall (<2 nm) size selected gold and silver nanoclusters monolayer protected with chiral and achiral thiol ligands ($M_n(SR)_m$). The optical properties of these nanoclusters were studied by UV-vis, Fourier transform infrared, photoluminescence and circular dichroism spectroscopy and analysed with Mie theory. The average molecular formula of the clusters, the particle sizes and molecular weight were determined by thermogravimetric analysis, elemental analysis, transmission electron microscopy, powder X-ray diffraction and matrix-assisted laser desorption ionization time-of-flight mass spectrometry.

Zusammenfassung

Der Fokus dieser Arbeit liegt in der Synthese und Charakterisierung von ultrakleinen (< 2 nm), größenselektierten Gold- und Silbernanoclustern, welche mit chiralen und achiralen Liganden geschützt wurden ($M_n(SR)_m$). Die optischen Eigenschaften dieser Nanocluster wurden mittels UV-vis-, Fourier-Transform-Infrarot-, Photolumineszenz- und zirkularer Dichroismusspektroskopie untersucht und mit Mie-Theorie analysiert. Die mittlere Summenformel der Cluster, die Partikelgröße und die molekulare Masse wurden mittels Thermogravimetrieanalyse, Elementaranalyse, Transmissionselektronenmikroskopie, Röntgen-Pulverdiffraktometrie und Matrix-unterstützte Laserdesportion/ionisations-Flugzeitmassenspektrometrie bestimmt.

CHAPTER 1

INTRODUCTION

1. Introduction

The research on metal clusters M_n has always been accompanied with the idea of adding a third dimension (3D) to the periodic table. The third dimension comprises the size or the number of atoms in clusters (figure 1),[1-5] While the other two dimensions are the periods and groups of the D. I. Mendeleeff periodic table invented in 1869.[6] Superatomic building blocks of multi-atom clusters have been found to exhibit new physical properties beyond those available from the standard elements in the periodic table; the properties of such clusters effectively enable the expansion of the periodic table to a third dimension.[1,8]

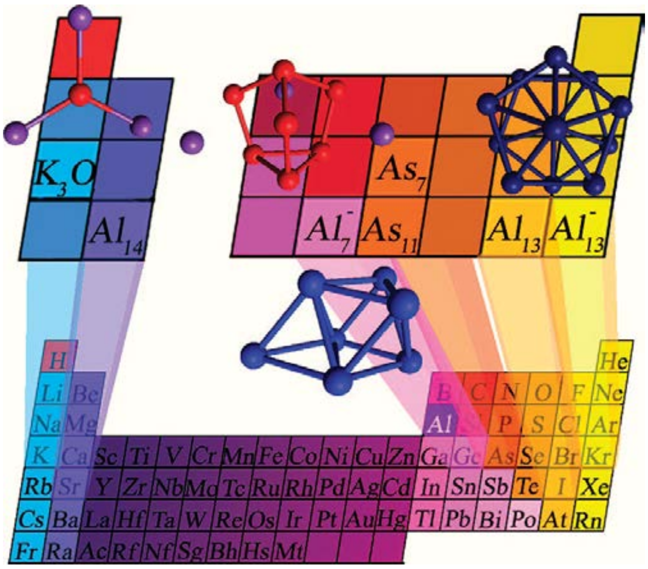

Figure 1: Three dimensional periodic table of cluster elements. Reprinted with permission from ref. 6. Copyright (2009) American Chemical Society.

There are two approaches to prepare nanoparticles; the first one is the top down approach, which is the subdivision of bulk matter into small particles. The big disadvantage of this approach, however, is that it gives a very large distribution of particles sizes. In contrast, the bottom up approach results in rather defined building blocks and is the best method to produce size selected clusters.[9-11]

In the late 1970s cluster science emerged as an independent research topic with pioneer research groups such as the groups of Schumacher[5] and Knight[2-4]. One of the main focuses of early research in this field was accounting for magic numbers (n = 2, 8, 18, 20, 34, 40, 58, 92, 138, …..), which are often observed in mass spectra as peaks of unusually high intensity. The appropriate aufbau rule of delocalized ‘‘superatomic orbitals’’ of metal clusters is $1s^2\ 1p^6\ 1d^{10}\ 2s^2\ 1f^{14}\ 2p^6\ 1g^{18}\ 2d^{10}\ 3s^2\ 1h^{22}$ ….., wherein s–p–d–f–g–h– refer to the angular-momentum nomencleature.[1-5,12] Magic cluster sizes correspond to the filling of electronic shells of these energy levels. Figure 2 reproduces the energy level of various wells.[1-4,13]

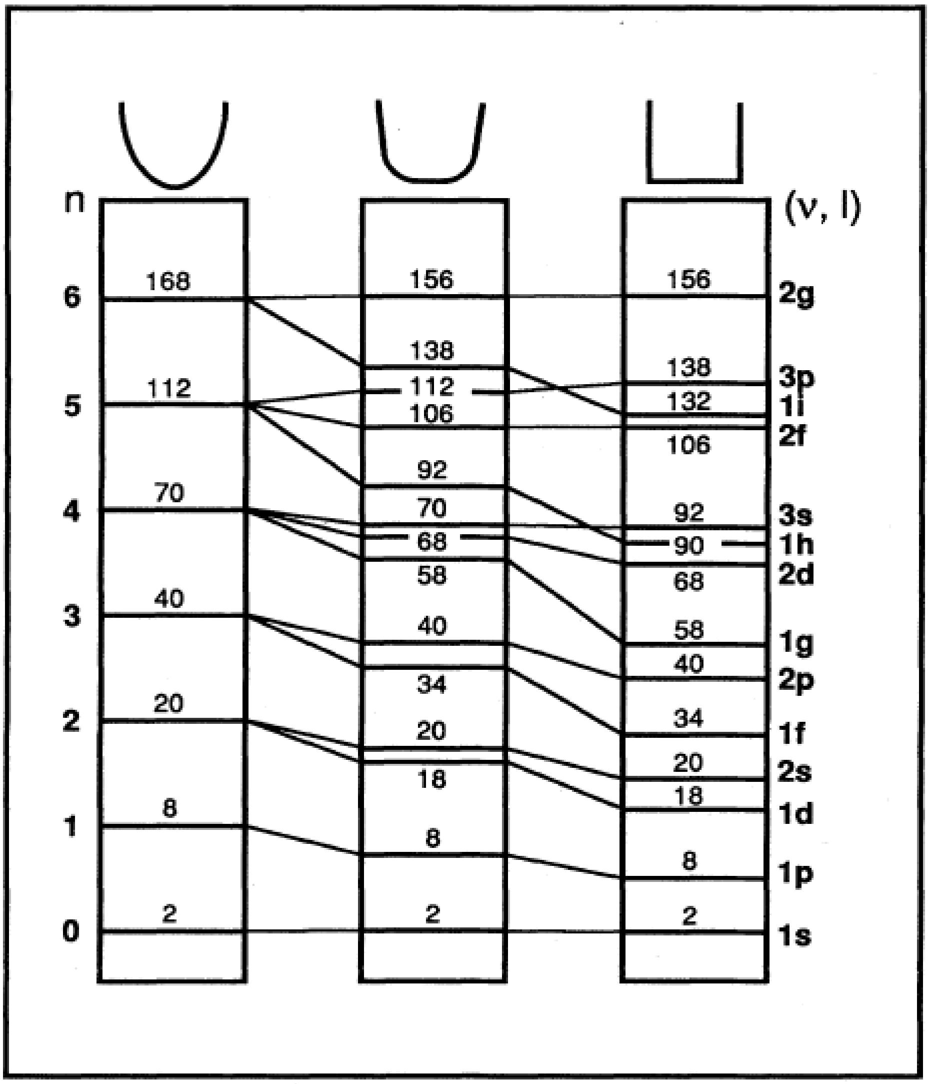

Figure 2: Examples of the electronic energy levels in various spherical potential wells. The simplest case in the isotropic harmonic well where the energy levels are equally spaced and each level has a degeneracy of $\upsilon(\upsilon+1)$. The rounded square well lifts the degeneracies for different angular momentum values l. The splitting get even larger for the square well, although the spherical symmetry preserves the angular momenta of the states. Reprinted with permission from ref. 13. Copyright (2000) Springer-Verlag Berlin Heidelberg.

The concept of magic sizes should be illustrated by the following example. An Al_{13} cluster has 39 valence electrons. Replacing one aluminum atom (Al) in an Al_{13} cluster by a carbon atom (C) leads to a system comprising 40 electrons (magic number). Hence, the $Al_{12}C$ cluster would be energetically stable and chemically inert, which has been confirmed theoretically.[14] The electronic structure of the $Al_{12}C$ cluster within the jellium concept[15-17] (see below) is $1s^2\ 1p^6\ 1d^{10}\ 2s^2\ 1f^{14}\ 2p^6$. The same electronic sequence occurs for Al_{13}^-(figure

3),[6] which was confirmed by Castleman and co-workers by showing that this cluster is chemically inert.[18]

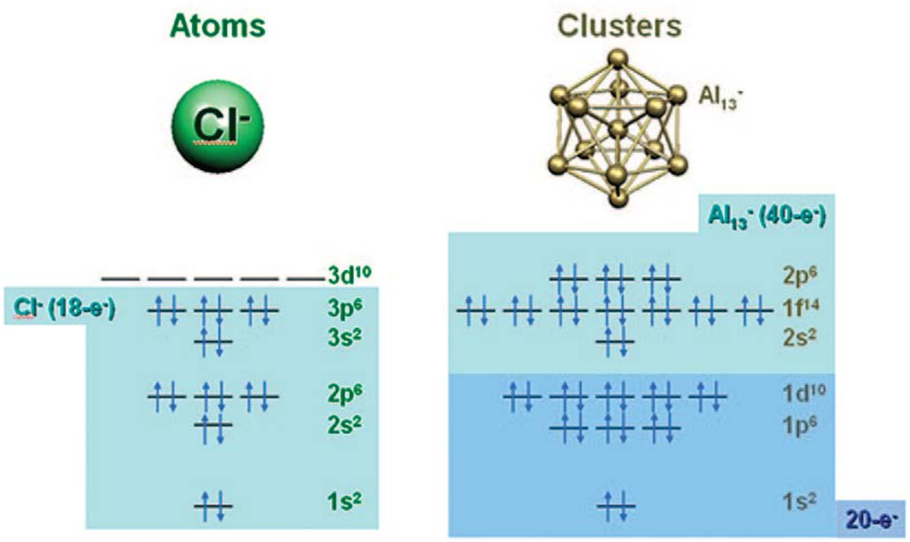

Figure 3. Energy levels in atoms and clusters. Also shown are the electronic levels in a Cl atom and that in an Al_{13} cluster. Reprinted with permission from ref. 6. Copyright (2009) American Chemical Society.

The Jellium model is a quantum mechanical model where the positively charged core is modeled by a spherical potential subsequently the one electron Schrödinger equation is solved. Figure 2 shows the results for three different potentials. The Jellium model is the simplest model to describe the electronic ground state of a metal cluster. This model is used in the calculation of metal properties, where the core electrons (not the valence electrons) and the nuclei are modeled as a uniform positively charged background.[15-17]

An early example of free clusters produced by Knight's group in the gas phase were sodium clusters.[2,3,13,15] Figure 4 shows mass spectrum of sodium clusters of N atoms per cluster (N =4-100), which were produced in a supersonic expansion with an argon carrier gas.[2] The spectra show distinct maxima at N = 8, 20, 40, 58, and 92. These can be understood in terms of the above mentioned one-electron shell model, in which independent delocalized atomic 3s electrons are bound in a spherically symmetric potential well.[2,3,13]

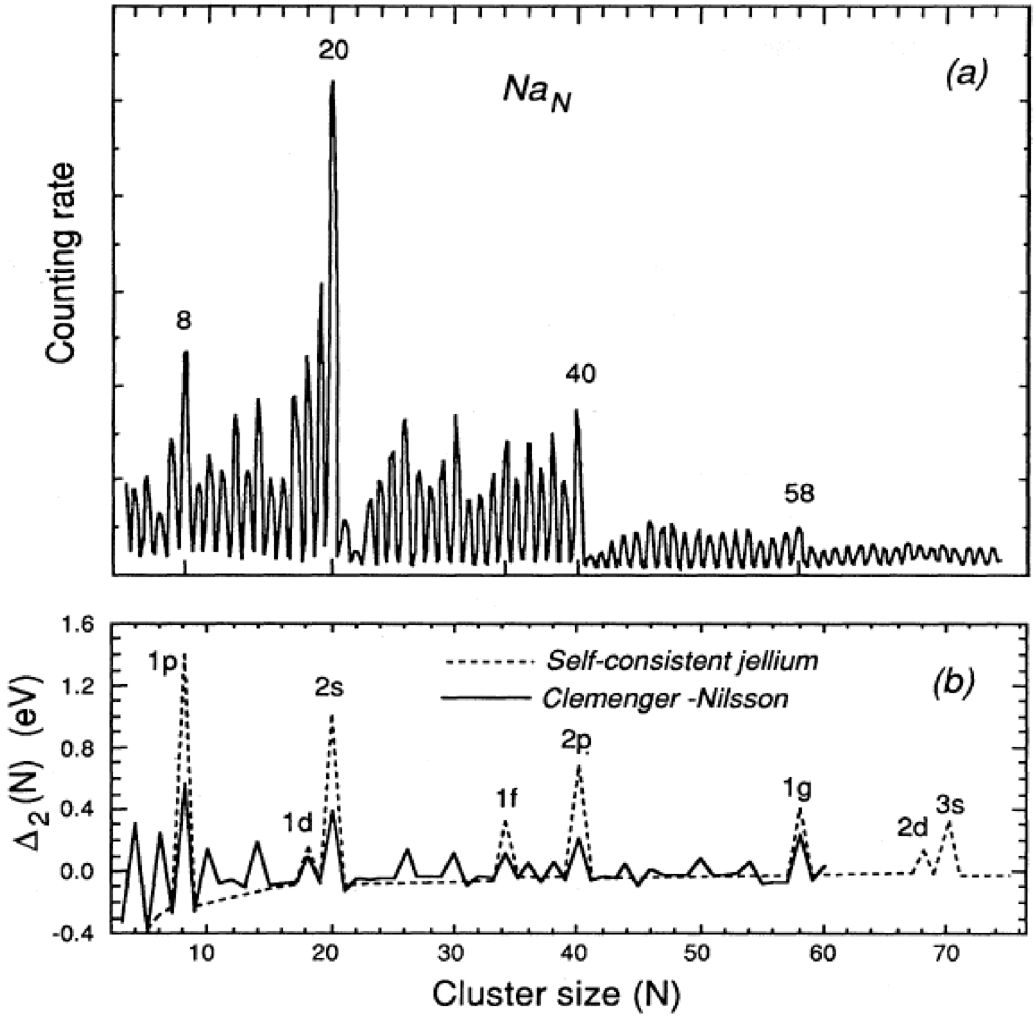

Figure 4: Mass spectrum of sodium clusters, N =4-75. (a) experimental (ref. 2, 1984); (b) dashed line, using Woods-Saxon potential (ref. 2, 1984); solid line, using the ellipsoidal shell (Clemenger-Nilsson) model (ref. 15, 1987). Reprinted with permission from ref. 13. Copyright (1993) American Physical Society.

Research on monolayer protected clusters was started by Brust and co-worker in 1994.[19] Noble metal clusters (Au, Ag, etc.) protected by ligands, such as thiolates,[20-22] phosphines,[23] and amines,[24] have stimulated major research interest in the last fifteen years. Scientific interest in these clusters is due to their unique material properties that bridge the gap between those of small molecules (e.g., organometallic compounds) and nanocrystals (>2 nm) (figure 5).[25-27] The research on thiolate-protected metal nanoparticles can be divided into three areas, i) from polydisperse to narrow-sized metal nanoparticles in the size range of ca. 2–5 nm; these nanoparticles are large enough to exhibit fcc crystallinity (and hence, are metal nanocrystals); ii) moving toward Au nanoclusters (<2 nm); in this area relatively monodisperse metal nanoclusters were obtained by post-synthetic size selection, and iii) synthesis of truly monodisperse $Au_n(SR)_m$ clusters (<1–2 nm) (figure 5).[25]

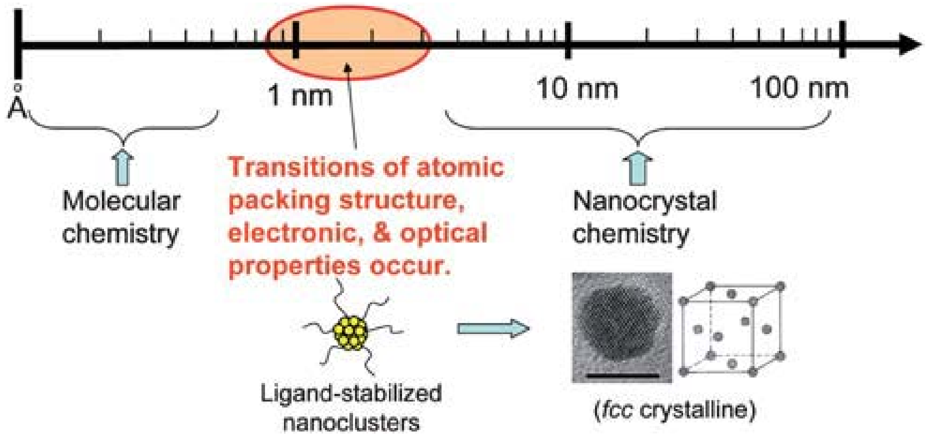

Figure 5: Metal nanoclusters, bridge organometallic complexes and nanocrystals. Reprinted with permission from ref. 25. Copyright (2010) The Royal society of Chemistry.

These monodisperse clusters are promising materials for both, fundamental research and applications. Among others, the structure, bonding, and stability of the thiolate-protected metal clusters are now well understood.[20,21,25,28] They have the potential to be applied in a wide range of areas, such as catalysis, biosensing, drug delivery, molecular electronics, and surface patterning.[29]

Walter et. al. used the simple electron counting equation originally induced for free clusters to determine the total number of electrons (n_e) in thiolate-protected gold cluster complexes (equation 1).[12]

$$n_e = N_{\upsilon A} - M - z \qquad (1)$$

n_e is the total number of electrons, N is the number of metal atoms, A the number in the core, υ is the atomic valence, M is the number of electrons withdrawn by the ligands and z is the overall charge on the cluster complex. For example the $Au_{102}(p\text{-}MBA)_{44}$ has 58 electrons ($N_{\upsilon A}$ = 102, M = 44, z = 0) and corresponds to a closed shell magic number.[12,2,3]

Knight[2-4] and Schumacher[5] introduced the term ‘‘very small clusters’’ to refer to 2–20 atoms, ‘‘small clusters’’ (20–500 atoms), and ‘‘large clusters’’ (500–10^7 atoms).[30] It is found that the special range of subnanometer to 2 nm gold nanoparticles are vastly different to larger Au nanoparticles (> 2 nm to 100 nm) in terms of atomic packing, electronic structure, magnetism, electrochemical and charge transport properties.[25]

The solution phase synthesis of metal nanoclusters is a practical application method, because it permits an easy scale-up and large scale production once a synthetic approach is developed. These clusters are protected by ligands (e.g. thiols, phosphines, amines), which typically form a monolayer on the cluster surface (hence, they are named monolayer-protected clusters). The ligand layer prevents the clusters from aggregating in solution or in the solid phase. On the other hand, the ligand layer may profoundly influence the physical and chemical properties of metal clusters, and even induce chirality or the change the optical and photoluminescence properties.[25]

1.1. Optical properties and stability of protected clusters

Plasmonic metal nanoparticles (Au and Ag) have a great potential for chemical and biological sensor applications, due to their sensitive spectral response to the local environment of the nanoparticle surface and the ease of monitoring the light signal due to their strong scattering or absorption.[25]

The surface plasmon resonance in noble metal nanoparticles (silver and gold) originates from the free electrons in the metals (d electrons), which move freely through the material. The mean free path in gold and silver is nearly 50 nm. So no scattering is expected from the bulk in particles smaller than 50 nm. Thus, all interactions are expected to be confined to the surface. When the wavelength of light is much larger than the nanoparticle size, it can induce standing resonance conditions as represented in figure 6. Light in resonance with the surface plasmon oscillation causes the free-electrons in the metal to oscillate in resonance with the light’s frequency causing a standing to oscillation. The resonance condition depends on the shape, size, and dielectric constants of both the metal and the surrounding material. Thus, changing the solvent will change the dielectric constant, and therefore the frequency of the surface plasmon resonance, too.[31]

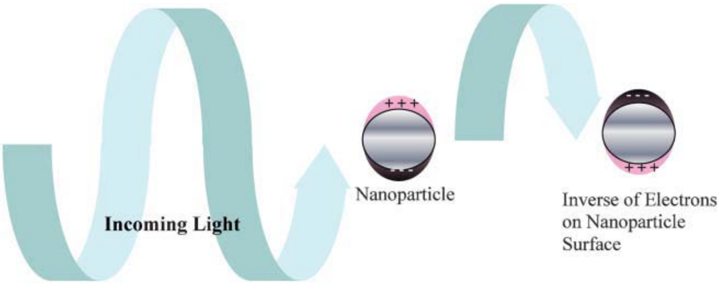

Figure 6: Origin of surface plasmon resonance due to coherent interaction of the electrons in the conduction band with light. Reprinted with permission from ref. 31. Copyright (2006) The Royal society of Chemistry.

Mie originally calculated the surface plasmon resonance by solving Maxwell’s equations for small spheres interacting with an electromagnetic field.[32a] Gan was able to extend this theory to apply to ellipsoidal geometries.[32b,c] Modern methods use the discrete dipole approximation (DDA), which allows one to calculate the surface plasmon resonance absorption for arbitrary geometries.[31,32d,e]

In this work Mie theory was used in combination with the Drude model to demonstrate that the peaks in the spectra originate from plasmonic transitions. In addition, the damping constant as well as the dielectric constant of the surrounding medium was determined for silver nanoclusters protected by 2-phenylethanethiol, 4-fluorothiophenol and L-glutathione (L-GSH) ligands (figure 7).[20]

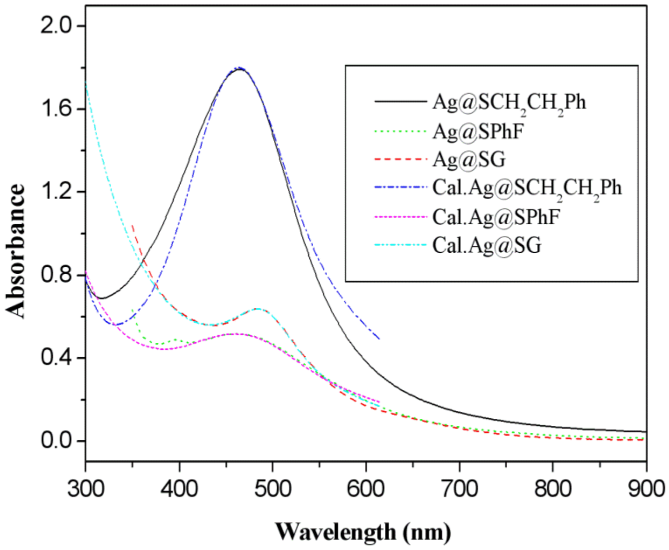

Figure 7: UV−vis absorption spectrum of all three types of silver nanoclusters and simulation of the plasmon resonance. All three spectra where fitted by a function obtained by using the Mie theory and the Drude model. Reprinted with permission from ref. 20. Copyright (2012) American Chemical Society.

Aikens et. al. calculated the optical absorption spectra of tetrahedral silver Ag_n (n =10, 20, 35, 56, 84, 120) clusters by time-dependent density functional theory. It was found that Ag_n clusters spectra evolve from molecular-like to plasmon-like with increasing n. The plasmon width increase with decreasing cluster size for typical cluster shape distributions.[33]

Silver and gold nanoclusters in the 2 nm regime exhibit a broad plasmon resonance peak at around 450 nm and 550 nm in the visible region.[21]These clusters lose molecule-like properties and develop an optical absorption band originating from the surface plasmon resonance of their free electrons. Small gold and silver clusters with several atoms (around 1 nm) have molecule-like optical transitions. This means that they will exhibit more than one absorption maxima, depending on the number of atoms which comprise the cluster.[21,22,34]

From figure 8 it can be clearly seen that the spectrum of silver nanoclusters protected by N-acetyl-L-cysteine (NALC), with average particles size nearly 2 nm, contains a single plasmon absorption peak at 480 nm. However, silver clusters of 1 nm diameter protected by L-glutathione (L-GSH) show two surface plasmon peaks at 478 nm and 641 nm.[21] The UV-vis spectra of the size selected gold clusters protected by 2-phenylethanethiol ligand give multiple characteristic absorption peaks at 400, 450 and 670 nm for $Au_{25}(SCH_2CH_2Ph)_{18}$ cluster, at 490, 520, 620, 750 and 1050 nm for $Au_{38}(SCH_2CH_2Ph)_{24}$. For $Au_{144}(SCH_2CH_2Ph)_{60}$ clusters the spectrum shows two peaks at 510 and 700 nm (figure 9).[22]

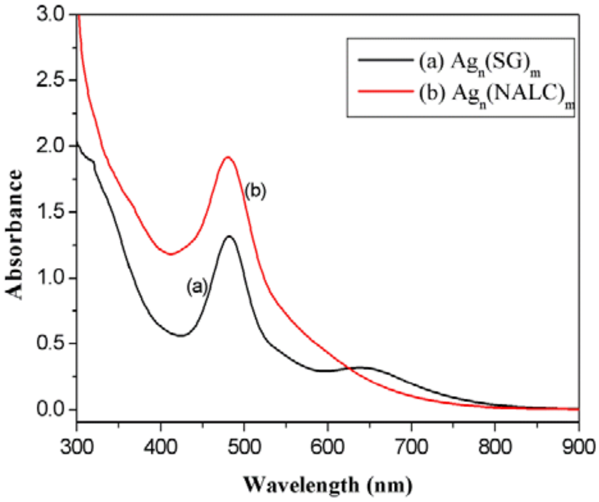

Figure 8: UV−vis absorption spectrum of $Ag_n(SG)_m$ (curve a) and $Ag_n(NALC)_m$ (curve b) nanoclusters. Reprinted with permission from ref. 21. Copyright (2013) American Chemical Society.

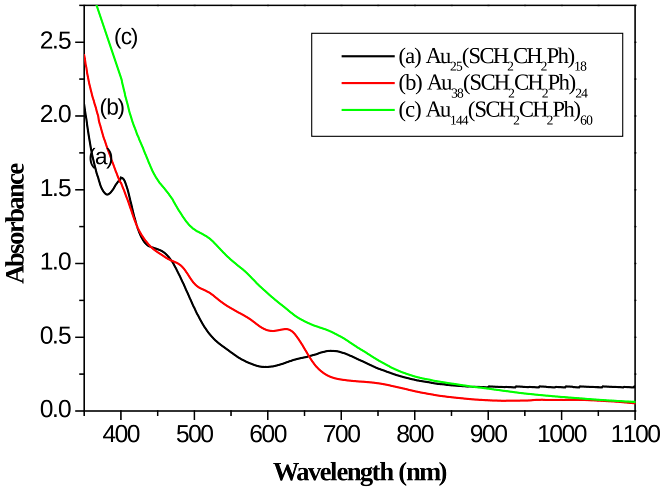

Figure 9: UV-vis absorption spectra of some size selected gold clusters. Reprinted with permission from ref. 22. Copyright (2013) the Owner Societies.

Usually UV−vis spectroscopy is used to examine the stability of clusters, because it is sensitive to changes of the metal core, such as the oxidation state and the number of metal atoms in the cluster. The silver and gold monolayer protected nanoclusters investigated in this work are stable for many months in a refrigerated environment in powder and solution form.[20,21] The stability of these clusters were checked by recording UV−vis spectra, and no change (neither in the peak positions nor the relative intensity of the absorbance) of the spectra was observed over time. Gold clusters are stable in air in powder and solution form, but silver clusters usually show less stability in air. For example, for silver clusters protected by captopril $Ag_n(Capt)_m$ the absorbance peak at 490 nm decreases to nearly half of its starting value after 8 h of air exposure. After ca. 24 h this peak vanished completely (figure 10).[35] This rapid decay can be attributed to a transformation to clusters of larger sizes under the exposure of oxygen. However, in this work stable silver clusters protected by 2-phenylethanethiol (2-PET),[20] and N-acetyl-L-cysteine (NALC) ligands were successfully prepared.[21]

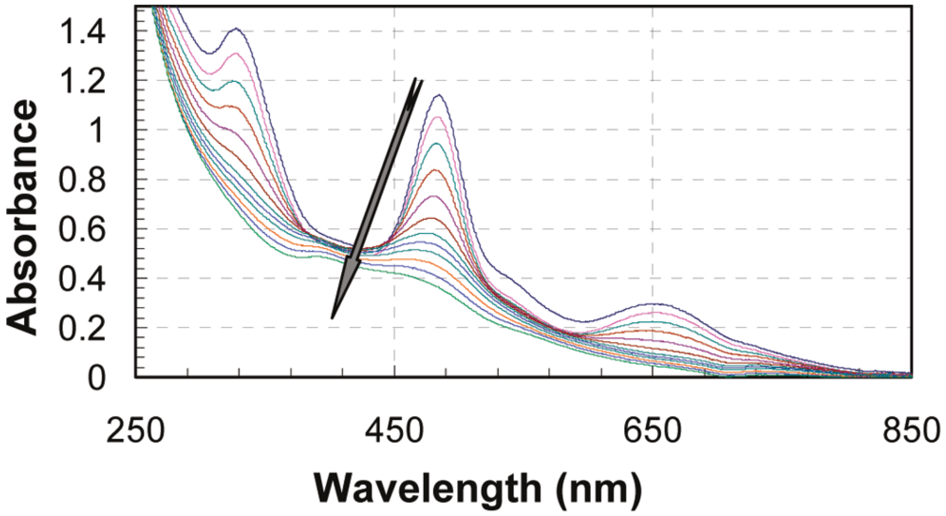

Figure 10: UV-vis spectra illustrating AgNC stability. The sample was prepared using captopril as a ligand. No deaeration of the solution was performed. Spectra were recorded every 2 h following the reduction. Half of the intensity of the peak at 490 nm was remaining after ca. 8 h. Peak vanished completely after ca. 24 h. Reprinted with permission from ref. 35. Copyright (2009) American Chemical Society.

1.2. Particle size and chemical composition determination

Transmission electron microscopy (TEM) and powder X-ray diffraction (XRD) analysis are the best analytical methods to determine the particle size of the monolayer protected clusters (MPCs). To obtain the chemical composition of MPCs and the ratio between the metal part and the organic (thiolate) part, thermogravimetric analysis (TGA), elemental analysis (EA) and atomic absorption spectroscopy (AAS) are applied.

1.2.1. Transmission electron microscopy (TEM)

Transmission electron microscopy is a very powerful technique to measure the particle size of protected clusters larger than 1 nm, because the large scattering cross section of the metal atoms results in a strong contrast in the TEM image. However, since the cluster samples are casted onto a surface, for example carbon-coated copper grids for performing TEM measurement, migration and coalescence of the particles may occur. In the case of monolayer protected clusters coalescence may be ruled out, because they are protected by the ligands. While conventional TEM is a powerful technique to determine particle sizes of a diameter larger than 1 nm, the contrast becomes very weak for very small particles (< 1 nm) and hence they might not be detected.[20,21]

Figure 11 shows a TEM image and accompanying size distribution of Ag@SCH_2CH_2Ph nanoclusters. The average diameter of the MPCs represents the Feret diameter (the distance between two parallel planes restricting the object perpendicular to that direction) and was determined in two different ways, in both cases assuming a spherical shape: one value represents the average diameter of all MPCs, and the other one is obtained from a Gaussian fit of the frequency distribution.[36] Both values are similar and therefore in this work Gaussian fits was used.

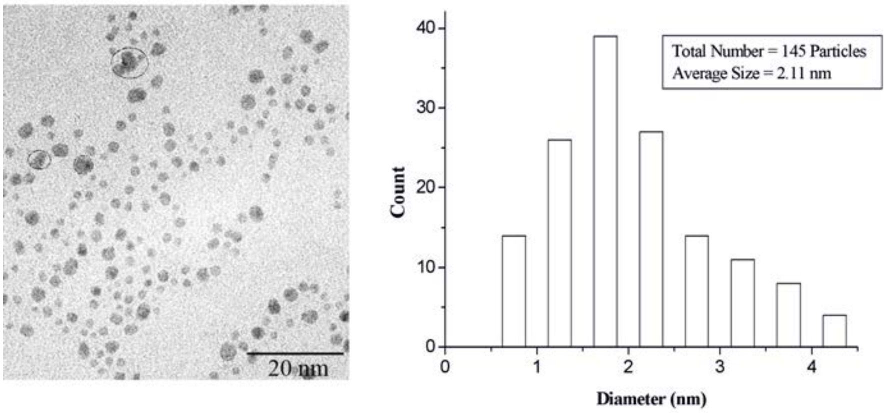

Figure 11: TEM image and size distribution of Ag@SCH_2CH_2Ph nanoclusters. Reprinted with permission from ref. 20. Copyright (2012) American Chemical Society.

1.2.2. Powder X-ray diffraction (XRD)

From the full width at half maximum (FWHM) of the X-ray diffraction peaks, the wavelength of the Cu Kα1 line $\lambda = 1.5418$ Å, and θ is the angle between the incident ray and the scattering planes, the particle sizes of nanoclusters can be estimated according to the Debye−Scherrer formula (eq 2).[37]

$$D = \frac{0.9\,\lambda}{\mathrm{FWHM}\,.\,\cos\theta} \qquad (2)$$

Bulk gold and Au nanocrystals (i.e., 2 − 100 nm) show an fcc structure. A different particle structure is observed in the cluster regime. Figure 12 shows sharp diffraction peaks of bulk gold metal at 2θ of 38.5° (indexed to the fcc (111) reflection), 44.6° (200), 64.8° (220) and 77.8° (311), since the planes of its face centered cubic (fcc) crystal lattice are separated by defined and large interplane spacing (d). However, in the case of 4 nm gold clusters protected by L-glutathione $Au_n(SG)_m$, broad peaks are observed at the same 2θ, indicating these particles exhibit a fcc like structure. The diffraction peaks at around 37.5° and 66.5° broaden with decreasing particle size.[38] This can be seen in figure 12 for $Au_n(SG)_m$ (2 nm) as well as $Au_{25}(SG)_{18}$ clusters. In these cases the average interplane spacing decreases, due to the small interatomic distances within the icosahedral core (Au_{13}) of these particles.

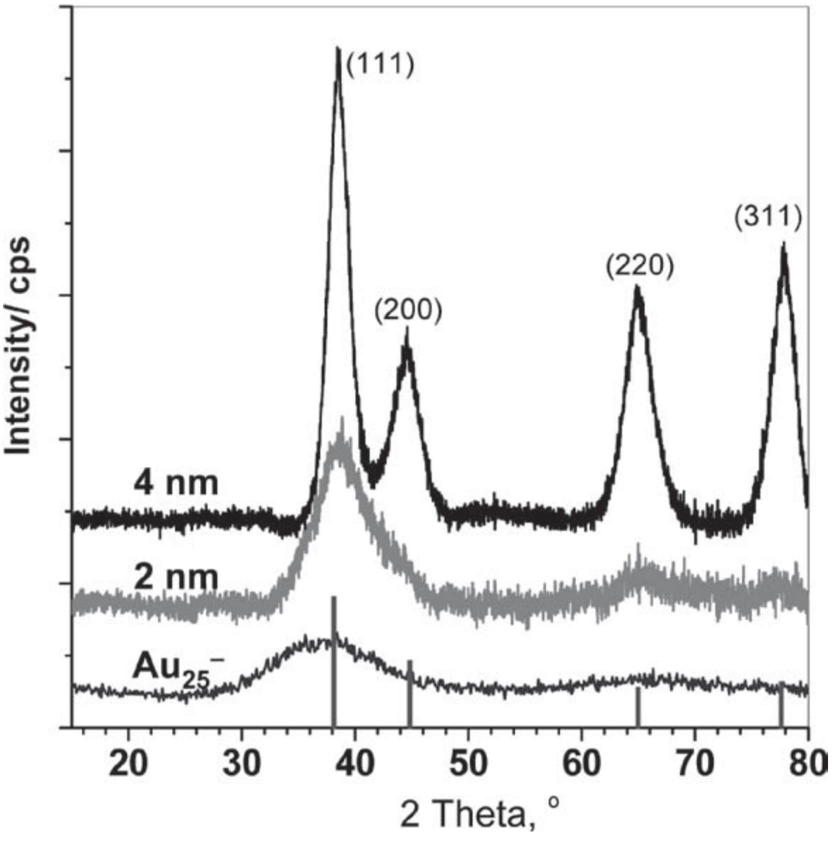

Figure 12: XRD patterns of 4-nm, 2-nm, and $Au_{25}(GS)_{18}$ nanoparticles. The stick pattern corresponds to bulk gold. (X-ray source: Cu Kα). Reprinted with permission from ref. 38. Copyright (2011) WILEY-VCH Verlag GmbH & Co. KGaA, Weinheim.

In this work a series of silver and gold clusters protected by L-glutathione (L-GSH) and N-acetyl-L-cysteine (NALC) ligands were measured. The particle sizes of these clusters were obtained using TEM and XRD as analytical tools. Table 1 shows the summary of this data.[21] The particle sizes of these clusters were determined by XRD and are in reasonable agreement with the sizes determined by TEM, however we believe the TEM analysis to be more accurate.

Table 1: The particles size of four different clusters by TEM and XRD. Reprinted with permission from ref. 21. Copyright (2013) American Chemical Society.

Clusters	**Particles Sizes from TEM**	**Particle Sizes from XRD**
$Ag_n(SG)_m$	~ 1nm	0.7 ± 0.06 nm
$Ag_n(NALC)_m$	Mean 2.37 nm	2.1 ± 0.22 nm
1st $Au_n(NALC)_m$	Mean 3.06 nm	2.63 ± 0.6 nm
2nd $Au_n(NALC)_m$	~ 1nm	0.74 ± 0.07nm

Negishi et. al. confirm that the core of the silver nanoclusters protected by 4-(tert-butyl)benzyl mercaptan (BBSH) is metallic silver (Ag^0), since the XRD diffraction of protected clusters looks different from the powder XRD diffraction of silver oxides (AgO and Ag_2O). They found that the diffraction peaks of clusters were in good agreement with the diffraction peaks of the silver metal, but no peaks were observed at positions corresponding to AgO and Ag_2O. This clearly indicates that the core of the protected clusters does not contain oxygen but is composed of only silver metal (figure 13).[39] The broadening of the diffraction peaks of monolayer protected clusters can be attributed to small sizes of the MPCs and to possible scattering by the ligands, surrounding the metal core.[40]

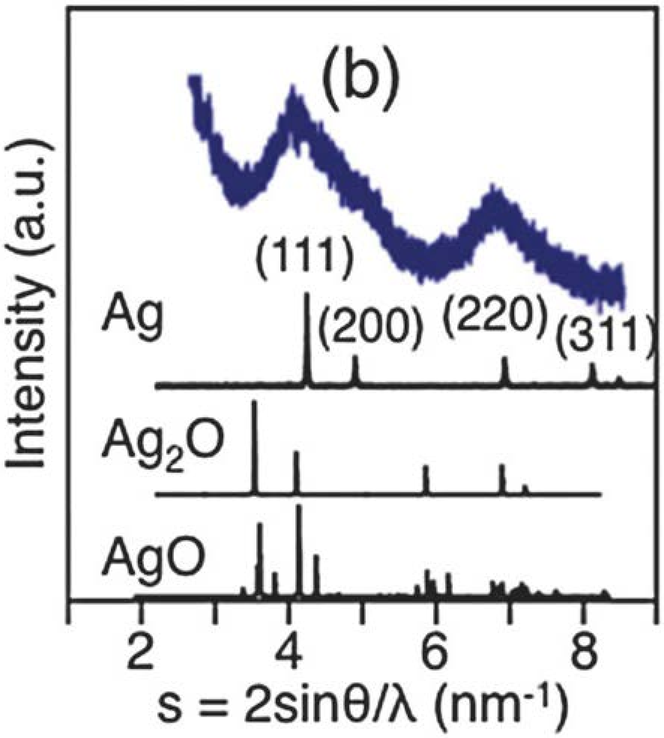

Figure 13: X-ray diffractogram of silver clusters, silver metal and two silver oxides. Reprinted with permission from ref. 39. Copyright (2011) The Royal Society of Chemistry.

1.2.3. Thermogravimetric analysis (TGA), elemental analysis (EA)

The most effective way to obtain the organic ligand mass fraction and the core mass fraction of the metal MPCs is thermal decomposition of the metal MPCs by the dissociation of the thiolate ligands. While this dissociation leads to the formation of different gases such as CO_2, NH_3, H_2O, SO_2 and H_2S, the residue will be the core metal. Figure 14 shows the thermal decomposition of the pure L-glutathione (L-GSH) ligand and 2 nm silver clusters protected by this ligand Ag@SG. The thermogravimetric curve of Ag@SG clusters shows four steps of mass loss upon heating from 40 to 900°C, but the pure ligand shows only three steps to complete the destruction. For hygroscopic substances the first step of cluster decomposition corresponds to the removal of adsorbed water molecules, since the pure ligand does not show any mass loss until 200°C.[20]

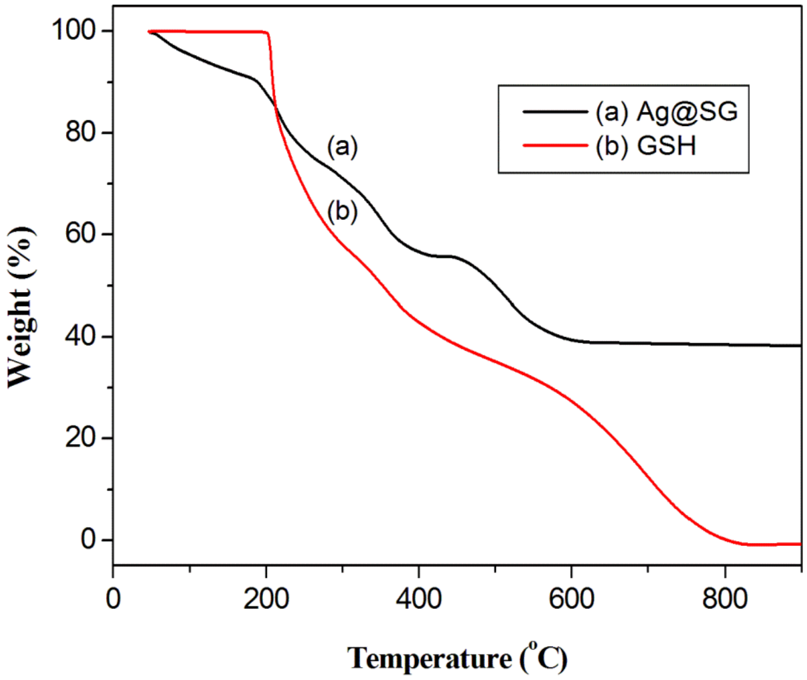

Figure 14: TGA of Ag@SG nanoclusters (curve a) and glutathione ligand (curve b). Reprinted with permission from ref. 20. Copyright (2012) American Chemical Society.

The composition of monolayer protected clusters is further supported by the elemental analysis and atomic absorption spectroscopy (AAS). Table 2 summaries thermogravimetric analysis (TGA), elemental analysis (EA), and atomic absorption spectroscopy (AAS) of the Ag@SCH_2CH_2Ph nanoclusters. The values of the metallic and organic parts of these clusters are the same in the TG analysis and elemental analysis. The molar ratio of C/H/S in Ag@SCH_2CH_2Ph nanoclusters is 7.96:9.08:1, which is in very good agreement with the molecular formula of phenylethylthiolate (C8H9S).[20]

Table 2: Elementals ratios of Ag@SCH_2CH_2Ph determined by thermogravimetric (TGA), elemental analysis (EA), and atomic absorption spectroscopy (AAS). Reprinted with permission from ref. 20. Copyright (2012) American Chemical Society.

Elements	Weight % from TGA	Weight % from EA and AAS
Ag	51.05	50.95
S	11.44	11.49
C	34.27	34.28
H	3.24	3.28

The average metal-to-ligand ratio (M/S) and the molecular formula of metal clusters were calculated from the TG analysis. The larger clusters show a higher metal-to-ligand ratio, because for larger particles the number of atoms inside the metal core becomes larger with respect to the number of the surface atoms of the particle.[20]

1.3. Separation and purification of clusters by polyacrylamide gel electrophoresis (PAGE) and size-exclusion chromatography (SEC)

Procedures for the preparation of monolayer protected nanoclusters are being improved in constantly, but until now only few methods yield monodisperse particles with high purity. The physical properties of nanoclusters are strongly size and shape dependent. Fine tuning of the properties for a specific purpose often requires a perfect control of these two parameters as well as high purity of the sample. Current methods for purification of nanocluster samples that require removal of unreacted free ligands and reducing agents involve centrifugation, reprecipitation, washing, dialysis and extraction to remove impurities. However, to separate monodisperse nanoclusters appropriate purification and separation methods must be used, like polyacrylamide gel electrophoresis (PAGE) or size exclusion chromatography (SEC).

Electrophoresis is the migration of charged molecules in buffered solution in response to an electric field created between a cathode and an anode (figure 15). Their rate of migration depends on the strength of the field, on the net charge, size and shape of the molecules as well as on the ionic strength, viscosity and temperature of the medium in which the molecules are moving.[41] As an analytical tool, electrophoresis is simple, rapid and highly sensitive. It is used analytically to study the properties of a single charged species, and as a separation technique.[42,43]

Generally, the sample is run in a support matrix such as paper, cellulose acetate, starch gel, agarose or polyacrylamide gel.[41] The matrix inhibits convective mixing caused by heating and provides a record of the electrophoretic run: at the end of the run, the matrix can be stained and used for scanning, autoradiography or storage. Due to their color, gold nanoparticles are directly visible by eye.

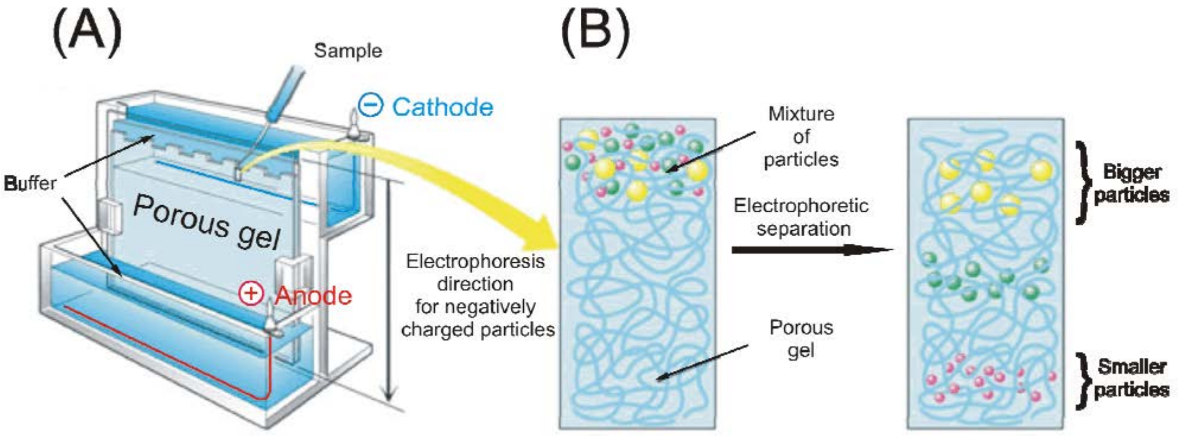

Figure 15: (A) Scheme of a vertical electrophoreses. (B) Position of the particles before (left) and after electrophoretic separation (right). Reprinted after modification from Biochemistry, Seventh Edition. Copyright (2012) W.H. Freeman and Company.

The most commonly used support matrices, agarose and polyacrylamide, provide a means of separating molecules by size (figure 15 B), because of their porous structure.[44] A porous gel may act as a sieve by retarding, or in some cases, completely obstructing the movement of large macromolecules while allowing smaller molecules to migrate freely. As dilute agarose gels are generally more rigid and easier to handle than polyacrylamide of the same concentration, agarose is used to separate larger macromolecules such as nucleic acids, large proteins and protein complexes.[44] On the other hand polyacrylamide is used to separate most proteins and small oligonucleotides that require a small gel pore size for retardation.[41]

Acrylamide gels are formed by the free radical polymerization of acrylamide and bis-acrylamide in a deaerated buffer.[45] This reaction is catalyzed by N,N,N',N' tetramethylethylenediamine (TEMED) and initiated by ammonium persulfate (APS). This separation method is very efficient but very time-consuming and thus impractical on a large scale.[45]

Polyacrylamide gel electrophoresis is used to separate and purify some charged silver[46] and gold[47] nanoclusters protected by the chiral ligands L-glutathione and N-isobutyryl-L-cysteine, respectively. Kumar et. al. succeeded in separating many bands from silver clusters Ag@SG (labeled “Ag:SG” in the original publication as written in the caption of figure 16). Some of them decomposed, but four of them were stable (figure 16 a and b).[46] Gautier et. al. separated 7 or 8 different sized gold clusters protected by N-isobutyryl-L-cysteine ligands, from sizes of 0.7 nm to 1.3 nm (figure 16 C).[47]

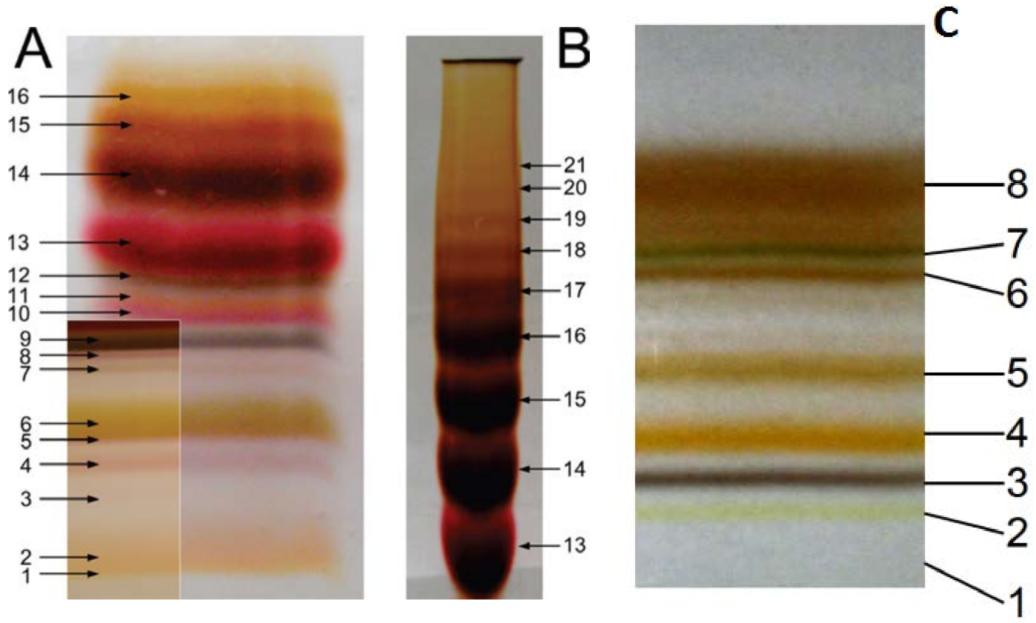

Figure 16: (A) Bands of discrete Ag:SG clusters. The smallest clusters are at the bottom and have the lowest index. Inset: finer bands revealed at a higher concentration. (B) Discrete higher mass clusters, synthesized with less glutathione. Reprinted with permission from ref. 46. Copyright (2010) American Chemical Society. (C) Polyacrylamide gel electrophoresis separation of N-isobutyryl-*L*-cysteine protected gold particles. The separation was performed for 17 hours at 150 V. Reprinted with permission from ref. 47. Copyright (2006) American Chemical Society.

Size-exclusion chromatography (SEC) is a chromatographic method on a semipreparative scale in the range 10 mg of sample loading. The molecules in solution are separated by their size and in some cases by molecular weight. It is usually applied to size selected ultrasmall gold nanoclusters (<2 nm), large molecules or macromolecular complexes.[48-50] This technique is named by two different terms, depending on the type of mobile phase used. When an aqueous solution facilitates the transport of the sample through the column, the technique is known as gel-filtration chromatography. When an organic solvent is used as a mobile phase, this technique is usually called gel permeation chromatography. Differences in elution time are based solely on the volume the analyte. Thus, small molecule can penetrate every corner of the stationary phase pores and will elute late. On the other hand, very large molecules cannot penetrate the pore system of the stationary phase and therefore will elute earlier.

This technique was used to separate polydisperse gold clusters protected by 2-phenylethanethiol (2-PET) ligand into two monodisperse gold clusters $Au_{38}(SCH_2CH_2Ph)_{24}$ and $Au_{40}(SCH_2CH_2Ph)_{24}$ and another semi monodisperse clusters Au_{102}/Au_{144} by Knoppe et. al.. The last cut is a fraction of plasmonic particles with average particle size 2.5±0.2 nm (figure 17).[48]

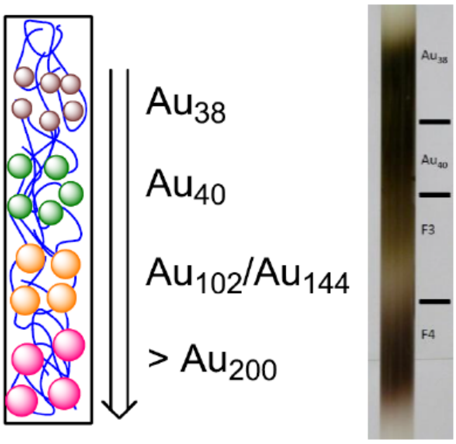

Figure 17: Left: Schematic representation of an SEC column for the size-selection of $Au_{38}(SR)_{24}$ clusters. Right: Photograph of a typical SEC-column during the first elution cycle. The fractions are marked with black separators. Reprinted with permission from ref. 48. Copyright (2011) American Chemical Society.

1.4. Determination the molecular weight of clusters by ESI-MS and MALDI-MS

To determine the molecular weight of monolayer protected clusters a suitable ion source and mass analyzer or mass spectrometer has must be chosen. These compounds usually have a propensity to fragment and possess high molecular weights. These properties make the analysis of such clusters with mass spectrometer challenging. To overcome the problems of fragmentation and high molecular mass, matrix-assisted laser desorption/ionization (MALDI) and electrospray ionization (ESI) are used as an ion source. Both techniques are known as soft ionization techniques, because the ionization process results in no or little fragmentation. In addition, ESI can in many cases produce multiply charged ions, which enables the determination the high molecular weight substances with mass analyzer of a significant lower mass range.[51]

There are many types of mass analyzers like time of flight (TOF), quadrupole, 3D ion traps, linear ion traps, a orbitraps. Usually time of flight (TOF) mass analyzers are used to determine the molecular weight of monolayer protected clusters, since two properties of TOF mass analyzers are in favor of the analysis of such systems. First, they have a higher level of sensitivity when e.g. compared to ion trapping devices. Secondly, the mass range of TOF is high, usually more than 100 kDa, and theoretically unlimited. Table 3 shows a comparison between mass range, mass accuracy and mass resolving power of different mass analyzers.[51]

Table 3: Typical specifications for different mass analyzers. Reprinted with permission from ref. 51a. Copyright (2012) Wiley-VCH Verlag & Co. KGaA, Boschstr. 12, 69469 Weinheim, Germany.

Mass analyzers	**Mass resolving power**	**Mass accuracy**	**Mass range**
Time of flight	1000-40 000	5-50 ppm	>100 000
Quadrupoles	100-1000	100 ppm	4000
3D Ion traps	1000-10 000	50-100 ppm	4000
Linear ion traps	1000-10 000	50-100 ppm	4000
Orbitraps	10 000-150 000	2-5 ppm	6000

Hence, electrospray ionization (ESI-TOF-MS) and matrix-assisted laser desorption/ionization (MALDI-TOF-MS) are used in combination with time of flight mass spectrometry to analyze and measure the molecular weight of biomolecules (biopolymers such as DNA, proteins, peptides and sugars)[52] and large organic molecules (such as polymers, dendrimers and other macromolecules).[53] In the last decay many researchers used these methods to determine the molecular weight and purity of monodisperse gold and silver nanoclusters.[22,54-58]

Dass et. al. studied the effect of laser intensity during MALDI-TOF mass spectrometry of $Au_{25}(SCH_2CH_2Ph)_{18}$ cluster in both positive and negative linear modes using a trans-2-[3-(4-tert-butylphenyl)-2-methyl-2-propenylidene]malononitrile (DCTB) matrix. High laser pulse intensities produced broad peaks at lower mass (~5 kDa) corresponding to loss of ligands and gold from the remnant cores upon ionization and fragmentation. As the laser pulse intensity was decreased, the broadening of the fragment peak intensities also decreased and two sharp peaks appeared at 6060 and 7391 kDa. Further reduction of the laser pulse intensity resulted in only the molecular ion peak of Au_{25} clusters at 7391 Da (figure 18) as visible in the spectrum.[54] Figure 19 shows the effect of different MALDI matrices used to measure $Au_{25}(SCH_2CH_2Ph)_{18}$ clusters in positive linear mode. The differences in the results in figure 18 may come from differing ionization mechanisms. The matrices sinapinic acid (SA), a 1:1 mixture of dihydroxybenzoic acid and R-cyano-4-hydroxycinnamic acid (UMM) and 4′-hydroxyazobenzene-2-carboxylic acid (HABA) are thought to promote proton transfer to the analyte or cation adduction.[54,55]

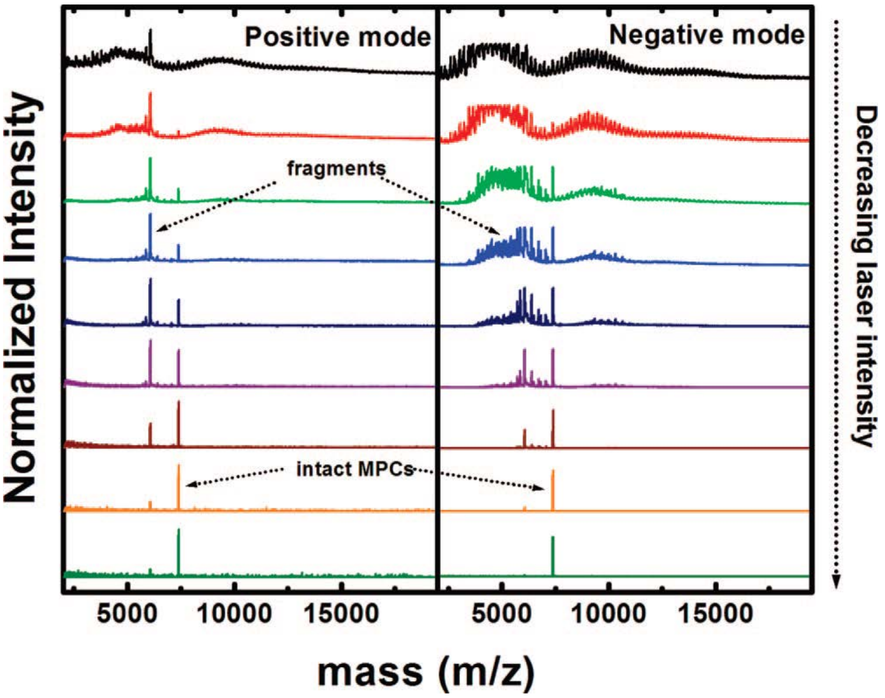

Figure 18: MALDI-TOF-MS spectra of $Au_{25}(SCH_2CH_2Ph)_{18}$ cluster in DCTB matrix with varying laser intensity delineating the molecular ions from fragment ions in positive and negative linear mode. Reprinted with permission from ref. 54. Copyright (2008) American Chemical Society

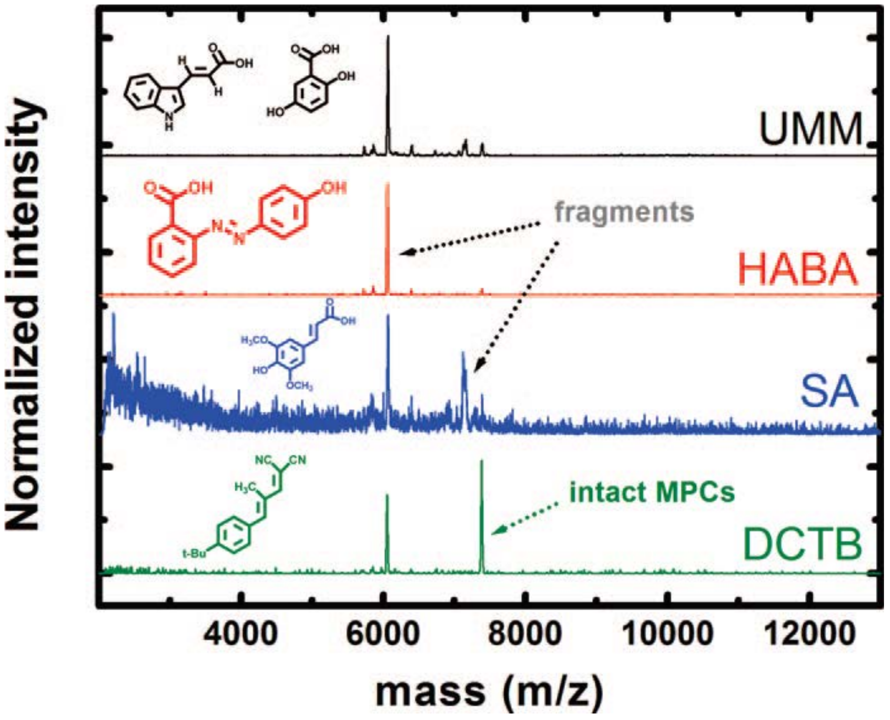

Figure 19: MALDI-TOF-MS spectra of $Au_{25}(SCH_2CH_2Ph)_{18}$ cluster in UMM, HABA, SA, and DCTB matrix showing the superiority of DCTB matrix in obtaining molecular ion over fragment ions. Reprinted with permission from ref. 54. Copyright (2008) American Chemical Society

Figure 20 shows the MALDI-TOF mass spectrometry of highly pure monodisperse $Au_{38}(SCH_2CH_2Ph)_{24}$ and $Au_{144}(SCH_2CH_2Ph)_{60}$ clusters. These mass spectra were obtained in a Bruker Autoflex MALDI-TOF mass spectrometer, after mixing the particle solution with

DCTB matrix in 1:1000 mol ratio. To keep fragmentation as low as possible the laser power was reduced to a threshold value.[22]

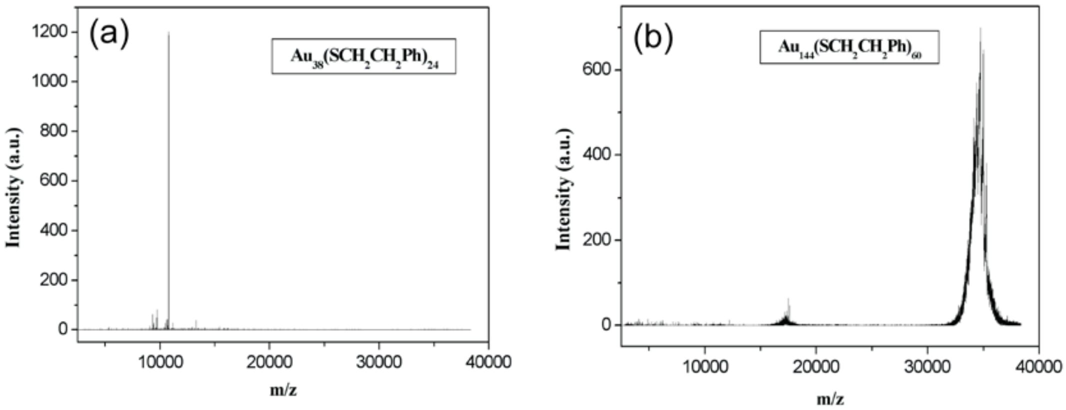

Figure 20: (a) MALDI spectra of Au_{38} clusters. At m/z = 10780 Da a dominant peak is found, which is assigned to the parent ion of $Au_{38}(SCH_2CH_2Ph)_{24}$. Additional peaks of very small intensity indicate some fragmentation in the MALDI process. (b) MALDI spectra of Au_{144} clusters.The broad peak at m/z = 35000 amu clearly confirms the existence of $Au_{144}(SCH_2CH_2Ph)_{60}$. A minor amount of impurities consisting of smaller clusters are indicated by the feature below 20000 amu. Reprinted with permission from ref. 22. Copyright (2013) the Owner Societies.

To determine the exact composition of the $Au_{144}(SCH_2CH_2Ph)_{60}$ cluster, electrospray ionization (ESI) mass spectrometry analysis is used, because it is a softer ionization technique in comparison laser desorption ionization (LDI) or matrix-assisted laser desorption ionization (MALDI). LDI and MALDI often result in nanoparticle fragmentation and thus complicate data interpretation. In ESI-MS analysis of $Au_{144}(SCH_2CH_2Ph)_{60}$ clusters, two sets of peaks were found at m/z 12k and 18k (figure 21). The m/z 12k set of peaks corresponds to a group of triply charged species, evidenced by the mass spacing of $M_{Cs}/3$ (CsOAc was added to the Au_{144} solution to promote particle ionization under ESI conditions). In addition to the plain nanoparticle signal at 12199.4 (M^{3+}), adducts of nanoparticles with various numbers of Cs^+ ions were also observed, including $[M - M_{Cs}]^{3+}$ (m/z =12243.3), $[M - M_{Cs2}]^{3+}$ (m/z =12287.7), $[M - M_{Cs3}]^{3+}$ (m/z = 12332.1), and $[M - M_{Cs4}]^{3+}$ (m/z = 12377.1), (figure 21B). Similarly, the mass peak set at m/z ∼18k is identified to be doubly charged species, (figure 21C).[56]

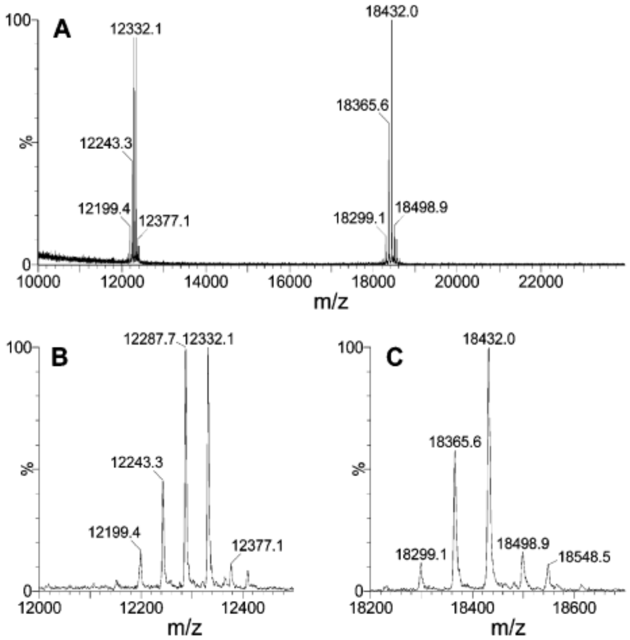

Figure 21: (a) ESI mass spectra of $Au_{144}(SCH_2CH_2Ph)_{60}$ nanoparticles. (b) Zoomed-in spectrum of the 3+ ion set. (c) Zoomed-in spectrum of the 2+ ion set. In both sets, adducts of $Au_{144}(SCH_2CH_2Ph)_{60}$ with various numbers of Cs^+ were detected in addition to the plain particle. Reprinted with permission from ref. 56. Copyright (2009) American Chemical Society

Opposed to gold clusters, determining the exact size of silver clusters is a challenging task, because the isotopic distributions of silver clusters are complicated significantly by the two abundant naturally occurring silver isotopes ^{107}Ag and ^{109}Ag, in addition to carbon and sulfur isotopes. Wu et. al. succeeded in determining the molecular weight of Ag_7 protected by 2,3-dimercaptosuccinic acid (DMSA) ligands (donoted as $Ag_7(DMSA)_4$) by ESI-MS analysis for first time (figure 22).[57] Cathcart et. al. also tried to measure $Ag_{25}(Capt)_{18}$ clusters. However, he was not able to observe characteristic patterns of intact AgNCs and detected MS spectra corresponding to diverse silver thiolate fragments, especially at higher desolvation (figure 23a). Deconvolution of the fragmentation patterns 15 yielded the assignment of the cluster composition as with 24 silver atoms and 16 captopril ligands, which may not be overly reliable, given the clear limitations in detecting larger fragments of clusters due to the isotope broadening of silver (figure 23b).[35] So there are limitations in determining the molecular weight of silver clusters up to clusters consisting of a few Ag atoms (less than 10).[58]

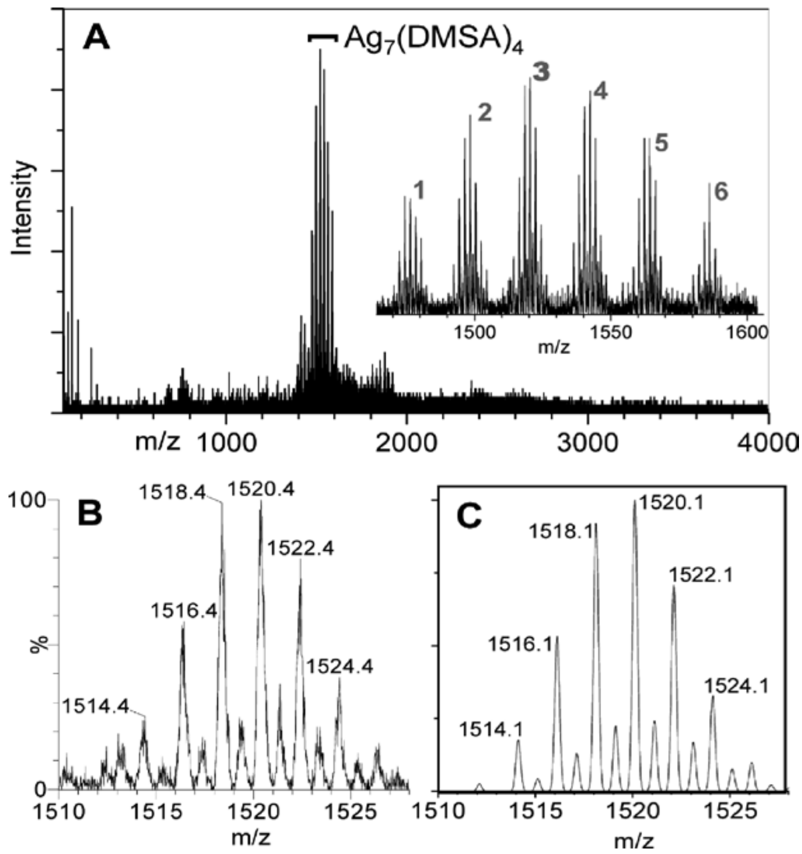

Figure 22: (A) ESI spectra of silver clusters (negative ion mode, inset shows the zoomed-in spectrum). (B) and (C) show the experimental and simulated isotopic pattern of Ag$_7$L$_4$ - 2H + 2Na, respectively. Reprinted with permission from ref. 57. Copyright (2009) American Chemical Society

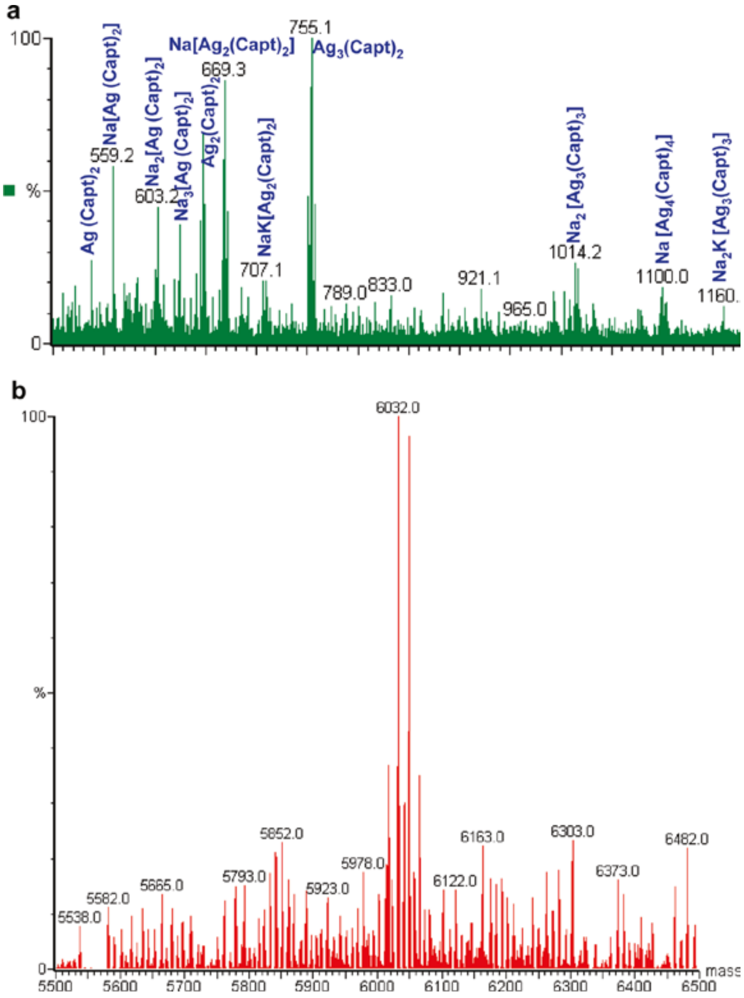

Figure 23: (a) Negative-ion ESI mass spectra of captopril-stabilized AgNCs with peak assignment. (b) Deconvoluted spectrum based on the data shown in (a). The displayed peak closely corresponds to the cluster composition of $Ag_{24}(Capt)_{16}$, one $Ag(Capt)_2$ less than tentatively proposed $Ag_{25}(Capt)_{18}$. “Capt” stands for captopril. Reprinted with permission from ref. 35. Copyright (2009) American Chemical Society

1.5. Chirality of monolayer protected nanoclusters

Chiral metal surfaces have been an interesting research field in the last ten years,[59] mainly motivated by applications in the field of chiral technologies such as enantioselective heterogeneous catalysis and chiral recognition. The use of chiral metal surfaces is a promising strategy for the preparation of enantiopure compounds, as in pharmaceutical research. The different types of chirality observed for bare metal surfaces are illustrated in figure 24. $Ag(643)^R$ and $Ag(643)^S$ are nonsuperimposable mirror images of one another. This intrinsic chirality is due to the presence of kinked steps with unequal step lengths on either side of the kinks (figure 24a).[59a] These chiral metal surfaces reacted in different ways with the two enantiomers of a chiral compound.[60,61] The adsorbed molecules can furthermore self-assemble and create different levels of organization, from small nanostructures that break local mirror symmetry to macroscale domains that destroy the reflection symmetry over the entire surface. This organizational chirality is depicted by the organization of *S*-alanine on Cu(110). The scanning tunneling microscopy (STM) image reveals a first level of organizational chirality due to the formation of nanoclusters made of 6 or 8 molecules.[62] So the metal surfaces can show either intrinsic or induced chirality, due to chiral kink sites (intrinsic) or adsorption of chiral adsorbates (induced).

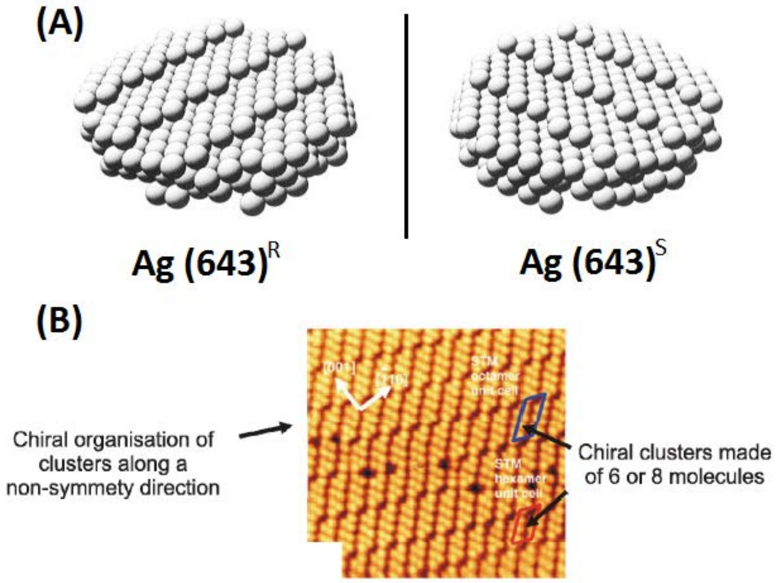

Figure 24: Chirality on extended metal surfaces. (A) Intrinsic chirality. Reprinted with permission from ref. 59a. Copyright (1996) American Chemical Society. (B) Organizational chirality. Reprinted with permission from ref. 62. Copyright (2005) Elsevier B.V. All rights reserved.

Chirality in thiolate-protected gold clusters was first observed by Whetten and co-workers in 1998 by studying gold nanoclusters protected by L-glutathione (L-GSH).[63] After purification of the clusters, CD spectra were recorded and Cotton effects were observed for transitions at higher wavelengths compared to the free glutathione ligand (figure 25).

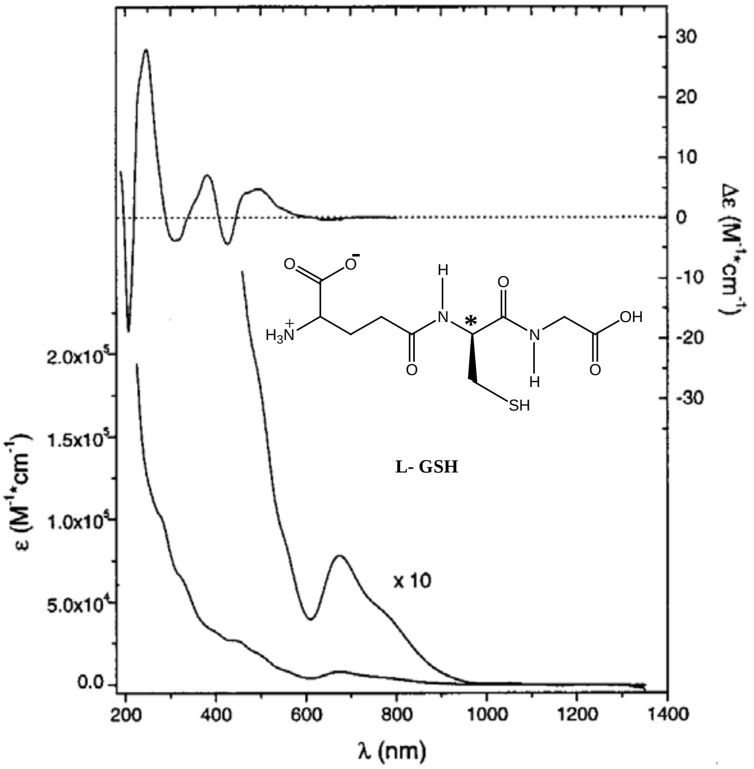

Figure 25. CD spectrum (top) and absorption spectrum (bottom) of L-GSH-protected gold clusters. Reprinted with permission from ref. 63. Copyright (1998) American Chemical Society.

In the last decades many researchers tried to explore the origin of chiroptical effects. Several models have been discussed. It was proposed that the clusters either have intrinsically chiral cores,[64,65] or the electrons might feel the dissymmetric field that is created by the chiral adsorbates, without a change in the geometric lattice of clusters (figure 26).[66]

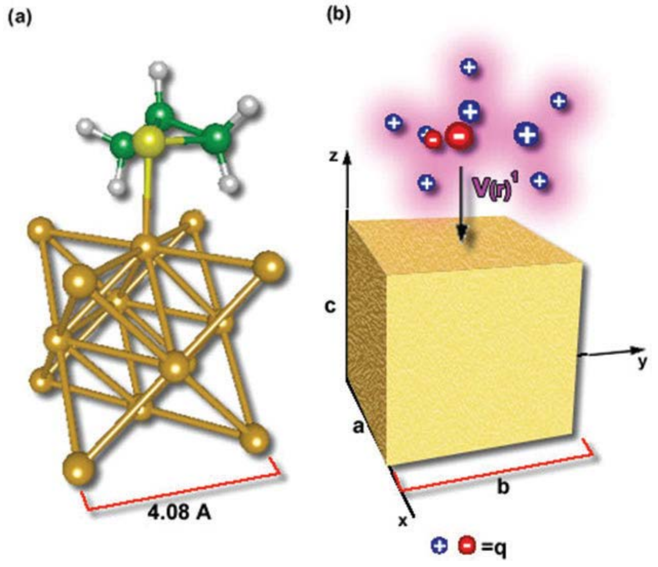

Figure 26: Schematic representation of (a) a molecular adsorbate and Au cluster (i.e. Au_{14}(R-methylthiirane) represented by (b) a system of point charges. Reprinted with permission from ref. 66. Copyright (2006) The Owner Societies.

The chirality of metal (Ag and Au) monolayer protected nanoclusters is highly affected by the particle size of the cluster core. With a decrease in the core size, the chirality of nanoclusters increases.[21] Figure 27 shows the circular dichroism (CD) of some different sizes of gold nanoclusters protected by L-glutathione (L-GSH). The first fraction of gold clusters (the average particle size 2.51 nm) show only very weak signals (curve a), but particles of fraction 2 (average particle size 1.89 nm) exhibit strong CD-signals (curve b) in the near UV and visible spectral regions. Like clusters of fraction 2, the CD spectrum of $Au_{25}(SG)_{18}$ nanoclusters (curve c) is dominated by several peaks.[21]

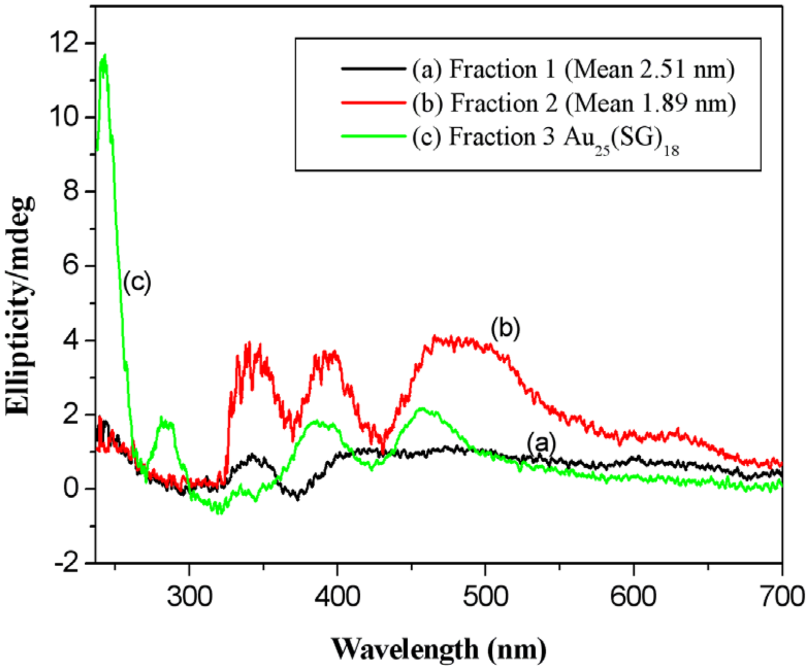

Figure 27: CD spectra of Au nanoparticles of different size protected by L-glutathione. Reprinted with permission from ref. 21. Copyright (2013) American Chemical Society.

Chirality cannot only be imparted to a gold cluster by protection with a chiral ligand, but the clusters themselves bear some intrinsically chiral features. The short -(SR-Au-SR)- or long -(SR-Au-SR-Au-SR)- oligomers with sulfur (ligands) and gold atoms arranged in chiral patterns along the surface of the cluster cores, add a second chiral feature.[67,68]

The staple motifs $–SR-(Au-SR)_n-$ (n = 1, 2, 3) are commonly found in the structures of thiolate protected gold clusters.[67-70] In the case of the monomer (n = 1), it can occur in *cis* and *trans* configurations (scheme 1). In a monomeric staple, four isomers can be formed from two monomers ((*S*, *S*), (*S*, *R*), (*R*, *S*) and (*R*, *R*)), since 2^m (m: number of stereogenic centers) permutations are possible. The assignment of the stereodescriptors is based on the five- or seven-membered rings that are formed by the staple motif (scheme 1).[71]

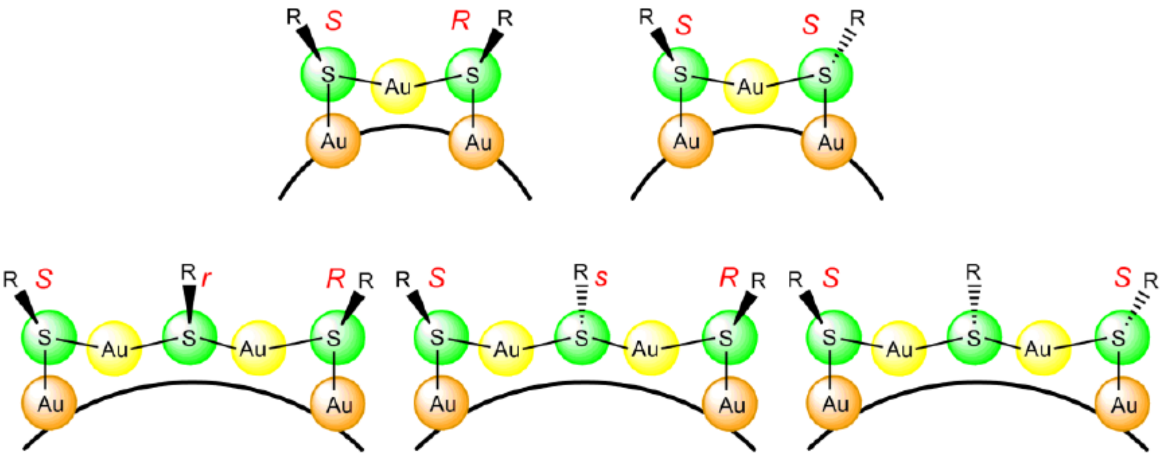

Scheme 1. Stereochemistry in the staple motifs. Top: Monomeric staples in cis (left) and trans (right) configuration. The stereodescriptors of the sulfur atoms are marked in red. Bottom: Dimeric staples in all-cis (left), zig-zag (middle) and trans-cis (right) configuration. For the all-cis and zig-zag case, the central sulfur atom is a pseudochiral center only (indicated by a small letter for the stereodescriptor). Note, that the central sulfur atom in the trans-cis case is not a pseudochiral center. More combinations are possible (overall 2^n = 4 and 8 respectively for monomeric and dimeric staples, since two or three stereogenic centers have to be considered). Orange: Au atoms on the surface of the cluster core (no charge); Yellow: Au adatoms (charge +1); Green: Sulfur (charge -1). Reprinted with permission from ref. 71. Copyright (2012) Macmillan Publishers Limited. All rights reserved.

Assignment of all absolute configurations of gold clusters becomes very complex at larger sizes. For instance, the $Au_{38}(SR)_{24}$ cluster has 2^{24} = 16,777,216 different configurations for the sulfur atoms (which partly can be ruled out due to steric reasons). This makes the prediction of CD spectra extremely complicated. It has been shown that certain configurations lead to chiral overlayers, which can induce a CD spectrum.[144] However, in a cluster that is protected by achiral ligands, the CD contributions are expected to cancel out. Nevertheless, when protecting a cluster with a chiral ligand, it is possible to stabilize certain configurations.[71]

Dolamic et. al. and Knoppe et. al. succeeded in separating two enantiomers of a gold cluster protected by achiral 2-phenylethanethiol ligand ($Au_{38}(SCH_2CH_2Ph)_{24}$) and ($Au_{40}(SCH_2CH_2Ph)_{24}$), respectively with chiral high-performance liquid chromatography (Chiral HPLC). The enantiomers show mirror-image circular dichroism responses and large anisotropy factors of up to $4x10^{-3}$ and $6x10^{-3}$, respectively (figure 29).[71]

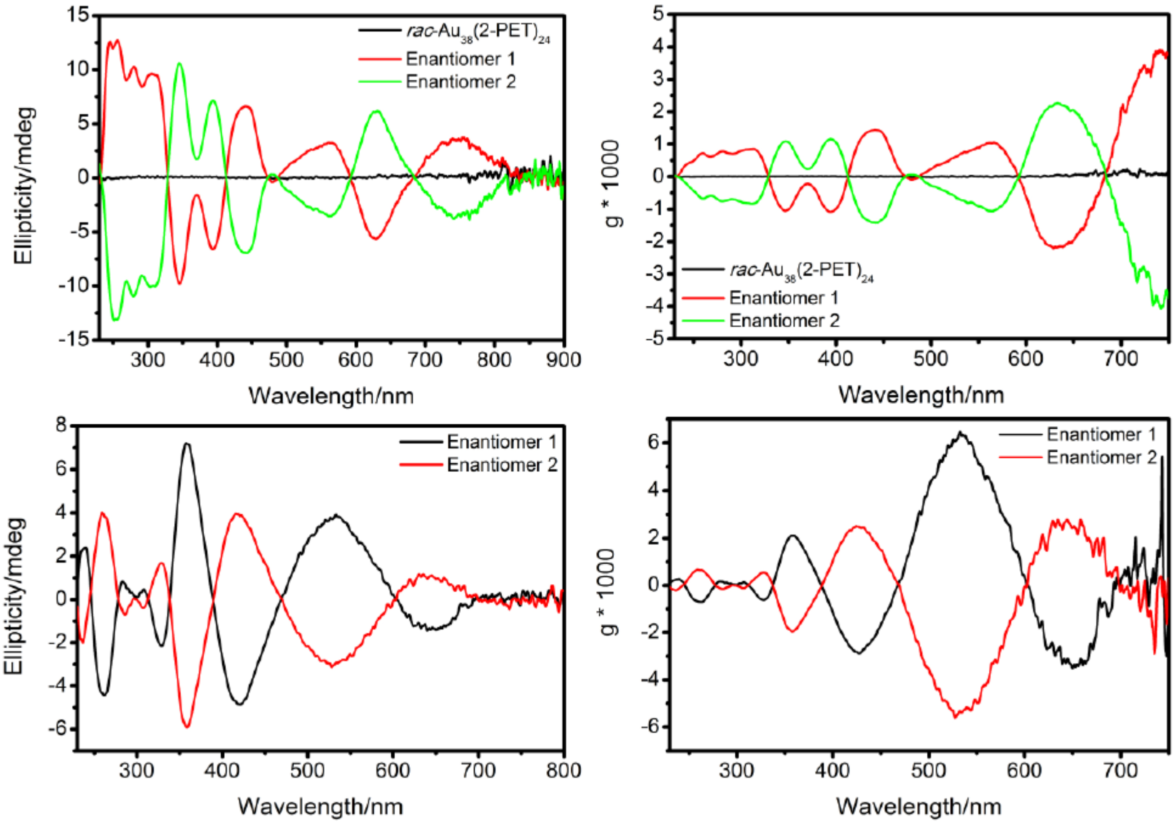

Figure 28: Top: CD spectra (left) and anisotropy factors (right) of the isolated enantiomers of Au$_{38}$(2-PET)$_{24}$. As expected, the racemate (blue) does not give any chiroptical response. Bottom: CD spectra (left) and extrapolated anisotropy factors (right) of Au$_{40}$(2-PET)$_{24}$. Reprinted with permission from ref. 71. Copyright (2012) Macmillan Publishers Limited. All rights reserved and Wiley-VCH Verlag GmbH & Co. KGaA, Weinheim.

In 2007 Jadzinsky et. al. published the first crystal structure of a thiolate-protected gold cluster.[67] The crystal structure bears intrinsic chirality due to the arrangement of the ligands on the surface of the cluster core (figure 29). As shown in figure 29, the particles are chiral and consist of a racemic mixture (figure 29 A). However, the central gold atoms are packed in a Marks decahedron (MD) which is highly symmetric and similar to the fcc structure of bulk gold (figure 29 B). The chirality arises from the number and geometry of equatorial atoms on the surface. The deviations in local symmetry may reflect the interaction of the equatorial atoms with the *p*-mercaptobenzoic acid (*p*-MBA) monolayer. Furthermore, most sulfur atoms bonded to two gold atoms in two different shells are stereogenic centers (figure 29c).[67]

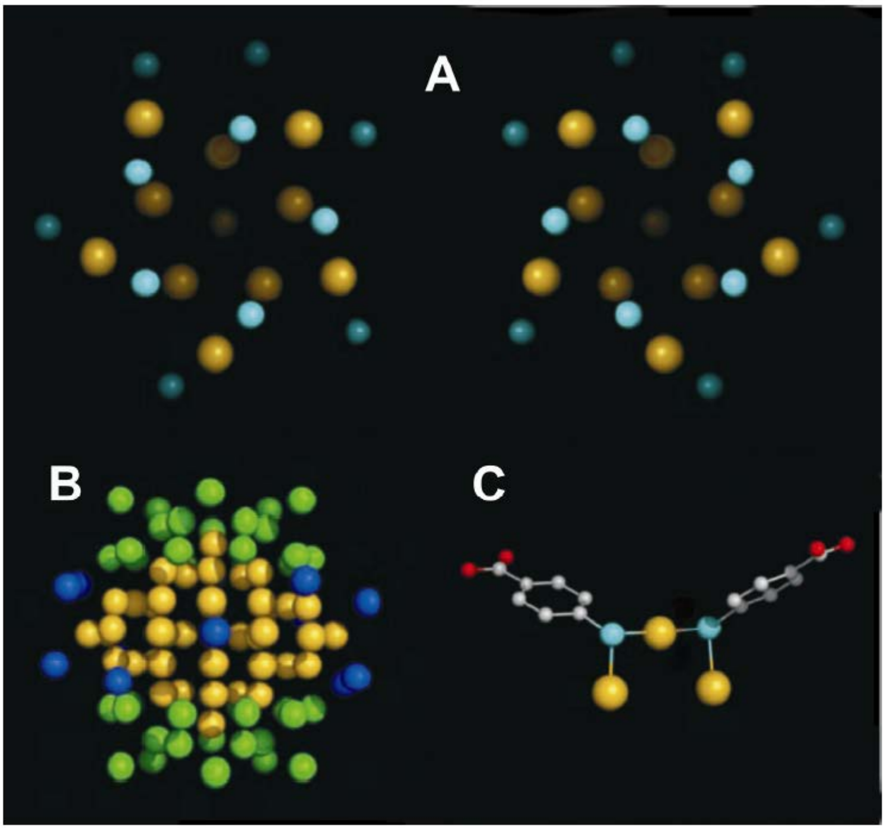

Figure 29: X–ray crystal structure determination of the Au_{102}(*p*-MBA)$_{44}$NPs. A) View down the cluster axis of the two enantiomers (gold atoms in yellow and sulfur atoms in cyan). B) Packing of gold atoms in the core. MD (2,1,2) in yellow, two 20-atom“caps” at the poles in green, and the 13-atom equatorial band in blue. C) Sulfur-gold interactions in the surface of the NPs. Example of two *p*-MBAs interacting with three gold atoms in a bridge conformation. Gold atoms are yellow, sulfur atoms are cyan, oxygen atoms are red, and carbon atoms are gray. Reprinted with permission from ref. 67. Copyright (2007) from AAAS.

1.6. Characterization of ligand-metal bonding by FTIR

Infra-red analysis elucidated the structural properties of the ligands binding to the metal nanoclusters. By comparing the IR absorption spectra of pure ligands with those of the protected metal nanoclusters, the disappearance of the S−H vibrational band (2535−2564 cm^{-1}) in the protected nanoclusters confirms an anchoring of ligands to the cluster surface through the sulfur atom.[20,72]

Figure 30 shows the vibrational spectrum of 2-phenylethanethiol (2-PET) ligand and the silver nanoclusters protected by this ligand. The antisymmetric (d^-) CH_2 stretching band at 2932 cm^{-1}, the symmetric (d^+) CH_2 stretching modes at 2851 cm^{-1},[73,74] and the C−H aromatic stretching bands in the range of 3025−3085 cm^{-1} appear at the same position for the pure ligand and the protected nanoclusters. The vibrational band of S−H at 2535−2564 cm^{-1} has completely disappeared upon the formation of the $Ag@SCH_2CH_2Ph$ nanoclusters (figure 30b). This indicates that the ligands are anchored to the silver cluster via the sulfur atom.[20]

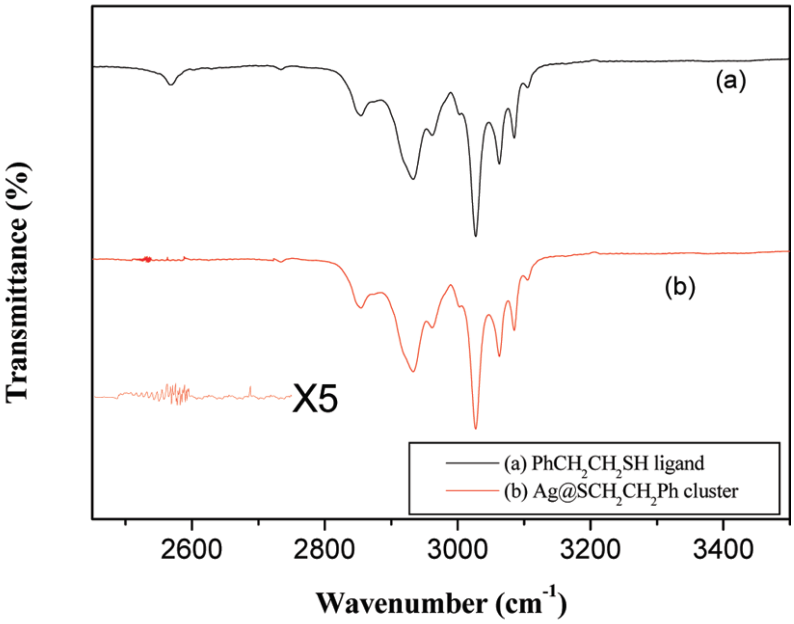

Figure 30. FTIR spectra of 2-phenylethanethiol $PhCH_2CH_2SH$ (a) and $Ag@SCH_2CH_2Ph$ nanoclusters with inset of $Ag@SCH_2CH_2Ph$ nanoclusters (× 5) (b). The spectra show that the band around 2560 cm^{-1} disappears in the spectrum of the cluster with respect to that of the bare ligand. This band can be assigned to the S−H stretching frequency, and its disappearance clearly indicates that the ligand is bound to the cluster via the sulfur atom. Since the spectrum of the clusters otherwise stays more or less unaltered, it can be concluded that no further changes happened to the ligand. Reprinted with permission from ref. 20. Copyright (2012) American Chemical Society.

The gold and silver nanoclusters can be protected not only with thiolates but also by amides[75] and L-amino acids.[76] Figure 31 shows the FTIR spectrum of bovine serum albumin (BSA), Au–BSA, folic acid (FA) and Au– BSA–FA nanocluster conjugates. A protein with a high proportion of α-helix shows an amide I band at 1654 cm^{-1} for BSA (figure 33a). The band appearing at 1545.00 cm^{-1} can be attributed to a strong primary amine scissoring, whereas the band centered at 3435.98 cm^{-1} can be attributed to primary amines. The band at 2958.79 cm^{-1} corresponds to C–H vibration and the broad band at 701.65 cm^{-1} can be attributed to $-NH_2$ and –NH wagging modes.[77] In the final conjugate of Au–BSA–FA nanoclusters, all the characteristic vibrational modes associated with FA, such as C–H stretching at 2943.00 cm^{-1} and aromatic ring stretching of the pyridine and p-amino benzoic acid moieties in the range of 1476–1695 cm^{-1} can be clearly seen. Peaks at 1336.00 and 912.00 cm^{-1} show the presence of aromatic C–H in-plane and out-of-plane bending, respectively.[78] The line broadening appearing over 1652–1350 cm^{-1} is indicative of the covalent linkage of FA with BSA.

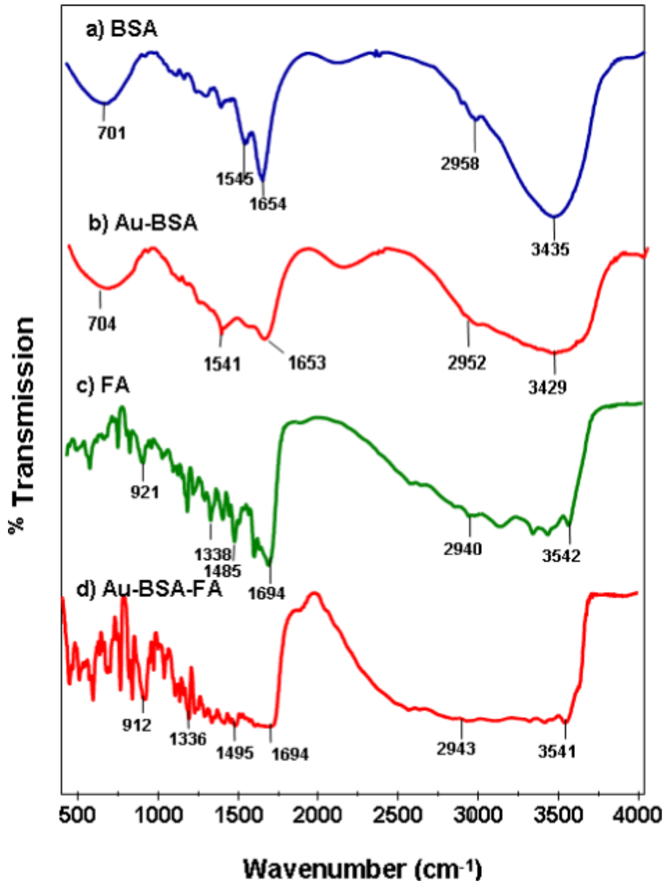

Figure 31: FTIR spectra of (a) BSA, (b) Au–BSA, (c) FA and (d) Au–BSA–FA samples, recorded in KBr-supported pellets. The characteristic vibration bands related to BSA and FA can be clearly seen in the final conjugates of Au–BSA–FA. Reprinted with permission from ref. 75. Copyright (2010) IOP Publishing Ltd Printed in the UK.

In this work infra-red spectroscopy of some size selected gold clusters protected by 2-phenylethanethiol ligands have been studied.[22] Figure 32 displays the infrared spectra of the neutrally charged $Au_{25}(SCH_2CH_2Ph)_{18}$ cluster and the bare 2-phenylethanethiol ligand. As usual the S-H stretching vibration peak at 2567 cm^{-1} is visible only in the spectrum of the ligand (figure 32b) and disappears in that of the Au_{25} clusters. This confirms the ligand is anchored to the gold cluster surface via the sulfur atom.[20] In the Au_{25} cluster spectra the peaks associated with aromatic stretching vibrations are red-shifted and overlap with the aliphatic modes resulting in just two peaks below 3000 cm^{-1} (2980 cm^{-1} and 2854 cm^{-1}). This phenomena appears only for the $Au_{25}(SCH_2CH_2Ph)_{18}$ cluster.[22] This significant change in the IR spectrum of $Au_{25}(SCH_2CH_2Ph)_{18}$ is not only of fundamental interest but also allows for determining *in-situ* the purity and monodispersity of the sample by FTIR spectroscopy during synthesis.

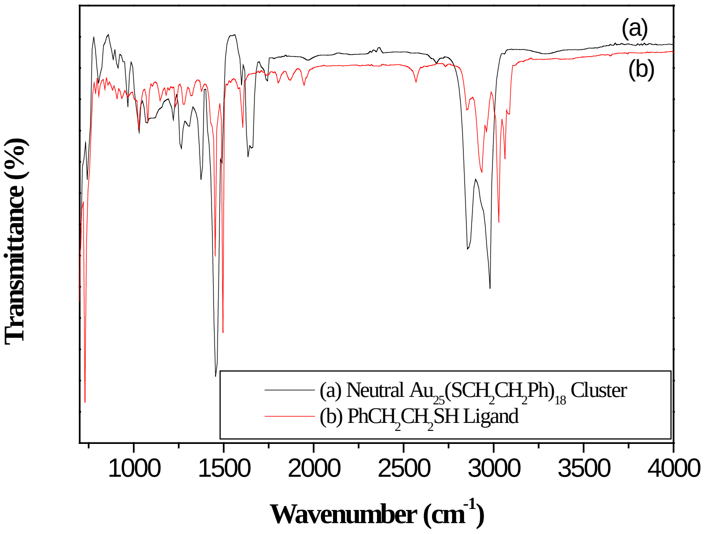

Figure 32: FTIR spectra of the neutral form of $Au_{25}(SCH_2CH_2Ph)_{18}$ (Au_{25}^0) cluster (a) and the 2-phenylethanethiol ($PhCH_2CH_2SH$) ligand (b). In the spectra of the ligand only transitions of aliphatic as well as aromatic C-H stretching modes can be found. In the spectra of Au_{25} clusters the latter transitions are strongly red-shifted and overlap with the aliphatic modes. Thus, only two peaks can be found in this spectral region for Au_{25}. Reprinted with permission from ref. 22. Copyright (2013) the Owner Societies.

1.7. Photoluminescence spectroscopy of protected clusters

The photoluminescence of metal (gold and silver) nanoparticles has become a highly interesting research field in chemistry because of the application of the clusters in sensors, biolabeling and drug delivery or for efficient energy transfer.[79] However, the origin of fluorescence still remains unclear. Jin and co-workers studied the fluorescence properties of $Au_{25}(SR)_{18}$ (SR= SCH_2CH_2Ph, $SC_{12}H_{25}$ and SC_6H_{13}) clusters and suggested two possible mechanisms to interpret the origin of the fluorescence, (i) the fluorescence may arise from the metal core or (ii) from the interaction of the metal core and the surface ligands. In the latter case, the interaction of the ligands with the cluster can either take place via charge transfer through the metal-sulphur bonds, or by direct donation of delocalized electrons from electron-rich groups in the ligand molecules.[80]

Luminescence lifetimes of the nanoparticles were found to be strongly dependent on excitation wavelengths, and singlet and triplet excited states involving the emission were found to be degenerate in energy.[81] After excitation of 1.7 nm gold nanoparticles protected by L-glutathione (GSAuNPs) at 420 nm an orange-colored emission with a maximum at 565 nm was observed. The luminescence lifetime of this emission was approximately a microsecond (1.7 μs (79%)/0.35 μs (21%)). When the excitation wavelength was shifted to 530 nm orange-colored emission was observed at the same wavelength maximum, but with considerably shorter lifetimes (2.8 ns (81%)/33 ns (19%)).[68] This fluorescent lifetime is on the same order of fluorescent gold nanoclusters (Au^0), where nanosecond emission originates from singlet excited states.[82] The dramatic decrease in luminescence lifetimes of orange-emitting particles at different excitation wavelengths implies that triplet and singlet excited states in the luminescent gold nanoparticles are degenerate in energy (figure 33).[81] This observation is in good agreement with the theoretically reported degeneracies between singlet and triplet states in Au_{56} clusters.[83] When the particle size of these nanoparticles is a little larger (2.1 ± 0.4 nm), these particles show a yellow emission at 545 nm after excitation at 415 nm. Again, the emission lifetime is dependent on the excitation wavelengths.[81]

The photoluminescence of these gold nanoparticles exhibit d and sp bands.[84-86] As the sizes of both orange-emitting and yellow-emitting of this nanoparticles are around 2 nm, the energy level spacing within the sp band is too small to give visible emission.[30] This emission can most likely be assigned to transitions between LUMO levels in the sp band and HOMO levels in the d band, but not to transitions within the sp band.[81]

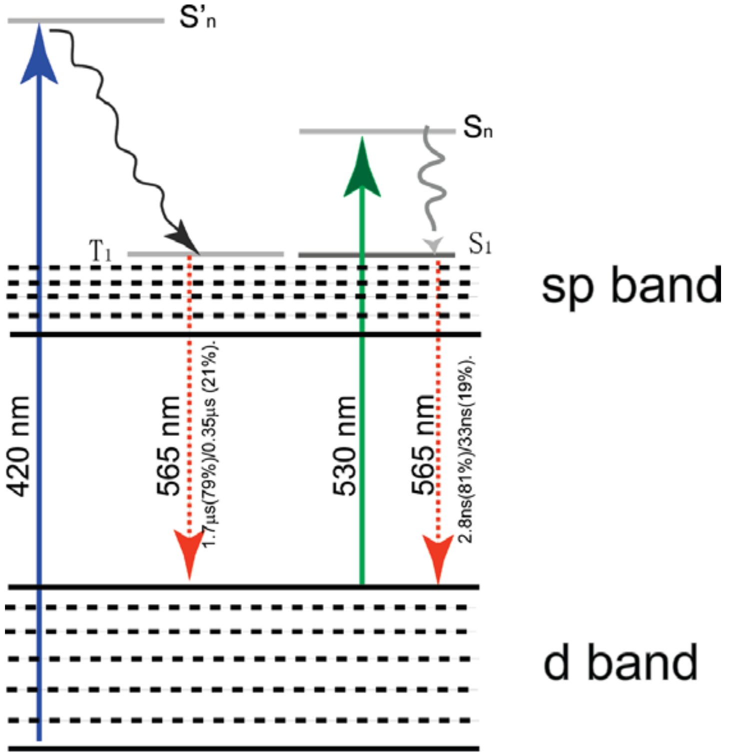

Figure 33: A possible optical transition scheme for orange-emitting GS-AuNPs where the luminescence originates from transitions between d and sp bands. When the NPs are excited at 420 nm, the electrons will be relaxed from triplet states in sp bands to some ground states in d bands, leading to microsecond emission. Once the excitation wavelength is shifted to 530 nm, the electrons will be decayed from singlet excited states in the sp band to singlet states in ground states and give out nanosecond emission. The triplet and singlet excited states in the luminescent gold nanoparticles are degenerate in energy. Reprinted with permission from ref. 81. Copyright (2010) American Chemical Society.

Murray and co-worker studied the effect of ligand exchange of nonpolar ligands by more polar thiolate ligands through near-infrared photoluminescence of monolayer-protected $Au_{38}(SCH_2CH_2Ph)_{24}$ and $Au_{140}[S(CH_2)_5CH_3]_{53}$ clusters (MPCs) (figure 34). The polar ligands are thiophenolates with a variety of *p*-substituents (chloride and bromide), alkanethiolates ω-terminated by alcohol, acids, or quaternary ammonium groups, and thio-amino acids. The intensity of near-infrared (NIR) luminescence of Au_{38} and Au_{140} clusters increases linearly with the number of new polar ligands (figure 34). The increased intensities are larger for thiophenolate ligands having more electron-withdrawing substituent like chloride and bromide (figure 34a and b). By enhancing the electronic polarization of the bonds between the Au core atoms and their thiolate ligands the luminescence properties increases.[87]

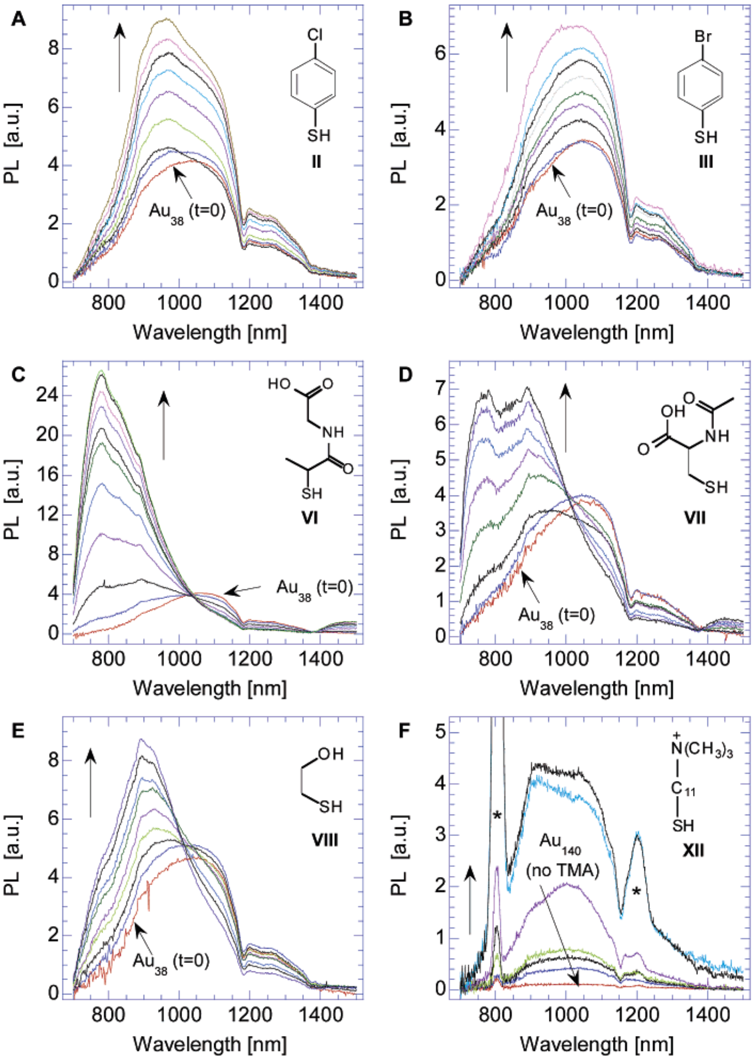

Figure 34: Luminescence spectra of $Au_{38}(SC_2Ph)_{24}$ MPCs in THF (excited at 450 nm) during (in situ) ligand exchange with (A) 4-chlorothiophenol (**II**), (B) 4-bromothiophenol (**III**), (C) tiopronin (**VI**), (D) *N*-Acetyl-L-cysteine (**VII**), and (E) 2-mercaptoethanol (**VIII**). Panel F shows luminescence spectra (excited at 400 nm) of $Au_{140}[S(CH_2)_5CH_3]_{53}$ MPCs in CH_2Cl_2 for increasing times (bottom to top) of ligand exchange with TMA (**XII**), following isolation and cleanup of the exchange product. Asterisks indicate artifacts from second- and third order excitation leakage due to wide slits; the sharp minimum at 1165 nm is due to background

solvent/ligand absorption. Reprinted with permission from ref. 87. Copyright (2006) American Chemical Society.

In this work the photoluminescence spectra of prepared nanoclusters in aqueous solutions were studied at room temperature. All measurements were conducted in aerated conditions. The cluster concentrations for the PL measurements were 1 mg/ml and a linear increase of the PL intensities with cluster concentration was observed. Figure 35 shows the emission spectra of two different sizes of silver clusters protected by two different ligands, L-glutathione ($Ag_n(SG)_m$) and N-acetyl-L-cysteine ($Ag_n(NALC)_m$). $Ag_n(SG)_m$ clusters show a photoluminescence maximum at 660 nm and $Ag_n(NALC)_m$ clusters exhibit a broad peak with a maximum at 611 nm (50 nm blue shifted) in their photoluminescence spectra after exciting the samples at 478 nm and 480 nm, respectively.[21]

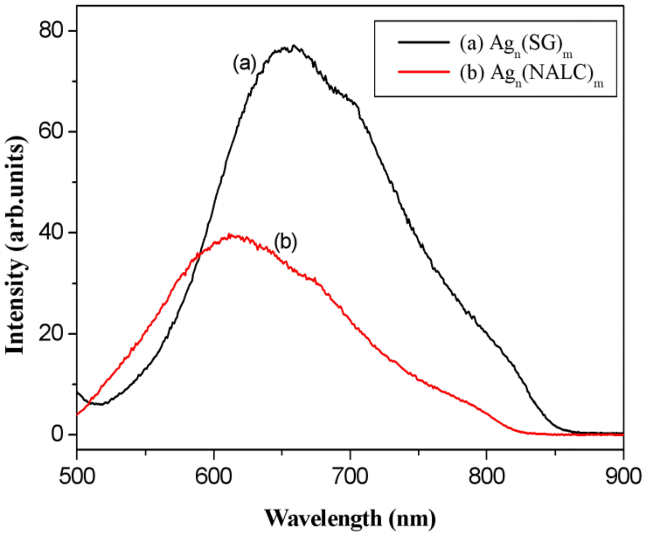

Figure 35: Photoemission spectra of $Ag_n(SG)_m$ (curve a) and $Ag_n(NALC)_m$ (curve b) nanoclusters. While the spectra of $Ag_n(SG)_m$ clusters show one broad maximum at 660 nm, the emission spectra of $Ag_n(NALC)_m$ clusters are shifted to the blue and give one maximum at a wavelength of 611 nm. The emission was initiated by exciting the clusters with a wavelength of 478 and 480 nm for $Ag_n(SG)_m$ and $Ag_n(NALC)_m$, respectively. Reprinted with permission from ref. 21. Copyright (2013) American Chemical Society.

The photoluminescence of monolayer protected clusters is highly affected by the size of the core clusters and the polarity of protecting ligands. As in figure 36, the emission peak maximum at 738 nm of $Au_{25}(SG)_{18}$ is higher than that for clusters of the same size but protected by the less polar ligand, N-acetyl-L-cysteine, after excitation by 450 nm. When exciting gold clusters of different sizes but protected by the same ligands (NALC or L-GSH) with 450 nm, the emission maximum also appears at different wavelengths. It is found that by decreasing the particles size the emission peak shifts to higher wavelengths (red shift).[21]

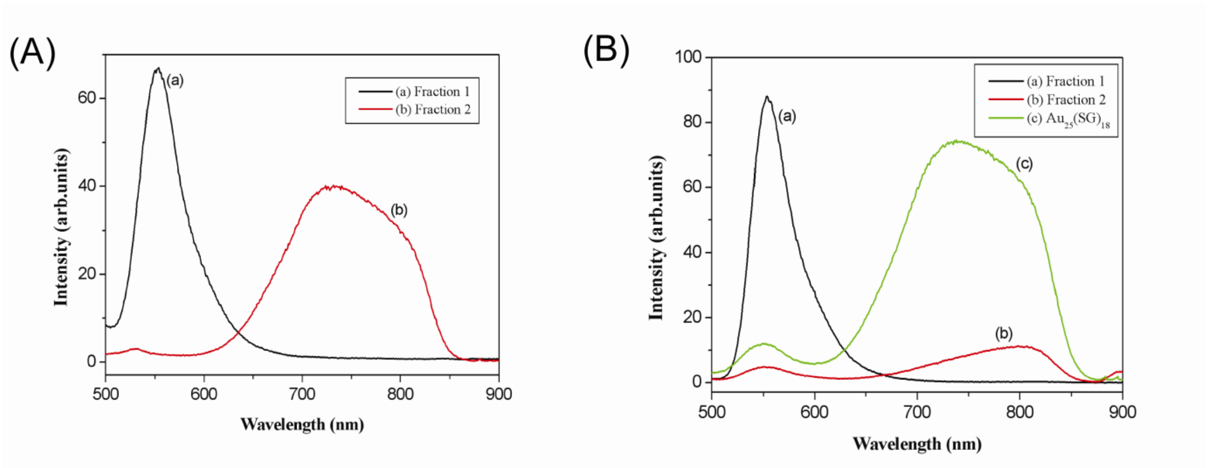

Figure 36: PL-spectra of the fractions of gold clusters protected by N-acetyl-L-cysteine (A) in comparison to the spectra of the fraction of Au-clusters protected by L-glutathione (B). A: The cluster of the first fraction of $Au_n(NALC)_m$ (curve a) gives one emission maximum at 554 nm. Clusters of fraction 2 are smaller in size (about 1 nm in diameter) and show one broader peak at 738 nm (curve b). Their position as well as the shape of this peak is almost identical to that of monodisperse clusters of $Au_{25}(SG)_{18}$ (curve c in B), however lower in intensity. Due to their similar size, clusters of fraction one (curve a in B, average size around 2.5 nm), which are protected by L-gutathione, show the same PL-properties as fraction 1 of Au clusters protected by NALC (A, curve a, average size about 3 nm) as well. All the emission spectra were recorded by exciting the clusters with 450 nm. Reprinted with permission from ref. 21. Copyright (2013) American Chemical Society.

1.8. Crystal structure of size selected gold clusters

To understand the properties of monolayer protected gold nanoclusters detailed information about how the gold atoms and the protected ligand are actually arranged is highly desirable. Therefore, the complete crystal structure provides valuable insight into the fundamental properties of the clusters. Many conformers of Au_{25} clusters have been proposed including extended interlocked rings[88] or interlinked-platonic solids.[89] Jadzinsky et. al. first succeeded in solving the crystal structure of an MPCs $Au_{102}(p\text{-SPhCOOH})_{44}$.[67] From its crystal structure it was found that the central gold atoms are packed in a Marks decahedron, and surrounded by additional layers of gold atoms in unanticipated geometries. The p-MBAs ligand interacts not only with the gold atoms but also with one additional ligand, forming a rigid surface layer (figure 29). The second crystal structure was published by Murray and co-worker in 2008. In their work they determined the structure of another thiolate protected gold nanocluster $[TOA^+][Au_{25}(SCH_2CH_2Ph)_{18}^-]$, where TOA^+ is tetraoctylammonium cation ($N(C_8H_{17})_4^+$). The crystal structure reveals three types of gold atoms: (i) one central gold atom whose coordination number is 12 (12 bonds to gold atoms, figure 37a); (ii) 12 gold atoms formed the vertices of an icosahedron around the central atom, whose coordination number is 6 (five bonds to gold atoms and one to a sulfur atom), and (iii) 12 gold atoms are stellated on 12 of the 20 faces of the Au_{13} icosahedron, and form six oligomers of

($Au_2(SCH_2CH_2Ph)_3$) around the Au_{13} core (figure 37b).[90] The Au-Au distance from the central gold atom to the shell of gold atoms surrounding it in the icosahedral core is 2.79 ± 0.01 Å, while other Au-Au bonds of the core are longer (2.93 ± 0.06 Å). The Au-S distance between the icosahedral core gold atoms bonded to sulfur atoms is 2.38 ± 0.01 Å, while the distance between stellated gold and sulfur atoms is 2.32 ± 0.01 Å.[90]

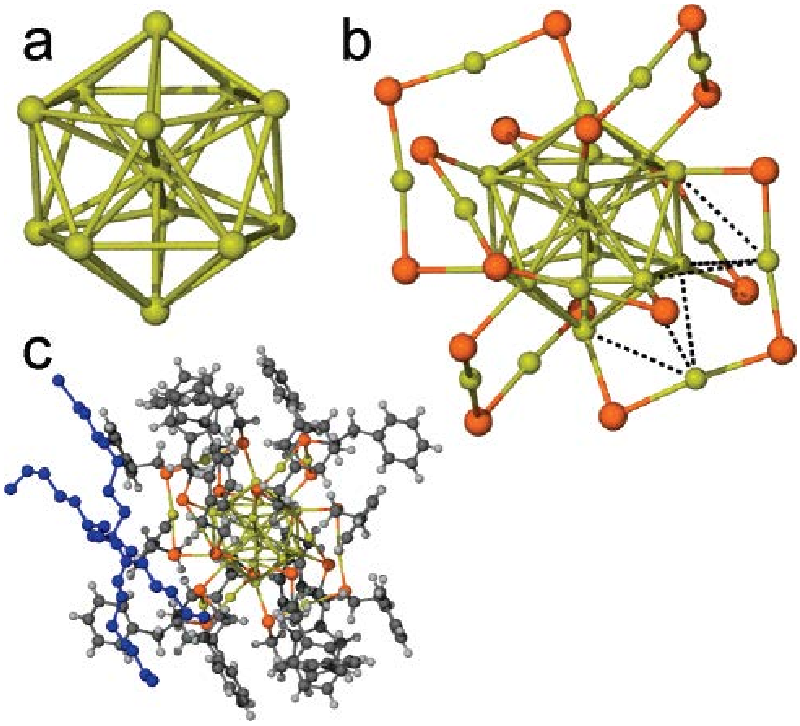

Figure 37: Breakdown of X-raycrystalstructure of $[TOA^+][Au^{25}(SCH_2CH_2Ph)_{18}^-]$ as seen from [001]. (a) Arrangement of the Au_{13} core with 12 atoms on the vertices of an icosahedron and one in the center. (b) Depiction of gold and sulfur atoms, showing six orthogonal $-Au_2(SCH_2CH_2Ph)_3-$ "staples" surrounding the Au_{13} core (two examples of possible aurophilic bonding shown as dashed lines). (c) $[TOA^+][Au_{25}(SCH_2CH_2Ph)_{18}^-]$ structure with the ligands and TOA^+ cation (depicted in blue) (Legend: Gold = yellow; Sulfur = orange; Carbon = gray; Hydrogen = off-white; the TOA^+ counterion is over two positions with one removed for clarity). Reprinted with permission from ref. 90. Copyright (2008) American Chemical Society.

The gas phase geometry of $Au_{25}(SCH_2CH_2Ph)_{18}$ (figure 38a) was optimized starting from the coordinates of the crystalline sample after removal of the counter ion TOA^+.[91] By adding TOA^+ ions distortions in the oligomeric S-Au-S-Au-S units in the anionic form of Au_{25} clusters are induced even in the gas phase geometry. The reason comes from steric interactions of TOA^+ ions with three of the S-Au-S-Au-S units, which means that in the close-packed crystal two neighboring clusters interact with all six gold-thiolate ligand units (figures 38 b and c).[91] The presence of the TOA^+ cation confirms that the Au_{25} cluster is 1- in charge, which is also found by mass spectrometry.[92]

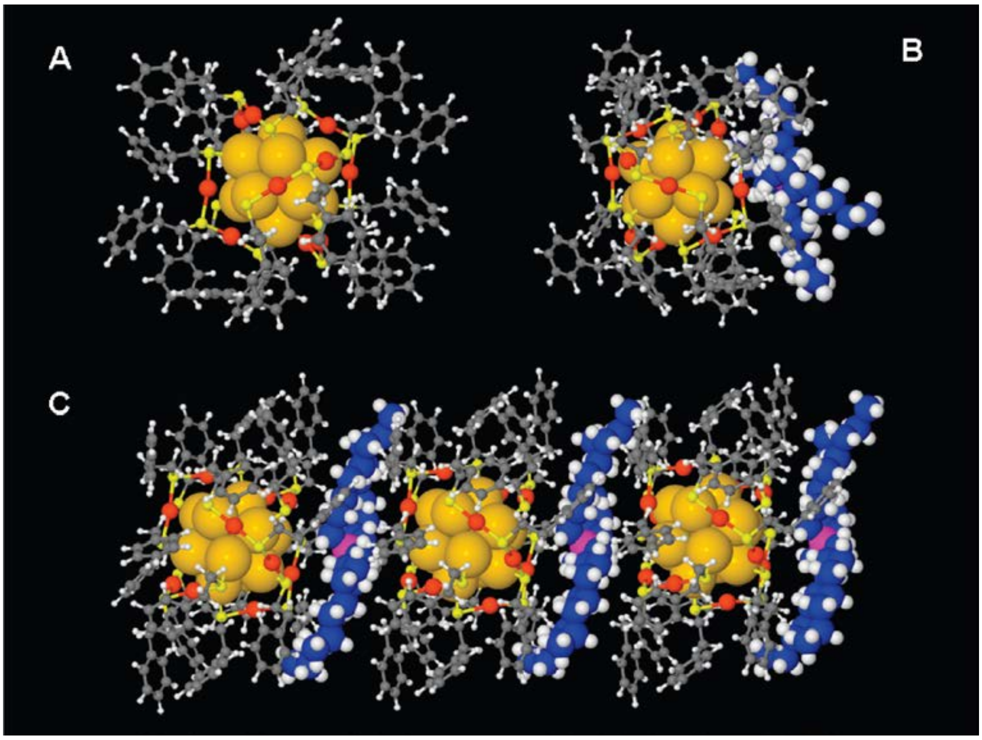

Figure 38. (A) Geometry of the $Au_{25}(SEtPh)_{18}^-$ in the gas phase and (B) with the TOA^+ counterion in the crystal. (C) The unit cell in (B), replicated three times along the *c* axis of the crystal. Note the alternation of the nanoparticle and TOA^+. The triclinic unit cell parameters are *a*=16.111 Å, *b* =17.331 Å, and *c* = 18.581 Å for the box sides, and α = 106.27°, β= 105.49°, and γ = 90.96° for the angles. Reprinted with permission from ref. 91. Copyright (2010) American Chemical Society.

Lopez-Acevedo et. al. used density-functional theory (DFT) to study the structural, electronic, and optical properties of the thiolate-protected $Au_{38}(SR)_{24}$ cluster (R = CH_3 and C_6H_{13}) and confirmed data from powder X-ray crystallography analysis (R = $C_{12}H_{25}$). A low-energy structure which can be written as $Au_{23}@(Au(SR)_2)_3(Au_2(SR)_3)_6$ having a biicosahedral core and a chiral arrangement of the protecting gold-thiolate $Au_x(SR)_y$ units, yields good agrement between the computed study (for R = C_6H_{13}) and the measured (for R = $C_{12}H_{25}$) powder X-ray diffraction function (figure 39).[93]

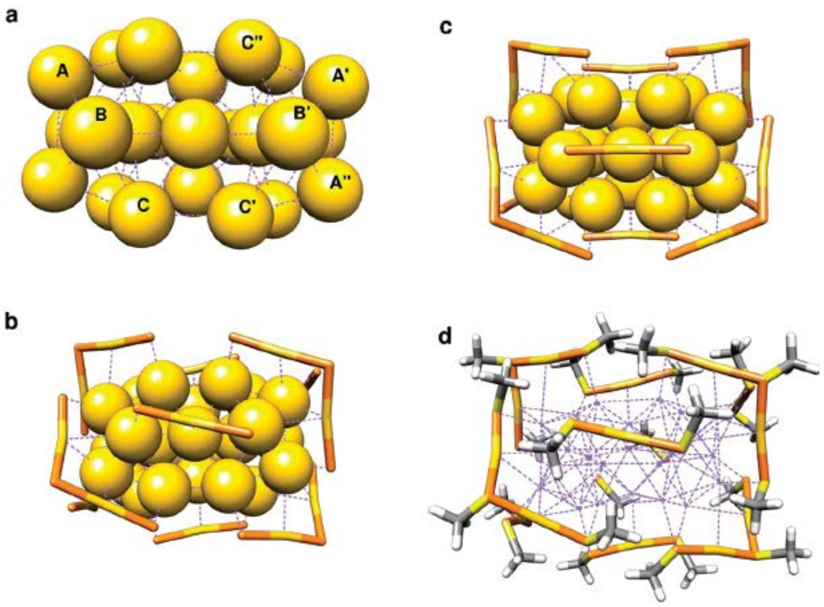

Figure 39. (a) Au_{23} core with labeling of the surface Au atoms involved in determining the symmetry of the ligand layer. (b) Chiral D_3 arrangement of the Au-S atoms. (c) C_{3h} arrangement of the Au-S atoms. (d) Optimal SCH_3 distribution on structure. Reprinted after modification with permission from ref. 93. Copyright (2010) American Chemical Society.

The $Au_{144}(SR)_{60}$ cluster was studied by density-functional theory (DFT) computations. It was found that its structure consists of a large icosahedral Au_{114} core protected with 30 RS-Au-SR oligomer units.[94] The polyhedral geometry of the Au_{114} core (figure 40) can be described as an rhombicosidodecahedron. The two first shells of the core have 12 and 42 atoms, respectively, forming a Mackay icosahedral packing structure (MI) containing 54 atoms plus a central atom (55 atoms) and 20 triangular faces. The third shell has 60 symmetry-equivalent atoms at vertices of 12 pentagons, 30 squares, and 20 equilateral triangles.[94a] The protective oligomers (RS-Au-SR) units each cap diagonally one square, causing a slight reconstruction of the core surface (figure 40).[94]

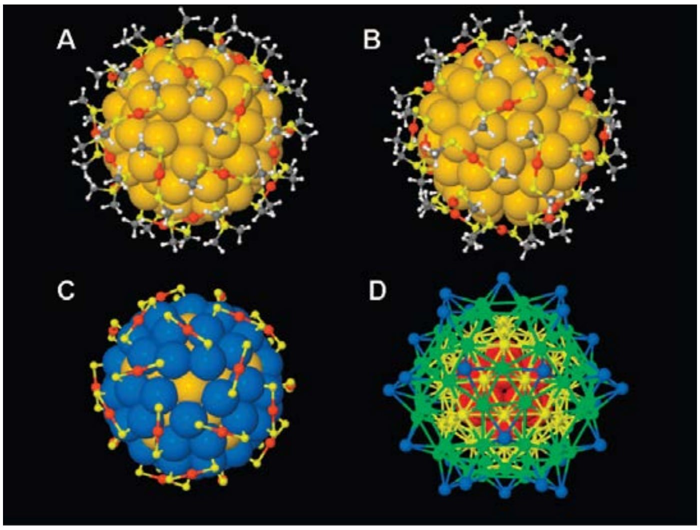

Figure 40. (A), (B) Relaxed structure of $Au_{144}(SR)_{60}$ viewed down a 5-fold (A) and a 3-fold (B) symmetry axis. Key: yellow, Au in the Au_{114} core; orange, Au in the RS-Au-SR unit; bright yellow, S; gray, C; white, H. (C) highlights the chiral arrangement of the RS-Au-SR units covering the 60-atom surface of the Au_{114} core (blue). (D) shows all the 144 gold atoms, with different atom shells denoted by different colors. Reprinted with permission from ref. 94b. Copyright (2009) American Chemical Society.

1.9. Unexpected properties of $Au_{25}(SR)_{18}$ nanoclusters

In recent years, much progress has been made in the synthesis of $Au_n(SR)_m$ nanoclusters with high yields and high purity. With such techniques, many size selected clusters like $Au_{25}(SR)_{18}$, $Au_{38}(SR)_{24}$ and $Au_{144}(SR)_{60}$ can be yielded.[95-97] Among these well-defined clusters, $Au_{25}(SR)_{18}$ has been the most extensively studied.[95-114] $Au_{25}(SR)_{18}$ clusters exhibit interesting properties, like oxidation by air, unexpected reactivity with different types of salts, unusual photoluminescence properties, high stability with different protecting ligands, and unexpected phenomena in infra-red study. Here we will summarize most of these studies

1.9.1. Conversion of anionic $[Au_{25}(SCH_2CH_2Ph)_{18}]^-$ cluster to charge neutral cluster

A solution-phase of $[Au_{25}(SCH_2CH_2Ph)_{18}]^-$ anionic cluster oxidize and convert into neutral charge cluster $[Au_{25}(SCH_2CH_2Ph)_{18}]^0$ when exposed to air for several hours or reacted with hydrogen peroxide (H_2O_2). The one electron loss of the Au_{25}^- cluster and conversion to Au_{25}^0 is a surprise in light of the chemical inertness of gold nanoparticles. The optical absorption properties of the charged cluster are different from the neutral form. The blue curve of figure 40 shows the UV-vis spectra of the anionic form of Au_{25} with three main absorption bands at 400, 450 and 670 nm, and two small shoulders at 800 and 550 nm. Upon reduction the 400 nm peak becomes more prominent, while the 450 nm peak is less intense compared to the neutral form. In addition a small shoulder at 630 nm appears and the 800 nm shoulder disappears (figure 41, red curve). The peak at 800 nm is characteristic of the Au_{25}^- cluster. From these results the intensity of the 450 nm and 800 nm bands are transferred to the 400 nm and 630 nm bands upon oxidation, respectively (figure 41).[98,95]

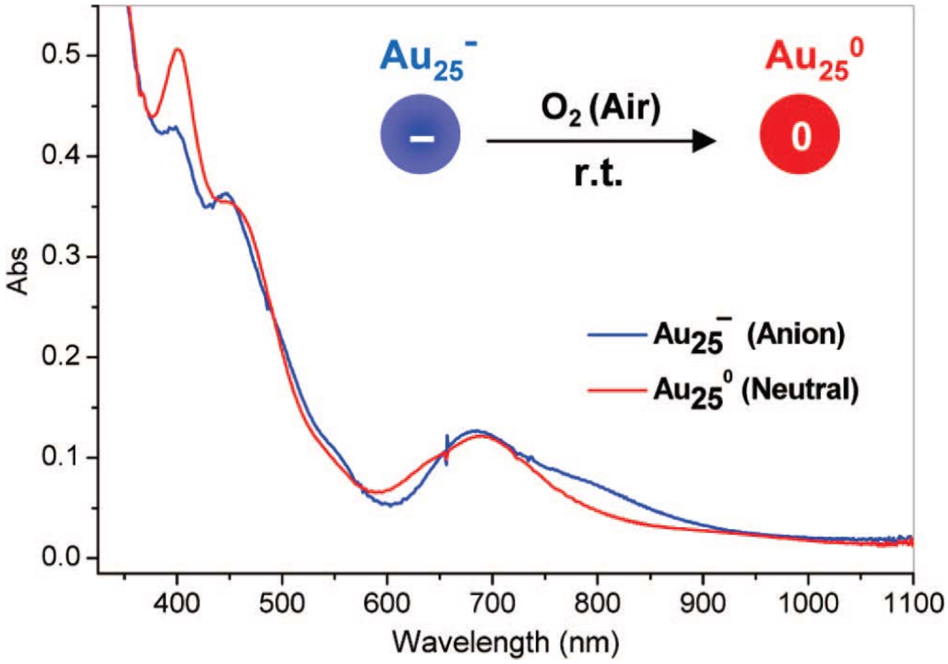

Figure 41. The optical absorption spectra of anionic (blue profile) and neutral (red profile) 25-gold-atom clusters in solution. Reprinted with permission from ref. 98. Copyright (2008) American Chemical Society.

The crystal structure of the anion cluster Au_{25}^- exhibits distortions, which are not observed in the neutral cluster form (Au_{25}^0). One sulfur atom in the S-Au-S-Au-S motif of the Au_{25}^- cluster is bent downwards, while another is bent upward in the atomic plane (σ_h symmetry plane along x-y, y-z and x-z) (figures 42 A and C). In contrast, such distortions do not appear in the neutral cluster (figures 41 B and D). The ligand orientations in the Au_{25}^0 cluster are also different than those in the Au_{25}^- cluster. These structural distortions in Au_{25}^- are not only caused by the negative charge at the cluster core, but also a solid-state effect resulting from the presence of the bulky TOA^+ counterion in the unit cell (figure 42).[98]

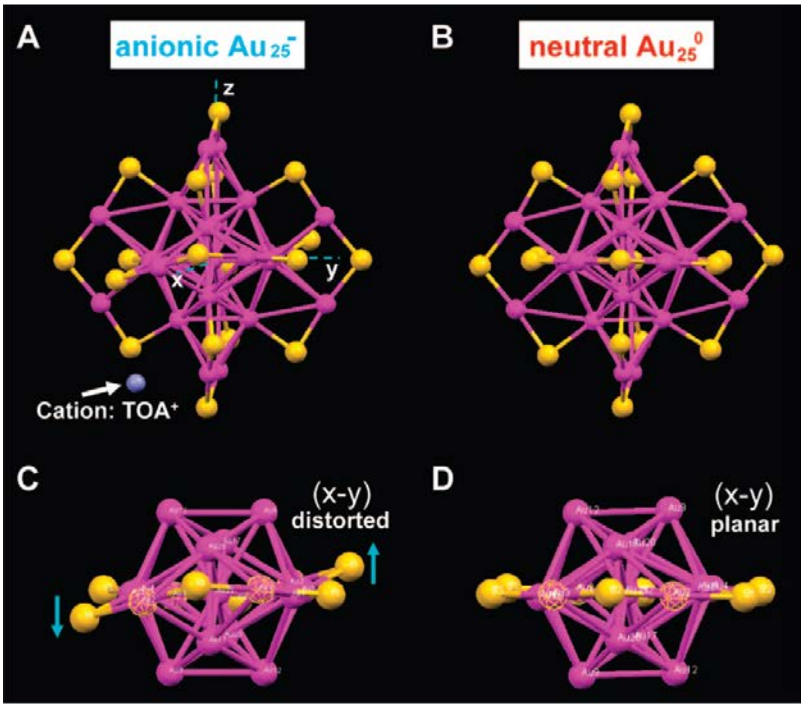

Figure 42. Comparison of the crystal structures of Au_{25} anionic (A,C) and neutral (B,D) clusters. Both clusters are capped by 18 phenylethanethiol ligands (for clarity C and H atoms are omitted); for anionic Au_{25}, the counterion is tetraoctylammonium TOA^+ (only N (in blue) is shown for clarity). Reprinted with permission from ref. 98. Copyright (2008) American Chemical Society.

1.9.2. Conversion of neutral $[Au_{25}(SCH_2CH_2Ph)_{18}]^0$ clusters to anionic charged cluster

The $[Au_{25}(SCH_2CH_2Ph)_{18}]^0$ cluster was converted into the anionic form $[Au_{25}(SCH_2CH_2Ph)_{18}]^-$ by reaction with two types of salt. The first type was NaBr. Acetone was chosen as the solvent since acetone can dissolve both reactants Au_{25}^0 and NaBr. The ratio between NaBr and Au_{25}^0 was about 10:1 per mole. Within 10 min of stirring at room temperature, the Au_{25}^0 clusters were completely converted to Au_{25}^- after interaction with NaBr. The decomposition of Au_{25}^- clusters started after ~30 min of stirring, evidenced by the optical spectral changes, including the disappearance of the 400 nm peak and the damping of the 670 nm peak as well as the emergence of a new peak at ~815 nm (figure 43A). These observations indicate that, after the conversion of Au_{25}^0 to Au_{25}^-, the $Au_{25}^-Na^+$ product is not sufficiently stable in the presence of NaBr. The reaction process was also monitored by mass spectrometry (MALDI-MS) (figure 43B).[99]

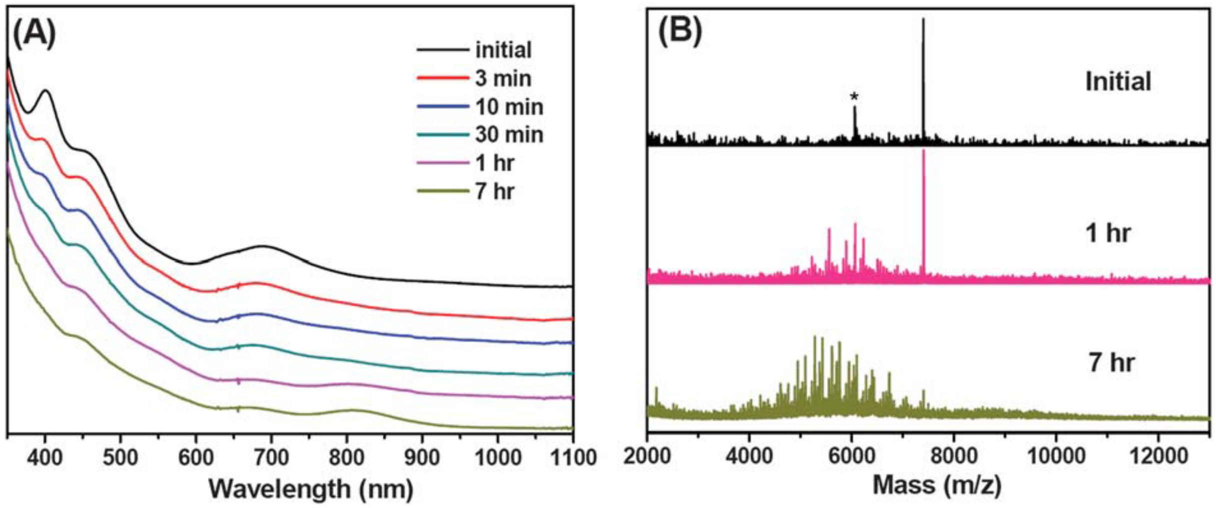

Figure 43: Reaction of Au_{25}^0 clusters with NaBr in acetone monitored by (A) UV-vis spectroscopy and (B) mass spectrometry. The spectra are vertically shifted for clarity. Molar ratio of NaBr/Au_{25}^0 = 10 : 1. For MALDI-MS, negative mode spectra were collected. The asterisk shows the fragment ($Au_{21}(SCH_2CH_2Ph)_{14}$, 6058 Da) of $Au_{25}(SCH_2CH_2Ph)_{18}$ (7394 Da). Reprinted with permission from ref. 99. Copyright (2011) The Royal Society of Chemical.

The second type of salt was tetraoctylammonium halide (TOAX, X= Br^-,Cl^- and NO_3). Ten equivalents of TOABr were added to the Au_{25}^0 cluster in a methylene chloride (CH_2CH_2) solution. After one hour of stirring the initial Au_{25}^0 clusters were completely converted into Au_{25}^- clusters and were stable until 24 h of stirring. This reaction was followed up by UV-vis spectroscopy (figure 44 A). The Br^- ions attack the $[Au_{25}(SCH_2CH_2Ph)_{18}]^-$ surface and displace some thiolates, evidenced by the observation of halides bound to the clusters and resulting in mass peaks like $Au_{25}(SCH_2CH_2Ph)_{18-x}Br_x$ in the mass spectra (figure 44 B).[99]

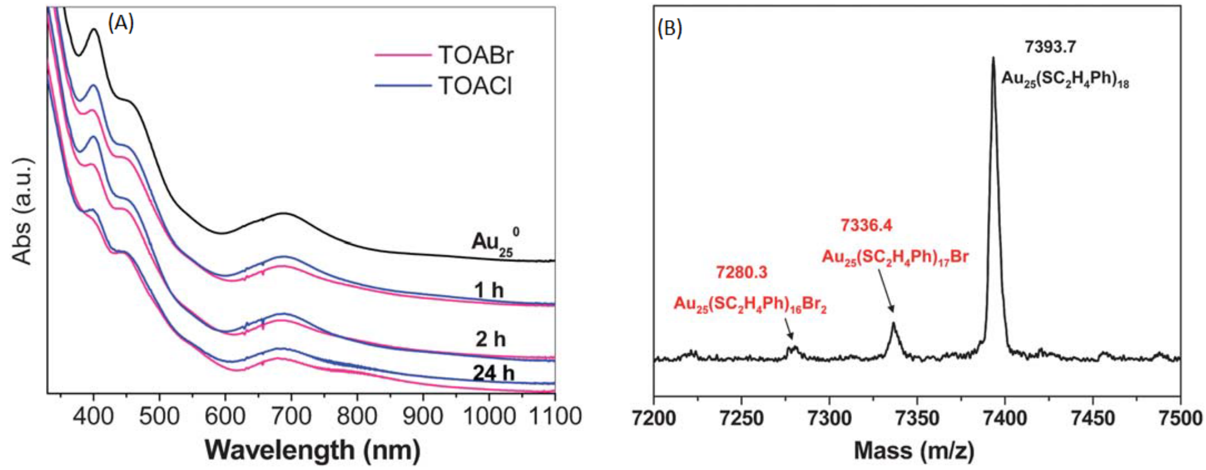

Figure 44: (A) Reaction of Au_{25}^0 (0.5 mg in 2 ml of CH_2Cl_2) with TOABr and TOACl, respectively. The optical spectra are vertically shifted for clarity. Molar ratio: TOAX/Au_{25}^0 = 10 : 1, where X = Br, Cl. (B) The zoom-in mass spectrum (MALDI-MS) of the 1 h reaction product. Reprinted with permission from ref. 99. Copyright (2011) The Royal Society of Chemical.

TOA^+ cations can stabilize the Au_{25}^- product by preventing a further attack from halide ions. However, in the case of NaX salts, the Na^+ ions do not provide any steric stabilization of the $[Au_{25}(SCH_2CH_2Ph)_{18}]^-$ clusters. Hence, degradation occurs when further attacked by halide ions, especially Br^- and I^- (scheme 2).[99]

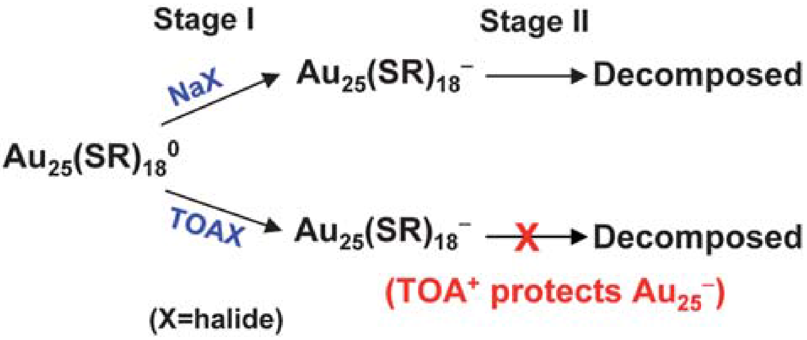

Scheme 2: The two stages of reaction of Au_{25}^0 with NaX and TOA-X salts (X = halide). Reprinted with permission from ref. 99. Copyright (2011) The Royal Society of Chemical.

1.9.3. Fluorescence of $Au_{25}(SR)_{18}$ clusters

Figure 45 shows the fluorescence spectra of the three thiolate protected Au_{25} species, $[Au_{25}(C_2H_4Ph)_{18}]^-$, $[Au_{25}(C_{12}H_{25})_{18}]^-$, and $[Au_{25}(C_6H_{13})_{18}]^-$, which were found to exhibit only weak fluorescence; their fluorescence quantum yields (QY) are ~1×10^{-4}, 5×10^{-5} and 2×10^{-5}, respectively, which are much lower than that of $[Au_{25}(SG)_{18}]^-$ (QY~2×10^{-3}).[100] The fluorescence intensity of the hydrophobic species follows the order $[Au_{25}(SC_2H_4Ph)_{18}]^- > [Au_{25}(SC_{12}H_{25})_{18}]^- > [Au_{25}(SC_6H_{13})_{18}]^-$. The fluorescence comes from not only the metal core, but also from the protected ligands. The fluorescence quantum yield increases with the ligand's capability of donating electron density to the metal core via the S-Au bond.[80]

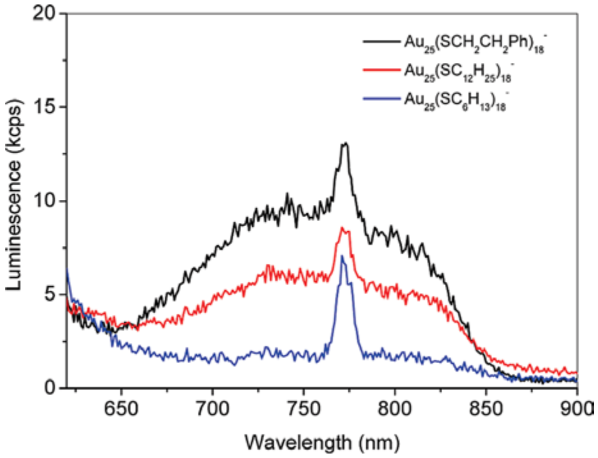

Figure 45: Weak fluorescence of $[Au_{25}(SR)_{18}]^-$ with different R groups ($-C_2H_4Ph$, $-C_{12}H_{25}$, and $-C_6H_{13}$). Note that the spike at ~770 nm is an artifact from the quartz cell; solvent, CH_2Cl_2; excitation, 514 nm (from a xenon arc source); slit width, 5 nm; solution concentration, OD_{514} ~ 0.05. Reprinted with permission from ref. 80. Copyright (2010) American Chemical Society.

There is also another interesting photoluminescence observation for the Au_{25} cluster: the increase in the electropositivity of the Au_{25} cluster metal core leads to a strong fluorescence enhancement. The neutral form of Au_{25}^0 nanoclusters can be oxidized to higher charge states; up to +2 using O_2, H_2O_2 and $Ce(SO_4)_2$ oxidants.[98,101] Differential pulse voltammetry and the MALDI-MS spectra show the different charge states of Au_{25} nanoclusters (figure 46). In figure 46 B the fluorescence spectra of neutral $[Au_{25}(SC_2H_4Ph)_{18}]^0$ clusters are displayed. The neutral clusters were found to have a 3-fold enhancement of fluorescence compared with the anionic species Au_{25}^-. Further increasing the electropositivity results in a further increase of the quantum yield, even to a drastic 10-fold increase for $[Au_{25}(SC_2H_4Ph)_{18}]^{2+}$.[80]

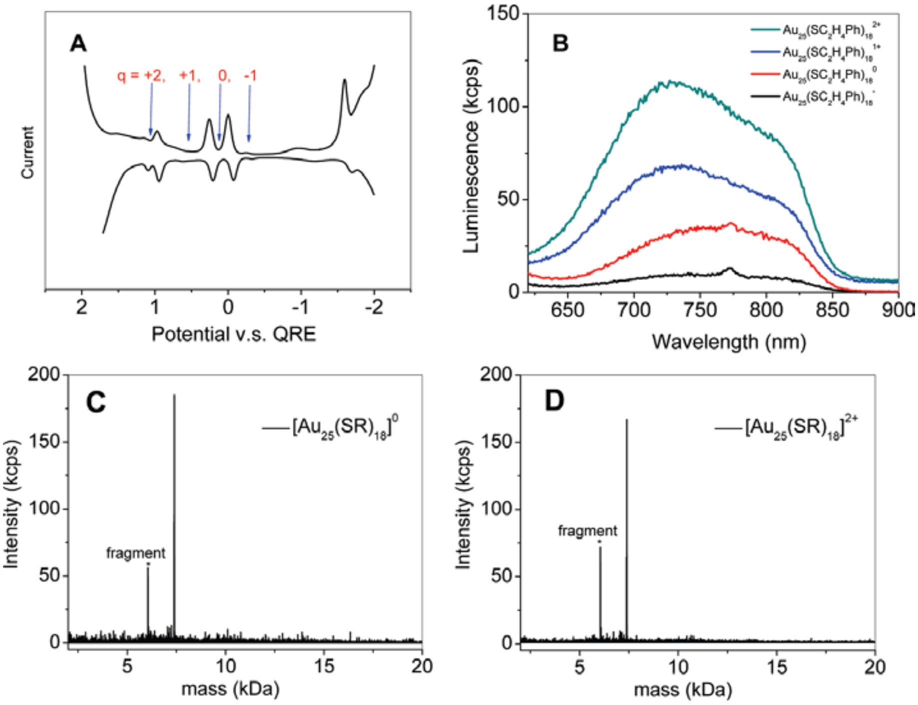

Figure 46: (A) Charge states of $Au_{25}(C_2H_4Ph)_{18}$ probed by differential pulse voltammetry (DPV). (B) Fluorescence spectra of $[Au_{25}(SC_2H_4Ph)_{18}]^q$ (q = -1, 0, +1, +2). (C, D) show MALDI-MS spectra of different charge states (q = 0, +2) of Au_{25} (similar mass spectrum of q = +1 is not shown). Reprinted with permission from ref. 80. Copyright (2010) American Chemical Society.

1.9.4. Structure of $Au_{25}(SR)_{18}$ with different ligands

The $Au_{25}(SR)_{18}$ structure was found to be independent of the surface ligands; the same Au_{25} core framework is retained regardless of the types of surface thiolate ligands (-SR); e.g., long chain alkylthiols like 1-dodecanethiol, 3-mercapto-2-butanol and 6-mercapto-hexane ($-SC_{12}H_{25}$, $-SC_4H_{10}O$, $-SC_6H_{13}$,),[102] aromatic thiols like 2-phenylethanethiol ($-SCH_2CH_2Ph$) and bulky molecules (like, glutathione, N-acetyl-L-cystine, N-formyl-glutathione and N-acetyl-glutathione).[21,72] Since UV-vis is mostly sensitive to changes of the metal core, all $Au_{25}(SR)_{18}$ clusters with all types of protected ligands exhibit the same UV-vis spectra with transitions at 400, 450 and 670 nm (figure 47).[72]

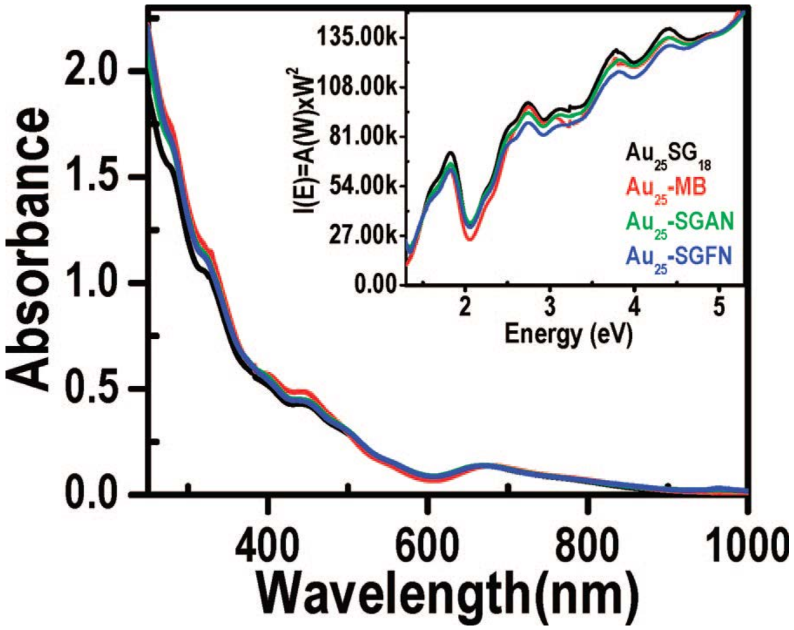

Figure 47. The UV-vis spectra of compounds $Au_{25}SG_{18}$ (black), Au_{25}-MB (red), Au_{25}-SGAN (green), and Au_{25}-SGFN (blue). Inset shows the plot of I(E) = A(W) × W^2 vs energy (eV). Reprinted with permission from ref. 72. Copyright (2010) American Chemical Society.

1.9.5. Reactivity of $[Au_{25}(SCH_2CH_2Ph)_{18}]^{1-}$ Nanoclusters with Metal Ions

$[TOA^+]$ $[Au_{25}(SC_2Ph)_{18}]^{1-}$ clusters show high reactivity with Ag^+, Cu^{2+}, and Pb^{2+} ions. A solution of $Au_{25}L_{18}{}^{1-}$ in CH_2Cl_2 was titrated with one and two equivalents of Ag^+ producing changes in the absorbance spectra with isosbestic points, and at 1:1 mol ratio the titration curve breaks, indicating a stoichiometric interaction (figure 48). The same effects appear when adding Cu^{2+} and Pb^{2+} cations, but the break occurs at 0.5:1 mol ratio metal/nanoparticle. Figure 48a shows the result after adding up to a 1:1 mol ratio of $Ag^+/Au_{25}L_{18}{}^{1-}$: (a) the shoulder at ca. 790 nm has almost disappeared, (b) the band at 682 nm is shifted to lower wavelengths, (c) the band at 605 nm increases, and (d) a nearly linear change in absorbance is observed. The spectral changes in figure 48a are accompanied by the appearance of isosbestic points at 438, 670, and 865 nm. By continuing the addition of Ag^+, up to a 2:1 $Ag^+/Au_{25}L_{18}{}^{1-}$ mol ratio (figure 48b), the spectral shape further changes and a new isosbestic point at 628 nm appears. Further additions of Ag^+ do not produce more isosbestic features. Finally, the spectrum has lost most of its original[103] fine structure and remains more or less featureless. The particle size of the isolated products from the solution after addition of

10:1 mol ratios of $Ag^+/Au_{25}L_{18}{}^{1-}$ were measured by TEM, and revealed a general increase in nanoparticle core size, to 1.3 ± 0.8 nm.[104]

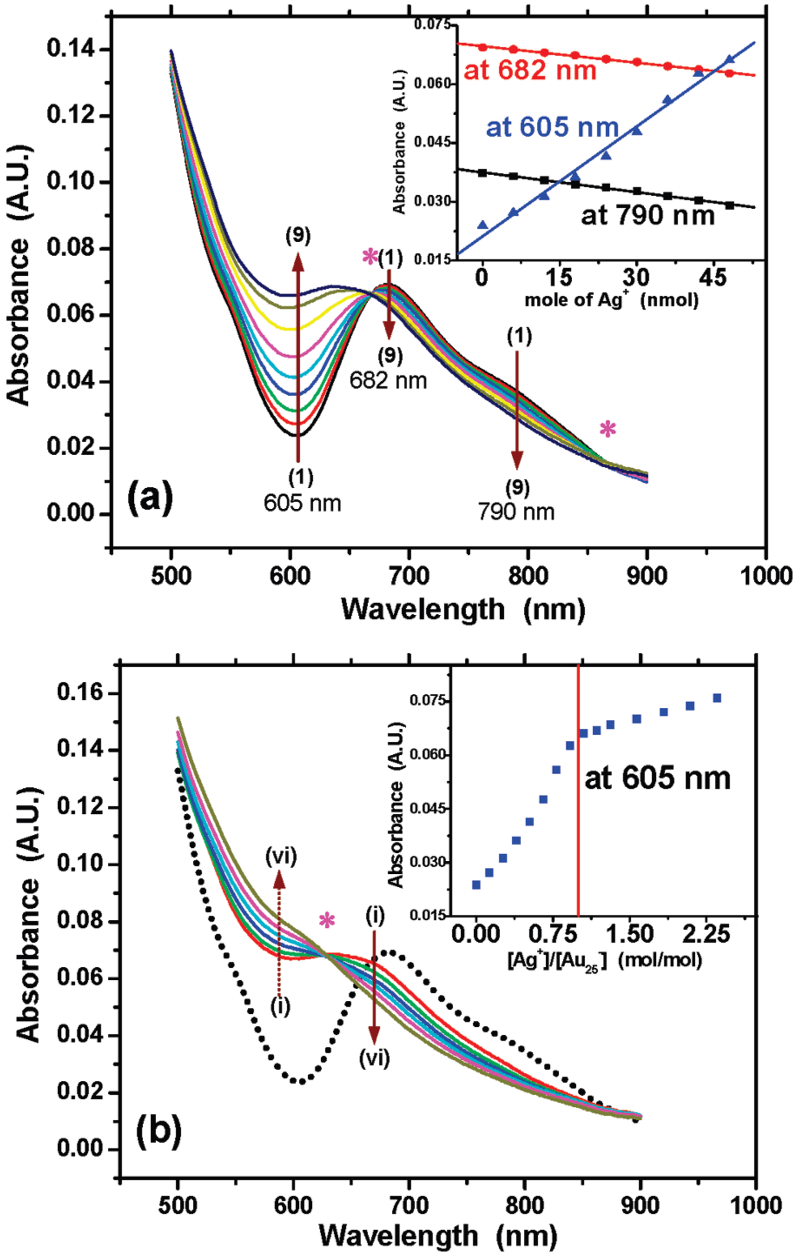

Figure 48. UV-vis absorption spectra of 0 to 2:1 mol ratio of Ag^+/Au_{25}. 46 nmol of $Au_{25}{}^-$ (15.3 μM in CH_2Cl_2) with Ag^+ added as 10 mM $AgNO_3$ in CH_3CN: **Panel a**: 0 to 1:1 Ag^+/Au_{25} mole ratio; Curves 1-9: 0, 6, 12, 18, 24, 30, 36, 42, and 48 nmol added Ag^+; **Panel b**: 1:1 to 2:1 Ag^+/Au_{25} mole ratio; Curves i to vi: 54, 60, 72, 84, 96, and 102 nmol added Ag^+. Dotted line is no added Ag^+. **Insets: Panel a**, absorbance at 605, 682, and 790 nm vs mole added Ag^+; **Panel b**: absorbance at 605 nm vs mole ratio Ag^+/Au_{25}. Isosbestic points (*) at 438, 670, and 865 nm. Reprinted with permission from ref. 104. Copyright (2010) American Chemical Society.

1.9.6. Quantum clusters of gold embedded in silica $Au_{25}@SiO_2$

Pradeep and co-worker succeeded in synthesizing monodisperse water-soluble Au_{25} from polydisperse gold clusters that were protected by glutathione (Au_mSG_n) by reaction with

(3-mercaptopropyl)trimethoxysilane (MPTS).[105]To prepare the quantum clusters (QCs) of Au_{25}@MPS, MPTS was added to the aqueous solution of Au_mSG_n at a pH of 6–7. The solution was stirred at room temperature for 1–10 min and the progress of the reaction was followed by UV-vis spectroscopy. Once Au_{25}@MPS is formed, it is possible to grow a thin silica layer on the QC surface since the clusters are protected by silanol. At basic pH (around 12), the hydrolysis and condensation of monolayers is enabled by heating the sample to 65° C for 30 min. After hydrolysis and condensation Au_{25}@MPS is transformed into Au_{25}@SiO_2, because under acid mediated hydrolysis the QCs immediately aggregate.[105] Figure 49 shows the UV-vis spectra of (a) polydisperse $Au_m(SG)_n$, which is featureless; (b) monodisperse Au_{25}@MPS gives three bands at 400, 455 and 700 nm. The last one is red shifted by nearly 30 nm compared to Au_{25} protected by thiol ligands. This can be attributed to the properties of the ligand and some aggregation; the latter was confirmed by TEM. (c) For Au_{25}@SiO_2 a redshift by 30 nm of the 670 nm peak is found as well and two additional peaks at 815 and 1015 nm appear, which may be attributed to intercluster interactions within the aggregate.[105] The QCs are very sensitive towards the electron beam and fuse together to form even bigger nanoparticles after prolonged electron-beam irradiation.[106] The silica growth however, greatly enhanced the stability of QCs against electron-beam-induced aggregation.

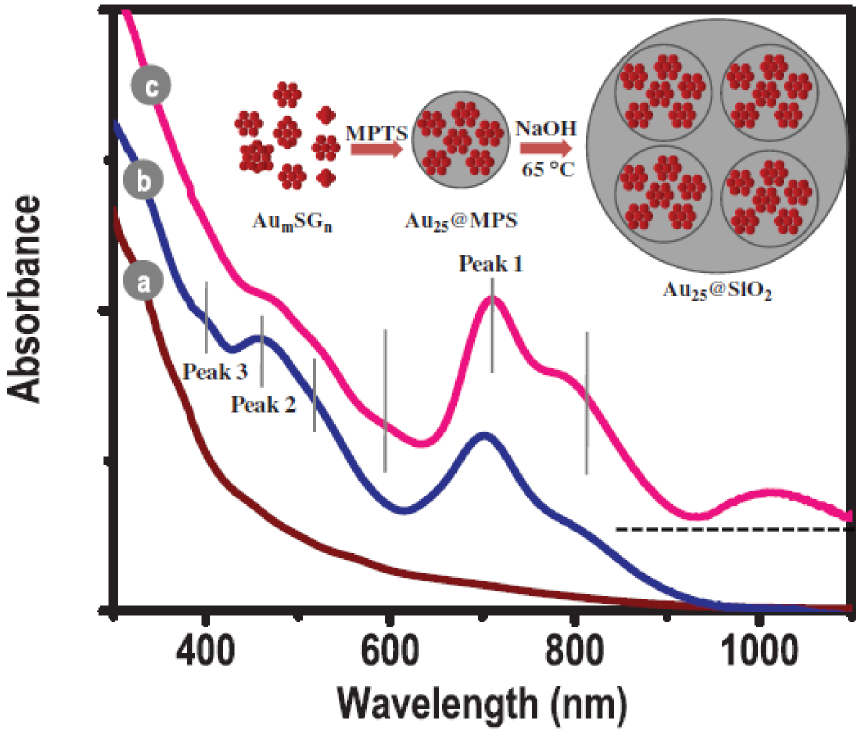

Figure 49: Optical absorption spectra of a) Au_mSG_n, b) Au_{25}@MPS, and c) Au_{25}@SiO_2. The features of the QCs are indicated with lines (see the text for explanation). Reprinted with permission from ref. 105. Copyright (2011) Wiley-VCH wileyonlinelibrary.com Verlag GmbH & Co. KGaA, Weinheim

1.9.7. Magnetic properties of $Au_{25}(SR)_{18}$ clusters

Magnetism is a long-lasting topic in the contemporary physics of metals. According to quantum theory, magnetism is essentially a spin property of electrons in an orbital. For gold, single atoms possess unpaired $6s^1$ electrons so are paramagnetic, while bulk gold is diamagnetic because the paramagnetism of the conduction electrons is counteracted by the orbital and ionic core diamagnetism.[107] The evolution of magnetism from paramagnetic gold atoms, to nanoparticles, to bulk is of fundamental interest and importance. For gas-phase gold clusters, theoretical work by Wang et al. has identified ultra-high magnetic moments in the gold-coated transition-metal anionic cluster $[Mn_{13}@Au_{20}]^-$.[108] In the case of thiolate-capped gold clusters, Negishi et al. reported an observation of paramagnetism in $Au_n(SG)_m$ clusters but the fundamental origin of magnetism was not understood due to the unavailable ability of crystal structures for the $Au_n(SG)_m$ clusters.[109] Zhu et. al. observed paramagnetism in neutrally charged $[Au_{25}(SR)_{18}]^0$ clusters.[110] The magnetism of the cluster can be reversibly switched on or off by controlling the charge state of the $[Au_{25}(SR)_{18}]^q$ cluster: the anionic cluster is non-magnetic while the neutral one is magnetic (figures 50A and B). A relationship between the crystal structure of $[Au_{25}(SR)_{18}]^0$ and magnetic properties were confirmed by DFT calculations. It was found that the unpaired spin in the $[Au_{25}(SR)_{18}]^0$ cluster arises from the highest occupied Kohn–Sham orbital (one of the triply degenerate HOMOs). Interestingly, the HOMO orbital exhibits distinct P-like character (figures 50C and D).[110-112] These results for the $[Au_{25}(SR)_{18}]^0$ nanoclusters demonstrate that the $Au_{25}(SR)_{18}$ cluster can be viewed as a thiolate-protected superatom.

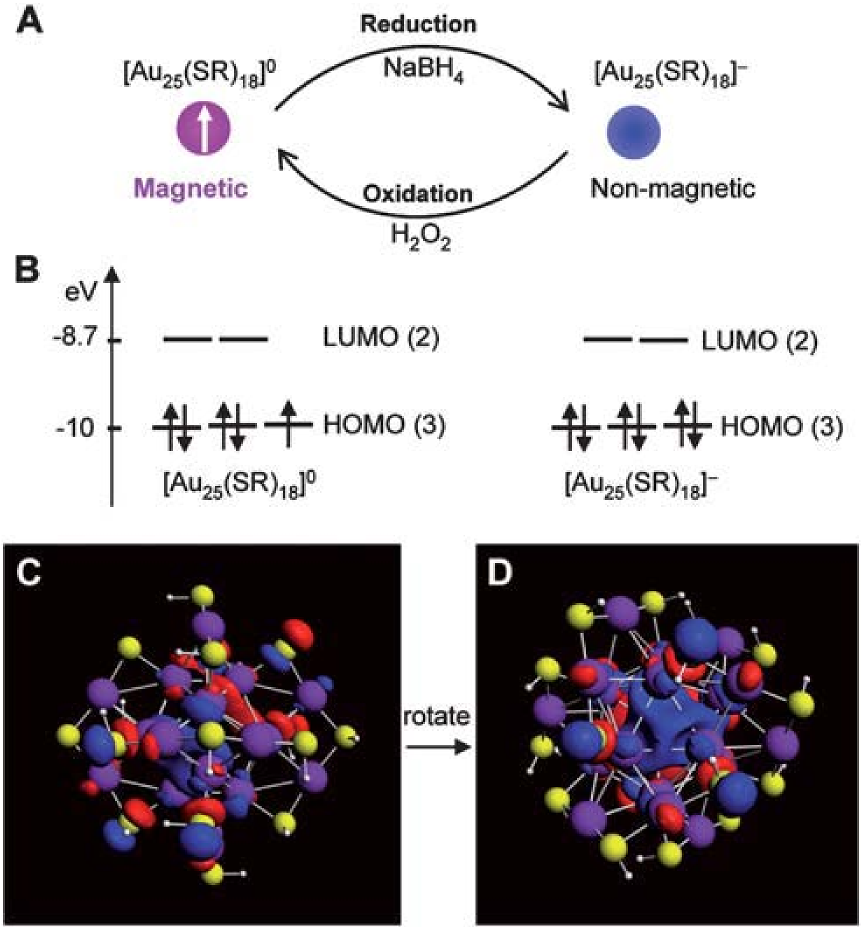

Figure 50: (A) Reversible conversion between the neutral and anionic $Au_{25}(SR)_{18}$ nanoclusters. (B) DFT calculated Kohn–Sham orbital level diagram for the neutral and anionic nanoclusters, respectively. (C–D) Views of the highest occupied Kohn–Sham orbital for $[Au_{25}(SH)_{18}]^0$ at the LB94//Xa/TZP level of theory. The HOMO possesses two lobes and exhibits distinct P-like character. (D) is rotated relative to (C) to show one of the lobes (contributed by three Au atoms in the icosahedral shell). Purple: Au, yellow: S, white: H atoms. Reprinted with permission from ref. 110. Copyright (2011) American Chemical Society.

1.9.8. Isolation of alloys of quantum clusters $MAu_{24}(SR)_{18}$ (M= Pd and Ag)

The synthesis of atomically precise alloy QCs of defined compositions is a challenge. Murray et al. synthesized $Pd@Au_{24}(SR)_{18}$[113] which was further isolated as $PdAu_{24}(SR)_{18}$ by Negishi et al.[114] $Ag_nAu_{25-n}(SR)_{18}$, and $(AuAg)_{140}(SR)_{60}$ (R=organic soluble alkyl/aryl groups) were obtained by simultaneously reducing metal salts under suitable conditions.[115] The isolation and characterization method of QC alloys of $Pd_1Au_{24}(SC_{12}H_{25})_{18}$ clusters are summarized in the following text.[116]

A dodecanethiolate-protected $Pd_1Au_{24}(SC_{12}H_{25})_{18}$ cluster was isolated in high purity using solvent fractionation and high-performance liquid chromatography (HPLC). The purity was confirmed by MALDI-MS (figure 51). The optical absorption spectrum of $[Pd_1Au_{24}(SC_{12}H_{25})_{18}]^0$ exhibits peaks at ~690 and ~620 nm, which is consistent with calculated results on $[Pd_1@Au_{24}(SC_1H_3)_{18}]^0$ in which the central gold atom of

$Au_{25}(SC_1H_3)_{18}$ is replaced with Pd. These results strongly indicate that the isolated $[Pd_1Au_{24}(SC_{12}H_{25})_{18}]^0$ has a core–shell $[Pd_1@Au_{24}(SC_{12}H_{25})_{18}]^0$ structure in which the central Pd atom is surrounded by a frame of $Au_{24}(SC_{12}H_{25})_{18}$ (figure 51c). The stability of $Pd_1@Au_{24}(SC_{12}H_{25})_{18}$ cluster was experimentally examined, and proved to be more stable against degradation in solution and laser dissociation than $Au_{25}(SC_{12}H_{25})_{18}$. These results indicate that the doping of a central atom is a powerful method to increase stability beyond the $Au_{25}(SR)_{18}$ cluster.[114]

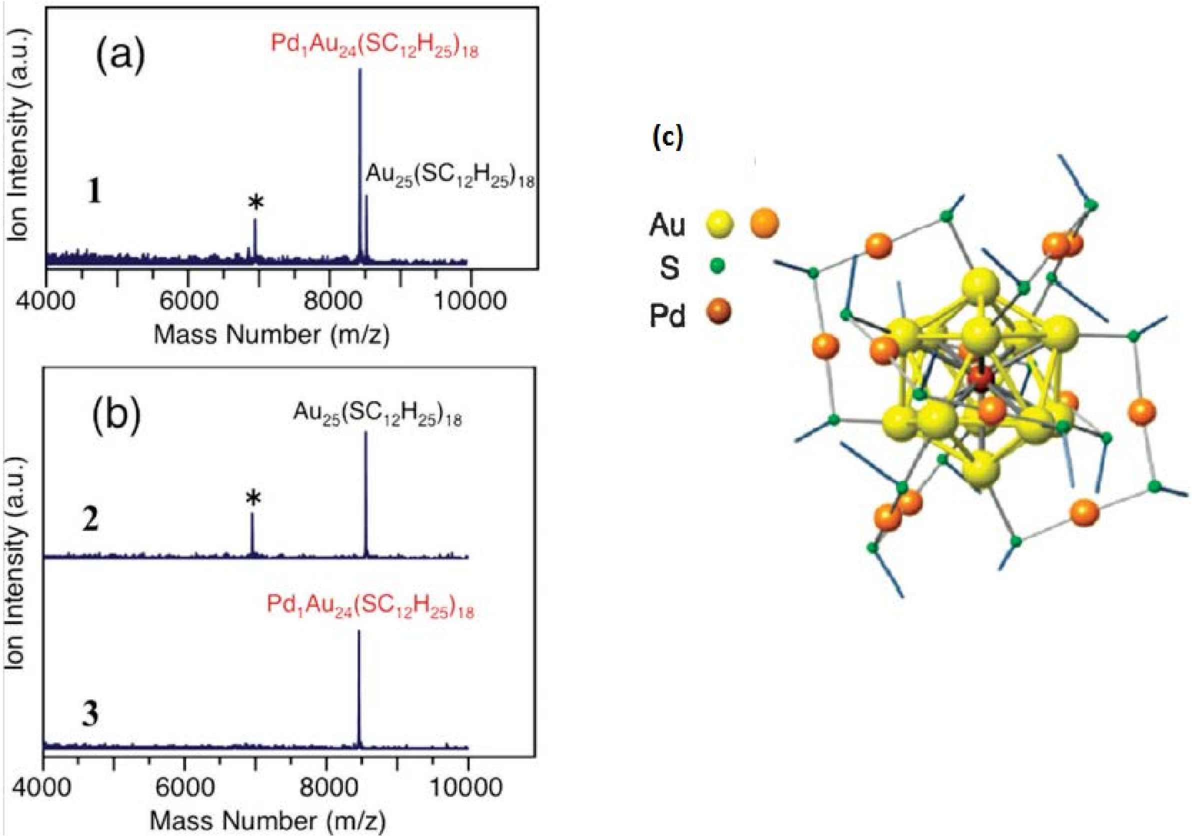

Figure 51: Negative-ion MALDI mass spectra of (a) fraction 1 extracted by acetone and (b) fractions 2 and 3 separated by HPLC. The asterisk indicates the fragment ion of $Au_{25}(SC_{12}H_{25})_{18}$ ($Au_{21}(SC_{12}H_{25})_{14}$; MW = 6956). Fractions 2 and 3 contain only the pure clusters $Au_{25}(SC_{12}H_{25})_{18}$ and $Pd_1Au_{24}(SC_{12}H_{25})_{18}$, respectively (c) Optimized structure of $Pd_1@Au_{24}(SC_{12}H_{25})_{18}$ cluster. Reprinted with permission from ref. 114. Copyright (2010) The Owner Societies

1.10. Applications of protected clusters

Gold, as a noble metal, was initially thought to be catalytically inert but has been demonstrated to be capable of catalyzing a variety of chemical reactions such as selective oxidation and hydrogenation in the form of small nanoparticles.[116-119] Nanoclusters (NCs) are of considerable interest because of their wide variety of potential application in various fields such as biosensing,[120] optics,[121] electronics, photonics,[122] catalysis,[123]nanotechnology[124] and drug or DNA delivery.[125,126] Chiral NCs are particularly interesting for asymmetry amplification at different length scales, which means as chiral catalysts for chemical synthesis and chiral selective membranes (enantioselectivity reactions) (figure 52).[127,128]

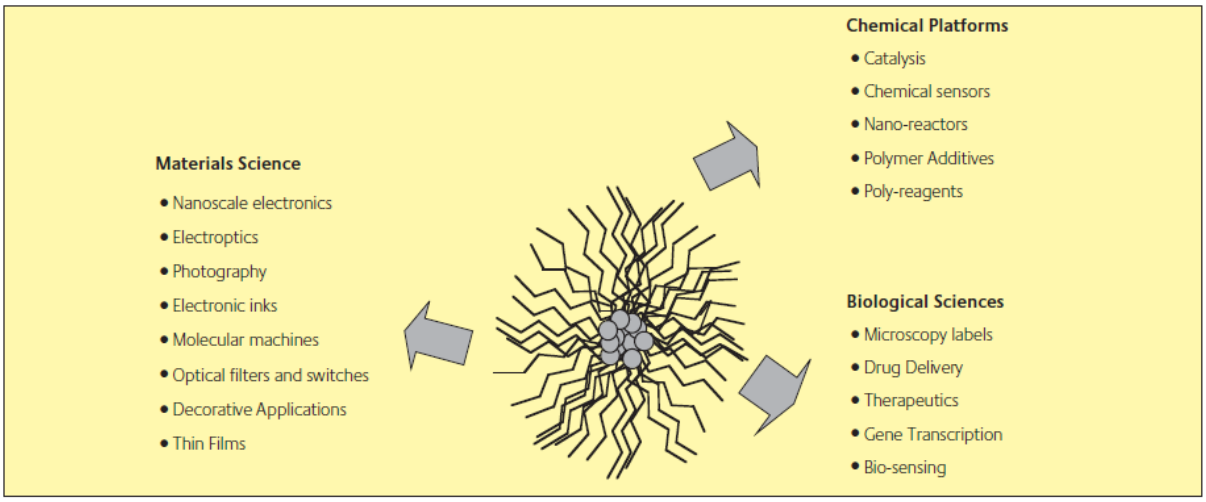

Figure 52: Possible application areas for monolayer-protected clusters. Reprinted with permission from ref. 128. Copyright (2002) Gold Bulletin.

Zhu et. al succeeded in the selective hydrogenation of α,β-unsaturated ketones (benzalacetone) with hydrogen (H_2) using monodisperse gold clusters protected by 2-phenylethanethiol ligands ($Au_{25}(SCH_2CH_2Ph)_{18}$). The ultrasmall $Au_{25}(SCH_2CH_2Ph)_{18}$ clusters (~ 1nm) can indeed catalyze the hydrogenation of the C=O bond in α,β -unsaturated ketones or aldehydes with 100% chemoselectivity towards the formation of α,β-unsaturated alcohols even at low temperatures (e.g. 0^oC). This catalytic reaction was carried out at 0^oC (or room temperature) in the solution phase and initiated by introducing H_2 at atmospheric pressure. The reaction products were analyzed by NMR spectroscopy and GC-MS.[129]

Supported catalysts are desirable for real-world applications and recycling. So for heterogeneous catalysis different metal oxides were used as support (e.g. Fe_2O_3, TiO_2 and SiO_2). Kinetic studies show that all three supported catalysts provided maximum conversions at a 3 hour reaction time in the reaction rate order $Au_{25}/Fe_2O_3 > Au_{25}/TiO_2 > Au_{25}/SiO_2$. The catalytic conversion and selectivity of this reaction are summarized in table 4. These supported ($Au_{25}(SCH_2CH_2Ph)_{18}$) catalysts show only a very small decrease in activity after being recycled six times.[129]

Table 4: The catalytic performance of ($Au_{25}(SCH_2CH_2Ph)_{18}$) catalysts for the selective hydrogenation of benzalacetone with H_2. [a] UA: unsaturated alcohol. [b] SK: saturated ketone. [c] SA: saturated alcohol. [d] Nanocrystals are roughly 3 nm in diameter. Reprinted with permission from ref. 129. Copyright (2010) WILEY-VCH Verlag GmbH & Co. KGaA, Weinheim.

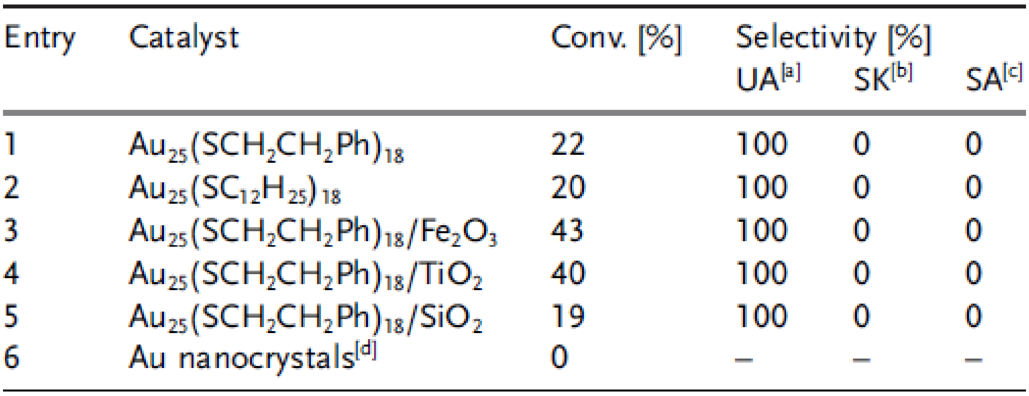

Entry	Catalyst	Conv. [%]	Selectivity [%] UA[a]	SK[b]	SA[c]
1	$Au_{25}(SCH_2CH_2Ph)_{18}$	22	100	0	0
2	$Au_{25}(SC_{12}H_{25})_{18}$	20	100	0	0
3	$Au_{25}(SCH_2CH_2Ph)_{18}/Fe_2O_3$	43	100	0	0
4	$Au_{25}(SCH_2CH_2Ph)_{18}/TiO_2$	40	100	0	0
5	$Au_{25}(SCH_2CH_2Ph)_{18}/SiO_2$	19	100	0	0
6	Au nanocrystals[d]	0	–	–	–

The origin of the catalytic activity of the monodisperse nanoscale gold clusters is still unclear and under intense debate. Jin and co-worker speculate about mechanisms that can explain this catalytic reaction: From the Au_{25} structure[90,130], the Au_{13} icosahedral core (which is electron-rich) is encapsulated by an incomplete shell consisting of the exterior 12 gold atoms in 6 oligomers with the ligand (which are electron-deficient).[27,130,131] Hence the electron-rich Au_{13} core may facilitate the adsorption and activation of the C=O bond,[132,133] while the exterior shell of Au atoms may provide a favorable environment for the adsorption and dissociation of H_2.[134]

For the sake of comparison the catalytic activity of gold clusters of different sizes ($Au_{25}(SCH_2CH_2Ph)_{18}$, $Au_{38}(SCH_2CH_2Ph)_{24}$ and $Au_{144}(SCH_2CH_2Ph)_{60}$ clusters) for the oxidation of styrene was studied by Jin and co-worker (scheme 3).[135] Catalytic oxidation reactions usually give many products and have low selectivity,[136,137] unlike hydrogenation reactions, where selectivity reaches to 100 %.[129]

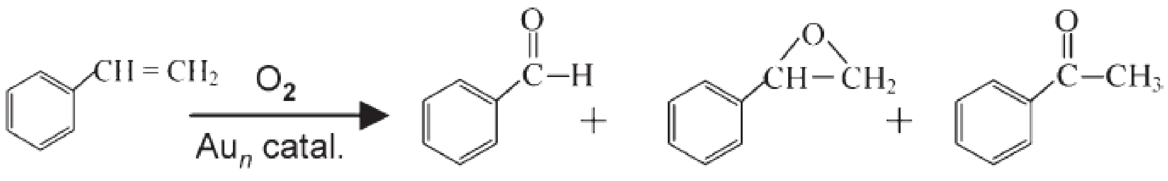

Styrene (in toluene)

1 Benzaldehyde (major)

2 Styrene epoxide (less major)

3 Acetophenone (minor)

Scheme 3: Selective oxidation of styrene by gold-cluster catalysts. Reprinted with permission from ref. 135. Copyright (2010) WILEY-VCH Verlag GmbH & Co. KGaA, Weinheim.

The catalytic oxidation of styrene by these size selected gold clusters gives benzaldehyde as a major and one epoxide as a less major product. Finally, acetophenone as a minor component is formed, too. The conversion and selectivity percentages for each cluster size and related products are summarized in table 5. From table 5 it can be concluded that the catalytic activity increases with decreasing of the cluster size.[135]

Table 5: The catalytic performance of thiolate capped $Au_n(SR)_m$ cluster catalysts for selective oxidation of styrene with O_2. The activity is averaged over three independent measurements (shown with standard deviation). Products 1–3 are as labeled in scheme 2. Reprinted with permission from ref. 135. Copyright (2010) WILEY-VCH Verlag GmbH & Co. KGaA, Weinheim.

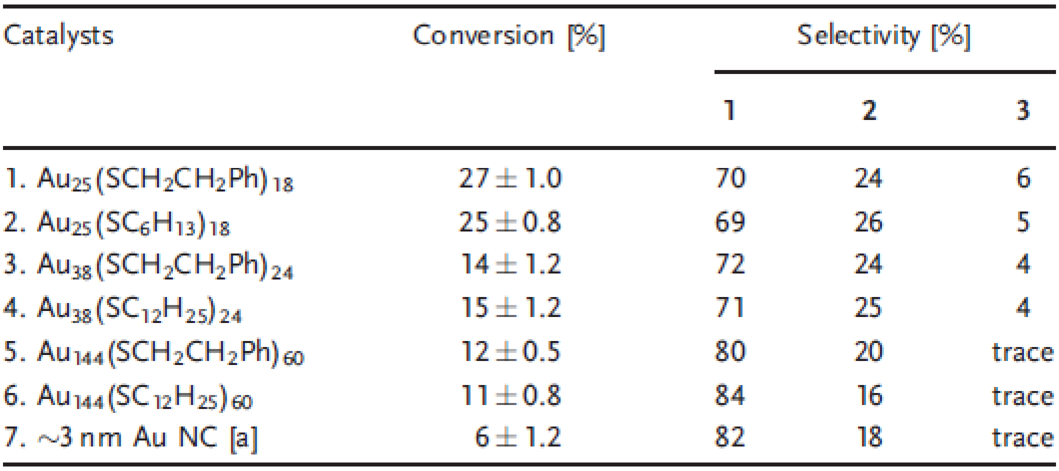

Catalysts	Conversion [%]	Selectivity [%]		
		1	2	3
1. $Au_{25}(SCH_2CH_2Ph)_{18}$	27 ± 1.0	70	24	6
2. $Au_{25}(SC_6H_{13})_{18}$	25 ± 0.8	69	26	5
3. $Au_{38}(SCH_2CH_2Ph)_{24}$	14 ± 1.2	72	24	4
4. $Au_{38}(SC_{12}H_{25})_{24}$	15 ± 1.2	71	25	4
5. $Au_{144}(SCH_2CH_2Ph)_{60}$	12 ± 0.5	80	20	trace
6. $Au_{144}(SC_{12}H_{25})_{60}$	11 ± 0.8	84	16	trace
7. ~3 nm Au NC [a]	6 ± 1.2	82	18	trace

CHAPTER 2

EXPERIMENTAL

2. Experimental

2.1. Chemicals

Due to its good availability silver nitrate was used ($AgNO_3$, ≥99% metals basis, Aldrich) to prepare silver clusters. For gold clusters tetrachloroauric(III) acid ($HAuCl_4 \cdot 3H_2O$, >99.99% metals basis, Aldrich) was used as source for Au atoms. These gold and silver clusters were protected by two different types of ligands. The first ones were achiral, this class of ligands was represented by 2-phenylethanethiol (2-PET, 99%, Aldrich) and 4-fluorothiophenol (4-FTP, 99%, Aldrich), (scheme 4). The second type chiral ligands L-glutathione (γ-L-Glutamyl-L-cysteinyl-glycine, γ-Glu-Cys-Gly, L-GSH) reduced (98%) and N-acetyl-L-cysteine (NALC, ≥99%, Sigma-Aldrich) was used, scheme 5 shows the chemical structure of the used chiral ligands. Sodium borohydride (99% metals basis, Aldrich) worked as a strong reducing agent to reduce gold (I) to gold metal and silver (I) to silver metal. Some of the preparation methods of silver clusters were conducted in a basic medium, for which potassium hydroxide (KOH, 90%, Aldrich) as a basic substance was taken. To prepare Au_{25} with different counterions tetraoctylammonium bromide (TOAB, ≥98%, Fluka) and cesium acetate (CsOAc, 99.9%, Aldrich) we used. As solvents for these experimental tetrahydrofuran (THF, HPLC grade, ≥99.9%, Aldrich), toluene (HPLC grade, ≥99.9%, Aldrich), methylene chloride (HPLC grade, ≥99.9%, Aldrich), ethanol (HPLC grade, Aldrich) and methanol (HPLC grade, Aldrich) were taken. All chemicals were used as received. Deionized water was purified by a Millipore Milli-Q water system to obtain Milli-Q water (resistivity 18.2 MΩ x cm). All glassware was thoroughly cleaned with aqua regia ($HCl:HNO_3 = 3:1$ v/v), rinsed with Milli-Q water, and then dried in an oven prior to use.

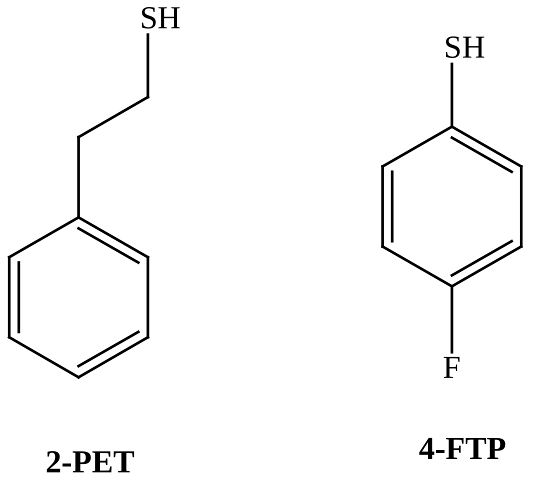

2-PET **4-FTP**

Scheme 4: 2-phenylethanethiol (2-PET) and 4-fluorothiophenol (4-FTP) achiral ligands.

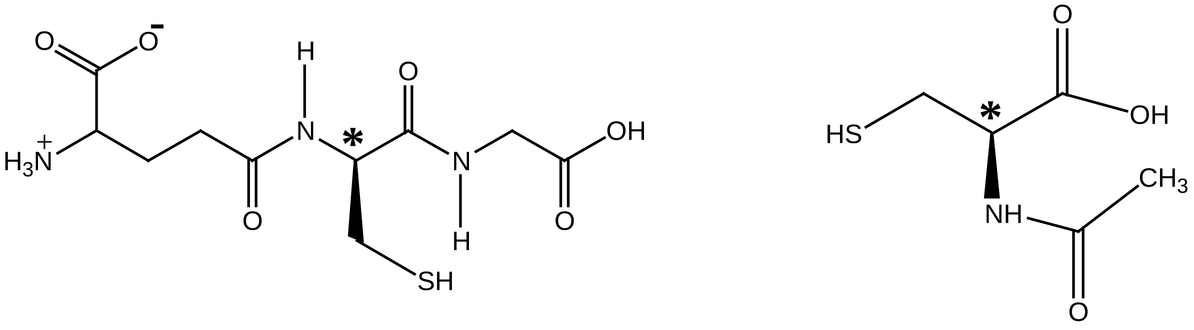

L- GSH

NALC

Scheme 5: L-glutathione (L-GSH) and N-acetyl-L-cysteine (NALC) chiral ligands.

2.2. Instrumentation and characterization

Here we will explain in brief all the instrumentals and equipments, which were used to determine the optical properties and chemical of the gold and silver nanoclusters. UV-vis spectroscopy, fourier transform infrared spectroscopy (FTIR) and photoluminescence spectroscopy (PL) enable to study the optical properties of the clusters. Transmission electron microscopy (TEM), powder X-ray diffraction (XRD) analysis, thermogravimetric analysis (TGA), elemental analysis (EA) and atomic absorption spectroscopy (AAS) was applied to determine the particles sizes and chemical composition of these clusters (AuNCs and AgNCs). The chiral properties of pure ligands and monolayer protected nanoclusters were measured by circular dichroism (CD) spectroscopy. The molecular weight and the purity of size selected gold clusters was measured by matrix-assisted laser-desorption/ionisation (MALDI) and electrospray ionization (ESI) analysis in combination with time of flight mass spectrometer (TOF-MS).

2.2.1. Matrix-assisted laser-desorption/ionisation (MALDI)

Mass spectra of size selected gold clusters protected by 2-phenylethanethiol ligand were obtained in a Bruker Autoflex MALDI-TOF mass spectrometer, after mixing the particle solution with DCTB matrix in 1:1000 mol ratio. To keep fragmentation as low as possible the laser power was reduced to a threshold value.[22]

Matrix-assisted laser desorption/ionization (MALDI) is a soft ionization technique similar to electrospray ionization (ESI) is used as an ion source for mass spectrometry. The discovery of MALDI gives the opportunity to analyze biomolecules or biopolymers (such as DNA, proteins, peptides and sugars) and large organic molecules (such as polymers, dendrimers and monolayer protected clusters). The MALDI process consist of two steps; the first one is the desorption or the evaporation the upper layer of the matrix material by a laser beam to produce a hot plume, which contains many species of neutral and ionized matrix molecules: protonated and deprotonated matrix molecules, matrix clusters and nanodroplets. Then the analyte molecules, which were drop-casted and dried over the chosen matrix (usually the molar ratio between analyte and matrix is on the order of 1:10 000) are ionized (protonated or deprotonated) by this hot plume (figure 53).[51b,138]

There are many matrices used in MALDI, which are crystalline molecules and heavily absorb laser light. The most commonly used are 3,5-dimethoxy-4-hydroxycinnamic acid (sinapinic acid), α-cyano-4-hydroxycinnamic acid and 2,5-dihydroxybenzoic acid (DHB). These matrixes are usually dissolved in highly pure solvents like water or organic solvents (e.g. acetonitrile or ethanol).[138]

The vaporization of matrix by laser gives ionic species from the matrix (Ma), which exhibit an absorption band in correspondence to the laser wavelength, as $Ma^{+\cdot}$ (odd electron molecular ions), Fr_i^+ (fragment ions), MaH^+ (protonated molecules), and Ma_nH^+ (protonated matrix clusters). These species, through gas-phase, ion–molecule reactions, gives rise to analyte positive ions (usually protonated molecules). Analogously, the formation of $[M–H]^-$ anions from the matrix can lead to deprotonated molecules of analyte (figure 53).[51b,138]

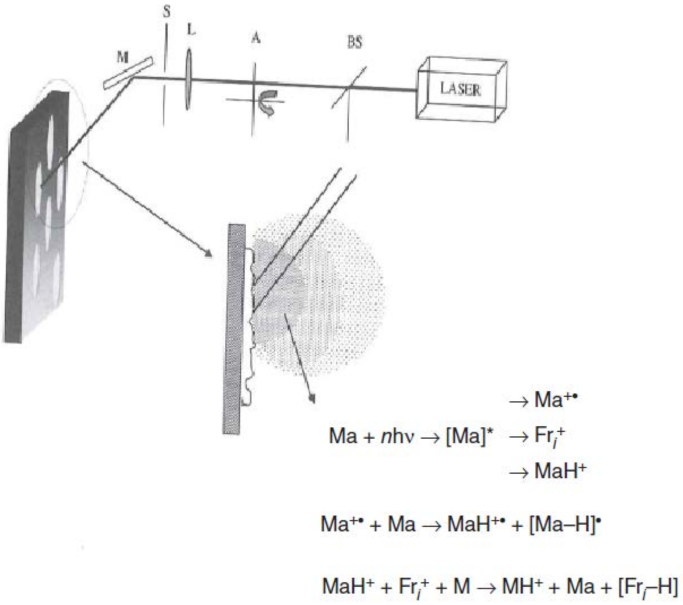

Figure 53. Scheme of MALDI ion source and reactions occurring in the high density plume originated by laser irradiation. BS, beam splitter (a portion of the laser beam is used to start the spectrum acquisition); A, attenuator (to regulate the laser beam intensity); L, focusing lens; S, slit; M, mirror. Reprinted with permission from ref. 51b. Copyright (2006) John Wiley & Sons Ltd, The Atrium, Southern Gate, Chichester, West Sussex PO19 8SQ, England.

2.2.2. Electrospray ionization (ESI)

Electrospray ionization (ESI) is a very important technique, because it is used in mass spectrometry to produce ions from macromolecules. Since ESI overcomes the propensity of macromolecules to fragment when ionized, this technique is a soft ionization technique, because there is very little fragments appear with the molecular ion. In some cases ESI is better suited than the atmospheric pressure ionization processes like MALDI, since it may produce multiply charged ions and therefore a smaller mass range of the MS is needed.[139,140]

Electrospray is based on the droplet production of a liquid solution from the sample in the presence of strong electrical fields. This solution is injected from a stainless steel capillary under high voltage (kilovolts) into the vacuum. A counter electrode is placed few-tenths of a millimeter away from it. The solution is then exiting from the needle as a charged Taylor cone or in a conical shape (figure 54).[138] If the sample is not charged, the protic solvents produce ionic species, due to their dissociation. In the case of the positive ion mode, a positive voltage is applied on this capillary, while the counter electrode is placed at a negative voltage. The opposite arrangement is used in the negative mode. In both cases a high number of charges (positive or negative) is present on the droplet surface.[138,141]

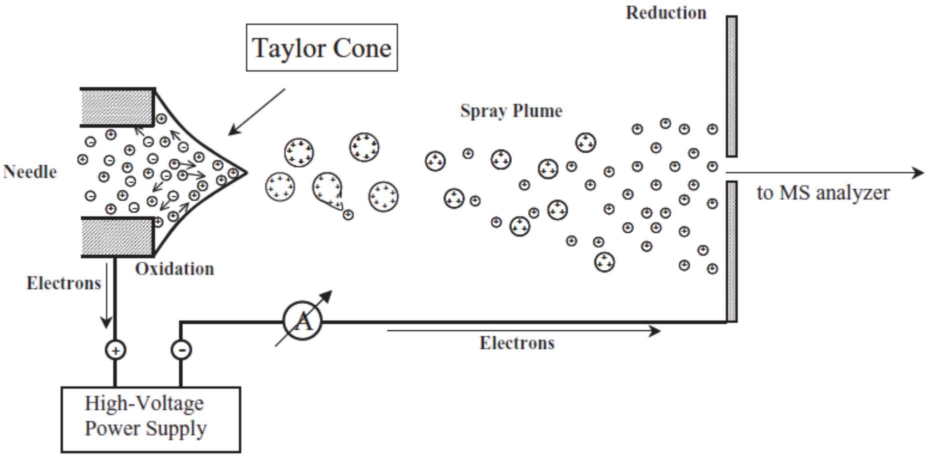

Figure 54. Schematic of an electrospray source showing the production of charged droplets from the Taylor cone. Reprinted with permission from ref. 138. Copyright (2010) John Wiley & Sons, Inc.

2.2.3. Time-of-flight mass spectrometer (TOF-MS)

TOF mass analyzers depend on the acceleration of ions with a m/z to a particular speed υ. The ions are obtained from an ion source like MALDI or ESI, and accelerated by a high electrical field (V) through a fixed potential into a drift region of a set length l (equation 3).[51]

$$\upsilon = [(2V/m)]^{1/2} \quad (3)$$

From equation 3 it is obvious that ions of different m/z values exhibit different speeds by the inversely proportionality to the square root of their m/z values. Since $\upsilon = l/t$, there is a relationship between time (t) and m/z for ions (equation 4).[51]

$$t = l(m/2V)^{1/2} \quad (4)$$

This equation shows that ions with different m/z arrive to the detector at different times, for this reason this equipment named time-of-flight mass spectrometer (figure 55).[51b]

Reflectron can correct the kinetic energy distribution of ions in the direction of ion flight. The reflectron usually uses a constant electrostatic field to reflect the ion beam in the direction of the detector. Since the more energetic ions penetrate deeper into the reflectron, and take a slightly longer path to the detector. However the less energetic ions of the same mass-to-charge ratio (m/z) penetrate a shorter distance into the reflectron, so take a shorter path to the detector. The flat surface of the ion detector is placed at the point where ions with different energies (which reflected by the reflectron) hit it at the same time.[142]

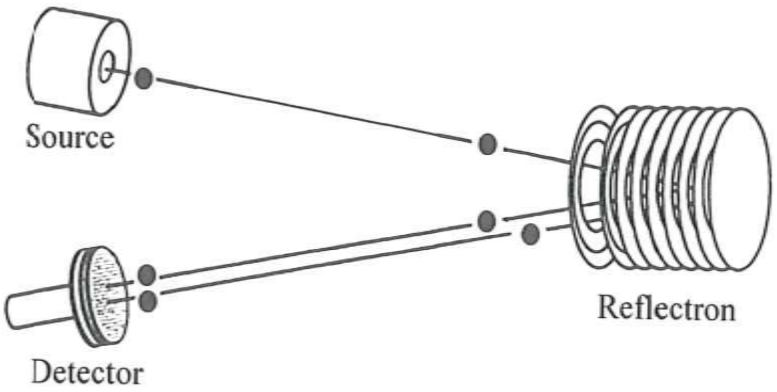

Figure 55: Scheme of reflectron TOF, Reprinted with permission from ref. 51b. Copyright (2006) John Wiley & Sons Ltd, The Atrium, Southern Gate, Chichester, West Sussex PO19 8SQ, England.

2.2.4. Circular dichroism (CD) spectroscopy

CD spectra of silver and gold nanoclusters protected by chiral ligands were measured with a Jasco J-710 spectropolarimeter using a quartz cell of 1 cm path length and solutions of about the same concentration (1 mg/ml) in water.[20,21]

Circular dichroism (CD) refers to the differential absorption of left and right circularly polarized light, passing through an absorbing optically active substance (figure 56). There are three ways to obtain the chiroptical properties of substances quantitatively by measuring the difference in absorption (ΔA), ellipticity (ψ) or rotation of polarized light. By recording the difference in absorption between the left and right helical rays and from Beer-Lambert law (equations 5 and 6) the circular dichroism (Δε) can calculate (equation 7), c refer to solution concentration, l is a pathlength.[143]

$$\Delta A = A_L - A_R = \log_{10}(I_0/I_L) - \log_{10}(I_0/I_R) = \log_{10}(I_R/I_L) \quad (5)$$

$$\Delta A = A_L - A_R = \varepsilon_L cl - \varepsilon_R cl = \Delta\varepsilon cl \quad (6)$$

$$\Delta\varepsilon = \Delta A/cl \quad (7)$$

Circular dichroism causes another effect is ellipticity (ψ). This ellipticity come from the different intense between the right and left circularly polarized light. There are relationship between ellipticity and different absorption (equation 8).[143]

$$\psi = 33\ \Delta A \quad (8)$$

The third possibility to determine the chiroptical properties is the measurement of the rotation of the plane of linearly polarized light through a substance. this method is the oldest one.[143]

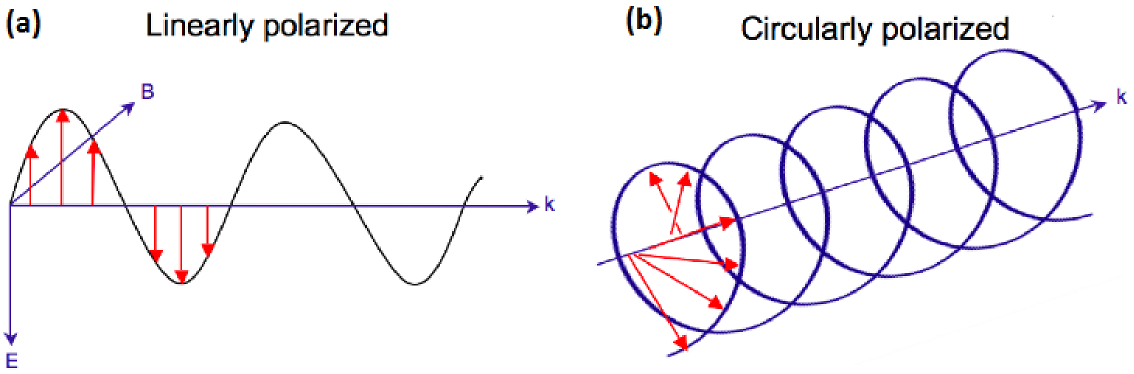

Figure 56: (a) Linear polarized light. (b) Circularly polarized light. Reprinted from ref. 144.

CD spectroscopy has a wide range of applications in many different research fields, which depends on the type of light used. Ultraviolet CD (UV-CD) is the most famous one, which is used to investigate the secondary structure of proteins,[143] and charge-transfer phenomena in many organic compounds and monolayer protected clusters.[21,145] To study the geometric and electronic structure near-infrared CD is used by probing metal d→d transitions.[146] Vibrational circular dichroism (VCD) or infrared CD is applied for elucidating the structural of small organic molecules. For protected cluster this technique is heavily used to investigate the presence of ligands.[47,143]

2.2.5. Transmission electron microscopy (TEM)

Silver and gold nanoclusters were prepared for TEM measurements by the production of 1−2 mg/mL nanocluster solutions. These solutions were obtained by dissolving the nanocluster material in solvents with the aid of sonication. For silver clusters of $Ag_n(SG)_m$, $Ag_n(NALC)_m$ and $Ag@SCH_2CH_2Ph$ in water, for Ag@SPhF silver nanoclusters soluble in toluene and for about 2 nm Ag@SG clusters in a mixture of water/ethanol, 1:1, were used. All sizes of gold clusters protected by L-glutathione and N-acetyl-L-cysteine (NALC) chiral ligands were dissolved in water. The samples were prepared for analysis by casting a droplet of MPCs solution onto carbon-coated copper grids. The solvent was then allowed to evaporate slowly. TEM images were obtained at a different magnification 100 000, 150 000 and 200 000, depending on the expected particles size of the clusters.[20,21] All the samples were recorded with a JEOL 100CX electron microscope operating at an acceleration voltage of 100 kV. The images were then analyzed using Image J software (version 1.44), which developed at the National Institutes of Health.

Transmission electron microscopy (TEM) is a type of microscopy technique, which is used to measure and detect very small materials on an atomic scale. In this technique a beam of electrons is transmitted through an ultra-thin film of the material on a carbon grid. This light beam interacts with the material as it passes through. The images of this interaction are formed, magnified and focused onto an imaging device, which usually is either a fluorescent screen, over a layer of a photographic film, or a sensor such as a charge-coupled device (CCD) camera.[147]

High-resolution transmission electron microscopy (HRTEM) can resolve distances smaller than one Angstrom (0.1 nm) can be resolved. A similar resolution can also be obtained by scanning tunneling microscopy (STM). TEM technique is highly used in protected clusters field, the particles size of the core metal of these clusters is determined by TEM. However by STM is hardly seeing the core metal, since the organic ligand will appear in the STM images, so the organic ligand will make hindrance to see the core metal. Therefore TEM has become a very powerful tool for many scientific fields like in cancer research, virology, materials science as well as pollution, nanotechnology, semiconductor research and in industrial applications.[147]

2.2.6. Powder X-ray diffraction (XRD)

Powder X-ray diffraction (XRD) was performed on a Rigaku powder diffractometer (Cu Kα1 source) with a wavelength of λ = 1.5418 Å. The detector consisted of an image plate detector (Stoe IP PSD). Fine powder samples were loaded on a quartz plate holder by spreading the powders as a smooth thin layer on to the plate. For all diffractograms, the following settings were used: scan range 20−100° (2θ), scan step 0.1°, integration time 4 s.

X-rays are electromagnetic radiation belong to a portion of gamma rays in the shorter wavelengths and with ultraviolet in the longer wavelengths. Its wavelength is in range 0.01–100 Å. The wavelength of X-rays used in X-ray diffraction is usually about 1 Å, which is comparable to the range of interatomic spacing in crystals.[148]

If a monochromatic X-ray beam hits a sample, a fraction of this light is absorbed by sample and the rest is scattered with the same wavelength as the incident beam. This type of scattering is called an elastic scattering or coherent scattering. From the specific diffraction pattern the atomic arrangement in the sample can be determined, if it is a single crystal, crystalline, amorphous like glass or liquid, which displayed in figure 57.[148]

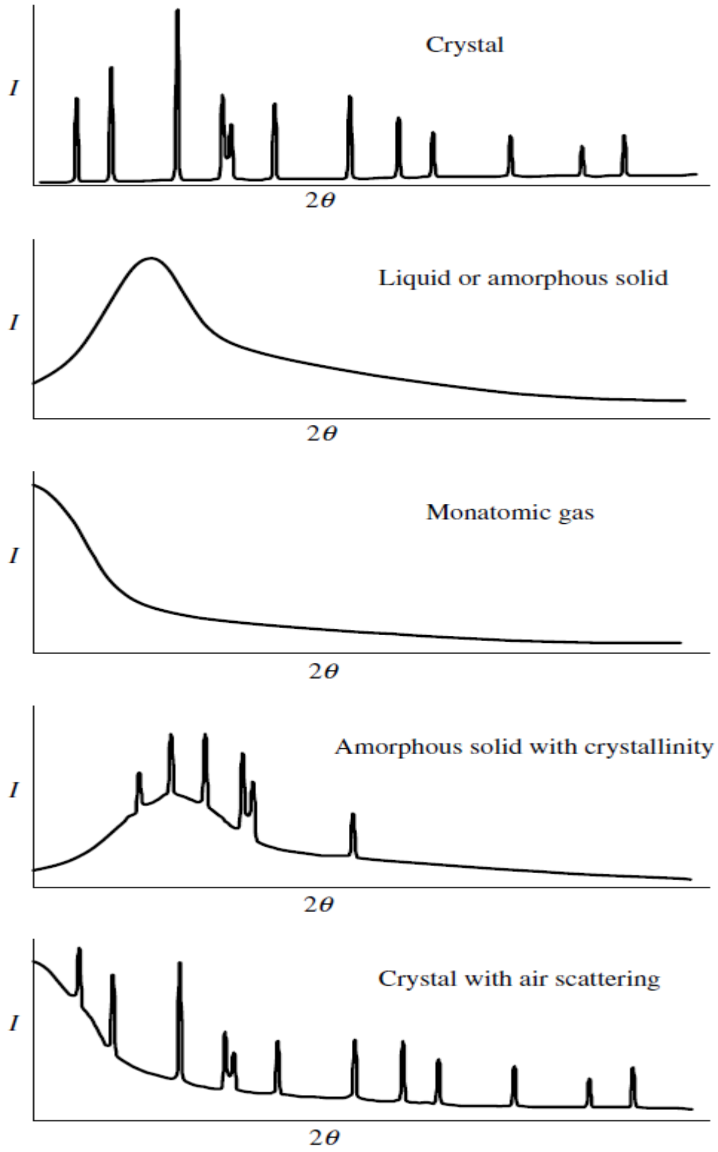

Figure 57: Diffraction patterns from crystalline solids, liquids, amorphous solids, and monatomic gases as well as their mixtures. Reprinted with permission from ref. 148. Copyright (2009) John Wiley & Sons, Inc.

There are many theories that are able to explain the relationship between the diffraction pattern and the material structure. The simplest one is described by the Bragg law ($n\lambda = 2d \sin\theta$). Figure 58a shows that the incident X-rays are reflected after they hit the crystal planes with the same angle θ. The diffraction peak is observed at angle θ when the Bragg condition is satisfied. This means that the wavelength is λ and the distance between each adjacent crystal planes equal d (d-spacing), and n is an integer number or the order of reflection (figure 58b).[148]

From the diffraction peak width (full width at half maximum, FWHM) at 2θ the particles size (D) of crystals or nanoparticles powder can be calculated with the Debye-Scherrer equation $D = 0.9.\lambda/\mathrm{FWHM}.\cos\theta$.[148,21]

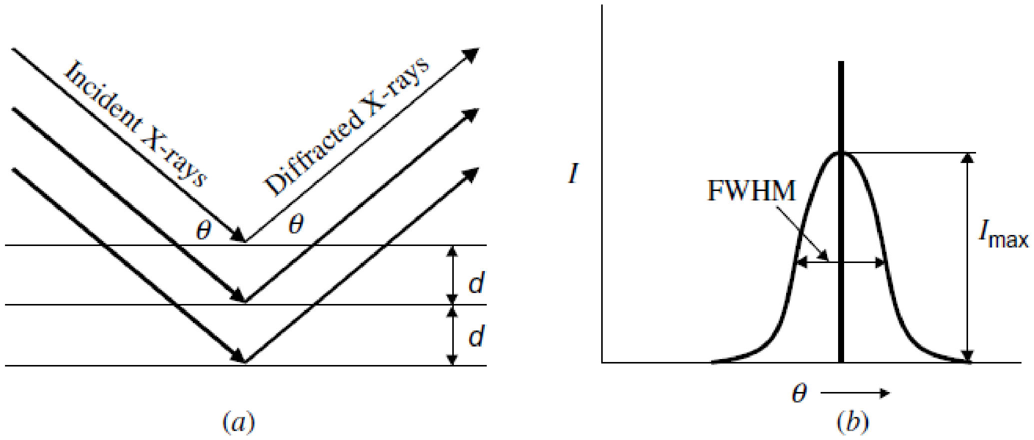

Figure 58: The incident X-rays and reflected X-rays make an angle of u symmetric to the normal of crystal plane (a). The diffraction peak is observed at the Bragg angle u (b). Reprinted with permission from ref. 148. Copyright (2009) John Wiley & Sons, Inc.

2.2.7. Photoluminescence spectroscopy (PL)

The photoexcitation and emissions studies for silver and gold nanoclusters were performed with a Varian Cary Eclipse fluorescence spectrophotometer with a xenon flash lamp as the excitation source. The band-pass for both excitation and emission monochromators was here kept at 5 nm.

Photoluminescence (PL) is a process in which a substance absorbs photons and then re-radiates by two methods, fluorescence and phosphoresces. In fluorescence the electron in the ground state is exited to an exited state and then re-irradiates from the exited state with the same spin multiplicity as the ground state with a higher wavelength. However in phosphoresces the electron is exited to triplet state with opposite direction and then the exited electron reoriented its direction to re-irradiate to ground state. This reorientation take some time, therefore the average lifetime of phosphoresces (10^{-4} to several seconds) is longer than the fluorescence (10^{-5} to 10^{-8} second) irradiation.[149] The spin of the promoted electron is still paired with the ground state electron in case exited singlet state. However in the triplet state the spins of the two electrons are unpaired, thus the magnetic properties of molecules in exited triplet state are paramagnetic and in exited singlet state is diamagnetic.[149]

The Jablonski diagram shows all these transitions, as well as other transitions like internal conversion processes in which the exited molecule is transformed to a lower energy level of exited another singlet state (S_2-S_1) without radiation emission. In case of an intersystem crossing process the spin of an exited electron is flipped and make a change in the multiplicity of molecule occurs. Hence, the molecule is transferred from singlet exited state to triplet exited state (figure 59).[149]

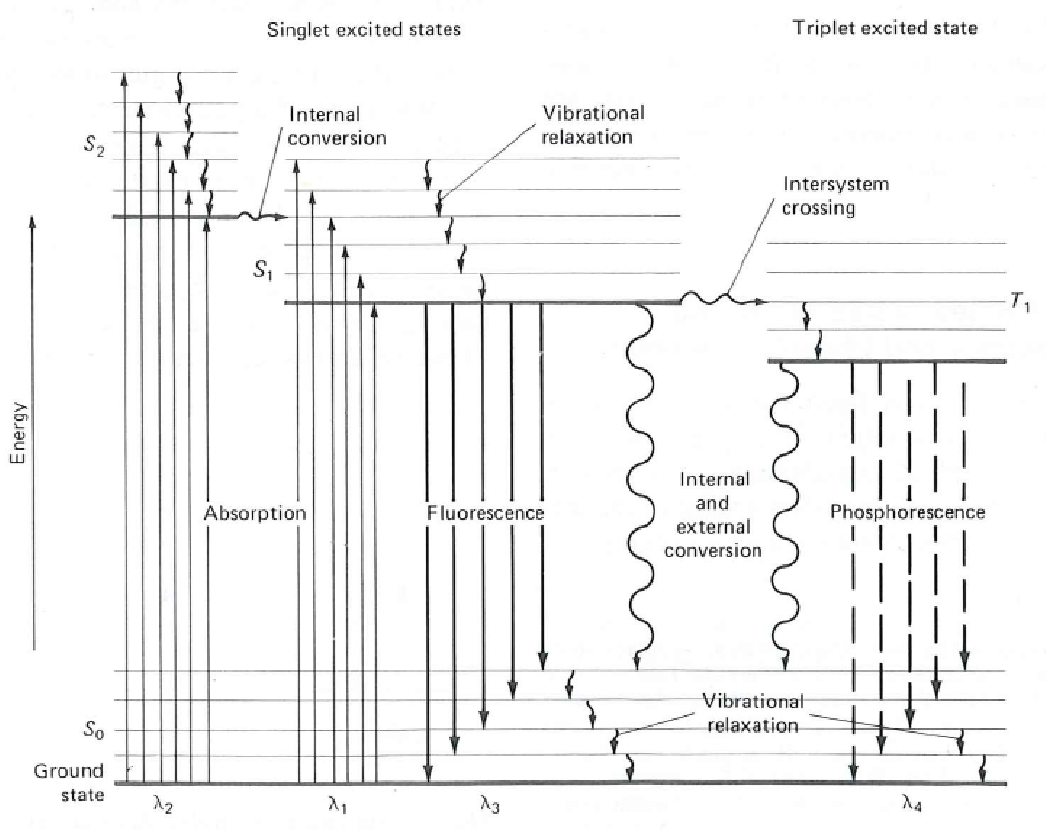

Figure 59: Partial energy diagram for a photoluminescent system. Reprinted with permission from ref. 149. Copyright (1992) Saunders College Publishing.

2.2.8. UV-vis spectroscopy

All UV-vis spectra of silver and gold nanoclusters were recorded at ambient temperature and in a wavelength range from 190 to 1100 nm with a single-beam spectrophotometer (Analytik Jena, Specord 40). Clusters solutions were prepared with a concentration of ~1 mg/mL and different solvents depending on the type of ligand protecting the clusters were used (i.e. toluene, tetrahydrofuran, and water).

UV-vis spectroscopy is used to measure the surface plasmon resonance (SPR) of silver and gold protected clusters. SPR is highly depending on the core metal type and their particles sizes. For example, silver clusters show surface plasmon resonances peak in the range 450 to 490 nm for 2 nm particle size, the same size of gold clusters exhibit SPR peak at around 550 nm. As well as UV-vis spectroscopy is used to examine the stability of protected clusters, since the UV-vis peak is sensitive to changes of the metal core, like the oxidation state and the particles size of the metal core.

2.2.9. Fourier transform infrared spectroscopy (FTIR)

Infrared spectra of 2-phenylethanethiol and 4-fluorothiophenol ligands and two silver nanoclusters Ag@SCH_2CH_2Ph and Ag@SPhF, as well as the three size selected gold nanoclusters $Au_{25}(SCH_2CH_2Ph)_{18}$ (different charges), $Au_{38}(SCH_2CH_2Ph)_{24}$, $Au_{144}(SCH_2CH_2Ph)_{60}$ were obtained using an FTIR spectrometer (Nicolet 380, resolution: < 0.9 cm−1, transmission mode). Each spectrum was recorded by accumulating 200 scans. The samples were prepared as dry, thin, optically translucent films by casting a drop of a toluene solution on a KBr disk.

We used another type of infrared spectroscopy for the water soluble ligands and clusters. The infrared spectra of L-glutathione ligand and Ag@SG nanoclusters were recorded with a FTIR spectrometer (Vertex70, Bruker, resolution: 2 cm−1, transmission mode). Again, a spectrum was obtained by accumulating 200 scans. All the samples were measured using a single-reflection diamond ATR accessory, which was installed into the Vertex FTIR spectrometer.

IR spectroscopy is used to confirm and elucidate the presence of the ligand in the protected clusters and how the ligand binding to the metal clusters. The disappearance of the S−H vibrational band at 2535−2564 cm^{-1} in the protected nanoclusters confirms an anchoring of ligands to the cluster surface through the sulfur atom.[20]

2.2.10. Thermogravimetric analysis (TGA)

Thermal gravimetric analysis (~ 1-2 mg sample tested) was conducted in a N_2 atmosphere (flow rate ~ 50 mL/min) with a TG/DAT Q5000 IR analyzer (TA Instruments, Inc.). All measurements for silver and size selected clusters were performed with a heating rate of 10 °C/ min, starting from room temperature and ranging up to 900 °C.

The effective method to determine the organic ligand fraction and metal core fraction of monolayer protected clusters (MPCs) is the thermal decomposition of the metal MPCs. Also the molecular formula of the protected clusters can be determined by TG analysis. The thermal stability of these clusters were studied by TGA.[20,21]

2.2.11. Elemental analysis (EA) and Atomic absorption spectroscopy (AAS)

To confirm the presence of ligands as it is in protected clusters we used an Euro EA apparatus. C, S, N, and H element contents were determined by an elemental analyzer that allowed the controlled combustion of the samples with subsequent chromatographic separation and the detection of the as-separated species with a TCD detector. To confirm the thermal gravimetric analysis, the amount of Ag in silver clusters (AgNCs) were determined by a fast sequential atomic absorption spectrometer (Varian AA 280 FS) using a Ag lamp as light source. AgNCs was dissolved in aqua regia, and the solution was then evaporated completely. The sample was redissolved in 10% HCl. For calibration, Ag solutions of different concentrations were prepared using the standard matrix.[20]

2.3. Methods

There are different methods to prepare gold and silver nanoclusters, which depend on the type of the ligand used to protect these clusters and the metal. Here we will give only short summary about the preparation and isolation methods of silver and gold nanoclusters. A detailed procedure is given in the published papers (chapter 3).

2.3.1. Preparation of silver nanoclusters

2.3.1.1. Preparation of organic-soluble silver nanoclusters Ag@SCH_2CH_2Ph or Ag@SPhF

The silver salt ($AgNO_3$) was dissolved in Milli-Q water, since the solubility of silver nitrate is high in water, then the ligands like 2-phenylethanethiol ($PhCH_2CH_2SH$) or 4-fluorothiophenol (FPhSH) soluble in organic solvent like methanol or tetrahydrofuran was added under ice-cold conditions with vigorous stirring. Cooling at 0^oC and stirring are very important in the formation of Ag(I)SR intermediate complex, since without these kinetically controlled conditions the silver clusters will agglomerate and give larger particles with a broad size distribution. The silver in the intermediate complex (Ag(I)SR) reduces to zero-valence state by dropwise addition of freshly prepared cold aqueous $NaBH_4$ solution with vigorously stirring. After more than one hour stirring the color of the solution has changed from colorless or pale yellow to dark brown indicating the formation of nanoparticles. The resulting precipitate was then collected through centrifugal precipitation and repeatedly washed with organic solvents to remove the unreacted material (e.g. unreacted ligands and Ag(I) thiolate complexes). Scheme 6 shows the preparation steps of Ag@SCH_2CH_2Ph nanoclusters.

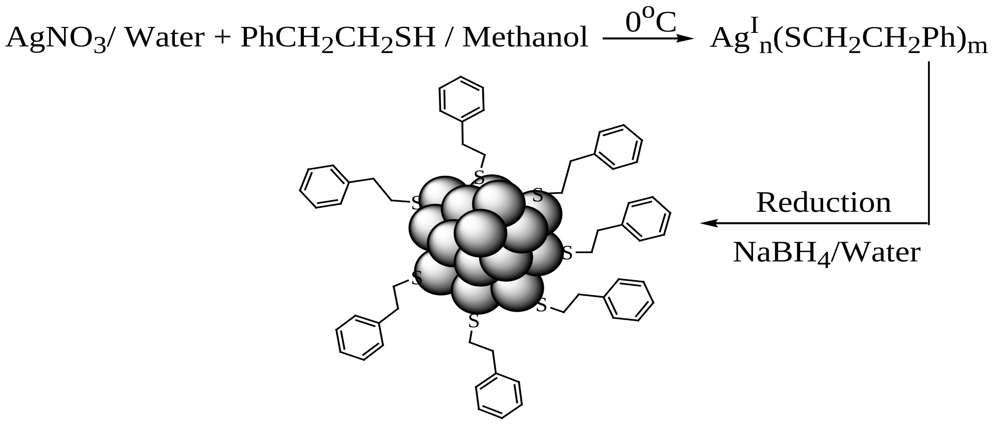

Scheme 6. Preparation steps of Ag@SCH_2H_2Ph, 1.56 mmol $AgNO_3$ in water and 9.33 mmol $PhCH_2CH_2SH$ in methanol were stirred under ice-cold conditions, 15.6 mmol $NaBH_4$ was dropwise added with vigorous stirring. The color of solution was changed to dark brown indicating the formation of nanomaterial. The reaction mixture was stirred for 1 h. The dark brown precipitate is Ag@SCH_2CH_2Ph nanoclusters. Reprinted with permission from ref. 20. Copyright (2012) American Chemical Society.

2.3.1.2. Preparation of water-soluble silver nanoclusters $Ag_n(SG)_m$ and $Ag_n(NALC)_m$

In water-soluble silver nanoclusters all the reactants are soluble in water, so the silver salt and ligands like L-glutathione or N-acetyl-L-cysteine were dissolved in Milli-Q water. Potassium hydroxide (KOH) was added to adjust the pH to about 10. Then, the freshly prepared cold aqueous solution of $NaBH_4$ was dropwise added to reduce Ag(I) to silver metal. The dropwise addition of $NaBH_4$ with vigorous stirring is the rate determining step in the preparation very small silver clusters protected by L-glutathione (~ 1 nm) (scheme 7).

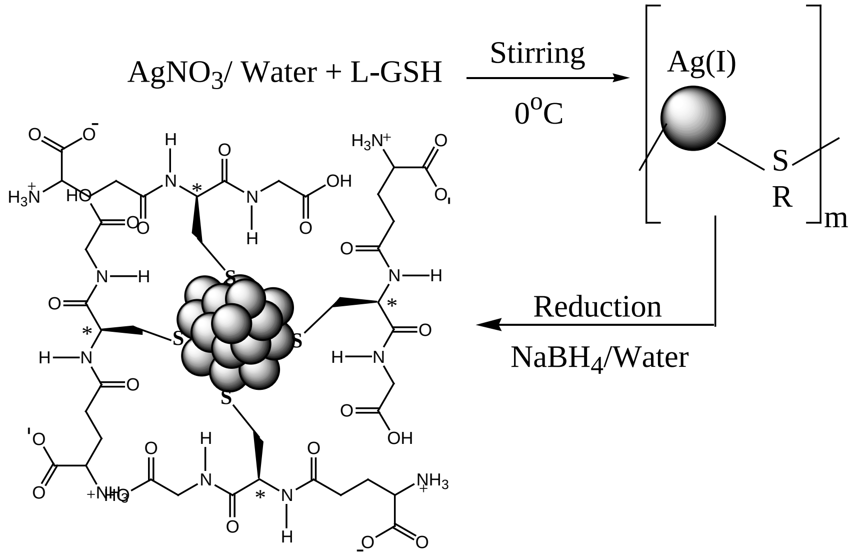

Scheme 7. Preparation steps of $Ag_n(SG)_m$ nanoclusters (~ 1 nm).

2.3.2. Preparation of gold nanoclusters

2.3.2.1. Preparation of multiple sizes of gold nanocluster $Au_n(SG)_m$ or $Au_n(NALC)_m$

We used tetrachloroauric (III) acid as a source of gold, which reacted with L-glutathione or N-acetyl-L-cysteine ligands in water at 0°C degree to Au (I). A cold aqueous solution of $NaBH_4$ was added to reduce Au (I) to gold metal. Then, methanol- induced precipitation method was applied to isolate the multiple sizes of gold clusters by controlling the amount of methanol adding and the speed and time of centrifuge. Three different sizes were separated; the larger nanoclusters were readily precipitated with only a small amount of added methanol, leaving smaller nanoclusters in the supernatant. Then, by controlling the amount of methanol added we isolated two other sizes of nanoclusters (figure 60).[38,21]

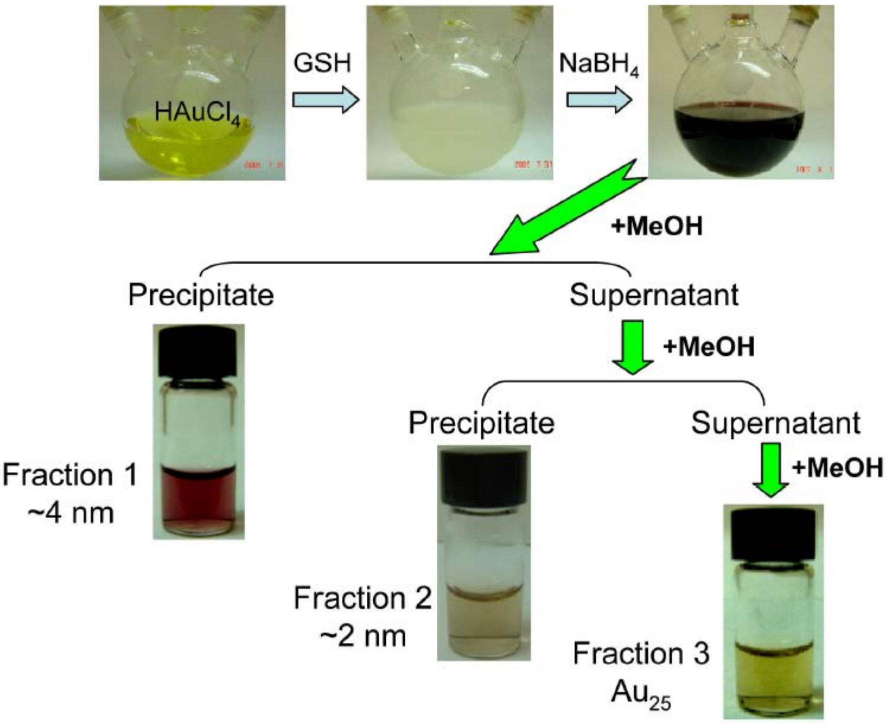

Figure 60: One-pot synthesis of Au-SG nanoparticles (where -SG represents glutathione) and separation of three major species by methanol induced precipitation (the photos of three sizes of Au nanoparticles were taken at the same concentration of around 0.14 mg mL^{-1} in water). Reprinted with permission from ref. 38. Copyright (2011) WILEY-VCH Verlag GmbH & Co. KGaA, Weinheim.

2.3.3. Preparation of size selected gold nanoclusters

Here we will write the detailed procedure for the preparation of three size selected gold clusters protected by 2-phenylethanethiol (2-PET) ligand, i.e. $Au_{25}(CH_2CH_2Ph)_{18}$, $Au_{38}(CH_2CH_2Ph)_{24}$ and $Au_{144}(CH_2CH_2Ph)_{60}$.

2.3.3.1. Preparation steps of $Au_{25}(CH_2CH_2Ph)_{18}$ nanoclusters

We followed the synthetic route of Jin and co-workers as it produces reasonable amounts of pure Au_{25} clusters by a one phase synthesis metods.[95] In a typical reaction, $HAuCl_4.3H_2O$ (124 mg, 0.32 mmol) was dissolved in 8.8 mL THF in a tri-neck flask, and the resulting solution was cooled to 0^o C with an ice bath over a period of 30 min. $PhCH_2CH_2SH$ (224 µL, 5 equivalents of the moles of gold) was slowly added to the flask and stirring was reduced to a very low speed (~60 rpm). The yellow solution turned colorless overnight, after which the stirring speed was changed to ~1200 rpm. Afterwards, an aqueous solution of $NaBH_4$ (120 mg, 10 equivalents per mole of gold, freshly dissolved with 3 ml ice cold Nanopure water) was rapidly added all at once. The reaction was allowed to proceed under constant stirring for 3 h. After that, the ice bath was removed and the solution was warmed to room temperature. The reaction was allowed to further proceed for over 114 h (aging process). After the removal of some precipitates (by-products), the solution was concentrated and cold water was added. The precipitates (Au_{25} nanoclusters) were then collected and thoroughly washed with ethanol (scheme 8).[95]

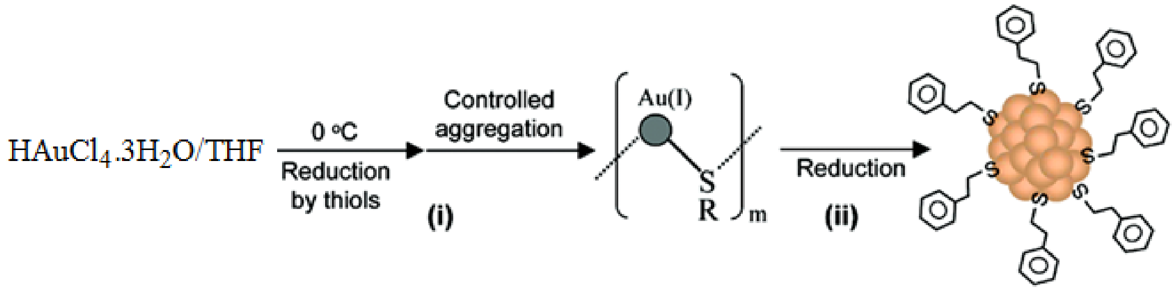

Scheme 8: Preparation step of $Au_{25}(SCH_2CH_2Ph)_{18}$ clusters by on phase method. Reprinted after modification with permission from ref. 95. Copyright (2008) The American Chemical Society.

2.3.3.2. Preparation different charge states of $Au_{25}(SCH_2CH_2Ph)_{18}$ nanoclusters

While the synthetic method described above already results in negatively charged $Au_{25}(SCH_2CH_2Ph)_{18}$ cluster,[95] these clusters are converted to neutral ones via oxidation by air or H_2O_2 (~30% aqueous). The organic solution (methylene chloride, toluene or tetrahydrofuran) of $Au_{25}(SCH_2CH_2Ph)_{18}^-$ nanoclusters was allowed to stand in air several hours.[95] To prepare the negatively charged Au_{25} cluster with different counterions, i.e. tetraoctylammonium (TOA^+) and Cs^+, all reactants were dissolved in toluene and 70% toluene/30% methanol, respectively. By the reaction with the salts (i.e. tetraoctylammonium bromide and caesium acetate; molar ratio of gold cluster to salt: 1:100) the neutrally charged

Au_{25} were converted to negatively charged ones again after stirring the solution at room temperature.[99] While in case of the TOA^+ counterion this conversion takes place within some minutes, the reaction with caesium acetate is significantly slower. In the latter case a complete conversion of the sample was obtained aver 10 hour of stirring. In each case, the conversion was monitored by UV-vis spectroscopy (figure 61). TOA^+ and Cs^+ were chosen as counterions since they are known to stabilize the anionic form of Au_{25} counterions, while smaller ions, such as Na^+ do not protect the cluster from oxidation.[86] Repeatedly, we checked the UV-vis spectra of clusters of $[Au_{25}(SCH_2CH_2Ph)_{18}]^-Cs^+$ and $[Au_{25}(SCH_2CH_2Ph)_{18}]^-TOA^+$ and found no significant oxidation of the clusters over three months.

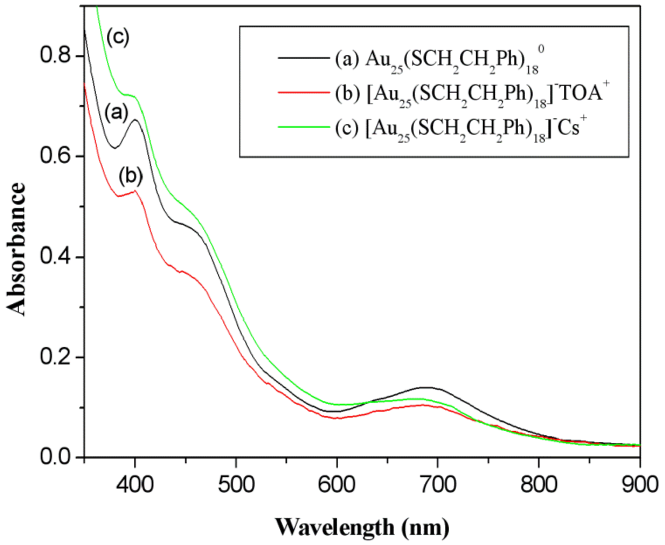

Figure 61: UV-vis spectra of Au_{25} clusters in (a) neutral form $Au_{25}(SCH_2CH_2Ph)_{18}^0$ and in the anionic form $Au_{25}(SCH_2CH_2Ph)_{18}^-$ with (b) TOA^+ and (c) Cs^+ as counterion. Nanoclusters of $[Au_{25}(SCH_2CH_2Ph)_{18}]^0$ exhibit a more distinct peak at 400 nm (figure S1a), while clusters of $[Au_{25}(SCH_2CH_2Ph)_{18}]^-$ in the negative charge state show a more pronounced transition at 450 nm and one of less intensity at 400 nm. In addition, a very small shoulder at around 780 nm (b and c) is found for negatively charged clusters, which does not appear in the neutral form. Reprinted with permission from ref. 22. Copyright (2013) the Owner Societies.

2.3.3.3. Preparation steps of $Au_{38}(CH_2CH_2Ph)_{24}$ nanoclusters

The preparation of monodisperse $Au_{38}(SCH_2CH_2Ph)_{24}$clusters was achieved by the exchange of glutathione ligands with 2-phenylethylthiol as reported in literature.[96] In a typical experiment, 98.5 mg (0.25 mmol) $HAuCl_4\cdot 3H_2O$ and 307.32 mg (1.0 mmol) GSH powder were mixed in 10 mL of acetone at room temperature under vigorous stirring for 20 min. The mixture (yellowish cloudy suspension) was then cooled to ~0 °C with an ice bath. After 20 min, 94.6 mg of $NaBH_4$ (2.5 mmol) in 3 mL cold nanopure water was rapidly added to the suspension under vigorous stirring. The color of the solution immediately turned black after the addition of $NaBH_4$, indicating the formation of Au nanoclusters. After 20 min, the black $Au_n(SG)_m$ nanoclusters were found to precipitate out and stick to the inner wall of the flask (50 mg).

Monodisperse $Au_{38}(SC_2H_4Ph)_{24}$ nanoclusters were obtained by reacting $Au_n(SG)_m$ with excess PhC_2H_4SH. Typically, a solution of $Au_n(SG)_m$ (40 mg, dissolved in 1.5 mL of nanopure water) was mixed with 60 µL of ethanol, 0.4 mL of toluene, and 0.4 mL of PhC_2H_4SH. Here, ethanol was added to prompt the phase transfer of $Au_n(SG)_m$ from water to the organic phase. The diphase solution was heated to and maintained at 80 °C under air. $Au_n(SG)_m$ clusters were found to transfer from the water phase to the organic phase in less than 10 min accompanied by the exchange of the protecting ligands. The thermal process was allowed to continue for 40 h at 80 °C. Over the long time etching process the initial polydisperse Au_n nanoclusters were finally converted to monodisperse $Au_{38}(SC_2H_4Ph)_{24}$ clusters. The organic phase was thoroughly washed with ethanol to remove the excess thiol ligands. Then the $Au_{38}(SC_2H_4Ph)_{24}$ nanoclusters were simply separated from Au(I)SG (poorly soluble in almost all solvents) by extraction with toluene. A yield of Au_{38} nanoclusters of ~25% (Au atom basis) was reproducibly obtained (scheme 9).[96]

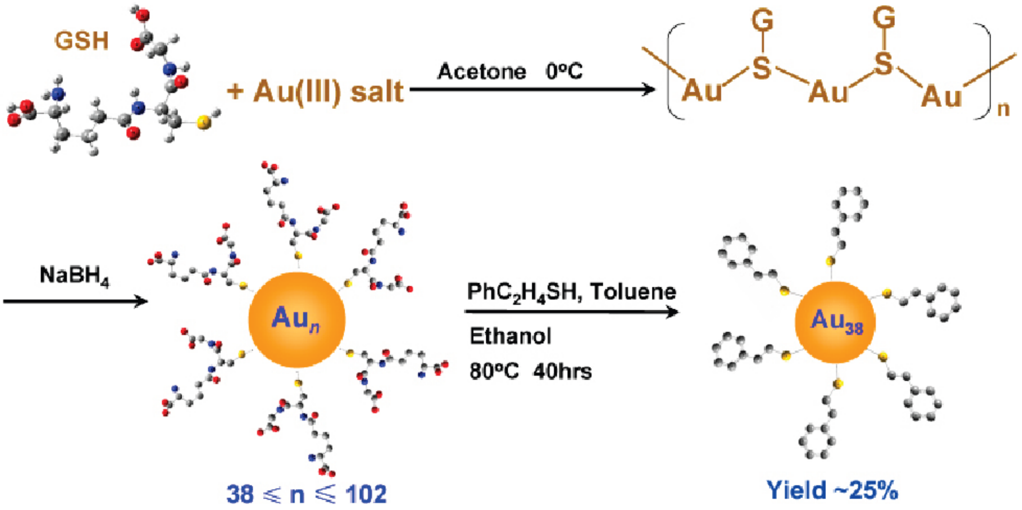

Scheme 9: A two-step procedure for synthesizing monodisperse $Au_{38}(SC_2H_4Ph)_{24}$ clusters in high yield. Reprinted with permission from ref. 96. Copyright (2009) The American Chemical Society.

2.3.3.4. Preparation steps of $Au_{144}(CH_2CH_2Ph)_{60}$ nanoclusters

We prepared Au_{144} cluster as reported by H. Qian et al.[56] Briefly, in a first step $HAuCl_4 \cdot 3H_2O$ (0.1773 g, 0.45 mmol) was dissolved in 5 ml nanopure water and TOAB (tetraoctylammonium bromide, 0.284 g, 0.52 mmol) was dissolved in 10 mL toluene. After mixing the two solutions in a 25 mL tri-neck round-bottom flask, the solution was vigorously stirred until phase transfer of Au(III) was achieved (the toluene phase became deep red while the aqueous phase became colorless). The clear aqueous phase was removed using a 10 mL syringe. The toluene solution containing Au(III) was cooled to ~0^{o} C with an ice bath (~30 min). Then, $PhCH_2CH_2SH$ (0.186 ml, ~ 3 eq. of Au) was added under fast magnetic stirring. The deep red solution turned gradually yellow and finally nearly clear with a white precipitate after about 1 hour. $NaBH_4$ (0.171 g, 4.5 mmol) was dissolved in 5 mL ice cold nanopure water. This solution was rapidly added to the flask all at once. The solution color immediately turned black. The reaction was allowed to proceed for ~24 hours and then the aqueous phase was discarded. The black toluene phase was dried by rotary evaporation. Ethanol was used to separate the Au nanoparticles from TOAB and other side products.

To obtain monodisperse Au_{144} nanoparticles, excess $PhCH_2CH_2SH$ was used to etch the as-prepared Au nanoparticles in a second step. Typically, 20 mg Au nanoparticles from the first step were dissolved in 1 mL toluene, and 0.6 mL neat PhC_2H_4SH was then added to the this solution. The solution was heated to and maintained at 80^{o}C for about 24 hours under constant magnetic stirring. After that, 20 mL methanol was added to the solution to precipitate the Au nanoparticles. Only Au_{144} nanoparticles and $Au(I)SCH_2CH_2Ph$ exist in the black precipitate. Au_{144} nanoparticles were extracted with CH_2Cl_2 and $Au(I)SCH_2CH_2Ph$ residuals (poorly soluble) were discarded. The yield was determined to 20~30 % (Au atomic basis).

CHAPTER 3

PUBLISHED PAPERS

3. Published papers

3.1. First paper (J. Phys. Chem. C, 2012, 116, 8034-8043)

3.1.1. Summary of the first paper

In this paper, we prepared some monolayer protected silver nanoclusters protected by 2-phenylethanethiol (2-PET) and 4-fluorothiophenol (4-FTP) achiral ligands and L-glutathione chiral ligand (L-GSH).

The synthesis steps of these clusters are nearly the same. This method depends on the reaction of silver salt (silver nitrate) with the ligand in suitable solvent to produce the intermediate complex Ag(I)SR. To reduce Ag(I) to Ag metal we used a very strong reducing agent, i.e. sodium borohydride ($NaBH_4$).

To characterize the as-prepared clusters we used several different analytical tools. The optical properties of these nanoclusters were studied by UV-vis spectroscopy. $Ag@SCH_2CH_2Ph$ and Ag@SG clusters give one broad absorption peak at 469 nm and 478 nm in toluene and water, respectively. Ag@SPhF in THF shows two absorption bands at 395 and 462 nm. Mie theory indicates the peaks in the UV-vis spectra of these clusters originate from plasmonic transitions. Transmission electron microscopy (TEM) was used to measure the morphology and the particle sizes for the three prepared silver nanoclusters; the three silver clusters show an average particle size of around 2 nm. The Image J program was used to determine the Gaussian fit distribution of the particles sizes for all three clusters. Thermogravimetric analysis (TGA) was used to study the thermal stability of these clusters. $Ag@SCH_2CH_2Ph$ and Ag@SPhF nanoclusters show a highly thermal stability untill 200 ^{0}C. Then, the protected ligand is complete destroyed and the silver cluster agglomerate. Ag@SG clusters shows four steps of mass loss upon heating from 40 to 900 ^{0}C. From TG analysis the Ag/S ratio can be calculated and the chemical formula of the ligands surround the clusters can be obtained. These calculations are confirmed by the elemental analysis and atomic absorption spectroscopy (AAS). Structural properties of the ligands binding to the nanoclusters were elucidated by FTIR analysis. By comparing the IR absorption spectra of pure ligands with those of the protected silver nanoclusters, we found that the only difference is the disappearance of the S−H vibrational band (2535−2564 cm^{-1}) in the spectra of the protected silver nanoclusters. This confirms the anchoring of ligands to the cluster surface through the sulfur atom. Circular dichroism (CD) spectra were used to measure the chirality of clusters.

THE JOURNAL OF PHYSICAL CHEMISTRY C
Article
pubs.acs.org/JPCC

Preparation and Spectroscopic Properties of Monolayer-Protected Silver Nanoclusters

Mostafa Farrag,[†] Martin Thämer,[†] Martin Tschurl,*[,†] Thomas Bürgi,[‡] and Ueli Heiz[†]

[†]Lehrstuhl für Physikalische Chemie, Technische Universität München, Lichtenbergstrasse 4, 85748 Garching, Germany
[‡]Département de Chimie Physique, Faculté Des Sciences, University of Geneva, Quai Ernest-Ansermet 30, 1211 Genève 4, Switzerland

Ⓢ *Supporting Information*

ABSTRACT: Silver nanoclusters protected by 2-phenylethanethiol (**1**), 4-fluorothiophenol (**2**), and L-glutathione (**3**) ligands were successfully synthesized. The optical properties of the prepared silver nanoclusters were studied. The absorption signal of Ag@SCH_2CH_2Ph in toluene can be found at 469 nm, and Ag@SPhF in THF shows two absorption bands at 395 and 462 nm. Ag@SG in water absorbs at 478 nm. Mie theory in combination with the Drude model clearly indicates the peaks in the spectra originate from plasmonic transitions. In addition, the damping constant as well as the dielectric constant of the surrounding medium was determined. In addition, the CD spectra of silver nanoclusters protected by the three ligands (**1**−**3**) were also studied. As expected, only the clusters of type **3** gave rise to chiroptical activity across the visible and near-ultraviolet regions. The location and strength of the optical activity suggest an electronic structure of the metal that is highly sensitive to the chiral environment imposed by the glutathione ligand. The morphology and size of the prepared nanoclusters were analyzed by using transmission electron microscopy (TEM). TEM analysis showed that the particles of all three types of silver clusters were small than 5 nm, with an average size of around 2 nm. The analysis of the FTIR spectra elucidated the structural properties of the ligands binding to the nanoclusters. By comparing the IR absorption spectra of pure ligands with those of the protected silver nanoclusters, the disappearance of the S−H vibrational band (2535−2564 cm^{-1}) in the protected silver nanoclusters confirmed the anchoring of ligands to the cluster surface through the sulfur atom. By elemental analysis and thermogravimetric analysis, the Ag/S ratio and, hence, the number of ligands surrounding a Ag atom could be determined.

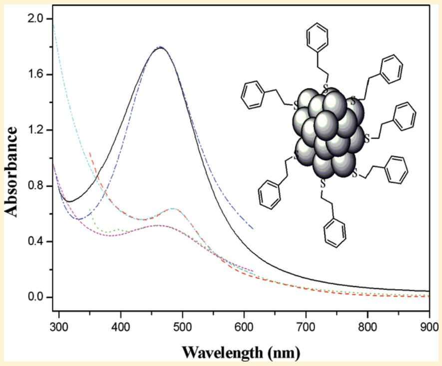

■ INTRODUCTION

Noble metal clusters have stimulated major research interest in recent years.[1−3] Thiolate monolayer-protected clusters (MPCs) consist of a metallic core that is surrounded by ligands that stabilize the clusters and can subsequently being modified. In addition, it is possible to dissolve, dry, and redissolve these types of nanoparticles without suffering from degradation.[4] Usually, ligand-protected clusters possess properties that make them accessible to synthetic altering, which is essential for various applications.[5−10] The optical and electronic properties of the metal nanoclusters (MNCs) have made them suitable for many applications in various fields of science, such as bioscience,[5−7] nanophotonics,[8] and nanoelectronics.[9,10] Therefore, NPs have attracted large research efforts, and their properties depend strongly on the particle size[11−13] and shape,[14,15] the surrounding medium,[16] and the aggregation state.[15]

Concerning their optical properties, the dominating feature in the optical spectra of silver nanoclusters is usually the surface plasmon resonance, which can be described by the classical Mie theory. The resonance position and the peak width depend on many factors and give insight into several physical properties of the MPCs. For small silver clusters (<10 nm), the Mie theory predicts almost no influence of the cluster size on the position of the resonance, which is located around 350 nm for small spherical Ag clusters in vacuum (calculated from Mie theory). However, already small changes in the electronic properties of the surrounding medium of the cluster lead to strong shifts of the peak.

On the basis of the properties of these shifts, the electronic interaction between the cluster and its surroundings can be derived. Since MPCs consist of a metallic core covered by ligands, the surroundings of the cluster is governed by these ligands, and therefore, additional information about the metal−ligand bond can be obtained from these shifts. The cluster size in that region of a couple of nanometers has mainly an influence on the peak width caused by the free mean path effect[17] of the free electrons inside the cluster. Here, the width increases with decreasing cluster size due to additional scattering processes of the oscillating electrons at the cluster surface.

Received: October 31, 2011
Revised: March 2, 2012
Published: March 5, 2012

dx.doi.org/10.1021/jp210453v | *J. Phys. Chem. C* 2012, 116, 8034−8043

Another effect that leads to a broadening of the surface plasmon is the so-called electron spill out effect.[18] This effect can be highly enhanced by delocalization of the conduction electrons over the ligands. However, the influence of ligands on the electron spill out is not yet fully understood.

For very small Ag clusters (<8 atoms) the concept of a plasmon does not hold anymore because the energy bands of the cluster split into discrete energy levels. Here, the broad plasmon absorption band is predicted to split into sharp molecular-like transitions;[19] however, the spectra of the Ag clusters used in this work can be treated using the classical description of surface plasmons because their size is in the nanometer scale.

It is well-known that metal surfaces can exhibit an intrinsically chiral structure.[20] Furthermore, chirality can be transferred to achiral metal surfaces by the adsorption of chiral molecules.[21,22] Similarly, metal NPs can exhibit chirality, which can be found by their optical activity of the electronic transitions that are metal-based; however, transfer of chirality from the adsorbate to the metal surface strongly depends on the structure of the former. Chiroptical techniques such as electronic circular dichroism (CD) and vibrational circular dichroism (VCD)[23] are valuable tools to elucidate this transfer of chirality from the ligand to the nanoparticles. Due to their organic shell, monolayer-protected AgNPs can be dissolved in various solvents and are thus amenable to these techniques.

A well-established route to prepare solution phase metal clusters is to use strong ligands (such as thiols) to protect the clusters and effect size control.[24−29] Among the noble metals, gold clusters are being extensively studied because of their chemical stability and relative ease of preparation, even under ambient conditions. Some well-defined, monodisperse Au_n nanoclusters have been reported, and their exact formulas have been determined by electrospray ionization mass spectrometry analysis (ESI-MS).[25−28] Work on understanding the electronic and atomic structures of this class of clusters has accelerated, including the complete structural determination of clusters consisting of 25, 38, and 102 gold atoms.[25−28]

Both Au and Ag are noble, free electron metals and have almost identical bulk lattice constants. On the basis of these similarities, Ag could be expected to follow the same shell closing rules as Au;[29] however, thus far, the shell closing rules for Ag remain unexplored. In the present study, we show that it is possible to synthesize Ag clusters that are protected by different ligands, which opens the door to study these important MNC in the future in more detail.

In this article, we report the synthesis of new silver nanoclusters protected by 2-phenylethanethiol (**1**) (Scheme 1), 4-fluorothiophenol (**2**), and L-glutathione (**3**) ligands by different protocols (see the Experimental Section). For the sake of characterization, the optical properties of these silver nanoclusters are studied by UV−vis spectroscopy and Fourier transform infrared spectroscopy (FTIR). The size and composition of AgNCs were assessed by thermogravimetric analysis (TGA), elemental analysis, and transmission electron microscopy (TEM).

■ EXPERIMENTAL SECTION

Chemicals. Silver nitrate ($AgNO_3$, ≥99% metals basis, Aldrich), sodium borohydride (99% metals basis, Aldrich), 2-phenylethanethiol (2-PET, 99%, Aldrich), 4-fluorothiophenol (4-FTP, 99%, Aldrich), and glutathione (γ-L-glutamyl-L-cysteinylglycine, γ-Glu-Cys-Gly, L-GSH) reduced (98%) were used for synthesizing the ligand-protected nanoparticles (for the chemical structure of the used ligands, see Scheme 1). The solvents used were tetrahydrofuran (THF, HPLC grade, ≥99.9%, Aldrich), toluene (HPLC grade, ≥99.9%, Aldrich), ethanol (HPLC grade, Aldrich), and methanol (HPLC grade, Aldrich). All chemicals were used as received. Deionized water was purified by a Millipore Milli-Q water system to obtain Milli-Q water (resistivity 18.2 MΩ x cm). All glassware was thoroughly cleaned with aqua regia (HCl/HNO_3 = 3:1 v/v), rinsed with Milli-Q water, and then dried in an oven prior to use.

Scheme 1. The Ligands Used for Protecting the Clusters: 2-PET, 4-FTP, and L-Glutathione

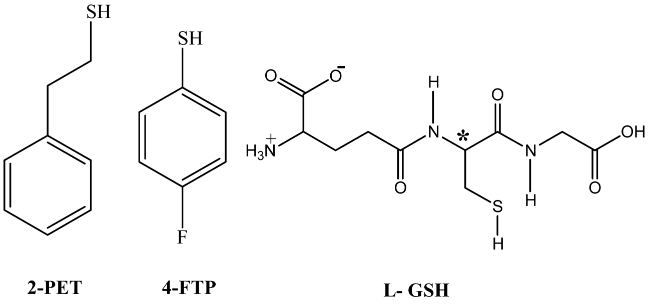

Preparation of $Ag@SCH_2CH_2Ph$ Nanoclusters. The silver salt ($AgNO_3$, 265 mg, 1.56 mmol) was dissolved in 5.3 mL of Milli-Q water and was added afterward to 1.25 mL (9.33 mmol) of $PhCH_2CH_2SH$ (2-PET) in 100 mL of methanol under ice-cold conditions with vigorous stirring (20 min). Silver was reduced to the zero-valence state by dropwise addition of freshly prepared aqueous $NaBH_4$ solution (590 mg, 15.6 mmol in 25 mL of ice-cold Milli-Q water) and stirring vigorously (~1100 rpm). The color of solution changed to dark brown, indicating the formation of nanomaterial. The reaction mixture was stirred for another 1 h. The resulting precipitate was then collected through centrifugal precipitation and repeatedly washed with methanol to remove the unreacted material (e.g., unreacted ligands and Ag(I) thiolate complexes). Finally, the $Ag@SCH_2CH_2Ph$ (**1**) nanocluster precipitate was dried and collected as a dark brown powder (Scheme 2).

Preparation of Ag@SPhF Nanoclusters. Thirty milligrams of silver nitrate (0.176 mmol) was dissolved in 18 mL of THF and stirred for 5 min. 4-Fluorothiophenol (4FTP) (38 μL, 0.357 mmol) was added to that solution and the resulting solution was stirred for another 15 min. During this time, the color of the solution changed from colorless to yellow, indicating the formation of Ag(I) thiolate complexes. A 71.5 mL THF solution of $NaBH_4$ (27 mg, 0.715 mmol) that had been stirred previously for a total of 30 min was then added slowly to the reaction vessel. A change in the the color of the solution from yellow to orange to brown and, finally, to dark brown over a period of 5 min was observed. The reaction mixture was left to stir for an additional 3 h, after which 11.5 mL of Milli-Q water was added. After stirring for another minute, the reaction vessel was then stored in a freezer (at −4 °C) for 7 days. Since the final product is soluble in THF, the THF layer was separated from the frozen aqueous layer by decantation. At this stage of the preparation, the solution was found to remain stable under refrigeration or even at room temperature for several months in the dark. At all reaction stages, the formation and the stability of the samples were checked using UV−vis spectroscopy due to the characteristic

Scheme 2. Preparation Steps of Ag@SCH$_2$H$_2$Ph^a

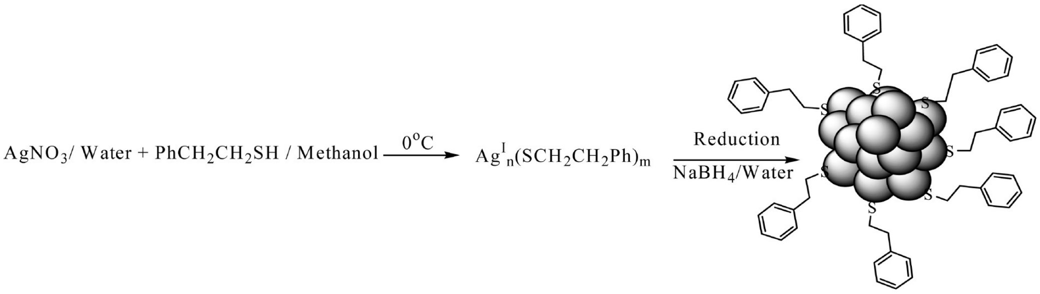

^{a}A 1.56 mmol portion of AgNO$_3$ in water and 9.33 mmol of PhCH$_2$CH$_2$SH in methanol were stirred under ice-cold conditions, then 15.6 mmol of NaBH$_4$ was dropwise added with vigorous stirring. The color of the solution changed to dark brown, indicating the formation of nanomaterial. The reaction mixture was stirred for 1 h. The dark brown precipitate is Ag@SCH$_2$CH$_2$Ph (**1**) nanoclusters.

absorption bands of the clusters that will vanish if the sample decomposes.

For the application of thermogravimetric analysis, elemental analysis, atomic absorption spectrometry, and transmission electron spectroscopy, a solid sample is needed. Therefore, the THF solution of the clusters was concentrated under vacuum at room temperature. Afterward, cold water was added, and the precipitate was then collected and dried under vacuum to obtain a solid sample of pure Ag@SPhF (**2**) nanoclusters.

Preparation of Ag@SG Clusters. A 94 mg portion silver nitrate (0.87 mmol) was dissolved in 10 mL of Milli-Q water, and 300 mg of L-glutathione (0.97 mmol) was added afterward. The solution was then stirred vigorously at room temperature for 30 min. The resulting solution was cooled to 0 °C in an ice bath over a period of 20 min, and a freshly prepared aqueous solution of NaBH$_4$ (378 mg, dissolved in 20 mL of ice-cold Milli-Q water) was added under vigorous stirring conditions (~1100 rpm). The reaction was allowed to proceed under constant stirring for 2 h. Following that, 25 mL of ethanol was added to precipitate the clusters. After filtration, the brown precipitate of Ag@SG (**3**) nanoclusters was washed with excess ethanol.

Instrumentation and Characterization. To obtain the UV–vis absorption spectra of type **1**, **2**, and **3** nanoclusters, solutions of ~1 mg/mL were prepared in toluene, tetrahydrofuran, and water, respectively. The spectra of all the solutions were recorded at ambient temperature from 190 to 1100 nm with a single-beam spectrophotometer (Analytik Jena, Specord 40). CD spectra of nanoclusters of type **1**–**3** were measured with a Jasco J-710 spectropolarimeter using a quartz cell of 1 cm path length and solutions of about the same concentration and using the previously described solvents. Infrared spectra of 2-phenylethanethiol and 4-fluorothiophenol as well as Ag@SCH$_2$CH$_2$Ph (**1**) and Ag@SPhF (**2**) nanoclusters were obtained using an FTIR spectrometer (Nicolet 380, resolution: < 0.9 cm^{-1}, transmission mode). Each spectrum was obtained by accumulating 200 scans. The infrared spectra of L-glutathione ligand and Ag@SG (**3**) nanoclusters were recorded with a FTIR spectrometer (Vertex 70, Bruker, resolution: 2 cm^{-1}, transmission mode). Again, a spectrum was obtained by accumulating 200 scans. All the samples were measured using a single-reflection diamond ATR accessory, which was installed into the Vertex FTIR spectrometer.

Thermal gravimetric analysis (~ 2 mg sample tested) was conducted in a N$_2$ atmosphere (flow rate ~ 50 mL/min) with a TG/DAT Q5000 IR analyzer (TA Instruments, Inc.). All measurements were performed with a heating rate of 10 °C/min, starting from room temperature and ranging up to 900 °C. Analysis of C, S, N, and H content was performed by an elemental analyzer (Euro EA) that allowed controlled combustion of the samples with subsequent chromatographic separation and the detection of the as-separated species with a TCD detector. The amount of Ag was analyzed by a fast sequential atomic absorption spectrometer (Varian AA 280 FS) using a Ag lamp as light source. AgNCs were dissolved in aqua regia, and the solution was then evaporated completely. The sample was redissolved in 10% HCl. For calibration, Ag solutions of different concentrations were prepared using the standard matrix.

Samples were prepared for TEM measurements by the production of 1–2 mg/mL nanocluster solutions. These solutions were obtained by dissolving the nanocluster material in solvents with the aid of sonication. For clusters of type **1** and **2**, water and toluene were used as solvents, respectively, and for the clusters of type **3**, a mixture of water/ethanol, 1:1, was used. The samples were prepared for analysis by casting a droplet of MPC solution onto carbon-coated copper grids. The solvent was then allowed to evaporate slowly. TEM images were obtained at a magnification of 100 000 for types **1** and **3** clusters and a magnification of 150 000 for type **2** clusters with a JEOL 100CX electron microscope operating at an acceleration voltage of 100 kV. The images were then analyzed using Image J software (version 1.44).

■ RESULTS AND DISCUSSION

After having successfully synthesized Ag MPCs they were characterized with respect to their chemical composition, the ligand–metal bonding, their size, and their stability. Furthermore, in this section, we present and discuss the optical spectra and show the CD spectra of all three types of clusters.

Chemical Composition of Ag MPCs. One way of deducing the exact number of silver atoms and thiolate ligands of the particle is to determine the Ag/S ratio. This ratio can be obtained by performing elemental analysis or thermogravimetric analysis. In both methods, the organic content is determined, and from that, the Ag/S atomic ratio can be calculated.[30]

TGA analysis shows that the organic weight loss of the 2-PET- and 4-FTP-protected silver nanoclusters is 48.95% (wt) from 224 to 246 °C and 35.85% from 201 to 225 °C (Figure 1), respectively. Therefore, the silver content of Ag@SCH$_2$CH$_2$Ph is calculated as 51.05% and for Ag@SPhF, as 64.15% (for a complete summary of the elemental composition

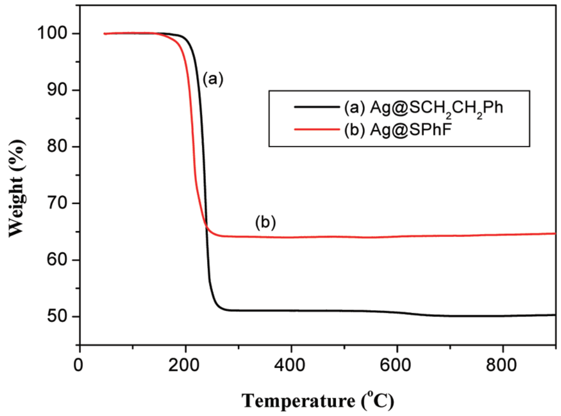

Figure 1. Theromgravimetric analysis of Ag@SCH$_2$CH$_2$Ph and Ag@SPhF nanoclusters. For Ag@SCH$_2$CH$_2$Ph nanoclusters (a), the percentage of the organic layer is 48.95%, and the rest is silver metal (51.05%). The decomposition of the clusters starts at 224 °C. Ag@SPhF nanoclusters (curve b) consist of an organic layer, which is 35.85% of their total mass. Again, the rest (64.15%) is only silver metal. These clusters start to decompose at 201.5 °C.

of these two clusters, see Tables S1 and S2 in the Supporting Information). The 48.95% (wt), and 35.85% loss converts to an Ag/S atomic ratio of 1/0.75 and 1/0.47, respectively. This composition is further supported by the elemental analysis of the Ag@SCH$_2$CH$_2$Ph and Ag@SPhF nanoclusters, which show that the organic content of these clusters consists of 34.28% C, 3.28% H, 11.49% S, and 20.41% C and 1.19% H, 8.95% S, 5.41% F, respectively (see again Tables S1 and S2 in the Supporting Information). Thus, the molar ratio of C/H/S in nanoclusters of type **1** is 7.96:9.08:1, which equals the molecular formula of phenylethylthiolate (C_8H_9S). Looking at the type **2** nanoclusters, a molar ratio of C/H/F/S = 6.08:4.23:1.01:1 is found, which is also in very good agreement with the chemical formula of 4-fluorothiophenolate (C_6H_4FS). In addition, by using atomic absorption spectroscopy, the percentage of Ag was directly obtained. It was found to be 50.95% for clusters of type **1** and 64.04% for clusters of type **2** (see Tables S1 and S2 in the Supporting Information), thus confirming composition obtained from thermogravimetric analysis.

In contrast to nanoclusters of types **1** and **2**, which show only one step of mass loss in their thermogravimetric curve, four steps can be found when heating Ag@SG (**3**) up to 900 °C (Figure 2a). In the first step (from 40 to 180 °C), the mass loss (9.16%) is caused by the evaporation of adsorbed water molecules. This assignment is based on the comparison with the curve of the ligand only, which shows no mass loss until 200 °C (Figure 2b). This phenomenon can also be found in the thermoanalysis of gold nanoparticles[31,32] protected by mercaptosuccinic acid.[31]

Concerning the other steps, they might be interpreted analogously to the TG curve of pure glutathione: In the thermoanaylsis of the bare ligand, three steps of decomposition can be found during heating from 40 to 900 °C (Figure 2b). The first step (200−300 °C) amounts to a loss of 41.74% of the total mass, corresponding to the hydrolysis of glutathione to hydrolyzed glutathione,[31] which equals 129 Da (the theoretical amount of this part is 42%). This is consistent with the work of Teranishi et al. who found that $Au_{25}(SG)_{18}$ shows the same weight loss plus one hydrogen atom (130 Da) in ESI mass spectroscopy.[27a]

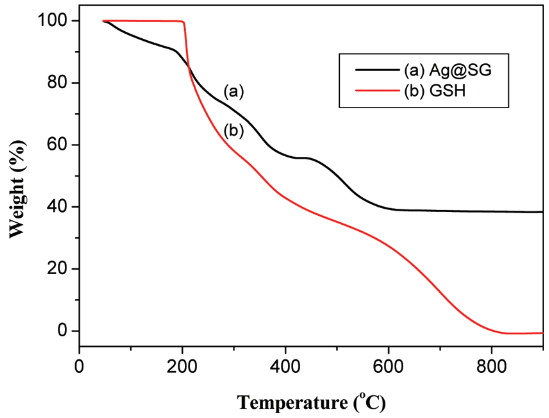

Figure 2. TGA of Ag@SG nanoclusters (curve a) and glutathione ligand (curve b). (a) Ag@SG shows four steps of mass loss upon heating from 40 to 900 °C. In the first step (40−180 °C), involves adsorbed water molecules (9.16%). The total mass loss during the remaining three steps from 180 to 900 °C amounts to 51.74% (16.71%, 18.09%, and 16.94%, respectively). (b) The first step (200.50−299.35 °C) amounts to 41.74%, the second step (299.35−451.94 °C) amounts to 19.37%, and the third step from 451.94 to 819.51 °C (38.90%) completes the destruction of glutathione.

The second step (300 − 452 °C) amounts to a mass loss of 19.37%, and the third step from 452 to 820 °C (38.90% mass loss) completes the destruction of glutathione. The total mass loss of these three steps is 100%, showing complete removal upon heating.

Note that the sum of the total mass loss of the last three steps of the TG curve of Ag@SG (**3**) equals 51.74%. This value is much less than that of the total organic content (69.09%) that is obtained from elemental analysis (see Table S3 in the Supporting Information). Therefore, it can be concluded that not all of fragments of the ligands are evaporated, and some of the organic residues still remain on the metal compound. Consequently, TG analysis overestimates the percentage of the Ag content (39.10%) in comparison with atomic absorption spectroscopy analysis 30.91% (see Table S3 in the Supporting Information).

Finally, the TGA residue was also investigated with atomic absorption spectrometry and elemental analysis. Although the first method showed the amount of Ag to be only 44.7% (instead of 100%), the latter method determined the composition of the organic species to be 22.75% C, 1.22% H, 1.17% N, 4.91% S, with the remaining amount being oxygen. These measurements independently confirm the ligand not to be evaporated into the gas phase entirely. The Ag/S atomic ratio for Ag@SG (**3**) is 1/0.76, as obtained from elemental analysis. The elemental analysis further shows that the Ag nanocluster of type **3** contains 26.13% C, 3.95% H, 7.01% S, 8.96% N, and 23.04% O (Table S3 in the Supporting Information). Thus, the molar ratio of C/H/N/O/S is found to be 9.95:16.28:2.92:5.99:1, which is in very good agreement to the molecular formula of glutathione ($C_{10}H_{16}N_3O_6S$), after subtracting the percentage of hydrogen (0.36%) and oxygen (2.11%) originating from adsorbed water (9.16%).

To summarize this section, clusters of type **1** and **2** consist of silver atoms and the ligand only. The TG curves of these species consist of only one step, indicating that the ligand boils off the cluster in just one process. Neither sample shows any impurities of water, and there are no residues left on the clusters after heating them to 900 °C. In case of type **1** nanoclusters, it is found that the molecular formula equals $Ag_{4n}L_{3n}$; in clusters of type **2**, the formula is found to be $Ag_{2n}L_n$. However, the behavior of type **3** nanoclusters is completely different. They are hygroscopic (indicated by the loss of water when starting the heat-up process), and like the bare ligand, the organic species decomposes when heated. Furthermore, it is not possible to evaporate the entire organic compound, so even after heating the clusters to 900 °C, residues of the ligands stick to the clusters. Like at nanoclusters of type **1**, again, the chemical formula of the species is $Ag_{4n}L_{3n}$ for type **3** clusters.

Characterization of Ligand−Metal Bonding. To characterize the bonding between the ligands and the cluster, FT-IR spectroscopy was used to observe changes in the vibrational spectra of the ligands upon adsorption. Figure 3 shows the vibrational spectrum of 2-phenylethanethiol (2-PET) with the antisymmertic (d^-) CH_2 stretching band at 2932 cm^{-1}, the symmetric (d^+) CH_2 stretching modes at 2851 cm^{-1},[33,34] and the C−H aromatic stretching bands in the range of 3025−3085 cm^{-1}. Also observed in the spectrum is the vibrational band at 2535−2564 cm^{-1} typical for the S−H excitation. As expected, this band completely disappears upon formation of the Ag@SCH_2CH_2Ph nanoclusters (**1**), as depicted in the inset of Figure 3. This indicates the ligands are anchored to the cluster via the sulfur atom.[35,36]

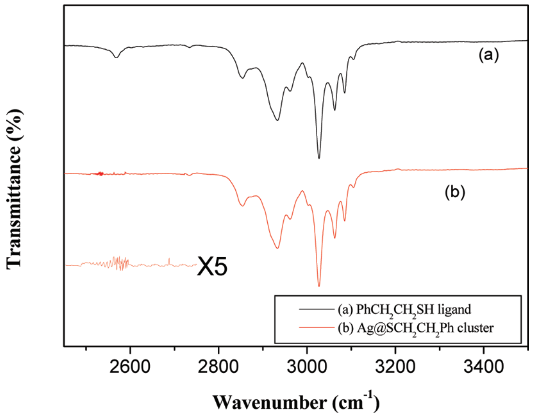

Figure 3. FTIR spectra of 2-phenylethanethiol $PhCH_2CH_2SH$ (a) and Ag@SCH_2CH_2Ph nanoclusters with inset of Ag@SCH_2CH_2Ph nanoclusters (× 5) (b). The spectra show that the band around 2560 cm^{-1} disappears in the spectrum of the cluster with respect to that of the bare ligand. This band can be assigned to the S−H stretching frequency, and its disappearance clearly indicates that the ligand is bound to the cluster via the sulfur atom. Since the spectrum of the clusters otherwise stays more or less unaltered, it can be concluded that no further changes happened to the ligand.

As expected, this observation is also true for the other two Ag-MPCs. The corresponding spectra are given in the Supporting Information (Figures S1−2), and the results can be summarized as follows: The presence of 4-FTP in Ag@SPhF nanoclusters (**2**) is manifested by C−H aromatic stretching bands in the range of 3025−3085 cm^{-1}; aromatic ring stretch moieties in the range of 1476−1695 cm^{-1}; and the C−F stretching band (symmetric) at ~1250 cm^{-1} (Supporting Information Figure S1b), which occurs at the same position as in the case of the parent 4-florothiophenol ligand (Supporting Information Figure S1a). The presence of L-GSH in Ag@SG nanoclusters (**3**) is confirmed by several bands (Supporting Information Figure S2b), such as the N−H stretching at 3310−3500 cm^{-1}. Furthermore, the hydrogen in the carboxylic acid is featured by the broad carboxylic acid O−H stretching band centered near 3000 cm^{-1}, which is superimposed on the C−H stretching bands (2800−3100 cm^{-1}).[31] The carbonyl group of the carboxylic group (C═O−OH) shows a characteristic band at ~1723 cm^{-1}. The C−O stretching vibration can be identified by the bands at 1315 and 1425 cm^{-1}. The peak at 937 cm^{-1} (in the range 875−960 cm^{-1}) is characteristic of the out-of-plane O−H bending mode, which occurs at nearly the same position as in the case of the parent glutathione ligand (Supporting Information Figure S2a). These results clearly point toward the stabilization of the metal cluster through sulfur bonds but otherwise support an unaltered ligand structure.

Cluster Size of the Ag-MPCs. There are, in general, several ways to determine the size of monolayer-protected metal clusters. The easiest method that can be used is UV−vis spectroscopy, since the optical properties of the metal particles change with their size. As we discuss below, the position and the width of the plasmon peak allows drawing some conclusions about cluster size; however, in contrast to bare metal clusters, the ligand has a strong effect on the plasmon peak, as well, and in the case of MPC the optical spectra, are

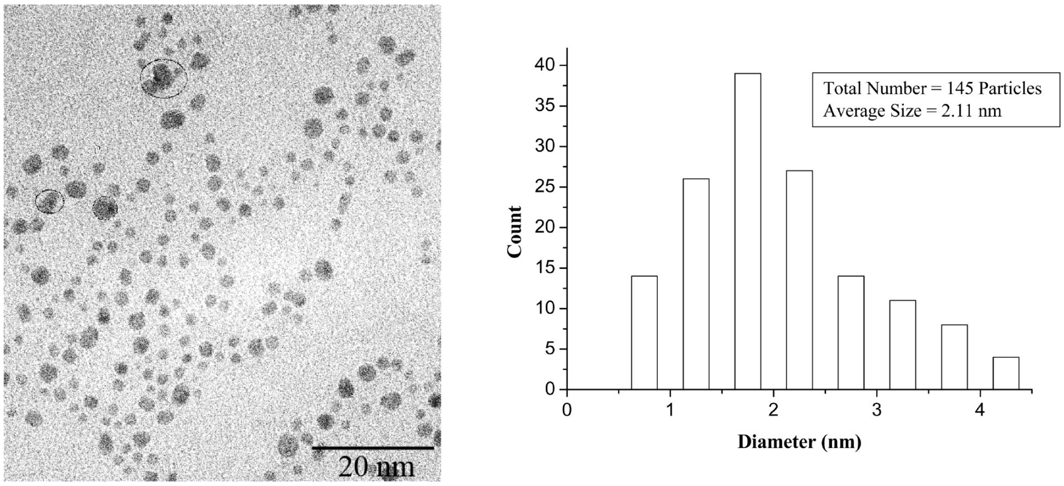

Figure 4. TEM image and size distribution of Ag@SCH_2CH_2Ph nanoclusters. A total of 145 particles were used to get the statistics for the size distribution of the clusters, which is shown on the left-hand side of the figure. The average size of the clusters was 2.11 nm.

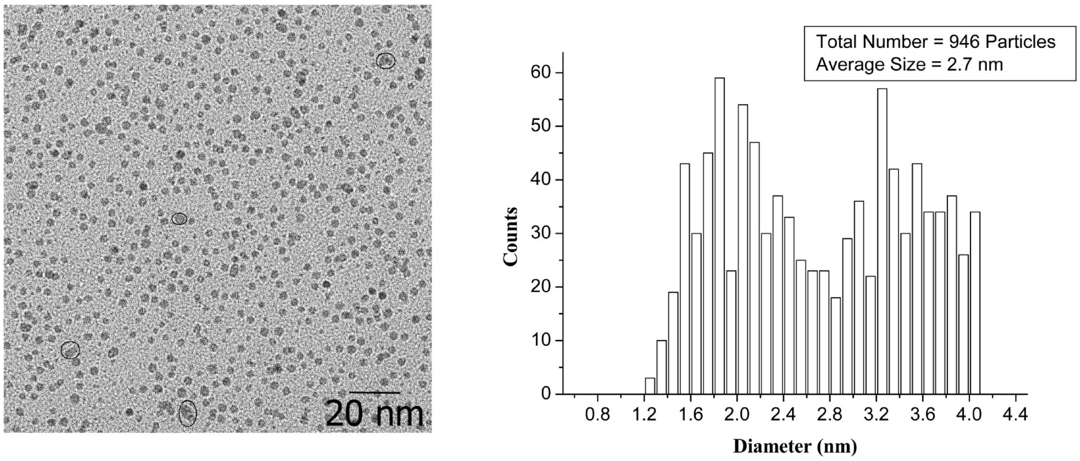

Figure 5. TEM image and size distribution of Ag@SPhF nanoclusters. These clusters show an average size of 2.7 nm (946 particles were used to obtain this average size); however, their distribution is not a Gaussian one, and it seems that it consists of two maxima.

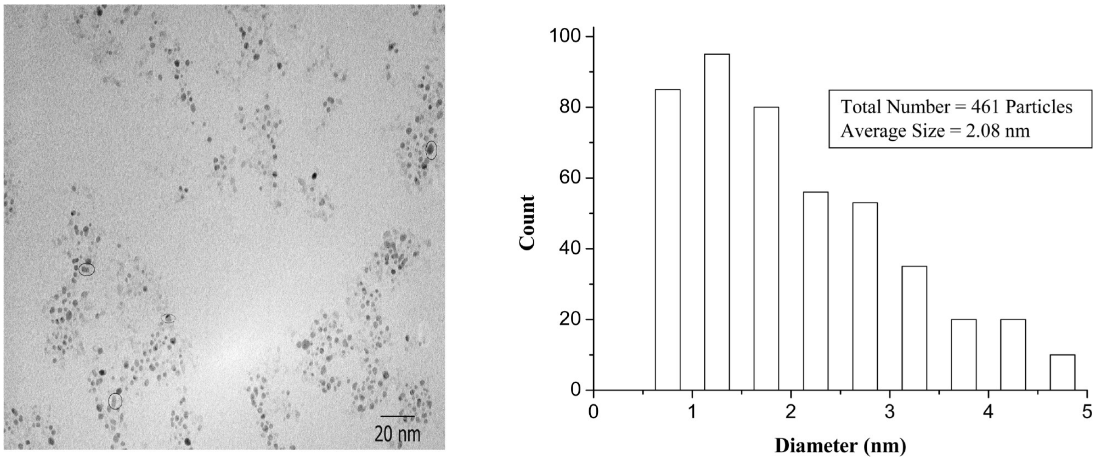

Figure 6. TEM image and size distribution of Ag@SG nanoclusters. Ag@SG nanoclusters consist of an average size of 2.08 nm (461 particles were used to obtain this average size).

rather helpful in determining the electronic properties of the cluster rather than deducing the size of the nanoparticles.

Another possibility is to use mass spectrometry. However, since the particles are rather large, a large mass range must be used, in particular, since the clusters do not form multiply charged ions easily.[37] In the case of Au-MPCs, it was shown[26a,c] that it is possible to obtain mass spectra with no or very little fragmentation; however, such experiments are not standard, and we did not characterize our samples by mass spectrometry.

Therefore, our method of choice was to use transmission electron microscopy. For clusters larger than 1 nm, TEM is in particular a very powerful technique. Because of the large scattering cross section of the metal atoms, such systems show a strong contrast in the TEM image. However, since the sample has to be deposited on a surface for performing TEM measurement, on this surface, migration and, finally, coalescence of the particle may occur. In this case, the measurement erroneously would suggest larger particle sizes than in reality. However, since our silver clusters are protected by ligands, this coalescence can more or less be ruled out, and just a sticking of the particle to each other might occur while they still possess an intact ligand shell (this effect will be called aggregation). As mentioned previously, conventional TEM is a very powerful technique for recording particles with a diameter larger than 1 nm; however, with smaller particles, the contrast becomes very weak so that very small particles might not be detected. Therefore, the statistics derived from the TEM images shown below give an upper limit of the cluster size.

Concerning the statistics, the center-of-particle and the particle size distribution were evaluated using the image processing program Image J developed at the National Institutes of Health. The average diameter of the MPCs represents the Feret's diameter and was determined in two different ways, in each case assuming a spherical shape: one value represents the average diameter of all MPCs, and the other one is received from a Gaussian fit of the frequency distribution, assuming that the larger diameters result from agglomerated MPCs.

Figures 4–6 depict typical TEM images together with size distribution histograms of the different MPCs of type **1**–**3**. In general, individual spherical nanoparticles can be seen for all the samples.[38] As mentioned above, larger core sizes are more easily visualized than small cores and can, as a consequence, become overcounted.[39] In addition, some of the MPCs in both TEM images have cores that are substantially nonspherical, and the differences in contrast within the same core indicate that they are composed of multiple grains. We attribute these nonspherical cores to the result of aggregation, in which two or a few smaller cores stick together (marked by circles), and therefore, we did not use it in the statistics. Using this setting, we obtained average sizes of 2.11, 2.7, and 2.08 nm for the dispersed particles by taking the average of 145, 946, and 461 particles for Ag@SCH$_2$CH$_2$Ph, Ag@SPhF, and Ag@SG nanoclusters, respectively. In addition, Ag@SPhF clusters show a bimodal distribution, probably originating from two different mechanisms during cluster formation.

UV−vis Spectra of the Synthesized Clusters. Figure 7 shows the absorption spectra of 2-PET- (**1**), 4-FTP- (**2**), and GSH- (**3**) protected silver nanoclusters. Although 2-PET-protected silver nanoclusters (**1**) in toluene exhibit a broad peak around 469 nm, FPhS-protected silver nanoclusters (**2**) in THF shows two absorption bands: one broad peak at 462 nm and a small absorption peak at 395 nm. GS-protected silver nanoclusters (**3**) in water absorb at 478 nm. All of the clusters exhibit broad peaks in the visible to near-UV region. Kitaev et al. have prepared monolayer-protected silver nanoclusters with a mixture of two ligands, captopril and glutathione, using a multistage cyclic reduction in oxidative conditions method.[40]

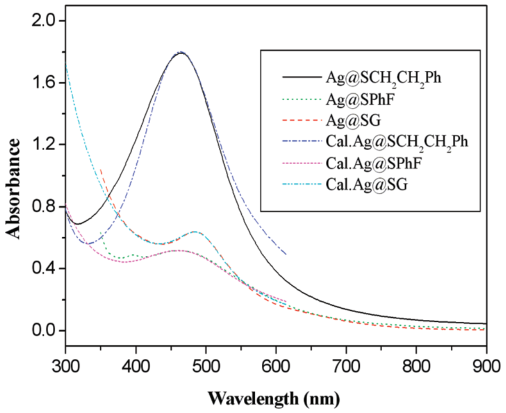

Figure 7. UV−vis absorption spectrum of all three types of nanoclusters (**1**−**3**) and simulation of the plasmon resonance. All three spectra where fitted by a function obtained by using the Mie theory[41] and the Drude model.[43] By varying the parameter for the damping constant ($\Gamma_{\mathrm{cluster}}$) and the dielectric constant of the environment of the cluster (ε_m), it can be shown that in all three cases, there is a strong spill-out effect of the electron density to the ligand, which is strongest in the case of Ag@SPhF.

The UV−vis spectra of these clusters give three absorption peaks, one sharp peak at 490 nm and two small peaks at 350 and 650 nm. The intensities of the last two peaks decrease with an increase in the percentage of glutathione, so this study perfectly agrees with the prepared cluster with glutathione of type **3**. In addition, fits for all three clusters are also displayed in this figure. The fit function is a calculated absorption by using the small particle approximation of the Mie theory.[41] Here, the absorption cross section of a spherical particle, which is small compared with the wavelength, can be expressed as follows:

$$\sigma_{\mathrm{abs}} = 9\frac{\omega}{c}\varepsilon_m^{3/2}V_0\frac{\varepsilon_2(\omega)}{[\varepsilon_1(\omega) + 2\varepsilon_m]^2 + \varepsilon_2(\omega)^2} \qquad (1)$$

V_0 denotes the particle volume and ε_m, the dielectric constant of the surrounding medium. $\varepsilon_1(\omega)$ and $\varepsilon_2(\omega)$ are the real and imaginary parts of the dielectric function, $\varepsilon(\omega)$, of the particle, respectively. The dielectric function of a silver cluster can be derived from the bulk optical constants.[42] To correct $\varepsilon_{\mathrm{bulk}}(\omega)$ for particle size and other influences (e.g., the electron spill-out effect), the damping constant of its free electron contribution has to be adapted. This can be done by describing the free electron contribution of $\varepsilon(\omega)$ with the Drude model:[43]

$$\varepsilon(\omega) = \varepsilon_{\mathrm{bulk}}(\omega) + \omega_p^2\left(\frac{1}{\omega^2 + \Gamma^2_{\mathrm{bulk}}} - \frac{1}{\omega^2 + \Gamma^2_{\mathrm{cluster}}}\right) + i\frac{\omega_p^2}{\omega}\left(\frac{\Gamma_{\mathrm{cluster}}}{\omega^2 + \Gamma^2_{\mathrm{cluster}}} - \frac{\Gamma_{\mathrm{bulk}}}{\omega^2 + \Gamma^2_{\mathrm{bulk}}}\right) \qquad (2)$$

The common textbook value of the plasma frequency for silver, ω_p, is 9.1 eV, and of the bulk damping constant, Γ_{bulk}, it is 0.018 eV. The corrected damping constant of the cluster, $\Gamma_{\mathrm{cluster}}$, is one of the fit parameters. The so-derived dielectric function can be inserted in eq 1.

For determining the extinction cross section of the solution, additional scattering losses from the ligands have to be considered, too. The scattering of the cluster can be neglected due to its small size; the ligand molecules, however, can form bigger agglomerates, which act as scattering centers. Here, only Rayleigh scattering is assumed. Consequently, the extinction cross section of the solution is expressed as

$$\sigma_{\mathrm{ext}} = \sigma_{\mathrm{abs}} + A\cdot\omega^4 \qquad (3)$$

The calculation was carried out using eq 3 with the fit parameters A, $\Gamma_{\mathrm{cluster}}$, and ε_m. The three fits are in good agreement with the measured data in Figure 7. In Table 1, the extracted values for the three MPCs are listed.

Table 1. Overview of the Values for the Plasmon Peak Position ($\lambda_{\max}$), the Effective Dielectric Constant of the Surrounding Medium (ε_m), and the Damping Constant of the Plasmon Excitation ($\Gamma_{\mathrm{cluster}}$)[a]

MPC	$\lambda_{\max}$ (nm)	ε_m (F·m^{-1})	$\Gamma_{\mathrm{cluster}}$ (eV)
Ag@SCH$_2$CH$_2$Ph	464	3.95 ± 0.1	0.9 ± 0.1
Ag@SPhF	461	4.2 ± 0.1	1.1 ± 0.1
Ag@SG	483	4.7 ± 0.1	0.55 ± 0.1

[a] The values are extracted from the fit of the UV-vis spectra of the three cluster samples.

The plasmon resonance of the silver cluster undergoes a strong red shift for all MPCs compared with the vacuum value (from 350 nm to ~470 nm). The reason for this effect is the strong electronic influence of the ligands on the metal core. From formula 1, it can be seen that the plasmon peak is located where the denominator has a minimum. This is the case when $\varepsilon_1(\omega) + 2\varepsilon_m = 0$. Consequently, a change in the electronic environment of the cluster shifts the resonance frequency. In the case of MPCs, the value, ε_m, does not have a direct physical meaning. It can be interpreted as an effective dielectric constant, however. Its value is influenced by properties of the chemical bond such as its strength, polarity, and polarizability.[44] The values of ε_m show big differences between the different MPCs, which suggests different properties of the Ag$_n$-S bonds.

The second derived value is the damping constant of the plasmon. As mentioned in the Introduction, there are mainly two effects that influence its value: cluster size and the electron spill-out that is highly dependent on the electronic properties of the cluster interface. The cluster size cannot be responsible for the observed differences in the measured values because the mean cluster sizes are very similar (see TEM images). The electron spill-out effect, in contrast, should be biggest for ligands, where the electrons of the cluster have to overcome the smallest energy barrier to be transferred to the ligand. This is the case for the $^-$SPhF ligand because its large π-electron system is highly polarizable. Consequently, the highest value of the damping constant is found for this MPC (1.1 eV).

Stability of the Silver Monolayer-Protected Clusters (Ag-MPCs). In addition, UV−vis spectroscopy can also be used for the investigation of the stability of the clusters. The samples are usually stored in a fridge at about 0 °C and sealed to avoid exposure to air. Every month, a UV−vis spectrum of the sample was recorded, always using nearly the same concentration (around 1 mg/mL). For all three types of cluster, it was observed that their spectra do not change at all over time (neither the peak positions nor the intensity of the absorbance). Therefore, it can be concluded that all our samples are highly stable at around freezing temperature and in the absence of air.

Silver clusters protected by 2-PET (**1**) are particularly stable, even when being exposed to air. There is no change in the intensity of the absorption peaks of the UV−vis spectra (a characteristic aging pattern) at all, even after 24 h exposure to air (see Figures 8 and S3 (Supporting Information)). In contrast to this species, AgNCs protected by 4-FTP (**2**) loose half of their absorbance after 30 min. After that, the absorbance decreases even further, but now, more slowly with time (Figures 8 and S4 (Supporting Information)). A similar behavior can be found for the Ag@SG clusters (**3**): The absorbance decreases slowly with time but not as fast as in the previous case (Figures 8 and S5 (Supporting Information)).

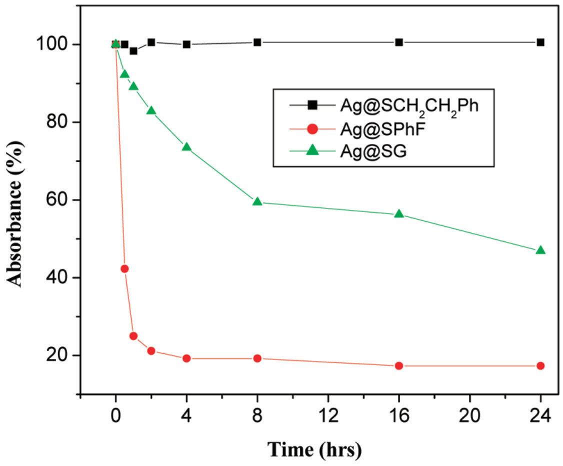

Figure 8. The kinetic study of the stability of nanoclusters (**1**−**3**) in air. The absorbance percentage of cluster **1** stays completely the same over a time period of 24 h, cluster **2** loses half of its absorbance percentage after 30 min, and in cluster **3** the degradation decreases.

We speculate that the silver-to-sulfur bond is more stable in Ag@SCH$_2$CH$_2$Ph than in Ag@SPhF and Ag@SG because the benzyl group is an electron-donating group, and hence, the stability of the Ag−S bond is increased, leading to a higher stability of the clusters of type **1**. In the case of Ag@SG, the carbonyl group is an electron-withdrawing group, and therefore, this effect leads to a lower stability of the Ag−S bond. In the case of 4-fluorothiophenol, the effect is even more pronounced because of the strong electron-withdrawing of the fluoride atom on the aromatic ring.

In addition, the electron spill-out from the clusters to the ligand also supports this assumption: Due to the electron delocalization over the aromatic system, the damping constant is largest at the clusters decorated with 4-fluorothiophenol. In the previous section, we attributed the damping constant to the spill-out effects of the electron density from the cluster to the ligand. This means that the barrier for an electron transfer to the ligand is lowest for Ag@SPhF MPCs because they show the highest damping constant (1.1 eV) of all three clusters. However, in the case of the two other types of clusters (**1** and **2**), the stability and the spill-out is reversed. This shows that the effect of the electron-withdrawing group might probably play a more important role in these cases.

Chirality of the Silver Monolayer-Protected Clusters (Ag-MPCs). During the process of cluster formation, chiral molecules can impart their chiral structure to achiral educts. Therefore, chiral clusters can be formed when they are protected by chiral ligands. The chiral substances show optical activity, which can be obtained using CD spectroscopy. Since the cluster and the ligand show different absorption bands, it can be determined if one or even both species are chiral.[22]

Figure 9 shows the CD spectrum of the used three ligands, 2-PET, 4-FTP, and GSH. As expected, the first two ligands are optically inactive, but L-GSH shows a strong CD signal at 220 nm. In Figure 10, the CD spectra of all three clusters decorated with different ligands are shown. Although in the case of the clusters that are protected with achiral ligands, no CD effect is visible, clusters that are coated with L-GSH show a CD peak at 281 nm and a second one with lower intensity at 480 nm. Although the peak in the lower wavelength range might be interpreted as the optical transition of the ligand, which is shifted to the red due to the interaction with the cluster, the second peak around 480 nm is a clear indication of metal-based optical activity.[21] The ellipticity of both peaks, however, is very small, which can be attributed to a relatively large distribution of the cluster size. Since for some sizes of clusters, the ellipticity might be negative and in other cases positive, these contributions might average out, leading to a quite small signal. Nevertheless, the effect is clearly visible, and we conclude that in the case of glutathione, the silver nanoclusters

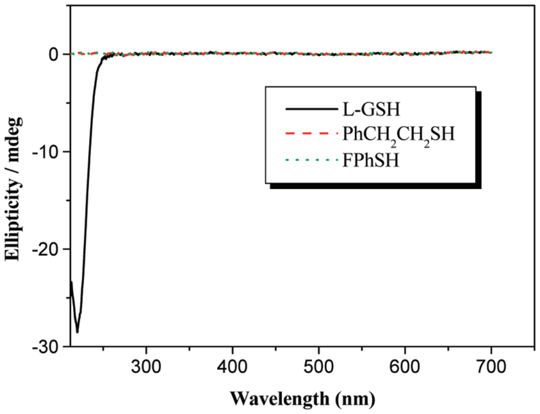

Figure 9. CD spectra of all three ligands used. L-Glutathione is optically active and shows a strong CD signal only at 220 nm. As expected, 2-phenylethanethiol and 4-fluorothiophenol are optically inactive.

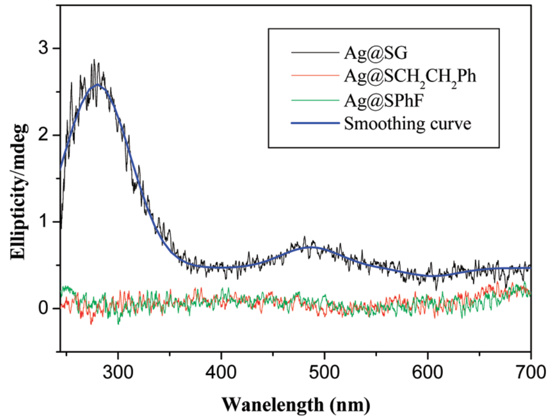

Figure 10. CD spectra of all three ligand-protected silver clusters (**1**−**3**). Ag@SG nanoclusters, which are coated with L-GSH show a strong CD peak at 281 nm and a second one with lower intensity at 480 nm, which is in very good agreement with the work of Cathcart and Kitaev.[40] Because of the nature of the achiral ligand, Ag@SCH$_2$CH$_2$Ph and Ag@SPhF nanoclusters show no optical activity at all.

of type **3** impart the chirality of this specific ligand, thus also becoming chiral.

■ CONCLUSIONS

We report herein synthesis and characterization of three new silver nanoclusters protected by 2-PET, 4-FTP, and L-GSH ligands. Our results show that spherical silver nanoparticles are produced. The average sizes of the dispersed particles are estimated to be 2.11, 2.7, and 2.08 nm by taking the average 145, 946, and 461 particles for Ag@SCH$_2$CH$_2$Ph, Ag@SPhF, and Ag@SG nanoclusters, respectively. Thermogravimetric analysis and elemental analysis deduce the exact number of silver atoms and thiolate ligands (1/0.75, 1/0.47, and 1/0.76) in the three nanoparticles (**1**−**3**), respectively. The absorption signal of Ag@SCH$_2$CH$_2$Ph in toluene can be found at 469 nm, and Ag@SPhF in THF show two absorption bands at 395 and 462 nm. Ag@SG in water absorbs at 478 nm. Disappearance of the S−H vibrational band (2535−2564 cm^{-1}) in the silver nanoclusters confirms the anchoring of ligands to the cluster surface through the sulfur atom. The spectroscopic measurements by means of UV−vis and FTIR spectroscopy of these clusters revealed that they are molecular in nature and that their optical and photophysical properties are heavily dependent on the ligands, which cover these silver clusters.

■ ASSOCIATED CONTENT

Ⓢ Supporting Information

FTIR spectra, elemental analysis, atomic absorption spectra, and UV-vis spectra of silver nanoclusters as a function of time at ambient conditions. This material is available free of charge via the Internet at http://pubs.acs.org.

■ AUTHOR INFORMATION

Corresponding Author

*E-mail: tschurl@tum.de.

Notes

The authors declare no competing financial interest.

■ ACKNOWLEDGMENTS

This work is supported by an ERC Advanced Grant (ERC-2009-AdG 246645-ASC3) and by the DAAD and Egyptian missions (German Egyptian Research Long Term Scholarship, GERLS). We kindly acknowledge the groups of Prof. Buchner and Prof. Rieger for carrying out the CD and FTIR and TGA measurement, respectively.

■ REFERENCES

(1) Habibpour, V.; Wang, Z. W.; Palmer, R. E.; Heiz, U. *J. Appl. Sci.* **2011**, *11*, 1164.

(2) Kunz, S.; Schweinberger, F. F.; Habibpour, V.; Rottgen, M.; Harding, C.; Arenz, M.; Heiz, U. *J. Phys. Chem. C* **2010**, *114*, 1651.

(3) Kartouzian, A.; Thaemer, M.; Heiz, U. *Phys. Status Solidi, B* **2010**, *247*, 1147.

(4) Brust, M.; Bethell, D.; Schiffrin, D. J.; Whyman, R. *J. Chem. Soc. Chem. Commun.* **1994**, 801−802.

(5) Gobin, A. M.; Lee, M. H.; Halas, N. J.; James, W. D.; Drezek, R. A.; West, J. L. *Nano Lett.* **2007**, *7*, 1929.

(6) Jain, P. K.; Lee, K. S.; El-Sayed, I. H.; El-Sayed, M. A. *J. Phys. Chem. B* **2006**, *110*, 7238.

(7) Verma, A.; Uzun, O.; Hu, Y. H.; Hu, Y.; Han, H. S.; Watson, N.; Chen, S. L.; Irvine, D. J.; Stellacci, F. *Nat. Mater.* **2008**, *7*, 588.

(8) Haynes, C. L.; McFarland, A. D.; Zhao, L. L.; Van Duyne, R. P.; Schatz, G. C.; Gunnarsson, L.; Prikulis, J.; Kasemo, B.; Kall, M. *J. Phys. Chem. B* **2003**, *107*, 7337.

(9) Park, I.; Ko, S. H.; Pan, H.; Grigoropoulos, C. P.; Pisano, A. P.; Frechet, J. M. J.; Lee, E. S.; Jeong, J. H. *Adv. Mater.* **2008**, *20*, 489.

(10) Sivaramakrishnan, S.; Chia, P. J.; Yeo, Y. C.; Chua, L. L.; Ho, P. K. H. *Nat. Mater.* **2007**, *6*, 149.

(11) Zheng, J.; Nicovich, P. R.; Dickson, R. M. *Annu. Rev. Phys. Chem.* **2007**, *58*, 409.

(12) Aikens, C. M.; Li, S. Z.; Schatz, G. C. *J. Phys. Chem. C* **2008**, *112*, 11272.

(13) Kelly, K. L.; Coronado, E.; Zhao, L. L.; Schatz, G. C. *J. Phys. Chem. B* **2003**, *107*, 668.

(14) Hu, M.; Chen, J. Y.; Li, Z. Y.; Au, L.; Hartland, G. V.; Li, X. D.; Marquez, M.; Xia, Y. N. *Chem. Soc. Rev.* **2006**, *35*, 1084.

(15) Wang, H.; Brandl, D. W.; Nordlander, P.; Halas, N. J. *Acc. Chem. Res.* **2007**, *40*, 53.

(16) Moores, A.; Goettmann, F. *New J. Chem.* **2006**, *30*, 1121.

(17) Kreibig, U; von Fragstein, C. *Z. Phys.* **1969**, *224*, 307.

(18) Zaremba, E; Persson, B. N. J. *Phys. Rev. B* **1987**, *35*, 596.

(19) Harb, M; Rabilloud, F; Félix, C. *J. Chem. Phys.* **2008**, *129*, 194108.

(20) Jadzinsky, P. D.; Calero, G.; Ackerson, C. J.; Bushnell, D. A.; Kornberg, R. D. *Science* **2007**, *318*, 430.

(21) Si, S.; Gautier, C.; Boudon, J.; Taras, R.; Gladiali, S.; Bürgi, T. *J. Phys. Chem. C* **2009**, *113*, 12966.

(22) Slocik, J. M.; Govorov, A. O.; Naik, R. R. *Nano Lett.* **2011**, *11*, 701.

(23) Gautier, C.; Bürgi, T. *ChemPhysChem* **2009**, *10*, 483.

(24) Wu, Z.; Lanni; Chen, E.; Bier, W. M. E.; Ly, D.; Jin, R. *J. Am. Chem. Soc.* **2009**, *131*, 16672.

(25) (a) Schaaff, T. G.; Knight, G.; Shafigullin, M. N.; Borkman, R. F.; Whetten, R. L. *J. Phys. Chem. B* **1998**, *102*, 10643. (b) Wang, Z.; Tan, B.; Hussain, I.; Schaeffer, N.; Wyatt, M. F.; Brust, M.; Cooper, A. I. *Langmuir* **2007**, *23*, 885.

(26) (a) Dass, A.; Stevenson, A.; Dubay, G. R.; Tracy, J. B.; Murray, R. W. *J. Am. Chem. Soc.* **2008**, *130*, 5940. (b) Kim, J.; Lema, K.; Ukaigwe, M.; Lee, D. *Langmuir* **2007**, *23*, 7853. (c) Dass, A. *J. Am. Chem. Soc.* **2009**, *131*, 11666.

(27) (a) Shichibu, Y.; Negishi, Y.; Tsukuda, T.; Teranishi, T. *J. Am. Chem. Soc.* **2005**, *127*, 13464. (b) Negishi, Y.; Chaki, N. K.; Shichibu, Y.; Whetten, R. L.; Tsukuda, T. *J. Am. Chem. Soc.* **2007**, *129*, 11322.

(28) (a) Zhu, M.; Qian, H.; Jin, R. *J. Am. Chem. Soc.* **2009**, *131*, 7220. (b) Qian, H.; Zhu, M.; Andersen, U. N.; Jin, R. *J. Phys. Chem. A* **2009**, *113*, 4281.

(29) Kumar, S.; Bolan, M. D.; Bigioni, T. P. *J. Am. Chem. Soc.* **2010**, *132*, 13141.

(30) Qian, H; Jin, R. *Nano Lett.* **2009**, *9*, 4083.

(31) Chen, S.; Kimura, K. *Langmuir* **1999**, *15*, 1075.
(32) Mohapatra, S.; Mallick, S. K.; Maiti, T. K.; Ghosh, S. K.; Pramanik, P. *Nanotechnol.* **2007**, *18*, 385102.
(33) Chung, C.; Lee, M. *J. Electroanal. Chem.* **1999**, *468*, 91.
(34) Hostetler, M. J.; Stokes, J. J.; Murray, R. W. *Langmuir* **1996**, *12*, 3604.
(35) Yao, H.; Saeki, M.; Kimura, K. *J. Phys. Chem. C* **2010**, *114*, 15909.
(36) Shibu, E. S.; Habeeb Muhammed, M. A.; Tsukuda, T.; Pradeep, T. *J. Phys. Chem. C* **2008**, *112*, 12168.
(37) Tracy, J. B.; Crowe, M. C.; Parker, J. F.; Hampe, O.; Fields-Zinna, C. A; Dass, A.; Murray, R. W. *J. Am. Chem. Soc.* **2007**, *129*, 16209.
(38) Branham, M. R.; Douglas, A. D.; Mills, A. J.; Tracy, J. B.; White, P. S.; Murray, R. W. *Langmuir* **2006**, *22*, 11376.
(39) Ang, T. P.; Chin, W. S. *J. Phys. Chem. B* **2005**, *109*, 22228.
(40) Cathcart, N.; Kitaev, V. *J. Phys. Chem. C* **2010**, *114*, 16010.
(41) Mie, G. *Ann. Phys.* **1908**, *25*, 377.
(42) Johnson, P. B.; Cristy, R. W. *Phys. Rev. B* **1972**, *6*, 4370.
(43) Kreibig, U.; Vollmer, M. *Optical Properties of Metal Clusters*; Springer: Berlin, New York, 1995.
(44) Lica, G. C.; Tong, Y. Y. *J. Phys. Chem.* **2004**, *108*, 19896.

Supporting Information

Table S1: Elementals ratios of Ag@SCH_2CH_2Ph determined by thermogravimetric (TGA), elemental analysis (EA), and atomic absorption spectroscopy (AAS).

Table S2: Elementals ratios of Ag@SPhF determined by thermogravimetric (TGA), elemental analysis (EA), and atomic absorption spectroscopy (AAS).

Table S3: Elementals ratios of Ag@SG determined by thermogravimetric (TGA), elemental analysis (EA), and atomic absorption spectroscopy (AAS).

Table S1

Elements	Weight % from TGA	Weight % from EA and AAS
Ag	51.05	50.95
S	11.44	11.49
C	34.27	34.28
H	3.24	3.28

Table S2

Elements	Weight % from TGA	Weight % from EA and AAS
Ag	64.15	64.04
S	9.03	8.95
C	20.32	20.41
F	5.36	5.41
H	1.13	1.19

Table S3

Elements	Weight % from TGA	Weight % from EA and AAS
Ag	39.10	30.91
S	5.41	7.01
C	20.27	26.13
N	7.09	8.96
H	3.75	3.95
O	24.34	23.04

Figure S1: FTIR spectra of 4-fluorothiophenol FPhSH (a) and of Ag@SPhF nanoclusters (b). By comparison of the two spectra it is observed that the band at around 2650 cm^{-1} disappeared in the spectrum of the nanoclusters. This clearly indicates that the ligand is bound to the cluster via the sulphur atom. Since almost all of the other bands in the spectrum stay unaltered, it is concluded that the ligand itself remains otherwise unchanged.

Figure S2: FTIR spectra of L-glutathione L-GSH (a) and of Ag@SG nanoclusters (b). For the cluster compound it is found that the S-H bond disappeared in comparison to the spectrum of the bare ligand. Therefore, it is concluded that the ligand is bound to the cluster via the sulphur atom but stays otherwise unaltered as no other significant changes in the IR spectrum is observed.

Figure S3. UV-Vis absorption spectrum of Ag@SCH$_2$CH$_2$Ph nanoclusters as function of time at ambient conditions. The optical spectra of the clusters stay identical over a time period of 24 hours. Since UV-Vis spectra are rather sensitive to aging, it is concluded that the clusters are stable even under exposure to air.

Figure S4. UV-Vis absorption spectrum of Ag@SPhF nanoclusters in air. The plasmon peak of the clusters strongly decreases while they are stored in air. Already after 30 minutes the intensity of the peak halved in value. Therefore, it is concluded that these clusters are very sensitive to oxygen.

Figure S5. UV-Vis absorption spectrum of Ag@SG nanoclusters in air. The plasmon peak of the clusters degradation decreases with time but not as fast as for Ag@SPhF clusters.

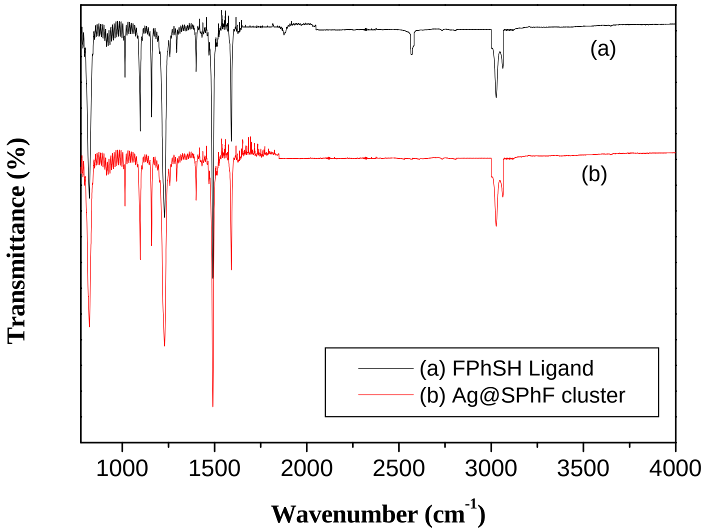

Figure S1

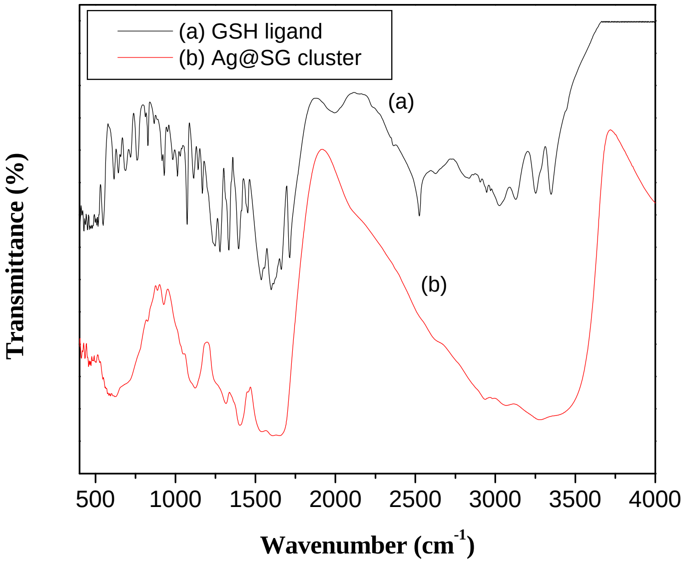

Figure S2

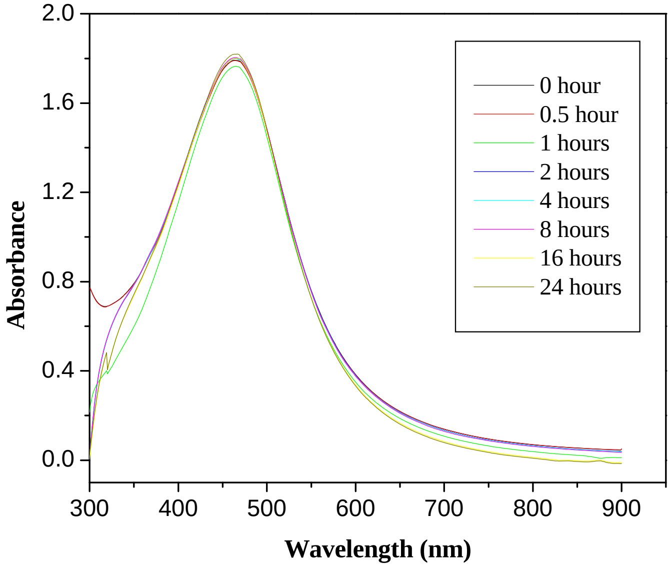

Figure S3

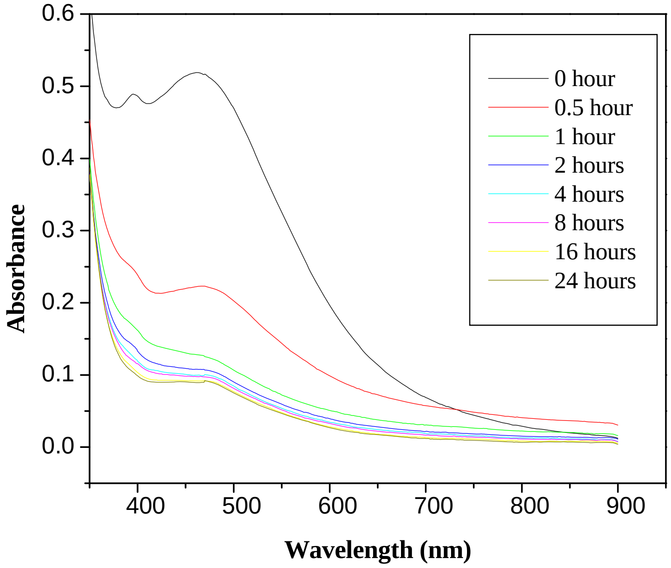

Figure S4

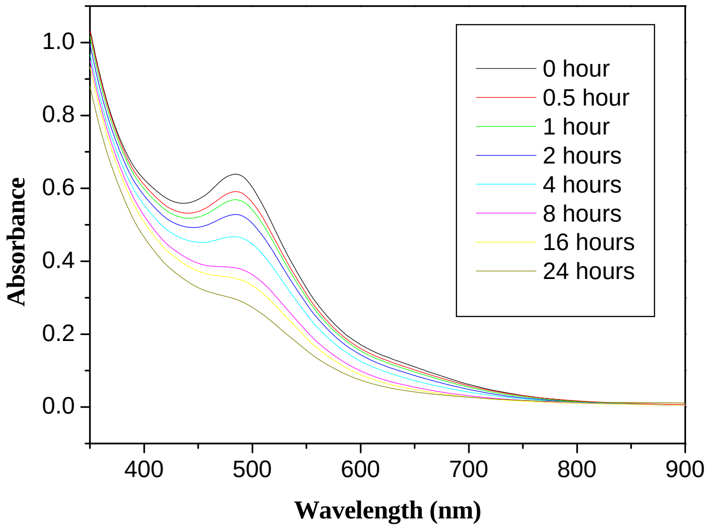
1.0
0.8
0.6
0.4
0.2
0.0
400
500
600
700
800
900
Absorbance
Wavelength (nm)
0 hour
0.5 hour
1 hour
2 hours
4 hours
8 hours
16 hours
24 hours

Figure S5

3.2. Second paper (Chem. Mater., 2013, 25, 862-870)

3.2.1. Summary of the second paper

We succeeded in this paper to prepare multiple sizes of gold and silver nanoclusters protected by two chiral ligands, i.e. L-glutathione (L-GSH), and N-acetyl-L-cysteine (NALC).

We explained here a new and easy method to prepare (most likely) monodisperse silver clusters protected by L-glutathione ligand, which we expect to consist of a Ag_{25} core. This method was also used to prepare silver clusters protected with N-acetyl-L-cysteine ligand ($Ag_n(NALC)_m$). However, these clusters showed a size distribution ranging from 1 nm to 3.5 nm, with an average size of around 2.37 nm.

Methanol-induced precipitation method was used to prepare and isolate multiple sizes of gold clusters protected by L-glutathione (L-GSH) and N-acetyl-L-cysteine (NALC). The synthesis of these gold clusters was done by the reduction of the corresponding metal salt of gold (Tetrachloroauric (III) acid ($HAuCl_4{\cdot}3H_2O$) with $NaBH_4$. We separated three fractions from gold clusters protected by L-glutathione by controlling the amount of methanol added and the speed of the centrifuge. The average particles size of the first fraction was 2.5 nm, the average size of the second fraction about 2 nm and the last fraction consisted of $Au_{25}(SG)_{18}$. However in the case of $Au_n(NALC)_m$ clusters we separated only two fractions, which size are about 3 nm and $Au_{25}(NALC)_{18}$.

UV−vis spectroscopy is sensitive to the particles size of the metal core, so it is commonly used to study the stability of monolayer protected clusters. The silver and gold nanoclusters are stable in a fridge in powder and solution form. Silver clusters show less stability if exposed to air in solution form, like $Ag_n(SG)_m$ cluster, however the solution form of gold clusters are stable in air. In this work we succeeded in preparing highly stable silver clusters protected by N-acetyl-L-cysteine (NALC). Circular dichroism (CD) spectroscopy was used to measure the chirality of these gold and silver clusters. The chirality of the ligands is transferred to the electronic states of the core metal. Chirality of clusters highly depends on the particles size of the core. It was found that when the particles size decrease the chirality increase. The optical properties of these nanoclusters in water were studied by UV−vis spectroscopy. Thermogravimetric analysis (TGA) was used to determine the average molecular formula of the nanoclusters, the average molecular formula of $Ag_n(SG)_m$ and $Ag_n(NALC)_m$ clusters are $Ag_{3n}L_{2n}$ and $Ag_{5n}L_n$, respectively. We also studied the fluorescent properties of these clusters by photoluminescence (PL) spectroscopy. To compare the structures of clusters and bulk metal we used powder X-ray diffraction.

CHEMISTRY OF MATERIALS

Article

pubs.acs.org/cm

Chiral Gold and Silver Nanoclusters: Preparation, Size Selection, and Chiroptical Properties

Mostafa Farrag, Martin Tschurl,* and Ulrich Heiz

Lehrstuhl für Physikalische Chemie, Technische Universität München, Lichtenbergstrasse 4, 85748 Garching, Germany

Supporting Information

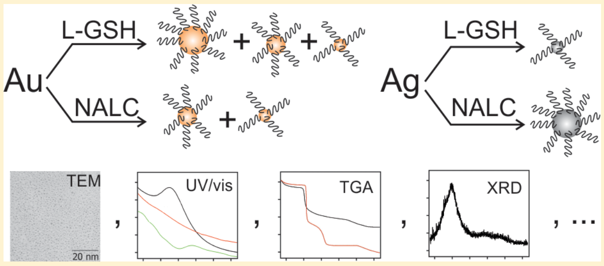

ABSTRACT: In this work we studied different properties of gold and silver nanoclusters (AuNCs and AgNCs) protected by the chiral ligands L-glutathione (L-GSH), and *N*-acetyl-L-cysteine (NALC), and we present a thorough characterization of the synthesized clusters. The synthesis was performed by reduction of the corresponding metal salt with $NaBH_4$. Fractions of gold nanoclusters with different sizes were isolated by methanol-induced precipitation. The ellipticity of the clusters was obtained by circular dichroism (CD) spectroscopy, showing that the chirality of the ligands is transferred to the metal core either in its structure or at least in its electronic states via perturbation of the electronic field of the ligands. The optical properties of gold and silver nanoclusters in water were studied by UV−vis spectroscopy. The absorption signal of the clusters shows characteristic bands, which can be assigned to plasmonic transitions of the metal core. In addition, UV−vis spectroscopy has served as a tool for studying the stability of these clusters in air. In general, gold nanoclusters are highly stable in air, and it was found that the stability of $Au_n(NALC)_m$ clusters even exceeds that of $Au_n(SG)_m$ clusters. In contrast to gold clusters, silver nanoclusters very often tend to decompose upon exposure to air. We found, however, that $Ag_n(NALC)_m$ are surprisingly stable at atmospheric pressures. The average molecular formula of the nanoclusters was determined by thermogravimetric analysis (TGA). The particle sizes of AuNCs and AgNCs were assessed by transmission electron microscopy (TEM) and powder X-ray diffraction (XRD) analysis. For studying the fluorescent properties of the metal nanoparticles, photoluminescence spectroscopy (PL) was performed. In summary, we succeeded to synthesize ligand-protected silver clusters ($Ag_n(NALC)_m$) with very high stability and rather narrow size distribution; furthermore, we could show the controlled precipitation to be applicable to other systems, such as that $Au_n(NALC)_m$, yielding two fraction of very narrow size distribution.

KEYWORDS: *chiral clusters, gold nanoclusters, silver nanoclusters, controlled precipitation, L-glutathione, N-acetyl-L-cysteine*

■ INTRODUCTION

In recent decades, several endeavors have been directed toward the investigation of chiral nanostructures. Like chiral surfaces, chiral clusters are of growing interest due to their potential use in enantioselective catalysis[1] and optoelectronics.[2] The fundamental properties and structural flexibility make, in particular, gold clusters (AuMPCs) protected by thiolate ligands an ideal tool for a vast range of different applications in various fields such as materials science, energy technology, chemistry, medicine, and biology.[3−5] The in situ functionalization of surfaces by chiral molecules is an effective way for inducing chirality on metal nanoclusters.[6] Furthermore, protecting the clusters by ligands that are either chemically bonded or physically adsorbed prevents nanoparticles and clusters from coalescence and preserves the properties of the metallic core.[7−11]

According to this strategy, we have already reported the synthesis and chiroptical properties of optically active silver nanoclusters protected with L-glutathione, with a size of about 2 nm.[7] Similar studies were carried out previously by Cathcart et al., who succeeded in preparing silver clusters protected by ligands such as captopril, L-glutathione, and cysteine by multistage cyclic reduction in oxidative conditions (CROC) and obtained clusters in a smaller size regime (around 1 nm). Studies on the stability of the synthesized Ag clusters protected by captopril showed that they are not stable in air.[12]

Tsukuda and co-workers succeeded in synthesizing and separating several fractions of size-selected gold clusters protected by L-glutathione $Au_n(SG)_m$ (n = 10, 15, 18, 22, 25, 29, 33, and 39, m = 10, 13, 14, 16, 18, 20, 22, and 24, respectively) by high-resolution polyacrylamide electrophoresis.[13a,b] Among all these different cluster sizes, $Au_{25}(SG)_{18}$ species have been demonstrated to be the most stable.[13c]

Gold clusters protected by *N*-acetyl-L-cysteine and tiopronin ligands were first synthesized by Murray and co-workers. Furthermore, they used UV−vis spectroscopy in combination with ion-pair HPLC for obtaining the UV−vis spectra for different cluster sizes. They found an average core diameter of the cluster ensemble of 1.7 ± 0.5 nm.[14] These clusters have been further applied for a new biosensing method for the

Received: October 18, 2012
Revised: January 31, 2013
Published: February 19, 2013

detection of phenolic compounds by near-infrared (NIR) luminescence quenching.[15]

For elucidating the conformation of a thiolate species adsorbed on gold clusters, the vibrational circular dichroism (VCD) of gold clusters protected by *N*-acetyl-L-cysteine ligand was studied.[16] These clusters of sizes of 1−2 nm were deposited over TiO_2 nanoparticles and characterized by attenuated total reflection (ATR-IR) spectroscopy, UV−vis spectroscopy, and transmission electron microscopy (TEM). While the clusters were stable on the semiconductor particles, it was found that they tend to agglomerate after removal of the protective ligand by UV radiation.[17]

In this work we present an alternative way of synthesizing gold clusters protected by *N*-acetyl-L-cysteine (for the chemical structure of the ligands used, see Scheme 1). By methanol-induced precipitation with controlled amount of added methanol and separation speed of the centrifuge as well as the time of stirring, fractions are obtained that consist of $Au_n(NALC)_m$ clusters of different sizes. This technique has already been successfully used for the separation of different sizes of gold clusters protected by L-glutathione.[18] In this work we demonstrate that this separation method works well for $Au_n(NALC)_m$ clusters and might even be generally applicable. In addition, we succeeded for the first time to synthesize silver clusters protected by *N*-acetyl-L-cysteine.

Scheme 1. Ligands Used for Protecting the Clusters: L-Glutathione (L-GSH) and *N*-Acetyl-L-cysteine (NALC)

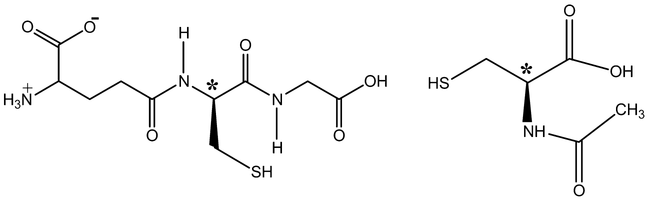

L- GSH

NALC

Because the CROC technique of Cathcard et al. takes place under a rather harsh chemical environment,[12] we present a milder synthetic way for obtaining $Ag_n(SG)_m$ clusters. For the sake of comparison and to obtain additional data (mostly photoluminescence and CD spectra), we have also used different fractions of Au clusters protected by L-glutathione, which we prepared by following the method of Jin and co-workers.[18] All four different species were characterized by UV−vis, photoluminescence and circular dichroism spectroscopy, thermogravimetry, and transmission electron microscopy, obtaining the average molecular formula, the size, the optical and chiral properties, and the stability.

■ EXPERIMENTAL SECTION

Chemicals. Tetrachloroauric(III) acid ($HAuCl_4{\cdot}3H_2O$, >99.99% metals basis, Aldrich), silver nitrate ($AgNO_3$, ≥99% metals basis, Aldrich), sodium borohydride ($NaBH_4$, ≥96%, Aldrich), potassium hydroxide (KOH, 90%, Aldrich), L-glutathione (γ-L-glutamyl-L-cysteinyl-glycine, γ-Glu-Cys-Gly, L-GSH) reduced (98%, Aldrich), and *N*-acetyl-L-cysteine (NALC, ≥99%, Sigma-Aldrich) were used for synthesizing the ligand-protected nanoparticles (for the chemical structure of the used ligands, see Scheme 1). As solvents, ethanol (HPLC grade, Aldrich) and methanol (HPLC grade, Aldrich) were used. All chemicals were used as received. Deionized water was purified by a Millipore Milli-Q water system to obtain Milli-Q water (resistivity 18.2 MΩ·cm). All glassware was thoroughly cleaned with aqua regia ($HCl{:}HNO_3$ = 3:1 v/v), rinsed with Milli-Q water, and then dried in an oven prior to use.

Preparation of $Ag_n(SG)_m$ Clusters (1). A 94 mg amount of silver nitrate (0.87 mmol) was dissolved in 10 mL of Milli-Q water, KOH (168 mg) was added to adjust the pH of solution to around 10, and then 300 mg of glutathione (0.97 mmol) was added while stirring the solution vigorously (∼1100 rpm) at room temperature for 30 min. Afterward, the resulting solution was cooled to 0 °C in an ice bath over a period of 30 min, prior to adding a freshly prepared aqueous solution of $NaBH_4$ (378 mg, dissolved in 20 mL of ice-cold Milli-Q water) dropwise for about 20 min while stirring vigorously (∼1100 rpm). The solution color became light yellow first and then changed to brown. The reaction was further allowed to proceed under constant stirring for 1 h. A 25 mL amount of ethanol was then added to precipitate the cluster. The brown precipitate consisting of $Ag_n(SG)_m$ was then washed with excess ethanol to remove unreacted material.

Preparation of $Ag_n(NALC)_m$ Clusters (2). In a basic solution of pH 10 (170 mg of KOH/12 mL of Milli-Q water), 96 mg of silver nitrate (0.93 mmol) was dissolved. A 163 mg amount of *N*-acetyl-L-cysteine (1 mmol) was added to this solution and then vigorously stirred (∼1100 rpm) at room temperature for 30 min. The resulting solution was then cooled to 0 °C with an ice bath over a period of 30 min, and a freshly prepared aqueous solution of $NaBH_4$ (386 mg, dissolved in 25 mL ice-cold Milli-Q water) was added dropwise during 20 min while stirring vigorously (∼1100 rpm). The solution's color became light yellow and then brown. The reaction was allowed to proceed under constant stirring for 1 h at 0 °C. Twenty-five milliliters ethanol was added afterward. The solution was shaken at the same time to precipitate the clusters. The brown precipitate $Ag_n(NALC)_m$ was collected and washed with ethanol.

Preparation of $Au_n(NALC)_m$ Clusters (3). Tetrachloroauric(III) acid (52.0 mg, 0.132 mmol) was first dissolved in Milli-Q water (26 mL) in a round-bottom flask. The solution was cooled to 0 °C using an ice bath over a period of 30 min. Then *N*-acetyl-L-cysteine (86 mg, 0.53 mmol) was slowly added to the flask under slow magnetic stirring (ca. 60 rpm). The solution turned clear after continuous stirring for 1.5 h. $NaBH_4$ (50 mg, dissolved in 6.5 mL of ice-cold water) was rapidly added to the clear gold salt solution under vigorous stirring (ca.1200 rpm). The solution immediately became dark, indicating the reduction of gold salt and formation of nanoparticles. The reaction was allowed to proceed for about 12 h. Then MeOH (35 mL) was slowly added while stirring. The precipitates (fraction 1, **3a**) were collected by centrifugation (5000 rpm, 10 min) and washed with 1 mL of MeOH/H_2O (1:1, v/v). After repeatedly washing with methanol (1 mL × 3), the fractions were then vacuum-dried. The remaining supernatant (fraction 2, **3b**) from centrifugation showed absorption peaks in its UV/vis spectra, which are characteristic of those of Au_{25}, however with lower relative intensities (see below). After concentration of this solution by rotary evaporation, the solid form cluster was isolated by adding MeOH, washed with MeOH (1 mL × 3), and dried in a vacuum.

Preparation of $Au_n(SG)_m$ Clusters (4). We followed the method developed by Jin and co-workers, as it produces reasonable amounts of pure Au_{25} clusters as well as different sized nanoparticles.[18]

Instrumentation and Characterization. To obtain the UV−vis absorption spectra of the nanoclusters (**1**−**4**), aqueous solutions of approximately 1 mg/mL were prepared. The spectra of all the solutions were recorded at ambient temperature from 190 to 1100 nm with a single-beam spectrophotometer (Analytik Jena, Specord 40). The CD spectra of all four types of nanoclusters were measured with a Jasco J-710 spectropolarimeter, using a quartz cell of 1 cm path length and solutions with the same solvent and concentration as for UV−vis spectroscopy. Thermal gravimetric analysis (TGA) (∼2 mg sample tested) was conducted in an N_2 atmosphere (flow rate 50 mL/min) with a TG/DAT Q5000 IR analyzer (TA Instruments, Inc.). All measurements were performed from room temperature with a heating rate of 10 °C/min to 900 °C. For TEM measurements, solutions with a concentration of 1−2 mg/mL were prepared by dissolving the nanocluster materials in Milli-Q water. A droplet of these MPC solutions was casted onto carbon-coated copper grids. The solvent was then allowed to evaporate slowly. TEM images were obtained at a magnification of 200 000 for type **1**, **4b**, and **4c** clusters, a magnification of 150 000 for type **3b** clusters, and a magnification of 100 000 for type **2**, **3a**, and **4a**, respectively. All samples were recorded with a JEOL100CX electron microscope operating at an acceleration voltage of 100 kV. The images were then analyzed by using Image J software (version 1.44). Powder X-ray diffraction (XRD) was performed on a Rigaku powder diffractometer (Cu Kα1 source) with a wavelength of $\lambda = 1.5418$ Å. The detector consisted of an image plate detector (Stoe IP PSD). Fine powder samples were loaded on a quartz plate holder by spreading the powders as a smooth thin layer on the plate. For all diffractograms, the following settings were used: scan range 20−100° (2θ), scan step 0.1°, integration time 4 s. The photoexcitation and fluorescence studies were performed with a Varian Cary Eclipse fluorescence spectrophotometer with a xenon flash lamp as the excitation source. The band-pass for both excitation and emission monochromators was here kept at 5 nm.

■ RESULTS AND DISCUSSION

Chemical Composition of M-MPCs. The thermal decomposition of Au MPCs and Ag MPCs has been demonstrated to occur by the dissociation of the thiolate ligands. While this dissociation leads to the formation of different gases such as CO_2, NH_3, H_2O, and H_2S, the core metal is left behind as the final mass. This is an effective way to obtain the organic ligand mass fraction and the core mass fraction of the MPCs, enabling the determination of the average chemical formula for the MPCs[19] and their metal-to-sulfur ratio.[7,20]

Figure 1 shows the thermogram representative for two sizes of gold clusters protected by NALC (for further thermogravimetric plots of the clusters in comparison with the thermal behavior of the respective ligand, see Supporting Information, Figures S1 and S2). In general, all TGA curves show several steps corresponding to the decomposition of the ligand. All clusters are found to be hygroscopic, which is indicated by the onset of the mass loss already at 40 °C temperature. In the measurements of all species, the decomposition of the ligand is completed before 900 °C and the residue consists of metal atoms only. This is supported by the metallic color of the residue. As seen in Figure 1, larger clusters show a higher metal-to-ligand ratio, because for larger particles the numbers of atoms inside the metal core becomes larger with respect to the numbers of the surface atoms of the particle. From the relative weight of the residue with respect to the total weight loss of organic molecules, the average ligand-to-metal ratio can be calculated and thus the average molecular formula of the clusters can be derived. The results together with all the thermogravimetric data are shown in Table 1.

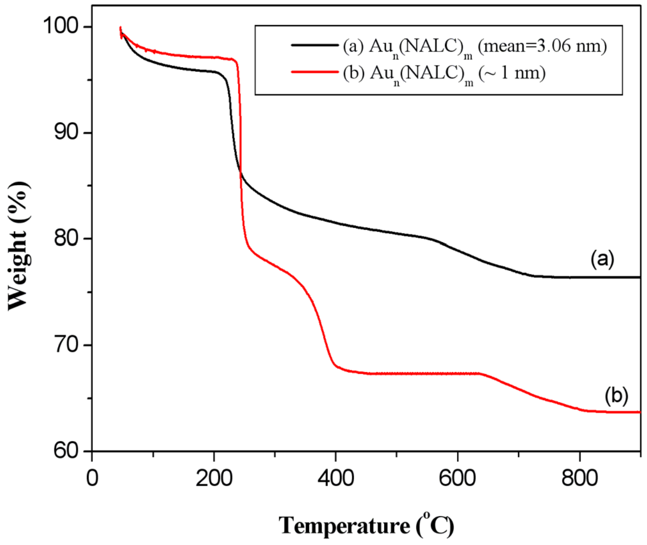

Figure 1. The thermogravimetric analysis of fraction 1 (curve a) and fraction 2 (curve b) from $Au_n(NALC)_m$ clusters (clusters of type **3a** and **3b**). Both fractions consist of clusters with the same ligand and metal but differ in their size. Both curves show an onset already at 40 °C, which is due to the removal of water molecules, showing that the clusters are hygroscopic. Furthermore, several steps can be found, which are due to the decomposition of the organic molecules. For both samples, the clusters, and the bare ligand, the destruction of the organic compound is complete before 900 °C. Therefore, the residual mass of the clusters samples consists of metal atoms only.

Clusters of silver decorated with NALC (**2**) have an average size of about 2.4 nm (see section below). Therefore, their metal-to-ligand ratio is clearly higher than that of the silver clusters protected by GSH (**1**), which are about 1 nm in size. In addition, the average chemical formula of the latter is very similar to that of fraction two of Au@NALC clusters (**3b**), which are similar in size. The first fraction of these gold clusters (**3a**), however, consists of larger clusters (about 3 nm), and therefore their metal-to-ligand ratio is twice as high as that of the smaller clusters.

Cluster Size of M-MPCs. To determine particle size of the clusters, two analytical methods, transmission electron microscopy (TEM) and powder X-ray diffraction (XRD) analysis, were applied. TEM is particularly suited for obtaining the sizes of particles larger than 1 nm. The scattering cross section of the metal particles is much larger than that of the surrounding ligand molecules, making it a perfect technique for determining the size of the metal core. It is found that particles of Ag@SG (**1**), particles of the second fraction of Au@NALC (**3b**), and the particles of $Au_{25}(SG)_{18}$ (**4c**) look very similar in their TEM images; they are uniformly distributed and have a diameter of about 1 nm (as seen in Figure 2). This is a clear indication that particles with a very narrow size distribution can be obtained with this synthesis method. Due to the similarity of the images with those of $Au_{25}(SG)_{18}$, which are known to consist of Au_{25} cores only,[18] clusters of Ag@SG and clusters of fraction 2 of Au@NALC may even be monodisperse as well. The other TEM micrographs with statistics of the particle size are given in the Supporting Information (Figures S3−S6).

While the second fraction of clusters of Au@NALC (**3b**) show small clusters of 1 nm, the first fraction (**3a**) consists of larger clusters of an average size of 3.06 nm with a smooth Gaussian distribution over all sizes (Figures S3). Clusters of Ag@NALC (**2**) are found to have similar core sizes but are somewhat smaller with an average diameter of 2.37 nm (Figures S4). However, the size distribution has a distinct tail to larger diameters or probably consists of a bimodal set as well.

Powder X-ray diffraction (XRD) was used to compare the structures of the silver nanoclusters protected by the two different ligands with that of bulk silver (Figure 3). The X-ray diffractogram of $Ag_n(SG)_m$ (**1**) powder (Figure 3a) exhibits a broad and intense feature at $2\theta = 37.6 \pm 0.7°$, which is centered at almost the same position as the peak of a silver (111) lattice.[21] According to the Bragg equation, this broad and intense peak indicates an average interplane spacing (d) of 2.32 ± 0.3 Å, which corresponds very well to the interplane spacing of 2.37 Å of Ag (111).[22] In contrast to silver clusters protected by GSH, $Ag_n(NALC)_m$ (**2**) nanoclusters show a significantly

Table 1. Results of the Thermogravimetric Analysis of All the Samples

sample	thermal degradation step	t_{onset} (°C)	t_{end} (°C)	weight loss (%)	weight (%) at 900 °C	M/S ratio	molecular formula
$Ag_n(SG)_m$	I	40	178	15.82	29.30	1:0.66	$Ag_{3n}L_{2n}$
	II	178	287	8.24			
	III	287	517	21.22			
	IV	517	845	25.42			
$Ag_n(NALC)_m$	I	40	178	8.83	68.69	1:0.22	$Ag_{5n}L_n$
	II	178	302	14.98			
	III	302	654	7.5			
first fraction $Au_n(NALC)_m$	I	40	201	4.21	76.61	1:0.3	$Au_{3n}L_n$
	II	201	365	13.63			
	III	365	750	5.55			
second fraction $Au_n(NALC)_m$	I	40	230	4.02	63.73	1:0.62	$Au_{3n}L_{2n}$
	II	230	321	19.93			
	III	321	432	9.16			
	IV	432	719	3.16			

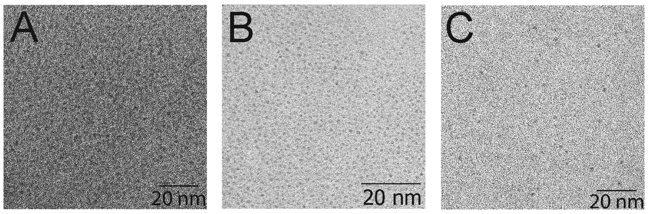

Figure 2. Transmission electron microscopy (TEM) images of $Ag_n(SG)_m$ (A), of the cluster of the second fraction of Au@NALC (B), and of clusters of Au_{25} $(SG)_{18}$. All three images look very similar and show clusters of around 1 nm with a very narrow size distribution. Due to the similarity of the images A and B with that of $Au_{25}(SG)_{18}$ clusters (C), the as-prepared particles may even be monodisperse. A larger image of each sample is given in the Supporting Information (Figures S17−S19).

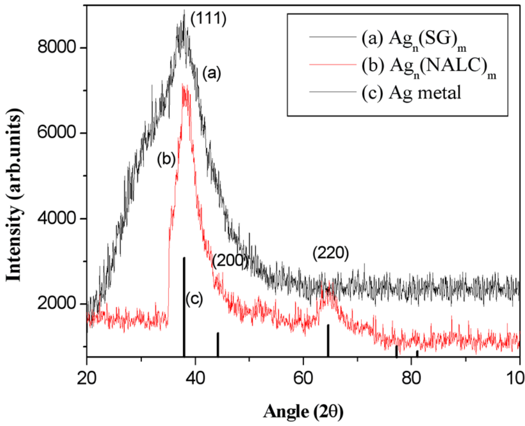

Figure 3. XRD patterns of $Ag_n(SG)_m$ (curve a) and $Ag_n(NALC)_m$ (curve b) nanoclusters. The X-ray diffractogram of $Ag_n(SG)_m$ (**1**) nanocluster powder sample exhibits a broad and intense (111) peak of silver at $2\theta = \sim 38°$. $Ag_n(NALC)_m$ (**2**) nanoclusters show a significantly less broadened diffraction peak at ~38° (111) and another broad one at around 65° (220). The stick pattern (curve c) is an indication of the diffraction peaks of the bulk Ag metal, which shows face-centered cubic (fcc) lattice (111), (200), (220), and (311) reflections.

less broadened diffraction peak at ~38.2 ± 0.3° (Figure 3b). Additionally, a broad peak at around 65° is found. By comparing the diffraction pattern of bulk silver (stick spectrum) with the spectrum of the clusters, the first peak can again be assigned to the (111) lattice while a second one is originating from the (220) lattice. Furthermore, another peak at 44° would indicate the existence of a (200) plane. Because this peak is very low in intensity it, however, could not be resolved in our spectra. By assigning the two peaks in the spectra it can be concluded that the clusters possess facets similar to those of a face-centered cubic (fcc) silver lattice. These results are in good agreement with those found by Murray and co-workers, who have reported a similar pattern for silver quantum dots protected by 4-*tert*-butylbenzyl mercaptan.[23]

The particle sizes of the silver nanoclusters (D) can be estimated according to the broadening of the full width at half-maximum (fwhm) of the (111) diffraction peak by the Debye−Scherrer formula (eq 1).[24]

$$D = \frac{0.9\lambda}{\text{FWHM} \times \cos\theta} \tag{1}$$

The wavelength of the Cu Kα1 line equals 1.5418 Å (see Instrumentation and Characterization). With a fwhm for nanoclusters **1** and **2** of 12.1 ± 1.0° (0.211 ± 0.02 rad) and 4 ± 0.4° (0.07 ± 0.01 rad), diameters of 0.7 ± 0.06 nm and 2.1 ± 0.22 nm, respectively, are obtained. The sizes are in reasonable agreement with those determined by TEM of about 1 nm for nanoclusters of type **1** and an average diameter of 2.37 nm for nanoparticles of type **2**. The powder X-ray diffraction pattern are shown for different fractions of $Au_n(NALC)_m$ nanocluster in Figure 4 together with the stick spectrum of pure gold.[18] While clusters of fraction 1 (**3a**, mean particles size 3.06 nm) show a well-defined diffraction pattern with four different distinct peaks at 2θ of 38.5 ± 0.6° (indexed to the fcc (111) reflections of gold), around 44° (200), 65° (220), and 78° (311), clusters of fraction 2 (**3b**, about 1 nm in diameter) exhibit a strongly broadened peak at 37.5 ± 0.8° and two other broad ones with very low intensity at around 65° and 78°. These XRD results are in very good agreement with the gold cluster fractions protected by L-glutathione,[18] which give similar reflections.[18] The fwhm values for the (111) diffraction peaks are 3.2 ± 0.8° (0.06 ± 0.014 rad) for clusters of type **3a** and 11.4 ± 1.1° (0.2 ± 0.02 rad) for clusters of type **3b**. From the Debye−Scherrer formula, the particle size is then calculated to 2.63 ± 0.6 nm for clusters of fraction 1 (**3a**) and 0.74 ± 0.07 nm for clusters of fraction 2 (**3b**). These results are again in reasonable agreement with the observation obtained from TEM measurements.

Optical Properties and Stability of M-MPCs. The absorption spectra of silver nanoclusters protected by L-glutathione (L-GSH) (**1**) and *N*-acetyl-L-cysteine (NALC)

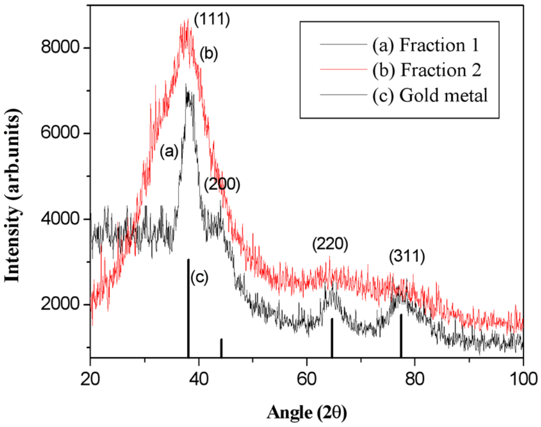

Figure 4. XRD patterns of nanoparticles of different sizes protected by NALC as ligand. Fraction 1 of $Au_n(NALC)_m$ nanoclusters (**3a**, mean particles size 3.06 nm) shows a well-defined diffraction pattern (curve a) with four distinct diffraction peaks at 2θ of 37.5° (111), 44° (200), 65° (220), and 78° (311). Fraction 2 (**3b**, particles of a diameter of about 1 nm, curve b) shows a significantly broadened diffraction peak at 37.5° and two other broad features of very low intensity around 65° and 78°. The stick pattern (c) indicates the diffraction peaks of bulk metal (i.e., Au), and the numbers in parentheses correspond to Miller indices of the lattices.

(**2**) in water are shown in Figure 5. While $Ag_n(SG)_m$ (curve a) nanoclusters exhibit one peak at 478 nm, a broad transition at 641 nm, and a small shoulder at 318 nm, $Ag_n(NALC)_m$ nanoclusters (curve b) feature a pronounced peak of relatively high intensity at 480 nm and a shoulder of very low intensity at 320 nm. Because particle sizes of the silver clusters protected by L-GSH are around 1 nm (Figure 2a) and hence smaller than for the clusters protected by NALC, the difference in the spectra of both species corresponds very well to the observation that in general surface plasmonic transitions are broader and of lower intensity for smaller clusters.[25]

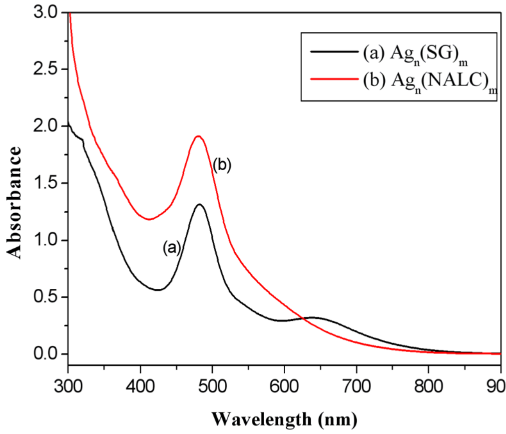

Figure 5. UV−vis absorption spectrum of $Ag_n(SG)_m$ (curve a) and $Ag_n(NALC)_m$ (curve b) nanoclusters. $Ag_n(SG)_m$ exhibits a one peak at 478 nm and another broad transition at 641 nm, as well as a small shoulder at 318 nm. $Ag_n(NALC)_m$ gives one pronounced peak at 480 nm and a small shoulder at 320 nm.

This behavior is also found for gold clusters: Because fraction 1 from gold clusters protected by *N*-acetyl-L-cysteine (**3a**) consists of an average particle size of around 3.06 nm, the UV−vis spectrum shows a well-defined surface plasmon absorption band at 534 nm (curve a in Figure 6). Due to their smaller size of about 1 nm, clusters of the second fraction (**3b**), however, show a multiband absorption spectrum with transitions at around 400, 450, and 670 nm (curve b). These absorption bands resemble very well the spectroscopic fingerprints of Au_{25} nanoclusters,[26] which are usually found for monodisperse clusters consisting of a metal core of exactly 25 atoms, such as $Au_{25}(SG)_{18}$[18] and $Au_{25}(SR)_{18}$ (SR = SCH_2CH_2Ph, $SC_{12}H_{25}$, and SC_6H_{13}).[27] Therefore, the UV−vis spectra of fraction 2 of the $Au_n(NALC)_m$ clusters again confirm the observations obtained from TEM of a very narrow particle size distribution and furthermore may suggest that the clusters are monodisperse and consist of core sizes of Au_{25} only.

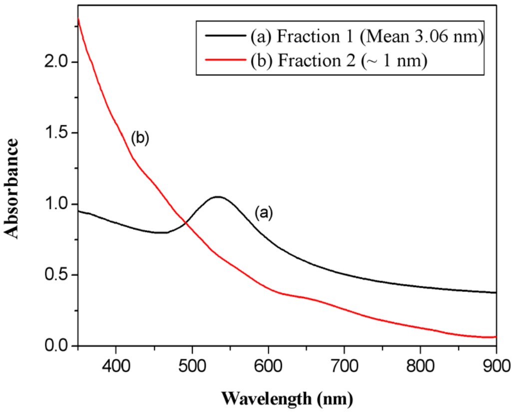

Figure 6. UV−vis absorption spectra of Au nanoparticles $Au_n(NALC)_m$ of different sizes. Fraction 1 consists of particles of an average size of 3.06 nm and shows a well-defined surface plasmon absorption band at 534 nm a (curve a). Particles of fraction 2 are much smaller (around 1 nm) and show a multiband absorption spectrum with distinct peaks at around 400, 450, and 670 nm (curve b). These absorption bands very well resemble the spectroscopic fingerprints of gold nanoclusters consisting of a metallic core of exactly 25 atoms.

Because UV−vis spectroscopy is sensitive to changes of the metal core, such as the oxidation state and the number of metal atoms of the cluster, it is commonly used for the investigation of the stability of clusters. The silver and gold nanocluster samples are stored in a fridge at 0 °C in powder and solution form and are sealed to avoid exposure to air. Each month the stability of the clusters was checked by recording UV−vis spectra, and it was found that no change (neither in the peak positions nor the intensity of the absorbance) was observed over time, showing that all our samples are highly stable at freezing temperature below 0 °C and in the absence of air.

However, when the clusters are exposed to air, the stability changes. Silver clusters protected by L-glutathione (**1**) undergo rather fast transformation, which results in the decrease of the absorbance peaks in an aqueous solution (Figure 7, and Figure S8 in the Supporting Information). The absorbance at 478 nm decreases to nearly half of its starting value after 8 h of air exposure. However, after that, the intensity of the peak stays constant for at least another 16 h. The rapid decay can be attributed to a transformation to clusters of larger sizes under the exposure of oxygen. This is supported by the observation that the UV−vis spectra very well resembles that of larger clusters of Ag@SG (larger than 2 nm)[7] after already 1 h.

In contrast to clusters protected by L-glutathione, $Ag_n(NALC)_m$ (**2**) nanoclusters are particularly stable even when being exposed to air. There is just a very small change in intensity of the absorption peak of the UV−vis spectra after the first few hours (see Figure 7, and Figure S9 in the Supporting

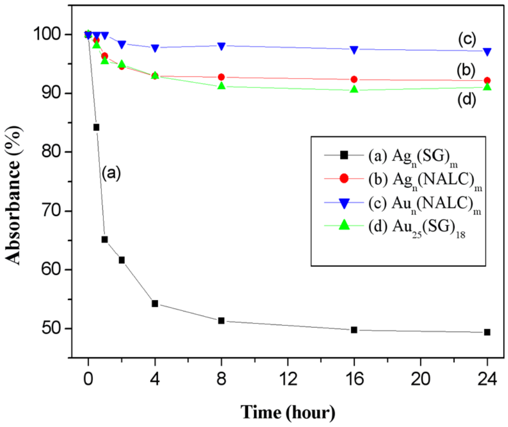

Figure 7. Kinetic study of the stability of nanoclusters (of type **1**–**4**) in air. The intensity of the plasmon peak of $Ag_n(SG)_m$ nanoclusters at 478 nm decreases to nearly half of its starting value already after 8 h, which indicated a rather poor stability of the clusters in air. However, all the other nanoclusters are stable even in the presence of oxygen. For all these species, a very small decay of the absorption signal is visible in the beginning, but the signal never falls below 90% of the starting value even after 24 h of exposure to air.

Information) and then the spectra remain constant for at least 24 h after the start of the measurements. This indicates that minor impurities might undergo decomposition while the vast majority of clusters remain stable. The stability of these clusters is comparable to that of silver clusters protected by 2-phenylethanethiol (2-PET), which show a surprisingly high stability as well.[7]

Usually, gold clusters are more stable than silver clusters. However, the stability of the silver clusters protected by NALC is found to be at least as good as that of $Au_{25}SG_{18}$ clusters (Figure 7, and Figure S10 in the Supporting Information). This observation is attributed to the effect of the protective ligands. This is further confirmed by the very high stability of the gold clusters protected by *N*-acetyl-L-cysteine (NALC) ligand, which do not undergo any decomposition in air at all within 24 h (Figure 7, and Figure S11 in the Supporting Information). One reason may be that *N*-acetyl-L-cysteine protects the metal from oxidation, an effect that is found for Au_{25} clusters protected by 2-phenylethanethiol (2-PET), which transforms the oxidation state of the clusters from anionic to neutral after being exposed to air.[26a] Because clusters protected by NALC show such good stability, they may be very well suited for future applications.

Chirality of M-MPCs. Circular dichroism requires not only rotation of linearly polarized light but also the presence of a discrete electronic transition in the metal core and/or of the ligand molecule of monolayer protected clusters. The magnitude of the CD effect for an electronic transition is directly related to the product of the electric dipole and magnetic dipole transition moments and thus is also proportional to the optical absorption. Small gold clusters protected by glutathione as ligand show strong chiroptical activity in the electronic transitions which are metal-based across the near-infrared, visible, and near-ultraviolet regions. Large clusters, however, just give very weak or not even any optical activity in this region.[6b]

The CD spectra of the two ligands used, L-glutathione and *N*-acetyl-L-cysteine, are governed by dominant peaks at 220 and 234 nm, respectively (see Figure S12 in the Supporting Information). The spectrum of $Ag_n(NALC)_m$ differs significantly from the spectrum of the bare ligand because it shows only one peak, which is of opposite sign and blue-shifted to 226 nm (see Figure 8, curve b). This peak, however, may still be interpreted as the optical transition of the ligand, which is shifted to shorter wavelengths due to the interaction with the cluster. On the other hand, peaks from possible optical activity of the metal core are missing. Because the size of these clusters is considerably big (mean diameter 2.37 nm), this is in perfect agreement with the above-mentioned observation that larger clusters show weak or even no activity in this spectral region.

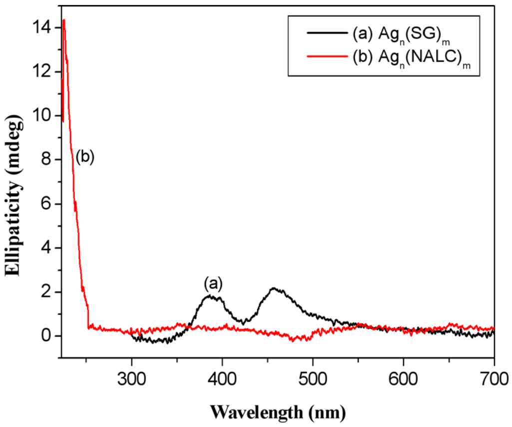

Figure 8. CD spectra of $Ag_n(SG)_m$ (curve a) and $Ag_n(NALC)_m$ (curve b) nanoclusters. $Ag_n(SG)_m$ nanoclusters show two peaks at 386 and 456 nm, which originate from metal-based transitions. $Ag_n(NALC)_m$ nanoclusters show only one peak at 226 nm. This peak might be interpreted as the optical transition of the ligand, which is shifted to the blue due to the interaction with the cluster.

Silver clusters of about 1 nm, which are protected by glutathione (clusters of type **1**) exhibit two peaks at 386 and 456 nm in their CD spectra (Figure 8, curve a). Because the positions of these peaks are in the range of the plasmon transition of the clusters (between 400 and 500 nm), these transitions may correspond to the metal-based optical activity. Thus, there is a strong indication that the cluster itself becomes chiral, with the chirality induced by the L-glutathione ligand. However, another possible interpretation of the CD signal in the range of the transitions of the metal core is the existence of strong chiral fields of the ligands only.[28a,b]

A similar effect of the cluster size is also found for gold clusters protected by chiral ligands. The CD spectra of the first fraction of gold clusters (**3a**) protected by *N*-acetyl-L-cysteine (NALC) give only one peak at 214 nm (see Figure 9), which is blue-shifted in comparison to the ligand's optical transition, whereas smaller clusters of the second fraction of $Au_n(NALC)_m$ (**3b**, 1 nm in diameter) show many peaks at 226, 327, 445, and 530 nm. Again the peak in the shortest wavelength range (226 nm) can be assigned to an optical transition of the ligand, while the peaks in the longer wavelength range most likely indicate chirality of the cluster or perturbation of its electronic state by the chiral field of the ligands.

The spectra of the three fractions of gold clusters protected with L-glutathione, which are shown in the Supporting Information (Figure S13), exhibit the same behavior. This further confirms the effect of the size of the metal core on the CD spectra of the cluster.

UV–Vis Photoluminescence Spectroscopy of M-MPCs. In the past decade several attempts have been made

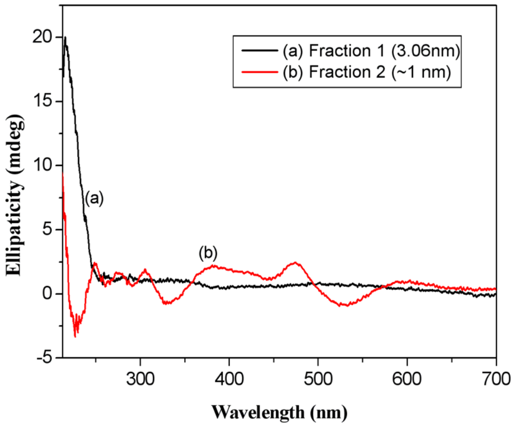

Figure 9. CD spectra of fraction 1 (curve a) and fraction 2 (curve b) for $Au_n(NALC)_m$ nanoclusters. The CD spectrum of the first fraction of gold clusters (**3a**) gives only one signal at 214 nm, which is the blue-shifted in comparison to the ligand's optical transition. (b) The second fraction of $Au_n(NALC)_m$ (**3b**), which consists of a smaller cluster of about ~1 nm shows many peaks at 226, 327, 445, and 530 nm. The latter three can be assigned to transitions of the metal core, which indicate that not only the ligand but also the cluster is chiral or at least that the electronic states of the cluster are perturbed by the chiral field of the ligands.

to study the fluorescence of metal (gold and silver) nanoparticles, but the origin of fluorescence still remains unclear. Jin and co-workers studied the fluorescence properties of $Au_{25}(SR)_{18}$ (SR = SCH_2CH_2Ph, $SC_{12}H_{25}$, and SC_6H_{13}) clusters and suggested two possible mechanisms to interpret the origin of the fluorescence.[27] The fluorescence may either arise from the metal core or from the influence of the protective ligands. In the latter case, the interaction of the ligands with the cluster can either take place via charge transfer through the metal−sulfur bonds or by direct donation of delocalized electrons from electron-rich groups in the ligand molecules.[27] Furthermore, it was found that ligands can strongly enhance the fluorescence of gold nanoparticles.[29] This clearly supports the theory of the interaction of the protecting molecules with the metal core, because the fluorescence is mostly affected by the plasmon resonance of the nanoparticles.[29]

Photoluminescence (PL) spectra of the prepared nanoclusters (**1**−**4**) were recorded in aqueous solutions at room temperature. All measurements were conducted in aerated conditions. The cluster concentrations for the PL measurements were 1 mg/mL, and a linear increase of the PL intensities with cluster concentration was observed. For obtaining the excitation spectra, the detection wavelength was set to the maximum of the emission spectra.

The excitation spectra, which are all shown in the Supporting Information, in combination with their corresponding emission spectra, show different maxima for the various samples. Because the photoluminescence spectra are affected by the plasmonic peaks of the clusters,[29] these maxima are related to the absorption features in the UV−vis spectra of the clusters.

For $Ag_n(SG)_m$ nanoclusters (**1**), three maxima are found: one at 277 and at 330 nm of high intensity as well as a broad one at 489 nm (Figure S14a in the Supporting Information). However, in the optical absorption of larger silver clusters ≥2 nm such as $Ag_n(NALC)_m$ (**2**) only one plasmonic peak can be found, which lies in the UV (Figure S14b).

By exciting the clusters with 478 nm (for particles of $Ag_n(SG)_m$) and 480 nm (for $Ag_n(NALC)_m$ cluster), the emission spectra are obtained, which are shown in Figure 10. $Ag_n(NALC)_m$ nanoclusters exhibit a broad peak with a maximum at 611 nm in their photoluminescence spectra. This peak is blue-shifted by almost 50 nm compared to the peak of the smaller silver clusters (1 nm in diameter) protected by L-glutathione, which give a peak at 660 nm. While the intensity of the PL is affected by the polarity of the ligand,[30] the position of the peak is mostly governed by the metallic core. Therefore, the blue-shift of the emission of larger clusters is more general and can also be observed for gold clusters, too, even when their ligand shell is different (see below).

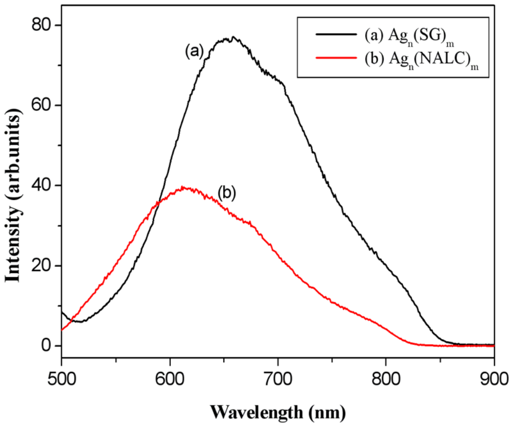

Figure 10. Photoemission spectra of $Ag_n(SG)_m$ (curve a) and $Ag_n(NALC)_m$ (curve b) nanoclusters. While the spectra of $Ag_n(SG)_m$ clusters show one broad maximum at 660 nm, the emission spectra of $Ag_n(NALC)_m$ clusters are shifted to the blue and give one maximum at a wavelength of 611 nm. The emission was initiated by exciting the clusters with a wavelength of 478 and 480 nm for $Ag_n(SG)_m$ and $Ag_n(NALC)_m$, respectively.

The fractions of gold clusters protected by *N*-acetyl-L-cysteine and L-glutathione again show different peaks in their excitation spectra (see Supporting Information, Figure S15). In general, larger clusters give intense peaks in the near UV, while smaller clusters show additional transitions in or close to the visible region. When exciting gold clusters protected by either NALC or L-GSH with 450 nm, their PL-emission spectrum is obtained (see Figure 11).

While larger clusters (about 3 nm) of fraction 1 give an emission peak at 554 nm, clusters of fraction 2, which are about 1 nm in diameter, show a broad PL-feature at a maximum of 738 nm. The PL-spectra of these smaller clusters is almost identical to those for monodisperse clusters of $Au_{25}(SG)_{18}$, which suggest that the core sizes are the same. Moreover, similar PL-spectra can be found for other clusters consisting of an Au_{25} core but of a different ligand shell as well, such as $[Au_{25}(SC_2H_4Ph)_{18}]^q$ (q = +2, +1, 0, −1)[27] or Au_{25} clusters protected by L-glutathione, *N*-formyl-glutathione, and *N*-acetylglutathione.[13c] This again strongly suggests that Au@NALC clusters of fraction 2 obtained by controlled precipitation are monodisperse or at least consist to a large extent of Au_{25} clusters. The effect of the particle size can also be seen, when the spectra of the largest clusters (always fraction 1) of Au@SG ((B), curve a) and Au@NALC ((A) curve a) are compared with each other: Both samples consist of particles of similar size (average diameter about 2.5 and 3 nm for SG-protected clusters and clusters with NALC as ligand,

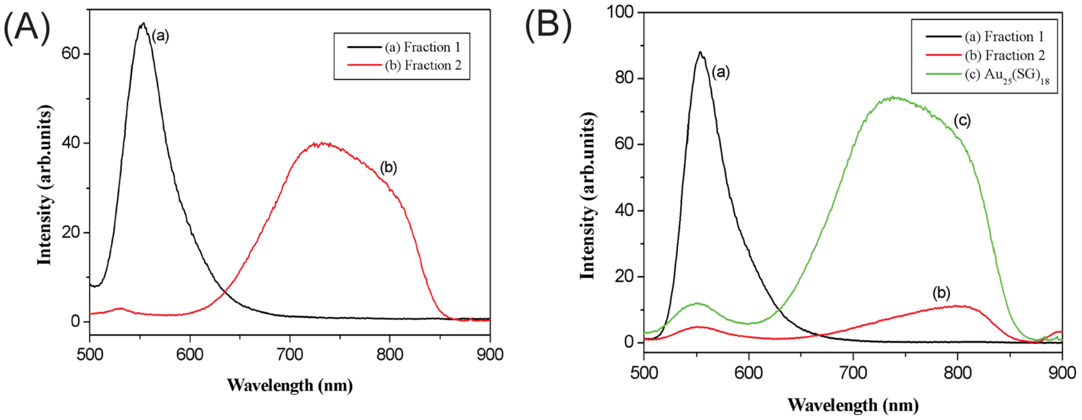

Figure 11. PL-spectra of the fractions of gold clusters protected by *N*-acetyl-L-cysteine (A) in comparison to the spectra of the fraction of Au-clusters protected by L-glutathione (B). A: The cluster of the first fraction of $Au_n(NALC)_m$ (curve a) gives one emission maximum at 554 nm. Clusters of fraction 2 are smaller in size (about 1 nm in diameter) and show one broader peak at 738 nm (curve b). Their position as well as the shape of this peak is almost identical to that of monodisperse clusters of $Au_{25}(SG)_{18}$ (curve c in B), however lower in intensity. Due to their similar size, clusters of fraction one (curve a in B, average size around 2.5 nm), which are protected by L-gutathione, show the same PL-properties as fraction 1 of Au-clusters protected by NALC (A, curve a, average size about 3 nm) as well. All the emission spectra were recorded by exciting the clusters with 450 nm.

respectively) and therefore give very similar photoemission spectra.

However, when the intensities of clusters of similar size but different ligands are compared with each other, it is found that the PL-intensities of clusters with L-glutathione are significantly higher than those of clusters with *N*-acetyl-L-cysteine when using the same concentration of clusters. This can be explained by the effect which was already mentioned previously, that the intensity of the PL depends on the polarity of the ligand rather than on the metal core.[30] Because the polarity of the L-glutathione ligand is significantly higher than that of *N*-acetyl-L-cysteine, they show photoluminescence intensities higher than that of the Au@NALC cluster.

■ CONCLUSIONS

We report herein the synthesis and characterization of silver and gold nanoclusters protected by the chiral ligands L-glutathione (L-GSH) and *N*-acetyl-L-cysteine (NALC). All samples were subjected to the same methods of characterization. While the TEM analysis revealed the particle size, the TGA data allowed for determining the average molecular formula. Powder X-ray diffraction enabled conclusions to be drawn about the morphology of the particles and CD spectra elucidated the chirality of the particles either in their structure or in their perturbed electronic states. In addition, the optical properties were further studied by UV−vis and photoluminescence spectroscopy.

Silver clusters protected by L-GSH were obtained by a new protocol, which is based on a single reduction cycle with $NaBH_4$. This method allows for the synthesis of clusters of about 1 nm with a very narrow size distribution. Furthermore, TEM images that look very similar to those of $Au_{25}(SG)_{18}$ clusters indicate that the sample may even consist of monodisperse silver clusters. While these clusters are very stable in absence of air, they agglomerate into larger particles when exposed to oxygen.

Silver clusters protected by NALC were synthesized for the first time. Particles with an average size of 2.37 nm and narrow size distribution were obtained. In contrast to most other silver clusters they are surprisingly stable, even when exposed to air, which makes them an ideal system for future studies and applications.

Gold clusters protected by NALC were subjected to controlled precipitation with methanol. Our results demonstrate that this separation technique may be generally applicable for ligand-protected gold clusters for obtaining fractions with a very narrow size distribution. By this separation technique, two fractions were obtained: While the first one consisted of clusters of about 3 nm, the second one showed a very narrow size distribution of around 1 nm in the TEM micrographs, which are similar to the TEM image of $Au_{25}(SG)_{18}$ clusters. Again this observation may indicate the presence of monodisperse samples. The monodispersity is further supported by the UV−vis and photoluminescence spectra, which show the typical characteristics of a sample consisting of Au_{25} cores. Finally, different fractions of $Au_n(SG)_m$ clusters were prepared for comparison with the other systems.

■ ASSOCIATED CONTENT

Ⓢ Supporting Information

Table with an overview of all samples, with their numbering, size, and chemical composition; TGA curves of Ag@SG cluster, of Ag@NALC clusters, and their corresponding ligands; TEM images including statistical analysis of Ag@NALC cluster, Au@NALC cluster of fraction 1, and clusters of Au@SG of fractions 1 and 2; UV−vis absorption spectra of all three fractions of gold clusters protected by L-glutathione and the UV−vis absorption spectrum of silver and gold nanoclusters as a function of time under ambient conditions; CD spectra of the bare ligands and of three fractions of Au@SG clusters; PL spectra in combination with the excitation spectra of all samples. Enlarged TEM images of Ag@SG clusters, the second fraction of Au@NALC clusters, and of clusters of $Au_{25}(SG)_{18}$. This material is available free of charge via the Internet at http://pubs.acs.org.

■ AUTHOR INFORMATION

Corresponding Author

*E-mail: tschurl@tum.de.

Notes

The authors declare no competing financial interest.

■ ACKNOWLEDGMENTS

This work is supported by an ERC Advanced Grant (ERC-2009-AdG 246645-ASC3) and by the DAAD and Egyptian missions (German Egyptian Research Long Term Scholarship-GERLS). We kindly acknowledge the groups of Prof. Buchner, Prof. Rieger, and Prof. Fässler for carrying out the CD, TGA, and XRD measurement, respectively. The authors thank TUM graduate school for their encouragement as well as Prof. Bürgi for helpful discussions.

■ REFERENCES

(1) (a) Baiker, A. *J. Mol. Catal. A: Chem.* **1997**, *115*, 473. (b) Wells, P. B.; Wilkinson, A. G. *Top. Catal.* **1998**, *5*, 39.

(2) Wei, J. J.; Schafmeister, C.; Bird, G.; Paul, A.; Naaman, R.; Waldeck, D. H. *J. Phys. Chem. B* **2006**, *110*, 1301.

(3) Murray, R. W. *Chem. Rev.* **2008**, *108*, 2688−2720.

(4) Han, G.; Ghosh, P.; Rotello, V. M. *Nanomedicine (London, U. K.)* **2007**, *2*, 113−123.

(5) Shenhar, R.; Rotello, V. M. *Acc. Chem. Res.* **2003**, *36*, 549−561.

(6) (a) Schaaff, T. G.; Knight, G.; Shafigullin, M. N.; Borkman, R. F.; Whetten, R. L. *J. Phys. Chem. B* **1998**, *102*, 10643. (b) Schaaff, T. G.; Whetten, R. L. *J. Phys. Chem. B* **2000**, *104*, 2630. (c) Wu, Z.; Gayathri, C.; Gil, R. R.; Jin, R. *J. Am. Chem. Soc.* **2009**, *131*, 6535−6542.

(7) Farrag, M.; Thämer, M.; Tschurl, M.; Bürgi, T.; Heiz, U. *J. Phys. Chem. C* **2012**, *116*, 8034−8043.

(8) Jadzinsky, P. D.; Calero, G.; Ackerson, C. J.; Bushnell, D. A.; Kornberg, R. D. *Science* **2007**, *318*, 430−433.

(9) Zhu, M.; Aikens, C. M.; Hollander, F. J.; Schatz, G. C.; Jin, R. *J. Am. Chem. Soc.* **2008**, *130*, 5883−5885.

(10) Heaven, M. W.; Dass, A.; White, P. S.; Holt, K. M.; Murray, R. W. *J. Am. Chem. Soc.* **2008**, *130*, 3754−3755.

(11) Wu, Z.; Lanni; Chen, E.; Bier, W. M. E.; Ly, D.; Jin, R. *J. Am. Chem. Soc.* **2009**, *131*, 16672.

(12) Cathcart, N.; Mistry, P.; Makra, C.; Pietrobon, B.; Coombs, N.; Jelokhani-Niaraki, M.; Kitaev, V. *Langmuir* **2009**, *25*, 5840−5846.

(13) (a) Negishi, Y.; Nobusada, K.; Tsukuda, T. *J. Am. Chem. Soc.* **2005**, *127*, 5261. (b) Shichibu, Y.; Negishi, Y.; Tsunoyama, H.; Kanehara, M.; Teranishi, T.; Tsukuda, T. *Small* **2007**, *3*, 835. (c) Shibu, E. S.; Habeeb Muhammed, M. A.; Tsukuda, T.; Pradeep, T. *J. Phys. Chem. C* **2008**, *112*, 12168.

(14) Choi, M. M. F.; Douglas, A. D.; Murray, R. W. *Anal. Chem.* **2006**, *78*, 2779−2785.

(15) Dong, W.; Dong, C.; Shuang, S.; Choi, M. M. F. *Biosens. Bioelectron.* **2010**, *25*, 1043−1048.

(16) Gautier, C.; Bürgi, T. *Chem. Commun.* **2005**, 5393−5395.

(17) Dolamic, I.; Gautier, C.; Boudon, J.; Shalkevich, N.; Bürgi, T. *J. Phys. Chem. C* **2008**, *112*, 5816−5824.

(18) Wu, B. Z.; Chen, J.; Jin, R. *Adv. Funct. Mater.* **2010**, *21*, 177−183.

(19) Hostetler, M. J.; Wingate, J. E.; Zhong, C. J.; Harris, J. E.; Vachet, R. W.; Clark, M. R.; Londono, J. D.; Green, S. J.; Stokes, J. J.; Wignall, G. D.; Glish, G. L.; Porter, M. D.; Evans, N. D.; Murray, R. W. *Langmuir* **1998**, *14*, 17−30.

(20) Qian, H. F.; Jin, R. C. *Nano Lett.* **2009**, *9*, 4083−4087.

(21) Yao, H.; Saeki, M.; Kimura, K. *J. Phys. Chem. C* **2010**, *114*, 15909−15915.

(22) Kumar, S.; Bolan, M. D.; Bigioni, T. P. *J. Am. Chem. Soc.* **2010**, *132*, 13141−13143.

(23) Branham, M. R.; Douglas, A. D.; Mills, A. J.; Tracy, J. B.; White, P. S.; Murray, R. W. *Langmuir* **2006**, *22*, 11376−11383.

(24) (a) Warren, B. E. *X-ray Diffraction*; Constable and Company: London, U.K., 1990; Chapter 13. (b) West, A. R. *Solid State Chemistry and Its Applications*; Wiley: New York, 1984.

(25) Wilcoxon, J. P.; Martin, J. E.; Provencio, P. *J. Chem. Phys.* **2001**, *115*, 998.

(26) (a) Zhu, M.; Aikens, C. M.; Hollander, F. J.; Schatz, G. C.; Jin, R. *J. Am. Chem. Soc.* **2008**, *130*, 5883. (b) Wu, Z.; Suhan, J.; Jin, R. *J. Mater. Chem.* **2009**, *19*, 622.

(27) Wu, Z.; Jin, R. *Nano Lett.* **2010**, *10*, 2568−2573.

(28) (a) Goldsmith, M.-R.; George, C. B.; Zuber, G.; Naaman, R.; Waldeck, D. H.; Wipf, P.; Beratan, D. N. *Phys. Chem. Chem. Phys.* **2006**, *8*, 63−67. (b) Lopez-Acevedo, O.; Tsunoyama, H.; Tsukuda, T.; Häkkinen, H.; Aikens, C. M. *J. Am. Chem. Soc.* **2010**, *132*, 8210−8218.

(29) (a) Zhou, C.; Sun, C.; Yu, M.; Qin, Y.; Wang, J.; Kim, M.; Zheng, J. *J. Phys. Chem. C* **2010**, *114*, 7727. (b) Fu, Y.; Zhang, J.; Lakowicz, J. R. *J. Am. Chem. Soc.* **2010**, *132*, 5540.

(30) Wang, G.; Guo, R.; Kalyuzhny, G.; Choi, J.-P.; Murray, R. W. *J. Phys. Chem. B* **2006**, *110*, 20282−20289.

Supporting Information

Chiral Gold and Silver Nanoclusters: Preparation, Size-Selection and Chiroptical Properties

Mostafa Farrag, Martin Tschurl, Ulrich Heiz

TECHNISCHE UNIVERSITÄT MÜNCHEN, LEHRSTUHL FÜR PHYSIKALISCHE

CHEMIE, LICHTENBERGSTRAßE 4, 85748 GARCHING, GERMANY

tschurl@tum.de

Table S1. Overview of the samples, their labelling, chemical composition and size.

Number	Sample	Average Size (from TEM)
1	$Ag_n(SG)_m$	about 1nm
2	$Ag_n(NALC)_m$	2.4 nm
3a	First fraction of $Au_n(NALC)_m$	about 3 nm
3b	Second fraction of $Au_n(NALC)_m$	about 1 nm
4a	First fraction of $Au_n(SG)_m$	2.5 nm
4b	Second fraction of $Au_n(SG)_m$	about 2 nm
4c	$Au_{25}(SG)_{18}$ (third fraction of $Au_n(SG)_m$)	about 1 nm

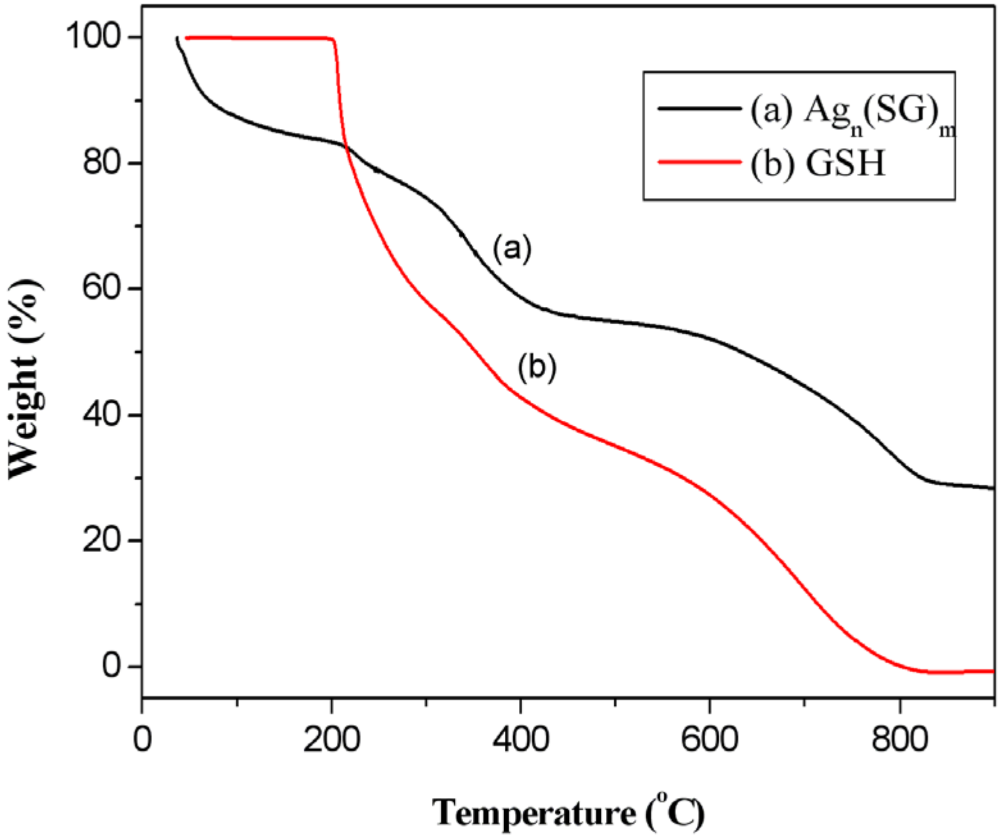

Figure S1. Theromgravimetric analysis (TGA) of $Ag_n(SG)_m$ (**1**) nanoclusters (curve a) and the bare glutathione ligand (curve b). $Ag_n(SG)_m$ cluster show four steps of mass loss upon heating from 40 to 900°C. There is an additional first step in TGA curve of the clusters, which results from the evaporation of water molecules, but otherwise the decomposition process of the ligand is very similar to that of the pure molecules.

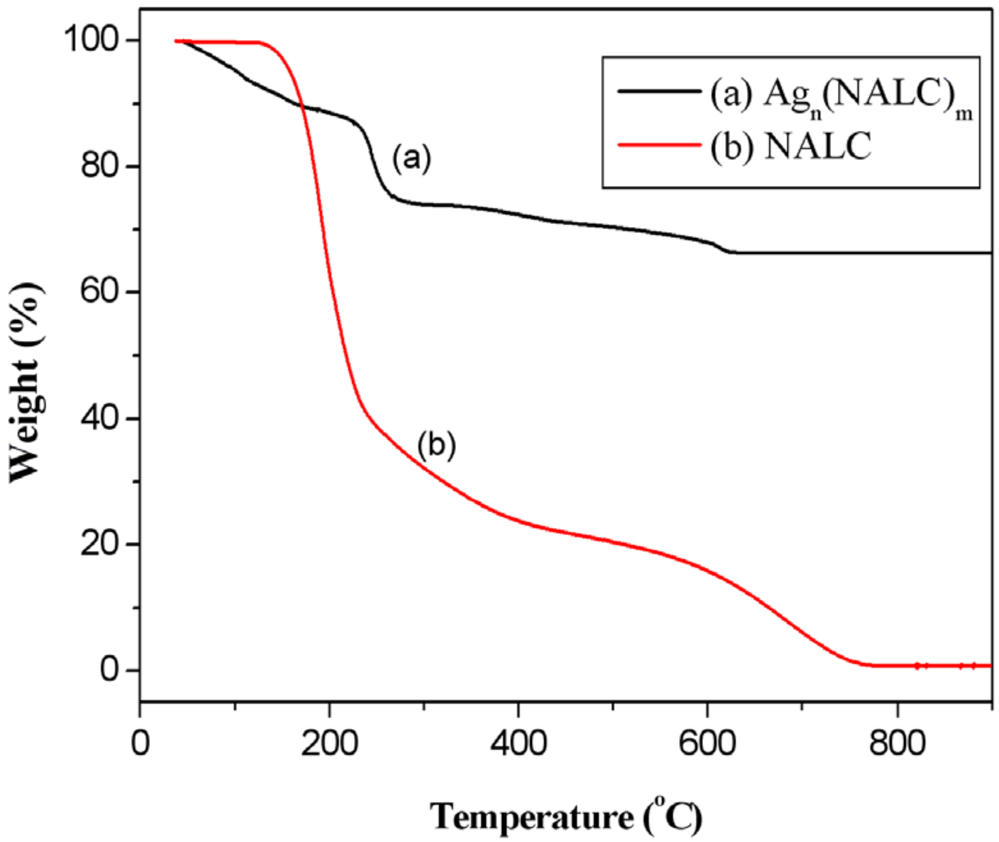

Figure S2. TGA of $Ag_n(NALC)_m$ (**2**) nanoclusters (curve a) and N-acetyl-L-cysteine ligand (curve b). $Ag_n(NALC)_m$ shows three steps of mass loss upon heating from 40 to 900°C and the first one is due to the removal of adsorbed water molecules. The similarity of the TGA curve of the ligand on the cluster with respect to that of the bare molecule indicates that the decomposition of the ligand is completed before 900°C.

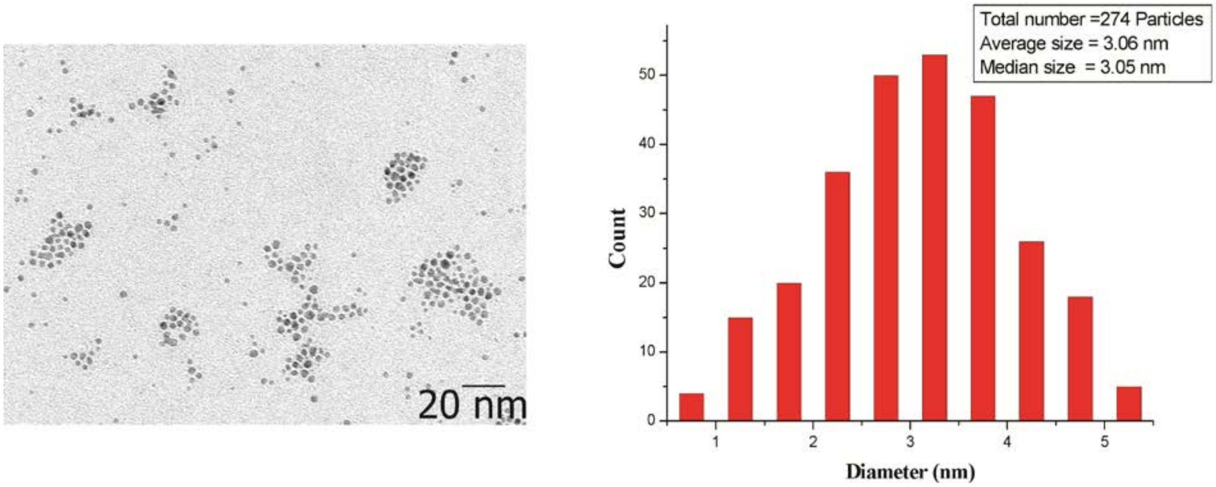

Figure S3. TEM image and statistics of the size of $Au_n(NALC)_m$ nanoclusters of fraction 1 (**3a**). $Au_n(NALC)_m$ nanoclusters consist of an average size of 3.06 nm (274 particles were used to obtain this average size) and a very smooth Gaussian distribution over the cluster size is found.

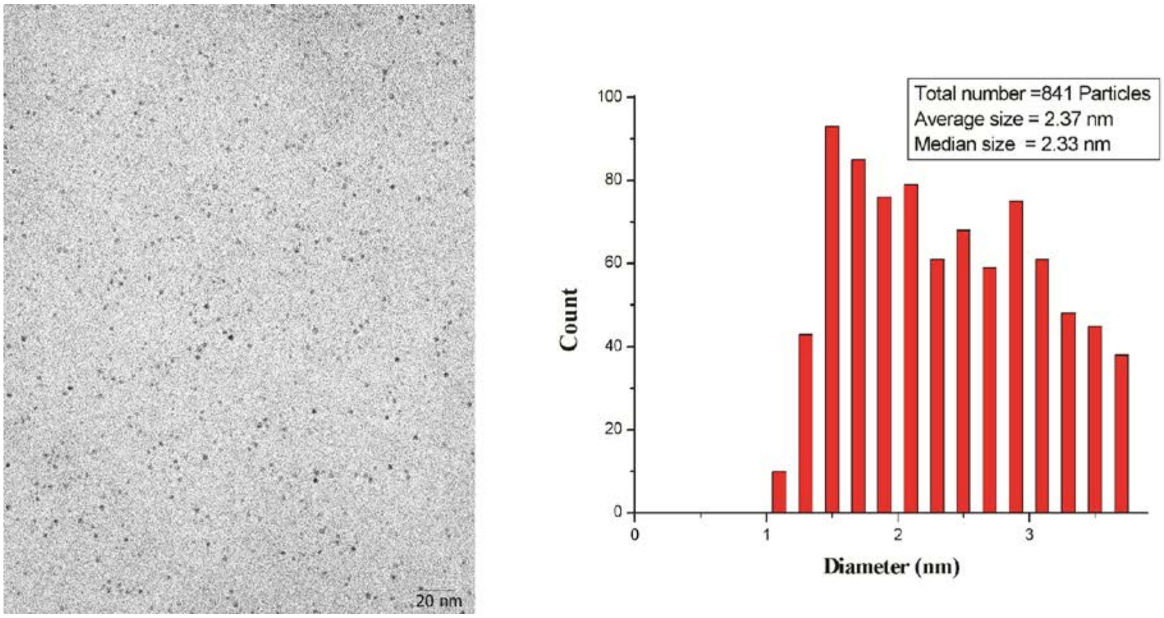

Figure S4. TEM image and size distribution of $Ag_n(NALC)_m$ nanoclusters (**2**). A total number of particles of 841 were used to obtain the size distribution of the clusters (figure on the left). The average size and median size of the cluster were found to be 2.37 and 2.33 nm, respectively.

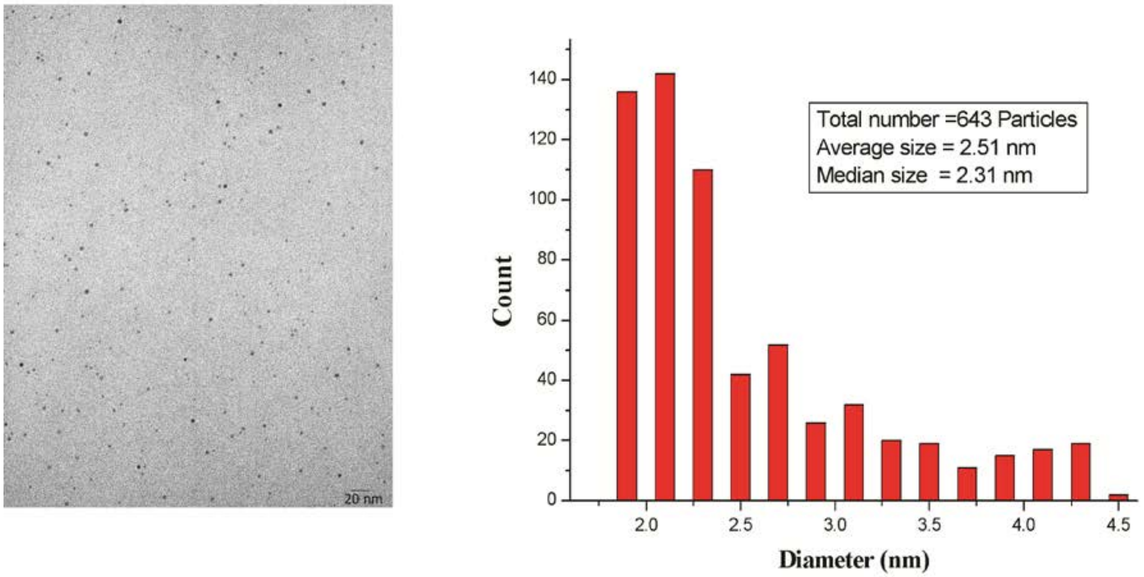

Figure S5. TEM image and size distribution of fraction 1 $Au_n(SG)_m$ nanoclusters (**4a**). These clusters show an average size of 2.51 nm. This value was obtained by averaging over 643 particles.

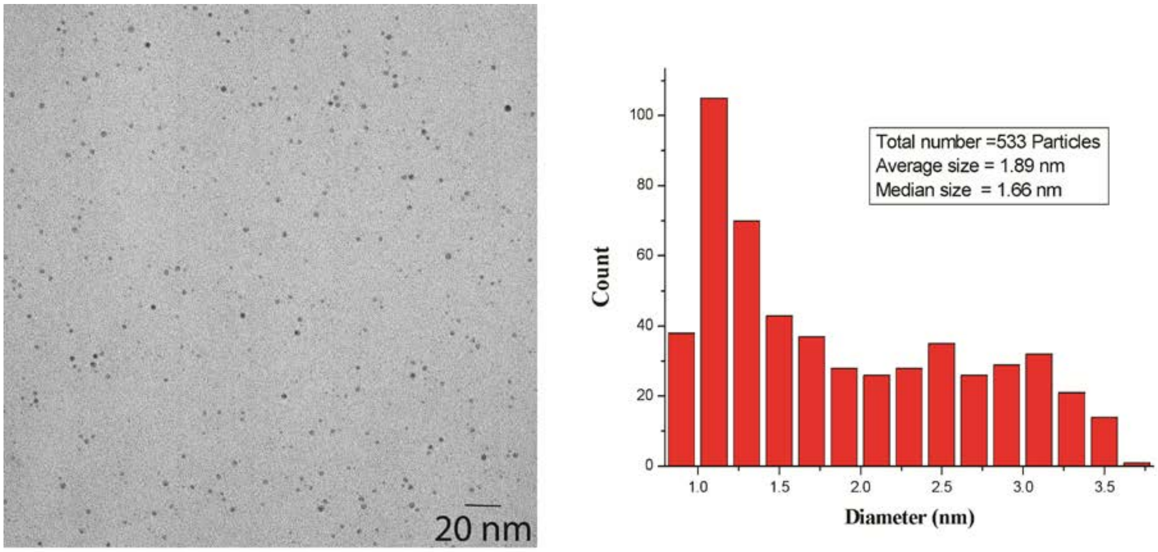

Figure S6. TEM image and size distribution of fraction 2 $Au_n(SG)_m$ nanoclusters (**4b**). This fraction consists of particles of smaller size than those of fraction 1 with average diameter of 1.89 nm (total number of particles for the statistics: 533).

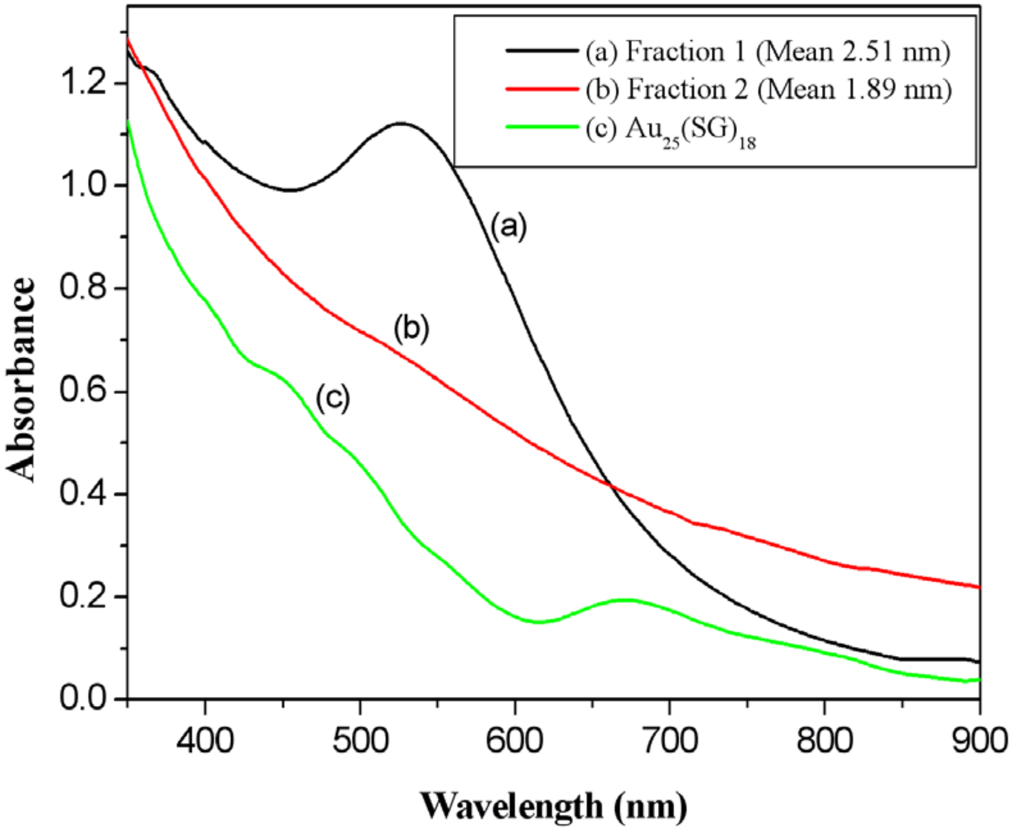

Figure S7. UV-vis absorption spectrum of Au nanoparticles of different size protected by L-glutathione. (a) Fraction 1 (**4a**) of gold clusters (average size 2.51 nm) shows a well-defined surface plasmon absorption band at 534 nm. (b) Cluster of the second fraction (**3b**, average size 1.89 nm) gives a featureless band without a distinct surface plasmon absorption peak. (c) $Au_{25}(SG)_{18}$ cluster (**4c**) show a multi-band absorption spectrum with distinct peaks at around 400 nm, 450 nm and 670 nm, these absorption bands indeed resemble the spectroscopic fingerprints of Au_{25} nanoclusters. The spectra as well as the particle size of the fraction is in good agreement with the work of Jin and co-workers.[1]

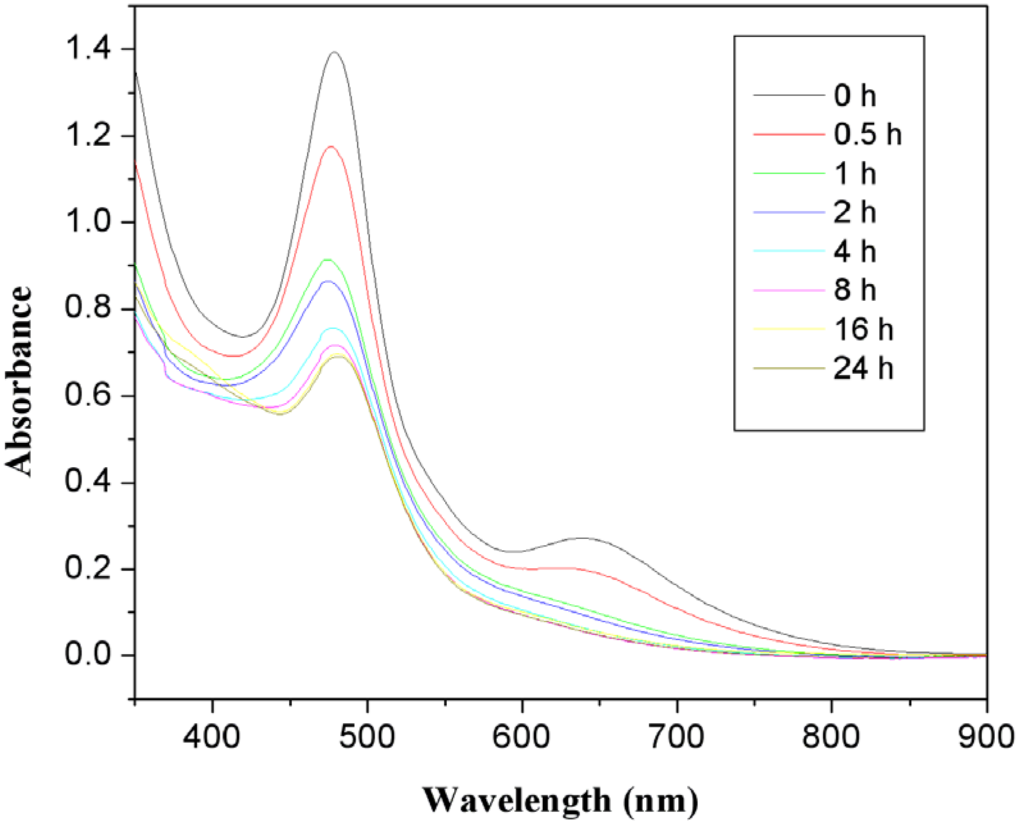

Figure S8. UV-vis absorption spectrum for the study of the stability of $Ag_n(SG)_m$ (**1**) nanoclusters in air. The absorbance intensity of $Ag_n(SG)_m$ nanoclusters at 478 nm decrease to nearly to half of its starting value already after 8 hour exposed in air. Then, the intensity of the peaks does not further decrease significantly for at least another 16 hours.

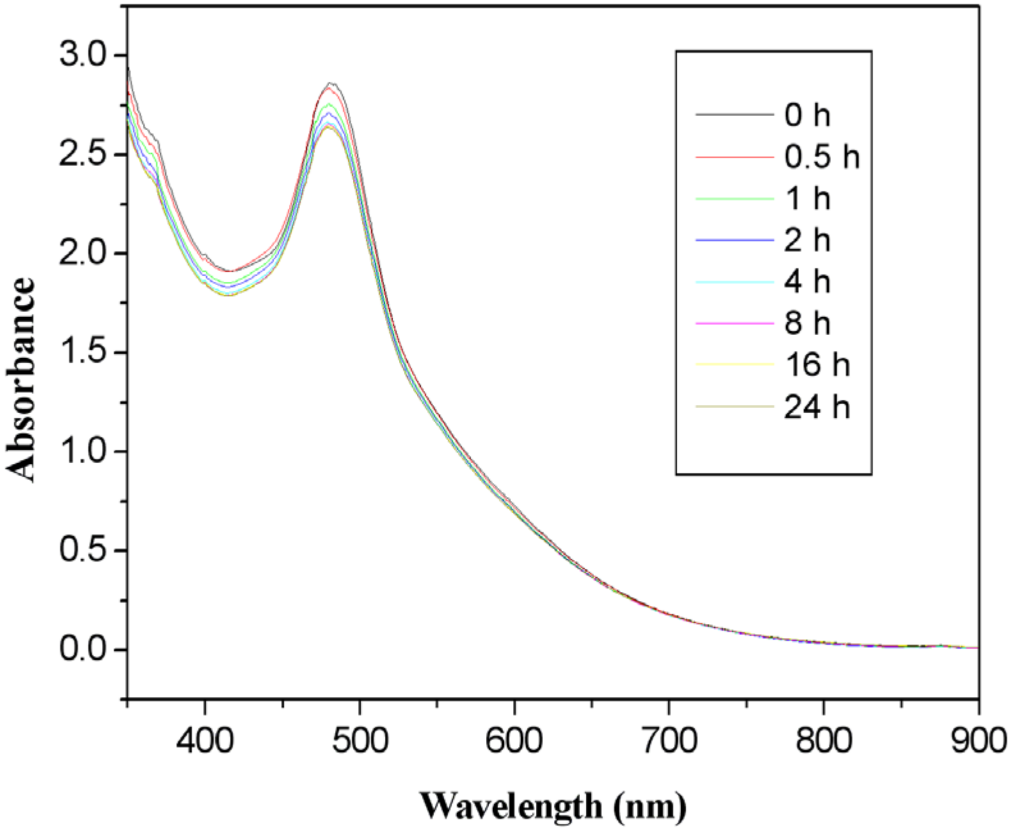

Figure S9. UV-vis absorption spectrum over time for study of the stability of $Ag_n(NALC)_m$ (**2**) nanoclusters at ambient conditions. The optical spectra of the clusters stay almost identical over a time period of 24 hours. Since UV-vis spectra are rather sensitive to aging, it can be concluded that the clusters are stable under these conditions.

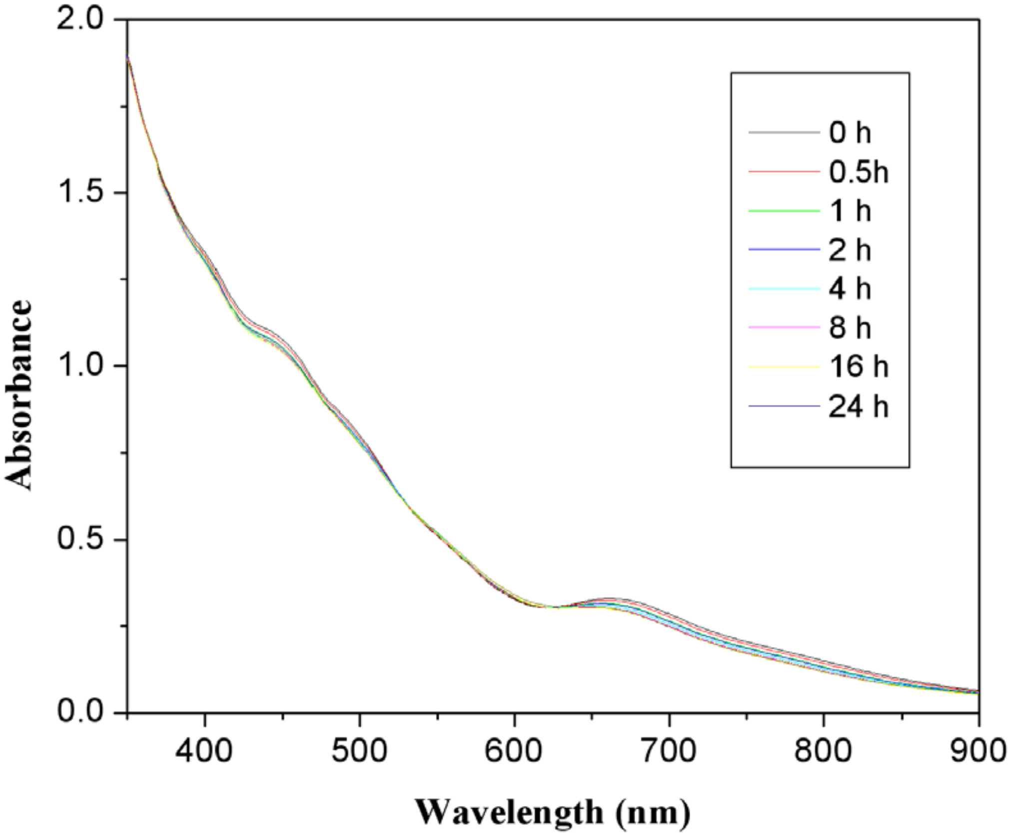

Figure S10. UV-vis absorption spectrum of $Au_{25}(SG)_{18}$ (**4c**) nanoclusters as function of time at ambient conditions. Just a very small decrease of the absorption can be observed over a period of 24 hours, showing that the clusters have good stability in air.

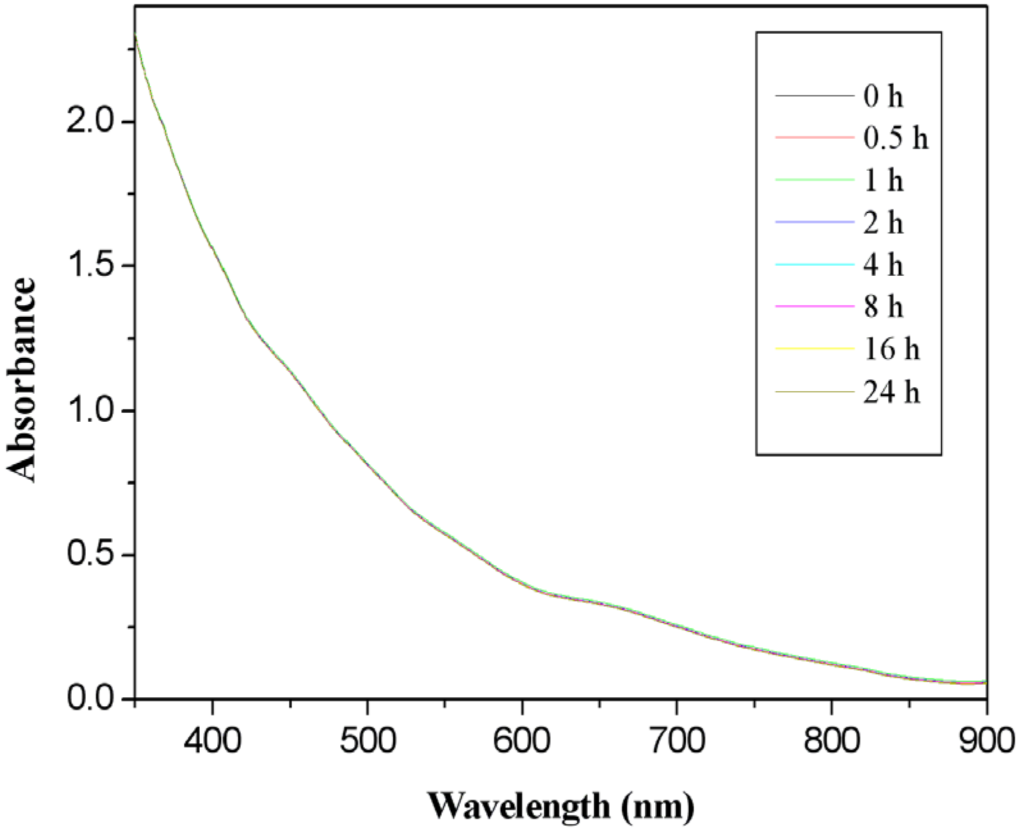

Figure S11. UV-vis absorption spectrum of stability of $Au_n(NALC)_m$ nanoclusters (**3b**) of about 1 nm in size as function of time under ambient conditions. The optical spectra of the clusters stay identical over a time period of 24 hours, indicating that the clusters are stable even under exposure to air.

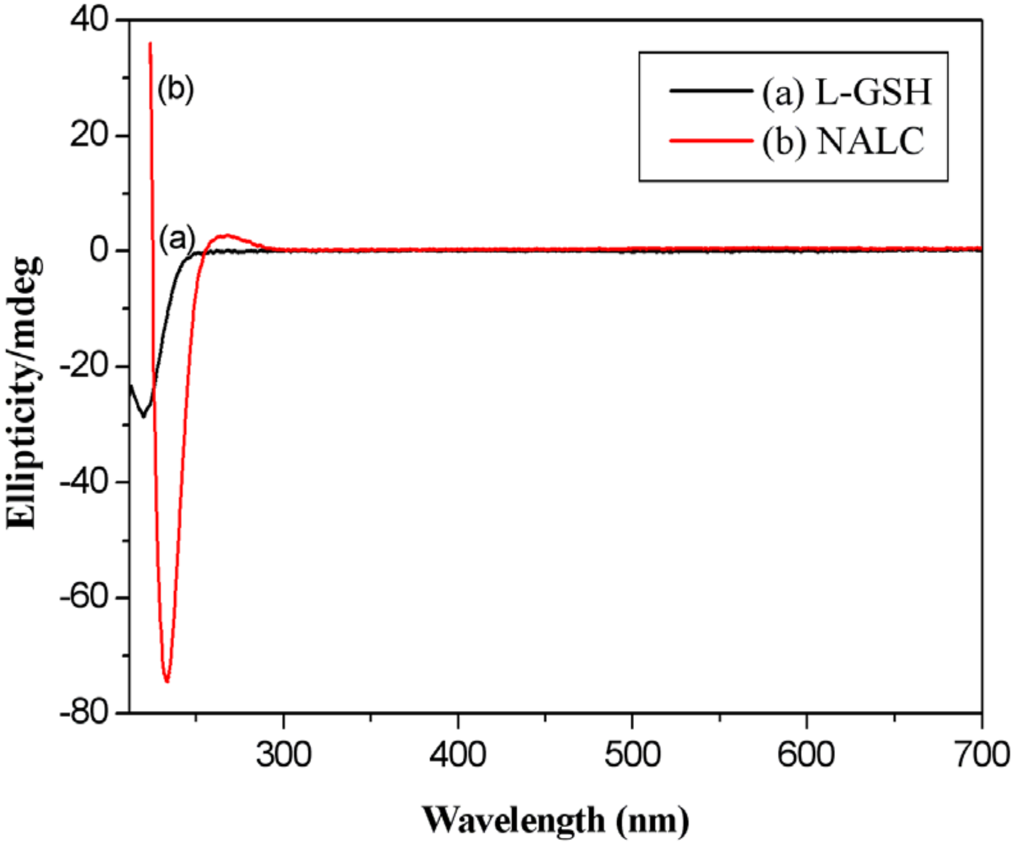

Figure S12. CD spectra of L-glutathione (curve a) and N-acetyl-L-cysteine (curve b). L-glutathione is optically active and shows a strong CD signal at 220 nm. N-acetyl-L-cysteine shows a very strong CD signal at 234 nm.

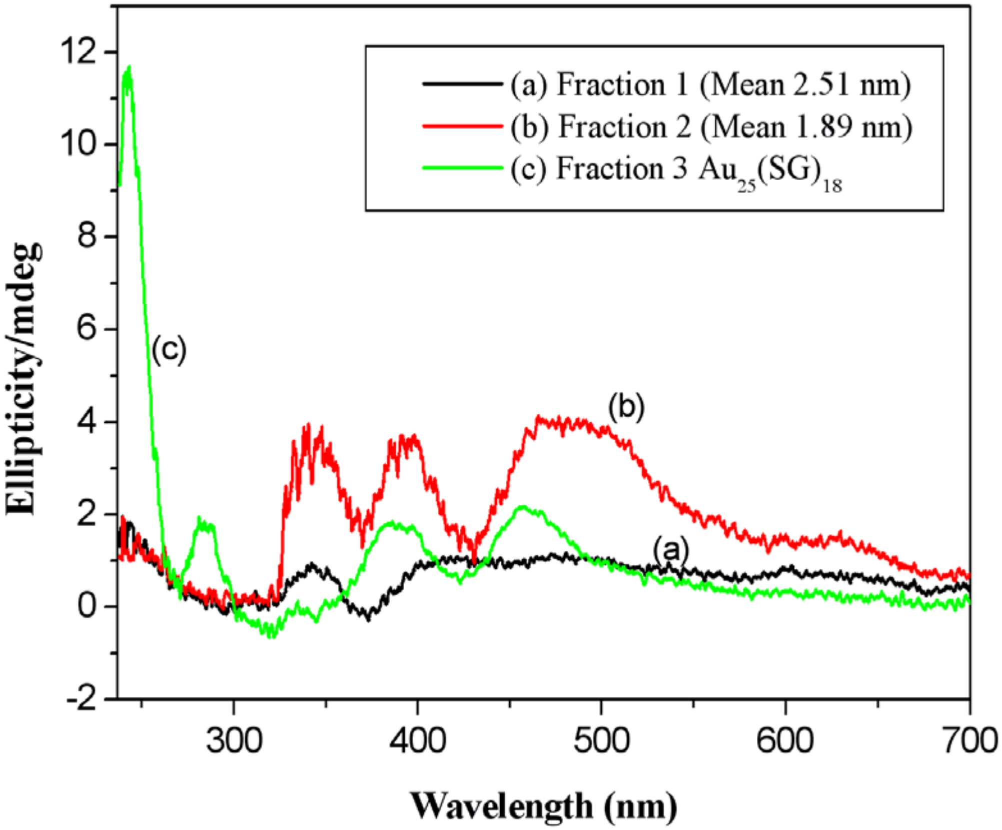

Figure S13. CD spectra of Au nanoparticles of different size protected by L-glutathione. While cluster of fraction 1 (average particle size 2.51 nm) show only very weak signals (curve a), particles of fraction 2 (average particle size 1.89 nm) exhibit strong CD-signals (curve b) in the near UV and vis. Like clusters of fraction 2, the CD spectrum of $Au_{25}(SG)_{18}$ nanoclusters (curve c) is governed by several peaks. The spectra are in good agreement with the work of Jin and co-workers[2] and indicate that smaller cluster consist of a metal core, which has a chiral structure.

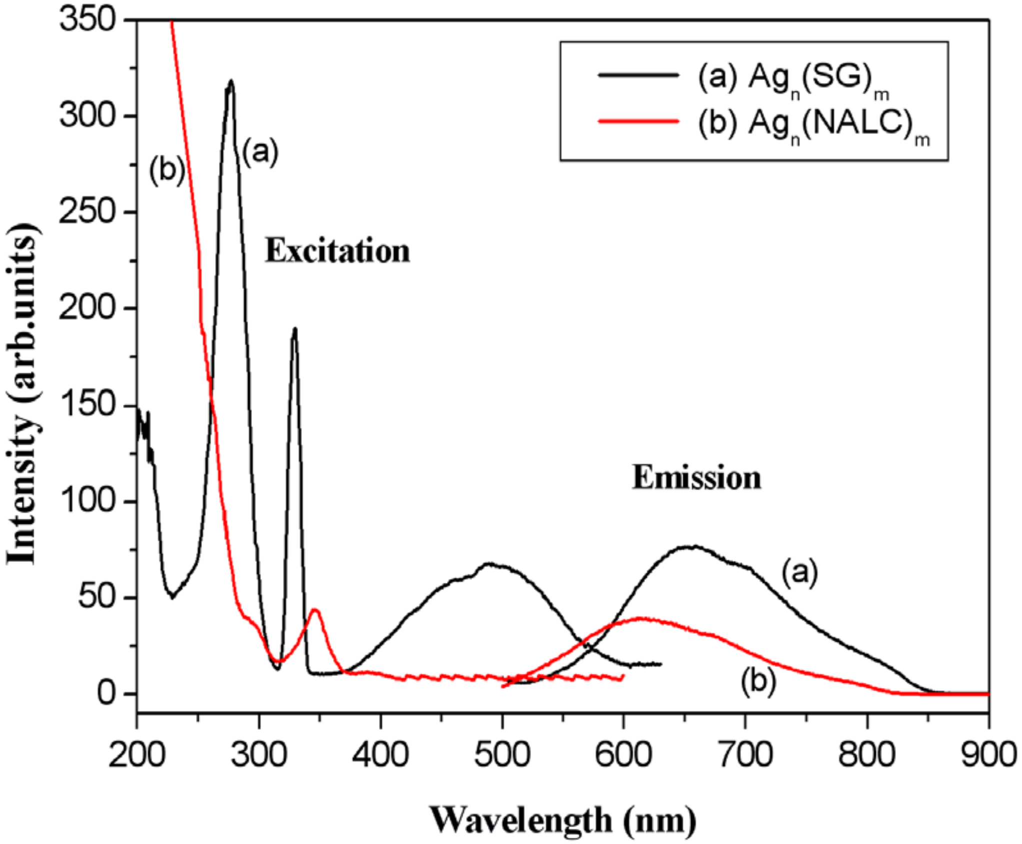

Figure S14. Photoexcitation and emission spectra of $Ag_n(SG)_m$ and $Ag_n(NALC)_m$ nanoclusters. Curve a): The excitation spectra of $Ag_n(SG)_m$ nanoclusters (measured by the emission at 660 nm) shows two excitation maxima. The most intense peak is at 277 and another broad band can be found at 489 nm (note that the peak at 330 nm is an artifact due to diffration). The emission spectra of these clusters are also shown is this figure. The spectra reveal one broad band with a maximum at 660 nm (excitation wavelength 478 nm). Curve b): The emission spectra (excitation at 480 nm) of $Ag_n(NALC)_m$ (**2**) nanoclusters show one maximum at a wavelength 611 nm. The excitation spectra of $Ag_n(NALC)_m$ exhibit one excitation band, which has its maximum at 346 nm and another small shoulder at ~290 nm. (The excitation spectra were obtained by recording the emission at 611 nm).

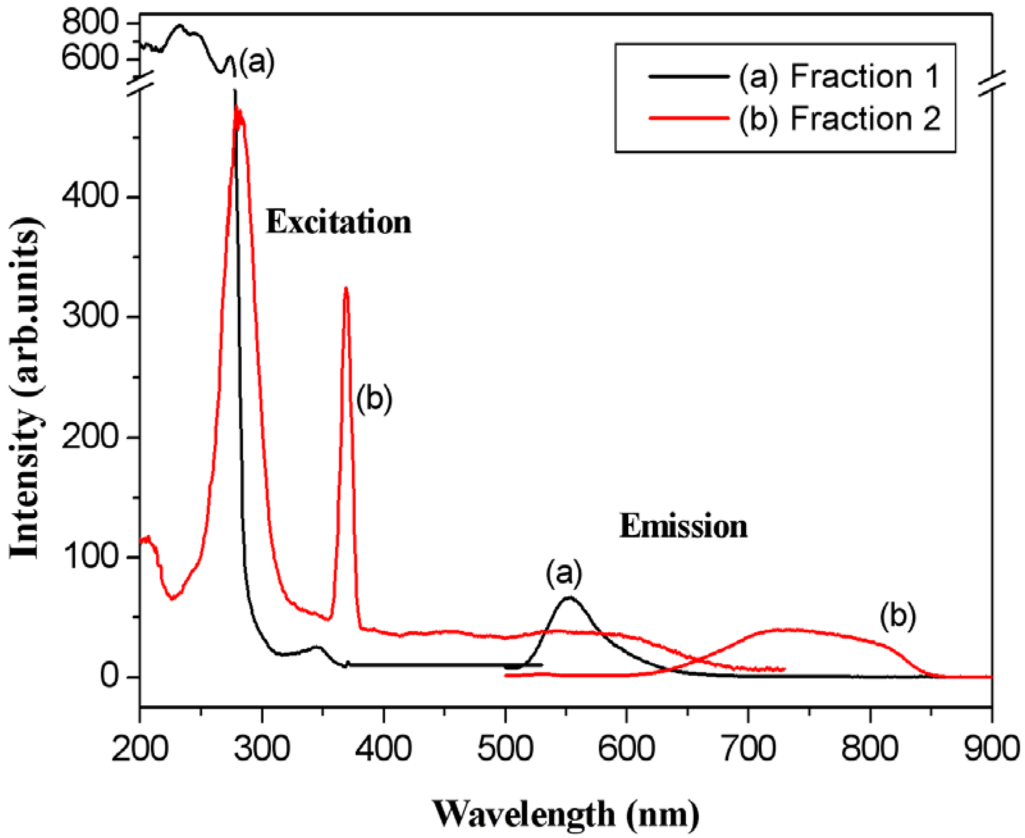

Figure S15. Photoexcitation and emission spectra of gold clusters protected by N-acetyl-L-cysteine of fraction 1 and 2. Curve a): The first fraction of $Au_n(NALC)_m$ nanoclusters gives one emission maximum at 554 nm (excitation at 450 nm). The excitation spectra show two excitation maxima at 232 and 346 nm, when recording the emission at 554 nm (note that the peak around 277 nm is a diffraction artifact). Curve b): The clusters of fraction 2 give a broad emission with a maximum at 738 nm (excitation at 450 nm). The excitation spectra show two major bands with maximum intensities at 282 and 545 nm (369 nm is again an artifact), when detecting the emission at 738 nm.

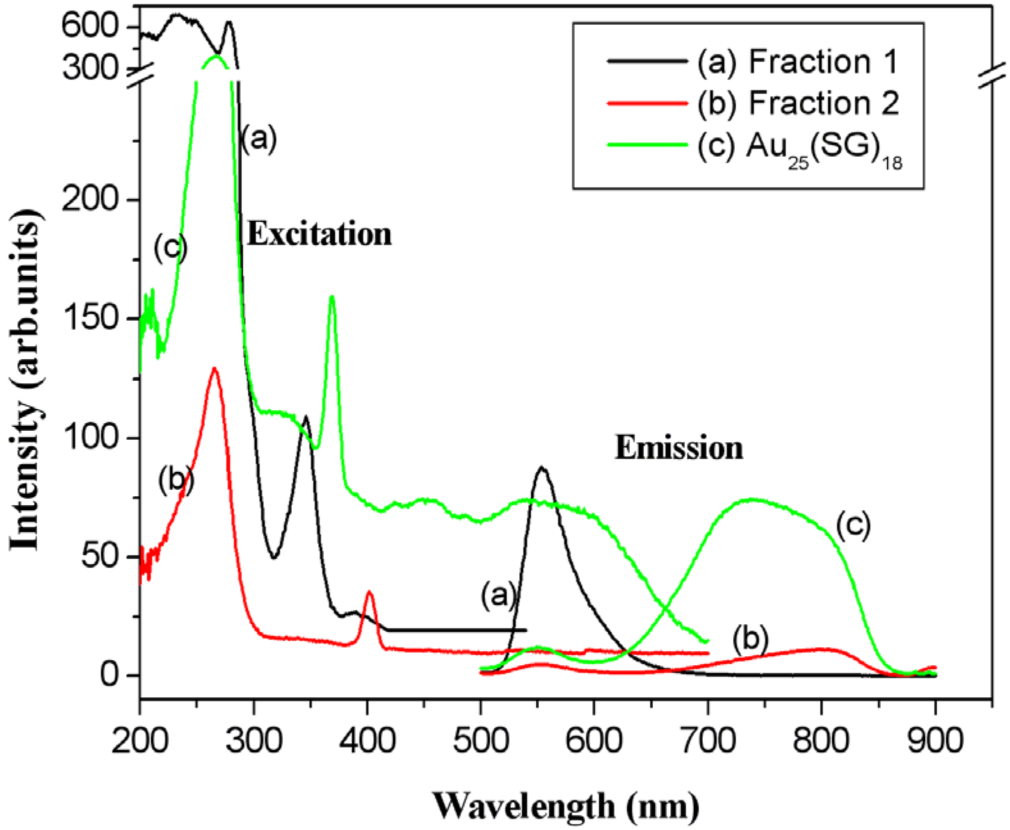

Figure S16. Photoexcitation and emission spectra of clusters protected by L-glutathione. Curve a): Cluster of the first fraction gives one emission maximum at 554 nm (excitation at 450 nm). The excitation spectra show two bands with maxima at 232 nm and 346 nm (the peak around 277 nm is an artifact due to diffraction), when recording the emission at 554 nm. Curve b): Particles of the second fraction exhibit two very weak emission bands with their maxima at 550 and 804 nm (excitation at 450 nm). When recording the emission at 804 nm, the cluster shows only one band with a maximum at 266 nm (402 nm is an artifact again) in their excitation spectra. Curve c): $Au_{25}(SG)_{18}$ cluster have a broad maximum emission with a maximum at 738 nm after excitation with 450 nm. The excitation spectra reveal two major bands with maxima at 267 and 540 nm (emission recorded at 738 nm and peak at 369 nm being an artifact).

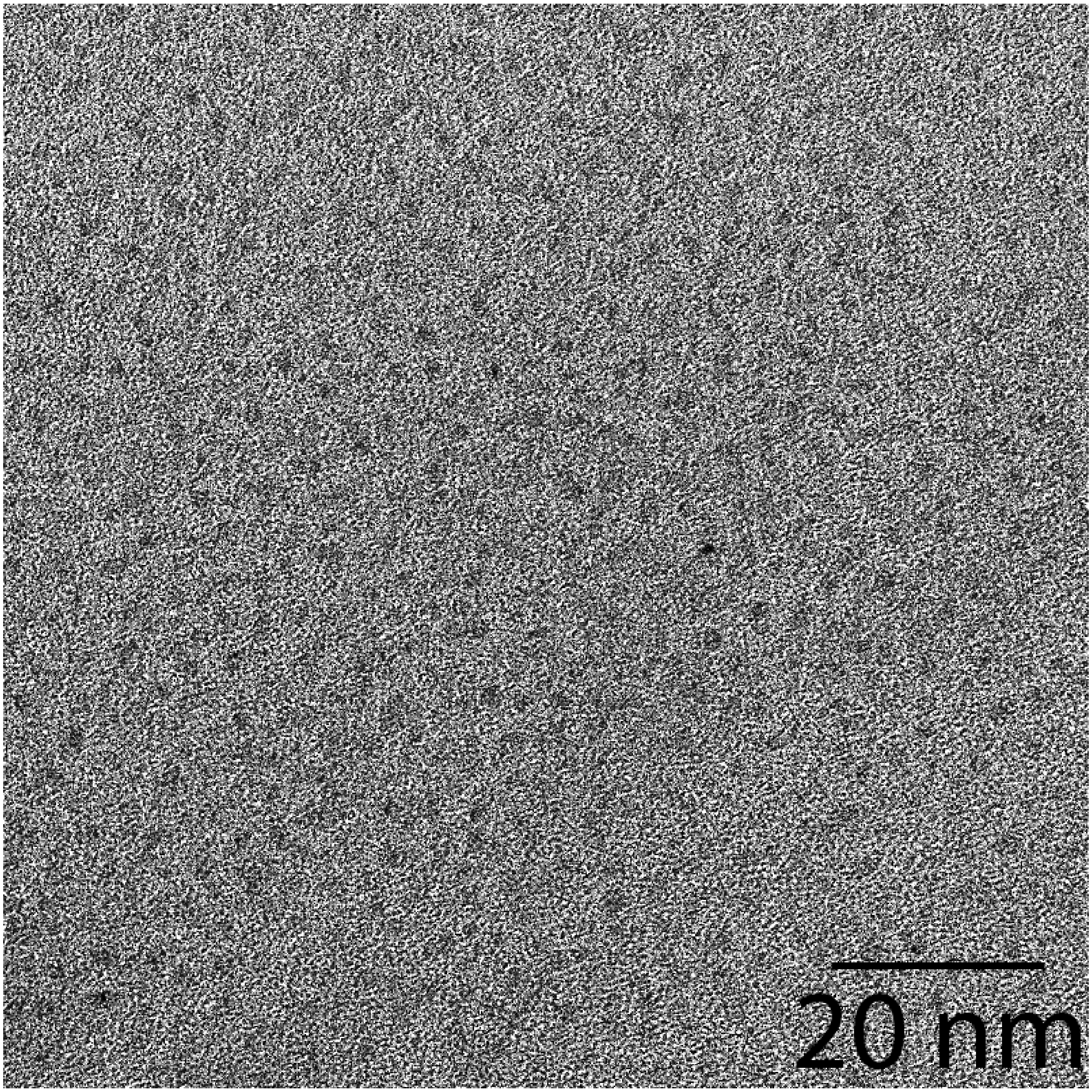

Figure S17. Full-size TEM image of clusters $Ag_n(SG)_m$ (**1**).

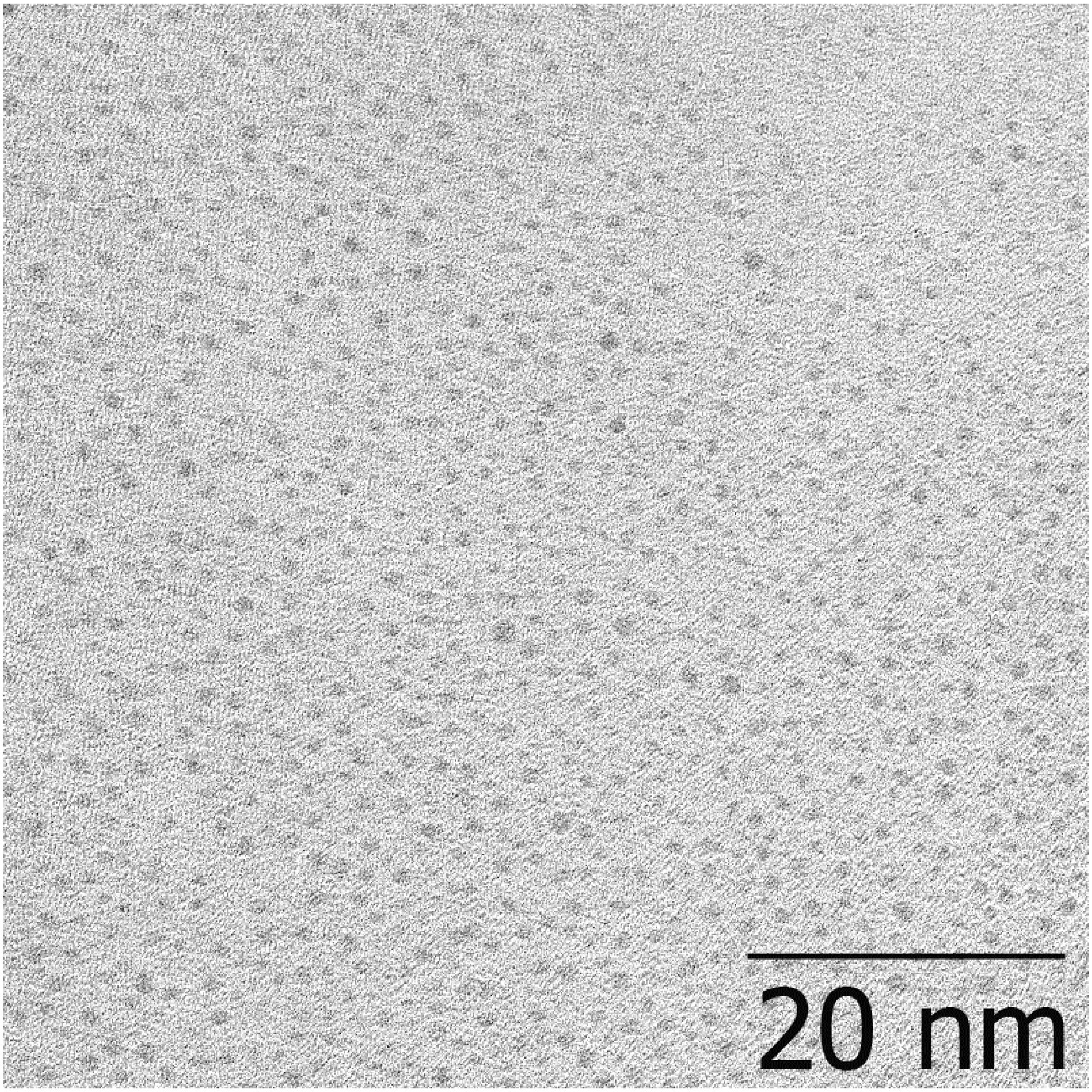

Figure S18. Full-size TEM image of cluster of the second fraction of Au@NALC (**3b**).

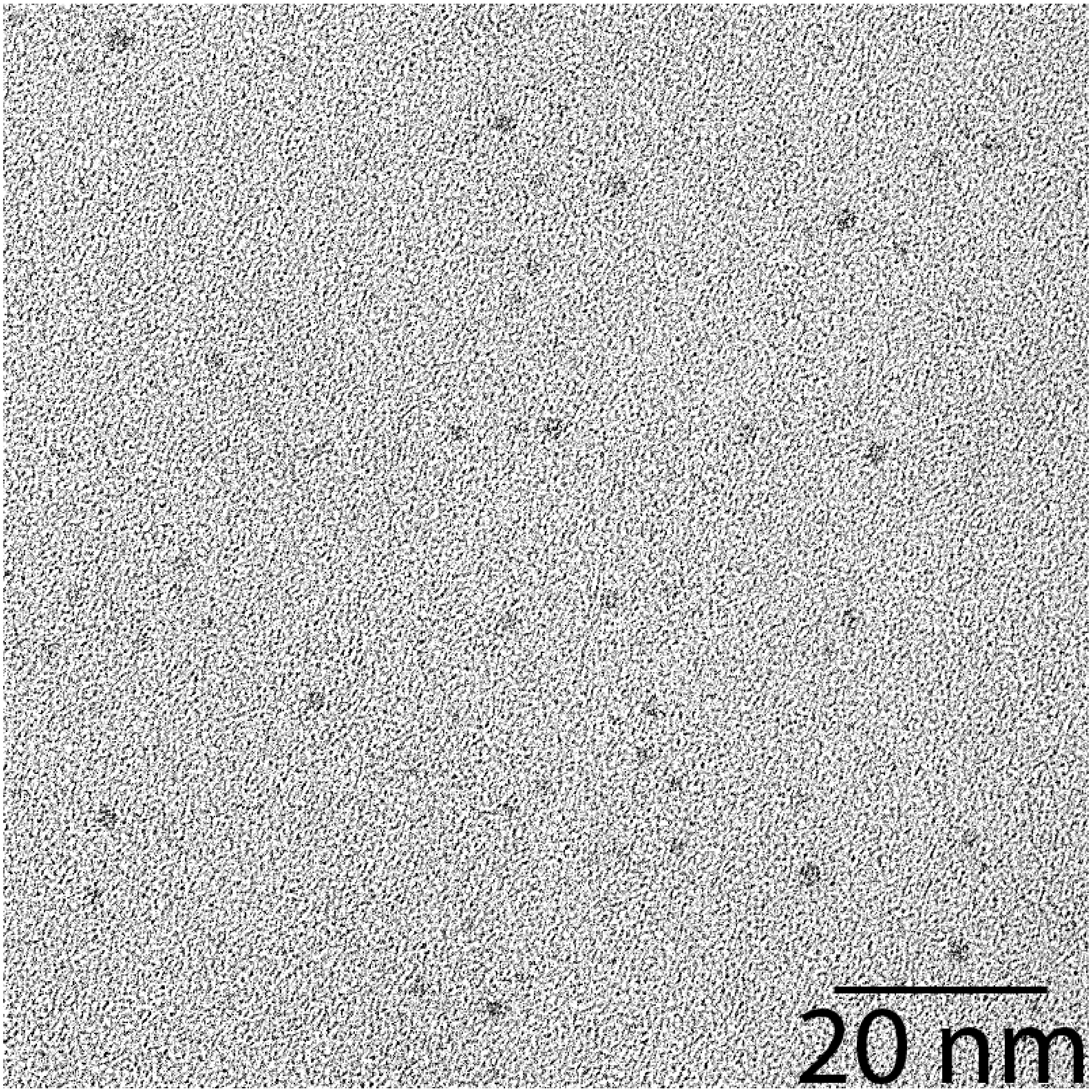

Figure S19. Full-size TEM image of cluster of the second fraction of $Au_{25}(SG)_{18}$ clusters (**4c**).

REFERENCES

(1) Wu, B. Z.; Chen, J.; Jin R. Adv. Funct. Mater. 2010, 21, 177-183.

(2) Wu, Z.; Gayathri, C.; Gil, R. R.; Jin R. J. Am. Chem. Soc. 2009,131, 6535-6542.

3.3. Third paper (Phys. Chem. Chem. Phys., 2013, 15, 12539-12542)

3.3.1. Summary of the third paper

In the third paper we used 2-phenylethanethiol (2-PET) ligand to protect three size selected monolayer nanoclusters, $Au_{25}(SCH_2CH_2Ph)_{18}$, $Au_{38}(SCH_2CH_2Ph)_{24}$ and $Au_{144}(SCH_2CH_2Ph)_{60}$ clusters.

We examined the purity of these clusters by matrix-assisted laser desorption/ionization time-of-flight mass spectrometry (MALDI-TOF). The spectra showed the molecular ion peak of these clusters $Au_{25}(SCH_2CH_2Ph)_{18}$, $Au_{38}(SCH_2CH_2Ph)_{24}$ and $Au_{144}(SCH_2CH_2Ph)_{60}$ at m/z = 7394 Da, 10780 Da and 35000 Da, respectively. The optical properties of these clusters were studied by UV-vis spectroscopy, which show multiple absorption peaks: $Au_{25}(SCH_2CH_2Ph)_{18}$ clusters exhibit three characteristic peaks at 400, 450 and 670 nm. $Au_{38}(SCH_2CH_2Ph)_{24}$ clusters give a characteristic UV-vis spectra with a series of peaks at 490, 520, 620, 750 and 1050 nm, also $Au_{144}(SCH_2CH_2Ph)_{60}$ clusters show only two characteristic peaks at 510 and 700 nm.

We discovered a very surprising phenomenon in this work. The infrared spectra of $Au_{25}(SCH_2CH_2Ph)_{18}$ clusters show a distinct shift of the aromatic C-H stretching band from 3030-3100 cm^{-1} to below 3000 cm^{-1}. The infrared spectra of $Au_{38}(SCH_2CH_2Ph)_{24}$ and $Au_{144}(SCH_2CH_2Ph)_{60}$ clusters do not show this distinct shift and their IR-spectra in the C-H stretching regime are similar to that of the bare ligand. The reason of this large shift for $Au_{25}(SCH_2CH_2Ph)_{18}$ is not clear up to now. A possible explanation is an electronic interaction of the aromatic rings of the ligands with each other or with the gold core. Moreover, the red-shift does neither depend on the charge of the metal core, nor on the counter ions, i.e. tetraoctylammonium (TOA^+) and Cs^+. This change in the IR spectrum of $Au_{25}(SCH_2CH_2Ph)_{18}$ is not only of fundamentally interest but can also be used to determine the purity of $Au_{25}(SCH_2CH_2Ph)_{18}$ cluster by FTIR spectroscopy during synthesis.

PCCP

RSC Publishing

COMMUNICATION

View Article Online
View Journal | View Issue

Infra-red spectroscopy of size selected Au_{25}, Au_{38} and Au_{144} ligand protected gold clusters†

Cite this: *Phys. Chem. Chem. Phys.*, 2013, **15**, 12539

Received 3rd April 2013,
Accepted 31st May 2013

DOI: 10.1039/c3cp51406d

www.rsc.org/pccp

Mostafa Farrag,[a] Martin Tschurl,*[a] Amala Dass[b] and Ulrich Heiz[a]

Through the discovery of ligand protected metal clusters with cores of a precise number of atoms, the exploration of the third dimension of the periodic table for fundamental research and also for applications has become less remote. So far, the exact number of metal atoms in the core has been determined unambiguously only using mass spectrometry and single crystal X-ray diffraction. Gold clusters protected by 2-phenylethanethiol ligands, for instance, show distinct magic numbers that correspond to either electronic or geometric shell closings. For efficient control of their synthesis simple-to-use *in situ* spectroscopies are required. In the specific case of $Au_{25}(SCH_2CH_2Ph)_{18}$ clusters (1) we found a distinct shift of the aromatic C–H stretching band from 3030–3100 cm^{-1} to below 3000 cm^{-1} whose origin is discussed as an electronic interaction of the aromatic rings of the ligands with each other or with the gold core. This IR-feature is specific for Au_{25}; the spectra of $Au_{38}(SCH_2CH_2Ph)_{24}$ (2) and $Au_{144}(SCH_2CH_2Ph)_{60}$ (3) clusters do not show this distinct shift and their IR-spectra in the C–H stretching regime are similar to that of the bare ligand. This significant change in the IR spectrum of $Au_{25}(SCH_2CH_2Ph)_{18}$ is not only of fundamental interest but also allows for *in situ* determination of the purity and monodispersity of the sample using FTIR spectroscopy during synthesis.

Ligand stabilized metal clusters have been attracting much attention owing to the promise to be widely used in applications such as nanoelectronics, optics, catalysis, chemical and biological sensing and biomedicine.[1–3] Based on the possibility of deliberately changing the confinement in the metal core, the electronic properties of these new hybrid materials can be tuned by exploring the third dimension of the periodic table, *i.e.* size. Much effort has been invested in the synthesis of such hybrid materials.[4–10] Brust *et al.* pioneered the preparation of thiol-stabilized gold nanoparticles by a two-phase synthetic approach.[6] Based on that technique Jin and co-workers succeeded in the preparation of size-selected gold clusters of Au_{25}, Au_{38} and Au_{144} protected by 2-phenylethanethiol.[7–9] Further, monodisperse Au_{25} nanoclusters stabilized by a variety of thiol ligands (2-phenylethanethiol, L-glutathione and 11-mercapto-1-undecanol) were successfully prepared by a one-pot synthetic method.[10] It has been found that the charge state of Au_{25} clusters protected by 2-phenylethanethiol can be converted from the neutral form of $[Au_{25}(SCH_2CH_2Ph)_{18}]^0$ clusters to the anionic form $[Au_{25}(SCH_2CH_2Ph)_{18}]^-$ after reaction with organic (*e.g.* tetraoctylammonium halides, TOAX) and metallic (NaX) salts.[11] While TOA^+ (tetraoctylammonium) counterions protect the anionic form from decomposition by hindering the attack by halide ions, Na^+ ions do not allow any steric stabilization of the $[Au_{25}(SCH_2CH_2Ph)_{18}]^-$ clusters. Hence, in the latter case degradation occurs when the clusters are being attacked by halide ions, especially Br^- and I^-.[11] Cyclic voltammetry (CV) and electron spin resonance (ESR) indicated that two consecutive single-electron transfer reactions occur between 2,2,6,6-tetramethylpiperidin-1-oxoammonium tetrafluoroborate ($TEMPO^+BF_4^-$) and $[Au_{25}(SCH_2CH_2Ph)_{18}]^-TOA^+$ nanoclusters. The use of oxoammonium cations allows the preparation of pure $Au_{25}(SCH_2CH_2Ph)_{18}{}^+$ nanoclusters.[12]

The structures of the ligand protected gold clusters investigated in this work are well-studied. Single crystal X-ray diffraction of $[Au_{25}(SCH_2CH_2Ph)_{18}]^-TOA^+$ revealed that the cluster consists of an Au_{13} icosahedral core in its anionic and neutral forms. This core is surrounded by 6 units of $(–Au_2(SCH_2CH_2Ph)_3–)$[13,14] and these units show some distortions in the anionic form; one of the sulfur atoms in the S–Au–S–Au–S motif is bent upward, while the inverted sulfur is bent downward.[14] Density-functional theory (DFT) calculations and powder X-ray crystallography were used

---

[a] *Technische Universität München, Lehrstuhl für Physikalische Chemie, Lichtenbergstraße 4, 85748 Garching, Germany. E-mail: tschurl@tum.de*

[b] *Department of Chemistry and Biochemistry, University of Mississippi, 352 Coulter Hall, University, Mississippi 38677, USA*

† Electronic supplementary information (ESI) available: A detailed description of the cluster synthesis, the chemicals used and the instrumentation for characterization, detailed discussion on UV-vis spectra of all three clusters of different sizes, the spectra of the two charge states of Au_{25} clusters and with two different counterions for the negatively charged form and discussion on MALDI spectra of all three clusters confirming the purity of the samples. See DOI: 10.1039/c3cp51406d

to study the crystal structure of thiolate-protected $Au_{38}(SR)_{24}$ clusters (R = CH_3, C_6H_{13}, $C_{12}H_{25}$ and CH_2CH_2Ph).[15,16] The low-energy structure of Au_{38} has a bi-icosahedral Au_{23} core and a chiral arrangement of the protecting gold-thiolate that is characterized by three short (S–Au–S) and six long (S–Au–S–Au–S) motifs.[15,16] The chiral arrangement of the achiral ligand ($PhCH_2CH_2SH$) in the Au_{38} cluster was confirmed experimentally by Bürgi and co-workers.[17] Using chiral high-performance liquid chromatography the racemic mixture of $Au_{38}(SCH_2CH_2Ph)_{24}$ was separated and both enantiomers indeed gave the expected mirror-image circular dichroism spectrum.[17] A structure-model of the third cluster investigated in this work, $Au_{144}(SCH_2CH_2Ph)_{60}$, was obtained by comparing DFT based structure factors to an experimental powder X-ray scattering function.[18] The Au_{144} cluster model proposes an icosahedral Au_{114} core with 30 units of (RS–Au–RS).[18a]

FTIR studies of ligand protected clusters are usually performed for elucidating how the ligand binds to the metal core. Therefore, for gold clusters protected by similar ligands (*e.g.* methanethiol and thiophenol) several FTIR studies exist.[4,18b,19] The spectra of all clusters mostly resemble the IR-spectra of the bare ligand. However, a common feature is the disappearance of the S–H vibrational band (2535–2564 cm^{-1}) indicating the binding of the ligand to the cluster *via* the sulfur atom. In addition, small perturbations of some rocking modes can be found but otherwise the IR-spectra are very similar to those of the bare ligands.[18b]

In the following, we present the IR-spectra of Au_{25}, Au_{38} and Au_{144} clusters protected by 2-phenylethylthiol as a ligand. The clusters were prepared by well-established methods mentioned above.[7–10] The purity of the synthesized gold clusters was first investigated using UV-vis spectroscopy[7–10] and further examined by MALDI-MS using a DCTB matrix at threshold laser intensities.[7b] The anionic Au_{25} clusters were neutralized upon spontaneous oxidation in air.[21] This conversion was monitored by UV-vis spectroscopy. The neutral Au_{25} clusters were again reduced by either tetraoctylammonium bromide or cesium acetate yielding $[Au_{25}(SCH_2CH_2Ph)_{18}]^-TOA^+$ and $[Au_{25}(SCH_2CH_2Ph)_{18}]^-Cs^+$, respectively (for all experimental details concerning preparation and characterization see the ESI†).

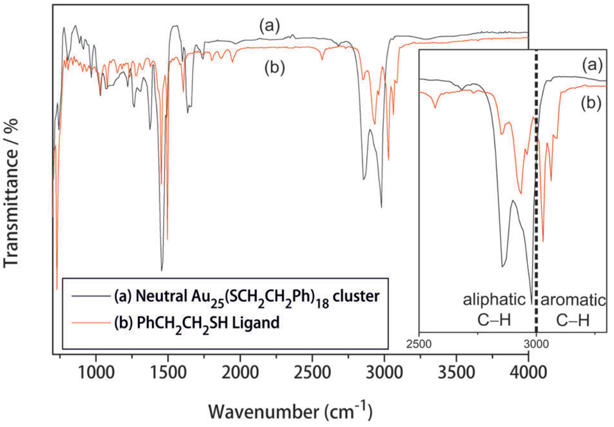

Fig. 1 FTIR spectra of the neutral form of $Au_{25}(SCH_2CH_2Ph)_{18}(Au^0_{25})$ clusters (a) and the 2-phenylethanethiol ($PhCH_2CH_2SH$) ligand (b). In the spectra of the ligand only, transitions of aliphatic as well as aromatic C–H stretching modes can be found (for an assignment see for example the vibrations of 2-phenylethanol[20]). In the spectra of Au_{25} clusters the latter transitions are strongly red-shifted and overlap with the aliphatic modes which can be better seen in the zoom of the inset. Thus, only two peaks can be found in this spectral region for Au_{25}.

Fig. 1 shows the infrared spectra of the neutral charge Au_{25} cluster and the bare 2-phenylethanethiol ligand, respectively. In both spectra the aromatic C–H bending modes of the monosubstituted aromatic ring at 700 and 750 cm^{-1} and aromatic C–C stretching at around 1450, 1500, 1580 and 1600 cm^{-1} (for a complete assignment see the IR spectrum of 2-phenylethanol)[20] appear at the same wavenumber. The peak at 2567 cm^{-1}, which can be assigned to the S–H stretching vibration, is only visible in the spectrum of the ligand and disappears in that of the Au_{25} clusters. This is a clear confirmation that the ligand is anchored to the cluster surface *via* the sulfur atom.[4] In the spectra of the ligand two methylene C–H stretching vibration peaks appear in the region of 2847–2932 cm^{-1} and the aromatic C–H stretching modes give rise to three peaks in the region from 3030 to 3100 cm^{-1} (zoom in Fig. 1). However, in the spectra of Au_{25} clusters the aromatic stretching vibrations are red-shifted and overlap with the aliphatic modes resulting in just two peaks below 3000 cm^{-1} (2980 cm^{-1} and 2854 cm^{-1}). This effect is characteristic of $Au_{25}(SCH_2CH_2Ph)_{18}$ clusters only, since the spectra of $Au_{38}(SCH_2CH_2Ph)_{24}$ and $Au_{144}(SCH_2CH_2Ph)_{60}$ are very similar to those of the bare ligand (Fig. 2). From a spectroscopic point of view this unexpected behavior cannot be explained straightforwardly. A first interpretation might suggest an electronic interaction of the aromatic ring system with the metallic core of the clusters, resulting in perturbation of the aromaticity of the benzene ring and hence in a red-shift of the C–H vibrations. However, from the single crystal structure of $Au_{25}(SCH_2CH_2Ph)_{18}$

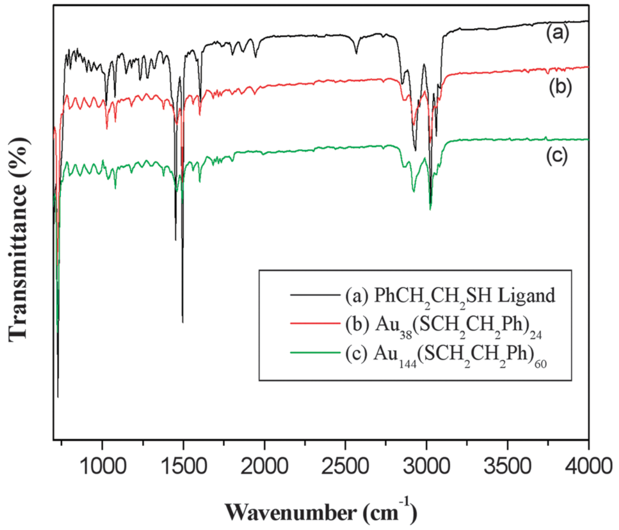

Fig. 2 FTIR spectra of the bare 2-phenylethanethiol ligand (a) in comparison with the neutral forms of $Au_{38}(SCH_2CH_2Ph)_{24}(Au^0_{38})$ (b) and $Au_{144}(SCH_2CH_2Ph)_{60}$-$(Au^0_{144})$ clusters (c). Except for the disappearance of the S–H stretching mode, indicating the binding of the ligand to the cluster *via* the S-atom, the spectra of the clusters completely resemble those of the bare ligand. In particular in the C–H stretching region all vibrations remain unaltered.

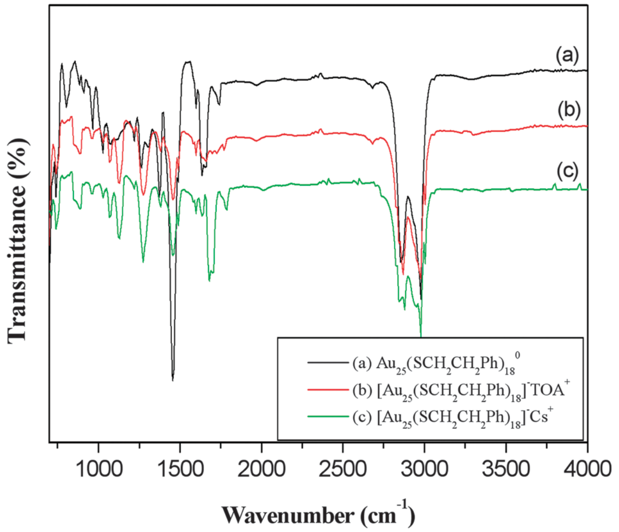

Fig. 3 FTIR spectra of the neutral form of $Au_{25}(SCH_2CH_2Ph)_{18}(Au_{25}^{0})$ clusters (a), the anionic form of $Au_{25}(SCH_2CH_2Ph)_{18}^{-}(Au_{25}^{-})$ clusters with tetraoctylammonium (TOA^+) (b) and Cs^+ (c) as counterions. All three spectra are similar to each other, indicating that the characteristic shift of the aromatic stretching vibrations is neither governed by the charge state of the cluster core nor by the counterion.

such an effect can be excluded, since the phenyl ring is not in close contact with the metal core.[13] Furthermore, the charge state of the gold core does not influence the IR-spectra (Fig. 3), which is an additional confirmation that the interaction of the metal with the ring system may be ruled out. In the course of this experiment $[Au_{25}(SCH_2CH_2Ph)_{18}]^0$ nanoclusters were reduced by either tetraoctylammonium bromide or cesium acetate (experimental details are given in the ESI†). In both cases $[Au_{25}(SCH_2CH_2Ph)_{18}]^-$ anions are obtained, but with different counterions (*i.e.* TOA^+ and Cs^+, respectively). In each case the spectra remain unaltered, which even allows for excluding the interaction of the counterion with the π-system of the benzene ring. In addition, the effect in the IR spectra is even more surprising, because the structures of all three cluster samples are quite similar; they all share icosahedral cores of different sizes with long (RS–Au–SR–Au–SR) and/or short (RS–Au–SR) bridging units.[13–17] Despite all structural similarities the most obvious difference of Au_{25} clusters with respect to clusters of Au_{38} and Au_{144} is their size. It can now be speculated that the higher density of ligands of the cluster (0.72 ligand molecules per Au atom in Au_{25} in comparison to 0.63 ligand molecules per Au atom in Au_{38} and 0.42 ligand molecules per Au atom in Au_{144} clusters) may lead to the interaction of the individual aromatic rings with each other. However, this interpretation is very speculative, since it is neither supported by the single crystal structure[13] nor does such an interaction usually result in large shifts (the shift is in the order of a couple of wavenumbers; see for example the recent work on the benzene di- and trimer[21]).

While a detailed understanding of the surprising difference in the IR spectra of $Au_{25}(SCH_2CH_2Ph)_{18}$ in comparison to those of the other clusters of larger size is still not possible and may inspire further studies, the anomaly in the spectra can serve as a fingerprint for the characterization of Au_{25} clusters. IR spectroscopy may therefore serve as a considerably easy analytical tool for analyzing the monodispersity of Au_{25} clusters after synthesis as well as for studying the catalysts under reaction conditions by applying *in situ* spectroscopy. The latter may be of particular interest, since small gold nanoclusters (<2 nm) are highly catalytically active in the oxidation of styrene[22a,b] and have shown 100% chemoselectivity for the hydrogenation of α,β-unsaturated ketones and aldehydes.[22c]

Acknowledgements

This work was supported by an ERC Advanced Grant (ERC-2009-AdG 246645-ASC3), and by the DAAD and Egyptian missions (German Egyptian Research Long Term Scholarship-GERLS). The authors thank TUM graduate school for their encouragement. We kindly acknowledge Prof. Häkkinen for helpful discussion.

Notes and references

1 N. Zheng and G. D. Stucky, *J. Am. Chem. Soc.*, 2006, **128**, 14278–14280.

2 E. S. Shibu, M. A. H. Muhammed, T. Tsukuda and T. Pradeep, *J. Phys. Chem. C*, 2008, **112**, 12168–12176.

3 C. J. Ackerson, P. D. Jadzinsky, G. J. Jensen and R. D. Kornberg, *J. Am. Chem. Soc.*, 2006, **128**, 2635–2640.

4 M. Farrag, M. Thamer, M. Tschurl, T. Bürgi and U. Heiz, *J. Phys. Chem. C*, 2012, **116**, 8034–8043.

5 M. Farrag, M. Tschurl and U. Heiz, *Chem. Mater.*, 2013, **25**, 862–870.

6 M. Brust, M. Walker, D. Bethell, D. J. Schiffrin, R. Whyman and C. Kiely, *J. Chem. Soc., Chem. Commun.*, 1994, 801–802.

7 (*a*) M. Zhu, E. Lanni, N. Garg, M. E. Bier and R. Jin, *J. Am. Chem. Soc.*, 2008, **130**, 1138–1139; (*b*) A. Dass, A. Stevenson, G. R. Dubay, J. B. Tracy and R. W. Murray, *J. Am. Chem. Soc.*, 2008, **130**, 5940–5946.

8 H. Qian, Y. Zhu and R. Jin, *ACS Nano*, 2009, **3**, 3795–3803.

9 H. Qian and R. Jin, *Nano Lett.*, 2009, **9**, 4083–4087.

10 Z. Wu, J. Suhan and R. Jin, *J. Mater. Chem.*, 2009, **19**, 622–626.

11 M. Zhu, G. Chan, H. Qianb and R. Jin, *Nanoscale*, 2011, **3**, 1703–1707.

12 Z. Liu, M. Zhu, X. Meng, G. Xu and R. Jin, *J. Phys. Chem. Lett.*, 2011, **2**, 2104–2109.

13 M. W. Heaven, A. Dass, P. S. White, K. M. Holt and R. W. Murray, *J. Am. Chem. Soc.*, 2008, **130**, 3754–3755.

14 M. Zhu, W. T. Eckenhoff, T. Pintauer and R. Jin, *J. Phys. Chem. C*, 2008, **112**, 14221–14224.

15 O. Lopez-Acevedo, H. Tsunoyama, T. Tsukuda, H. Häkkinen and C. M. Aikens, *J. Am. Chem. Soc.*, 2010, **132**, 8210–8218.

16 Y. Pei, Y. Gao and X. C. Zeng, *J. Am. Chem. Soc.*, 2008, **130**, 7830–7832.

17 I. Dolamic, S. Knoppe, A. Dass and T. Bürgi, *Nat. Commun.*, 2012, **3**, 798.

18 (*a*) O. Lopez-Acevedo, J. Akola, R. L. Whetten, H. Grönbeck and H. Häkkinen, *J. Phys. Chem. C*, 2009, **113**, 5035–5038;

(*b*) T. G. Schaaff, M. N. Shafigullin, J. T. Khoury, I. Vezmar and R. L. Whetten, *J. Phys. Chem. B*, 2001, **105**, 8785–8796.

19 (*a*) C. Chung and M. Lee, *J. Electroanal. Chem.*, 1999, **468**, 91–97; (*b*) M. J. Hostetler, J. J. Stokes and R. W. Murray, *Langmuir*, 1996, **12**, 3604–3612.

20 H. M. Badawi, *Spectrochim. Acta, Part A*, 2011, **82**, 63–68.

21 R. Kusaka, Y. Inokuchi and T. Ebata, *J. Chem. Phys.*, 2012, **136**, 044304.

22 (*a*) Y. Zhu, H. Qian and R. Jin, *Chem.–Eur. J.*, 2010, **16**, 11455–11462; (*b*) B. Y. Zhu, H. Qian, M. Zhu and R. Jin, *Adv. Mater.*, 2010, **22**, 1915–1920; (*c*) Y. Zhu, H. Qian, B. A. Drake and R. Jin, *Angew. Chem., Int. Ed.*, 2010, **49**, 1295–1298.

Supplementary information

Infra-red Spectroscopy of Size Selected Au_{25}, Au_{38} and Au_{144} Ligand Protected Gold Clusters

Mostafa Farrag[a], Martin Tschurl[a], Amala Dass[b], Ulrich Heiz[a]

[a] TECHNISCHE UNIVERSITÄT MÜNCHEN, LEHRSTUHL FÜR PHYSIKALISCHE CHEMIE, LICHTENBERGSTRAßE 4, 85748 GARCHING, GERMANY

[b] DEPARTMENT OF CHEMISTRY AND BIOCHEMISTRY, UNIVERSITY OF MISSISSIPPI, 352 COULTER HALL, UNIVERSITY, MISSISSIPPI 38677, USA.

1. Experimental Section:

Chemicals. Tetrachloroauric (III) acid ($HAuCl_4 \cdot 3H_2O$, >99.99% metal basis, Aldrich), sodium borohydride ($NaBH_4$, ≥96%, Aldrich), tetraoctylammonium bromide (TOAB, ≥98%, Fluka), cesium acetate (CsOAc, 99.9%, Aldrich), 2-phenylethanethiol (2-PET) and L-glutathione (γ-L-Glutamyl-L-cysteinyl-glycine, γ-Glu-Cys-Gly, L-GSH) reduced (98%, Aldrich) were used for synthesizing the ligand protected nanoparticles. As solvents tetrahydrofuran (THF, HPLC grade, ≥99.9%, Aldrich), toluene (HPLC grade, ≥99.9%, Aldrich), methylene chloride (HPLC grade, ≥99.9%, Aldrich), ethanol (HPLC grade, Aldrich), and methanol (HPLC grade, Aldrich) were taken. All chemicals were used as received. Deionized water was purified by a Millipore Milli-Q water system to obtain Milli-Q water (resistivity 18.2 MΩ x cm). All glassware was thoroughly cleaned with aqua regia ($HCl:HNO_3 = 3:1$ v/v), rinsed with Milli-Q water, and then dried in an oven prior to use.

Instrumentation. All UV-vis spectra were recorded at ambient temperature from 190 to 1100 nm with a single-beam spectrophotometer (Analytik Jena, Specord 40). Infrared spectra of the 2-phenylethanethiol ligand and the three gold nanoclusters were measured with an FTIR spectrometer (Nicolet 380, resolution: < 0.9 cm^{-1}, transmission mode). Each spectrum was obtained by accumulating 200 scans. The samples were prepared as dry, thin, optically translucent films by casting a drop of a toluene solution on a KBr disk. Mass spectra were obtained with a Bruker Autoflex MALDI-TOF mass spectrometer, after mixing the particle solution with DCTB matrix in 1:1000 mol ratio. To keep fragmentation as low as possible the laser power was reduced to a threshold value.[1]

Preparation of $Au_{25}(SCH_2CH_2Ph)_{18}$clusters (1).We followed the synthetic route of Jin and co-workers as it produces reasonable amounts of pure Au_{25} clusters.[2] In short, $HAuCl_4.3H_2O$ was reduced by $NaBH_4$ in the presence of the ligand ($PhCH_2CH_2SH$) in THF at 0°C and by continuous stirring. Monodisperse clusters were obtained by an aging process (i.e. a prolongation of the reaction time for another 114 h at room temperature) and the succeeding precipitation of the clusters.

Preparation different charge states of $Au_{25}(SCH_2CH_2Ph)_{18}$ clusters. While the synthetic method described above already results in negatively charged $Au_{25}(SCH_2CH_2Ph)_{18}$ cluster,[2] these clusters are converted to neutral ones via oxidation by air or H_2O_2 (~30% aqueous).[3] To re-prepare the negatively charged Au_{25} cluster with different counterions, i.e. tetraoctylammonium (TOA^+) and Cs^+, all reactants were dissolved in toluene and a 70% toluene/30% methanol mixture, respectively. By the reaction with the salts (i.e. tetraoctylammonium bromide and caesium acetate; molar ratio of gold cluster to salt: 1:100) the neutrally charged Au_{25} clusters were converted to their negatively charged formagain after stirring at room temperature.[4] While the conversion with TOA^+ as counterion is achieved within some minutes, the reaction with caesium acetate is significantly slower (full conversion after 10 h). For both cases, the conversion was monitored by UV-vis spectroscopy (see below). TOA^+ and Cs^+ were chosen as counterions since they are known to stabilize the anionic form of Au_{25} clusters, while smaller ions, such as Na^+ do not protect the cluster from oxidation.[4] Repeatedly, the UV-vis spectra of $[Au_{25}(SCH_2CH_2Ph)_{18}]^-Cs^+$ and $[Au_{25}(SCH_2CH_2Ph)_{18}]^-$ TOA^+ clusters were recorded and no significant oxidation of the clusters was found over three months.

Preparation of $Au_{38}(SCH_2CH_2Ph)_{24}$clusters (2). The preparation of monodisperse $Au_{38}(SCH_2CH_2Ph)_{24}$ clusters was achieved by the exchange of glutathione ligands (GSH) with 2-phenylethylthiol as reported in literature.[5] In short, glutathione-protected gold clusters were obtained via the reduction of $HAuCl_4 \cdot 3H_2O$ with $NaBH_4$ in the presence of the ligand (GSH) at 0°C and with vigorous stirring. After the reaction was finished, the clusters were collected as a precipitate and dissolved in water. The solution was then treated with an excess of PhC_2H_4SH in toluene and a small amount of ethanol, thus enabling ligand exchange. The diphase solution was heated to and maintained at 80°C under air, so that $Au_n(SG)_m$ clusters were transferred from the water phase to the organic phase accompanied by the exchange of the protecting ligands. Monodispersity of the clusters was achieved by an etching process at 80°C, which lasted over 40 h. With this synthetic route a yield of Au_{38} nanoclusters of ~25% (Au atom basis) was reproducibly obtained.

Preparation of $Au_{144}(SCH_2CH_2Ph)_{60}$clusters (3). Au_{144} clusters were prepared following the procedure of H. Qian et al..[6] Briefly, in a two phase reaction of water and toluene $HAuCl_4 \cdot 3H_2O$ and TOAB (tetraoctylammonium bromide) were dissolved under vigorously stirring. After the phase transfer of Au(III) was achieved (indicated by a red color of the toluene phase and a colorless aqueous phase), the aqueous phase was discarded and $PhCH_2CH_2SH$ was added to the cooled (0°C) toluene solution. Afterwards, reduction with $NaBH_4$ was performed. The reaction was allowed to proceed for ~24 hours and the black toluene phase was then dried by rotary evaporation. Ethanol was used to separate the Au nanoparticles from TOAB and other side products.

Monodisperse Au_{144} nanoparticles were obtained by etching the clusters at 80°C in the presence of excess $PhCH_2CH_2SH$ for 24 hours under constant magnetic stirring and the succeeding controlled precipitation with methanol. With this method usually a yield of 20 to 30 % (Au atomic basis) is achieved.

Characterization. For the particles' characterization two main methods were applied UV-vis spectroscopy and MALDI-TOF-MS. UV-vis spectroscopy is sensitive to the metal core and each cluster size studied in this work gives a typical spectrum[6-8], which is depend on change of the charge state, too. On the other hand, mass spectrometry enables an exact analysis of the size distribution of the clusters and the mass of the parent ion is obtained. Hence the chemical formula of the particle can be derived. The all these results are summarized in Figure S1, clearly confirming the monodispersity and purity of the samples. In addition, a more detailed description of the results is given in the sections below.

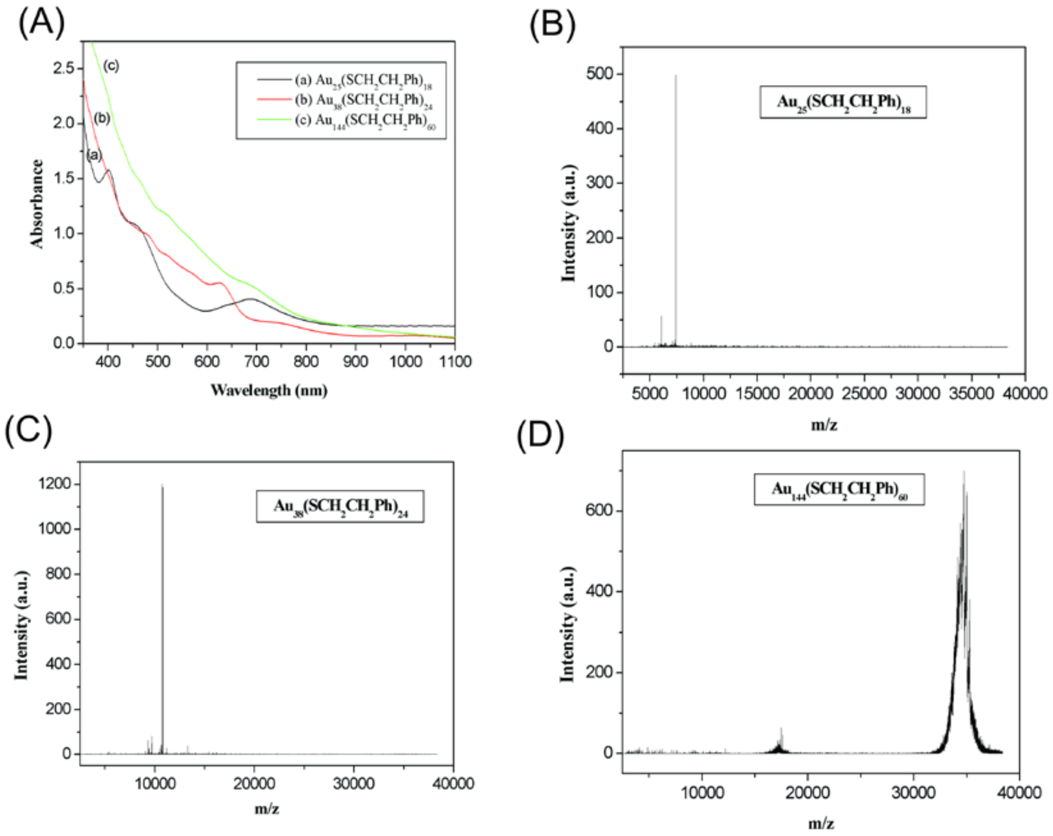

Figure S1. UV-vis spectra of size selected gold clusters as well as MALDI spectra of Au_{25} (B), Au_{38} (C), and Au_{144} (D) clusters. The mass spectra as well as the UV-vis spectra clearly confirm the purity and monodispersity of the samples (for a more detailed discussion see the sections below).

1. UV-vis spectroscopy was used to determine the charge states of the Au_{25} clusters. Neutrally charged $Au_{25}(SCH_2CH_2Ph)_{18}]^0$ nanoclusters show a more pronounced peak at 400 nm (Figure S1A), while $[Au_{25}(SCH_2CH_2Ph)_{18}]^-$ clusters give a more distinct peak at 450 nm. Furthermore, a transition of less intensity at 400 nm and very small shoulder at around 780 nm (see Figure S1) can be observed for negatively charged clusters. Note, that the shoulder does not appear in the neutral form.[3]

UV-vis spectroscopy was further used to characterize the individual samples, since this technique is sensitive to changes of the metal core. The spectrum of each cluster size is in good agreement with previous studies[2,5,6] and is shown in Figure S2.

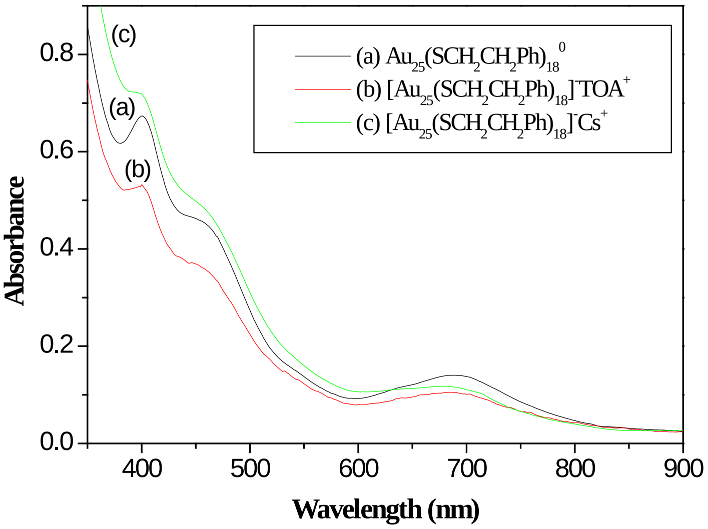

Figure S2. UV-vis spectra of Au_{25} clusters in (a) neutral form $Au_{25}(SCH_2CH_2Ph)_{18}^0$ and in the anionic form $Au_{25}(SCH_2CH_2Ph)_{18}^-$ with (b) TOA^+ and (c) Cs^+ as counterion.

Nanoclusters of $[Au_{25}(SCH_2CH_2Ph)_{18}]^0$ exhibit a more distinct peak at 400 nm (Figure S1A), while clusters of $[Au_{25}(SCH_2CH_2Ph)_{18}]^-$ in the negative charge state show a more pronounced transition at 450 nm and one of less intensity at 400 nm. In addition, a very small shoulder at around 780 nm (Figure S1B and C) is found for negatively charged clusters, which does not appear in the neutral form.[3]

2. MALDI-TOF spectra were used to assess the monodispersity of the clusters. All spectra are in good agreement with spectra published in literature [2,5,6] and confirm the monodispersity of the samples. The mass spectra of all samples are displayed in Figure S1.

The spectrum of Au_{25} clusters (Figure S1B) is dominated by one peak at m/z = 7394 Da, which is due to the parent ion of $Au_{25}(SCH_2CH_2Ph)_{18}$. Another smaller peak at m/z = 6052 Da can be found. This peak is due to fragmentation of the $Au_{25}(SCH_2CH_2Ph)_{18}$ clusters, since its relative intensity strongly depends on the intensity of the desorbing/ionizing laser beam.

For Au_{38} clusters (Figure S1C) a dominant peak at m/z = 10780 Da is found, which is assigned to the parent ion of $Au_{38}(SCH_2CH_2Ph)_{24}$. Additional peaks of very small intensity indicate some fragmentation in the MALDI process.

MALDI spectra of Au_{144} clusters (Figure S1D) give a broad peak at m/z = 35000 amu that clearly confirms the existence of $Au_{144}(SCH_2CH_2Ph)_{60}$. A minor amount of impurities consisting of smaller clusters may be indicated by the feature below 20000 amu.

References

1 A. Dass, A. Stevenson, G. R. Dubay, J. B. Tracy, and R. W. Murray, J. Am. Chem. Soc. 2008, 130, 5940-5946.

2 Z. Wu, J. Suhan and R. Jin, J. Mater. Chem., 2009, 19, 622–626.

3 M. Zhu, W. T. Eckenhoff, T. Pintauer, and R. Jin, J. Phys. Chem. C, 2008, 112, 14221-14224.

4 M. Zhu, G. Chan, H. Qianb and R. Jin, Nanoscale, 2011, 3, 1703-1707.

5 H. Qian, Y. Zhu and R. Jin, Nano, 2009, 3, 3795–3803.

6 H. Qian and R. Jin, Nano Lett., 2009, 9, 4083-4087.

7 (a) M. Zhu, E. Lanni, N. Garg, M. E. Bier, and R. Jin, J. Am. Chem. Soc., 2008, 130, 1138-1139. (b) A. Dass, A. Stevenson, G. R. Dubay, J. B. Tracy, and R. W. Murray, J. Am. Chem. Soc. 2008, 130, 5940-5946.

8 Z. Wu, J. Suhan and R. Jin, J. Mater. Chem., 2009, 19, 622–626.

CHAPTER 4

SUMMARY

4. Summary

The goal of the project was to gain a molecular level understanding of the local interactions between metal surfaces and molecules. Monolayer protected nanoparticles can be viewed as nanometer size analogues of extended hybrid materials. These nanomaterials are interesting, because their physical and chemical properties can easily be tuned for custom requirements by changing their size and their shape. Macro- and nano-hybrid materials have a wide range of potential applications in various fields such as catalysis, sensing, therapy, electronics, nanotechnology and optics.

Nanoparticles emerged as model systems for adsorbed chiral and achiral molecules on metal surfaces; the surface-to-volume ratio increases with decreasing particle size and thus more adsorbate molecules per metal atom can attach onto the cluster. A further advantage is the solubility of the nanoparticles, allowing the use of techniques such as circular dichroism (CD) spectroscopy, UV-vis spectroscopy, photoluminescence spectroscopy (PL), thermogravimetric analysis (TGA), elemental analysis (EA) and Fourier transform infrared spectroscopy (FTIR). These techniques need less effort compared to ultra high vacuum (UHV) techniques.

On the other hand, the reduction of size in a metal structure has strong implications on its properties. According to standard Mie-theory, the propagating surface plasmon resonances of a bulk metal shift into the visible when the particle size is decreased. Ultrasmall nanoparticles less than 2 nm in diameter (corresponding to ca 200 gold atoms) are commonly termed ‘clusters’ and their properties have been investigated in the gas phase and on supports.

Ligand-stabilized metal clusters have gained interest since they can be studied in solution and their preparation is based on classic ‘wet chemistry’, e.g. reduction of a metal salt in the presence of the protecting ligand. The adsorption of ligands on the surface of the clusters increases their stability due to the prevention of aggregation and allows for the introduction of functionalities by the manipulation of the ligand layer. In the case of gold, thiolates have been found to form stable clusters and the preparation is easily performed. The same is found for silver-thiolate clusters. They are stable in refrigerated conditions and as a solid phase in air, but some of them show less stability in air in the solution phase.

In this work gold and silver metals were chosen, because of their potential applicability in several fields, such as asymmetric catalysis, sensing, medicine, drug or DNA delivery, optics, photonics and nanotechnology. Usually, such particles are in the size range of 10 nm or larger. Due to the lack of data and the predictively interesting properties of smaller clusters, the focus of this work is in the investigation of clusters with sizes smaller than 2 nm.

It is expected that by decreasing the particle sizes, chemical reactivity and most of the physical properties will be change and modified.

In this thesis, we succeeded in preparing and characterizing some monolayer protected silver and gold nanoclusters (MPCs). Two types of ligands were used to protect these clusters. While for the first type the clusters were protected by achiral ligands like 2-phenylethanethiol (2-PET) and 4-fluorothiophenol (4-FTP), clusters of the second type were capped with chiral ligands like L-glutathione (L-GSH), and N-acetyl-L-cysteine (NALC). A strong reducing agent ($NaBH_4$) was used to transform the metal cation (M^{+1}) to neutral metal (M^0). Then, the clusters were separated from the mother liquor and purified by re-dissolving and re-precipitating the sample several times to remove any unreacted materials (metal salt and reducing salt). After the preparation and the purification of these clusters, their optical properties were studied by UV-vis spectroscopy. To confirm the presence of ligands in MPCs and to study the type of binding between metal and ligand, Fourier transform infrared spectroscopy (FTIR) was used. The chirality of clusters protected by chiral ligands was measured by circular dichroism (CD) spectroscopy to obtain the ellipticity – a value for the chirality – of the samples. Furthermore, the chemical composition and the ratio between metal and organic parts of gold and silver nanoclusters (AuNCs and AgNCs) were assessed by thermogravimetric analysis (TGA), elemental analysis (EA) and atomic absorption spectroscopy (AAS). To determine the particle size of these clusters, transmission electron microscopy (TEM) and and powder X-ray diffraction (XRD) were used.

Firstly, we prepared some silver nanoclusters protected by 2-phenylethanethiol and 4-fluorothiophenol achiral ligands. The synthesis was performed by reduction of the corresponding metal salt with $NaBH_4$. The metal salt of silver used was silver nitrate, $AgNO_3$. The optical properties of the prepared silver nanoclusters were studied by UV-vis spectroscopy. The absorption signal of $Ag@SCH_2CH_2Ph$ in toluene can be found at 469 nm, and Ag@SPhF in THF shows two absorption bands at 395 and 462 nm. For comparison between experimental and calculated UV-vis spectra Mie theory was used in combination with the Drude model, which clearly indicates that the peaks in the spectra originate from plasmonic transitions. In addition, the damping constant as well as the dielectric constant of the surrounding medium was determined. The morphology and size of the prepared silver nanoclusters were analyzed by transmission electron microscopy (TEM). TEM analysis of the two types of silver clusters showed size distribution of the particles from 1 nm to 5 nm, with an average size of around 2 nm. The average diameter of the MPCs represents the Feret’s diameter and was determined by assuming a spherical shape. The analysis of the FTIR spectra elucidated the structural properties of the ligands binding to the nanoclusters. By comparing the IR absorption spectra of pure ligands with those of the protected silver nanoclusters, the disappearance of the S−H vibrational band (2535−2564 cm^{-1}) in the protected silver nanoclusters confirmed the anchoring of ligands to the cluster surface through the sulfur atom. By elemental analysis, atomic absorption spectroscopy (AAS) and thermogravimetric analysis (TGA) the Ag/S ratio was determined and confirmed the presence of the original chemical formula of the ligands surround the clusters.

We also succeeded in preparing some silver nanoclusters protected by chiral ligands like L-glutathione (L-GSH), and N-acetyl-L-cysteine (NALC). Two different sizes of silver clusters protected by L-glutathione ligand were prepared by two different methods. The first silver clusters ($Ag_n(SG)_m$) have an average size of nearly 2 nm and the size of the second is about 1 nm, this sample may consist of monodisperse silver clusters. The transmission electron microscopy (TEM) analysis of the silver clusters protected by N-acetyl-L-cysteine ($Ag_n(NALC)_m$) showed a size distribution of the particles from 1 nm to 3.5 nm, with an average size of around 2.37 nm. The ellipticity of the clusters was obtained by circular dichroism (CD) spectroscopy, showing that the chirality of the ligands is transferred to the metal core either in its structure or at least in the electronic states via perturbation of the electronic field of the ligands. $Ag_n(SG)_m$ nanoclusters show two peaks at 386 and 456 nm, which originate from metal-based transitions. However, $Ag_n(NALC)_m$ nanoclusters of 2 nm show only one peak at 226 nm, which might be interpreted as the blue shift of an optical transition of the N-acetyl-L-cysteine ligand. The optical properties of silver nanoclusters in water were studied by UV−vis spectroscopy. The absorption signals of the clusters show characteristic bands, which can be assigned to plasmonic transitions of the metal core. The 2 nm silver clusters protected by L-glutathione Ag@SG, and N-acetyl-L-cysteine $Ag_n(NALC)_m$ exhibit one surface plasmonic peak at 478 and 480 nm, respectively. However, the small silver clusters (1 nm) protected by L-glutathione $Ag_n(SG)_m$ show two plasmonic peaks at 478 nm and 641 nm. The average molecular formula of the nanoclusters was determined by thermogravimetric analysis (TGA). $Ag_{3n}L_{2n}$ and $Ag_{5n}L_n$ are the average molecular formulas of the $Ag_n(SG)_m$ and $Ag_n(NALC)_m$ clusters, respectively. Powder X-ray diffraction (XRD) was used to compare the structures of the two silver nanoclusters and bulk silver metal. The X-ray diffractogram of $Ag_n(SG)_m$ powder shows a broad and intense feature at $2\theta = 37.6 \pm 0.7°$ and for $Ag_n(NALC)_m$ nanoclusters shows significantly less broad diffraction peaks at 38.2 ± 0.3° and 65°. By comparison the diffraction pattern of bulk Ag metal, with a face-centered cubic (fcc) lattice shows (111), (200), (220), and (311) reflections. Bulk silver metal shows sharp diffraction patterns since the planes of its face centered cubic (fcc) crystal lattice are separated by defined and large interplane spacing (d). However in the case of 2 nm silver clusters ($Ag_n(NALC)_m$) broad peaks at the same angles are found. This indicates that these particles exhibit a fcc-like structure, too. The broadening of the diffraction peaks increase as a function of a decrease of the particle size, as can be seen for e.g. $Ag_n(SG)_m$ (1 nm). This is attributed to the fact that the average interplane spacing becomes smaller corresponding to the atomic distances in the small core, which may be icosahedra (Ag_{13}). We studied the fluorescent properties of the silver nanoclusters by photoluminescence (PL) spectroscopy. The photoemission spectra of $Ag_n(SG)_m$ and $Ag_n(NALC)_m$ nanoclusters show one broad maximum at 660 nm and 611 nm after excitation with wavelengths of 478 and 480 nm, respectively.

UV−vis spectroscopy is sensitive to changes of the metal core, such as the oxidation state and the number of metal atoms in the cluster. Therefore, it is commonly used for the investigation of the stability of clusters. The silver nanoclusters are stable in a refrigerated state in powder and solution form and are sealed to avoid exposure to air. However, when the silver clusters are exposed to air, the stability changes. Silver clusters protected by L-glutathione (L-GSH) and 4-fluorothiophenol (4-FTP) undergo rather fast transformation, which results in the decrease of the absorbance peaks in aqueous solution. However, we succeeded in preparing two types of silver clusters that are particularly stable even when exposed to air. These clusters were protected by 2-phenylethanethiol (2-PET) and N-acetyl-L-cysteine (NALC) and no change in the intensity of the absorption peaks of the UV−vis spectra was observed at all, even after 24 h of exposure to air.

Secondly, we used a methanol-induced precipitation method to prepare and isolate fractions of different sized gold clusters protected by L-glutathione (L-GSH) and N-acetyl-L-cysteine (NALC) chiral ligands. The synthesis was performed by the reduction of the corresponding metal salt of gold (tetrachloroauric (III) acid ($HAuCl_4 \cdot 3H_2O$)) with $NaBH_4$.

By controlling the amount of methanol added and the speed and time of centrifugation, different sizes of clusters were separated and isolated. In the case of gold clusters protected by L-glutathione, three fractions were obtained with particle sizes of 2.5 nm, 2 nm and $Au_{25}(SG)_{18}$. However, the case of the $Au_n(NALC)_m$ clusters only two fractions were separated consisting of clusters of 3 nm and $Au_{25}(NALC)_{18}$ clusters. The UV-vis absorption spectra of Au_{25} clusters show multi-band absorption peaks at around 400 nm, 450 nm and 670 nm. These absorption bands indeed resemble a spectroscopic fingerprint for an Au_{25} core. The first fraction of gold clusters protected by L-glutathione (L-GSH) and N-acetyl-L-cysteine

(NALC) ligands show a well-defined surface plasmon absorption band at 534 nm. The second fraction of $Au_n(SG)_m$ clusters gives a featureless band without a distinct surface plasmon absorption peak. The average molecular formulas of each fraction of gold nanoclusters were determined by thermogravimetric analysis (TGA). Powder X-ray diffraction (XRD) was used to measure the particle size of the gold nanocluster fractions and to compare their structures with bulk gold metal. The fractions of gold clusters protected by N-acetyl-L-cysteine and L-glutathione again show different peaks in their excitation spectra. In general, larger clusters give intense peaks in the near UV, while smaller clusters show additional transitions in or close to the visible region. When exciting gold clusters protected by either NALC or L-GSH with 450 nm, their PL-emission spectrum is obtained. While the larger clusters (about 3 nm) of fraction 1 give an emission peak at 554 nm and $Au_{25}(SG)_{18}$ and $Au_{25}(NALC)_{18}$ clusters show a broad PL-feature at a maximum of 738 nm. We studied the chirality properties of all fractions of protected gold clusters by circular dichroism spectroscopy. The CD spectra of fraction 1 Au nanoclusters show only very weak signals at 214 nm, while fraction 2 gold clusters protected by L-GSH exhibit strong CD-signals in the near UV and vis regions. The CD spectra of $Au_{25}(SG)_{18}$ and $Au_{25}(NALC)_{18}$ nanoclusters are governed by several peaks.

Finally, we used 2-phenylethanethiol (2-PET) ligand to prepare some size selected monolayer protected gold clusters. Using this method $Au_{25}(SCH_2CH_2Ph)_{18,}$ $Au_{38}(SCH_2CH_2Ph)_{24}$ and $Au_{144}(SCH_2CH_2Ph)_{60}$ clusters were successfully produced with very high purity. The purity of these clusters was assessed by matrix-assisted laser desorption/ionization time-of- flight mass spectrometry (MALDI-TOF). The spectra are dominated by one peak at m/z = 7394 Da, 10780 Da and 35000 Da, which is due to the parent ion of $Au_{25}(SCH_2CH_2Ph)_{18}$, $Au_{38}(SCH_2CH_2Ph)_{24}$ and $Au_{144}(SCH_2CH_2Ph)_{60}$ clusters, respectively. Also, for the $Au_{25}(SCH_2CH_2Ph)_{18}$ clusters the exact number of the metal atoms in the core was determined unambiguously by single crystal x-ray crystallography by other groups. The UV-vis absorption spectra of $Au_{25}(SCH_2CH_2Ph)_{18}$ clusters exhibits three characteristic peaks at 400, 450 and 670 nm. $Au_{38}(SCH_2CH_2Ph)_{24}$ clusters give a spectrum with a series of characteristic transistions at 490, 520, 620, 750 and 1050 nm. For $Au_{144}(SCH_2CH_2Ph)_{60}$ clusters a spectrum with only two characteristic peaks at 510 and 700 nm is obtained. The charged form of $Au_{25}(SCH_2CH_2Ph)_{18}$ clusters are converted to neutral ones via oxidation by air or H_2O_2 (~30% aqueous). Also, the negatively charged Au_{25} clusters were prepared from the neutral form with different counterions, i.e. tetraoctylammonium (TOA^+) and Cs^+. Through the study of these size selected gold clusters with infrared spectroscopy an interesting phenomena specific for Au_{25} was found. $Au_{25}(SCH_2CH_2Ph)_{18}$ clusters show a distinct shift of the aromatic C-H stretching band from 3030-3100 cm^{-1} to below 3000 cm^{-1}, whose origin is discussed as an electronic interaction of the aromatic rings of the ligands with each other or with the gold core. The spectra of $Au_{38}(SCH_2CH_2Ph)_{24}$ and $Au_{144}(SCH_2CH_2Ph)_{60}$ clusters do not show this distinct shift and their IR-spectra in the C-H stretching regime are similar to that of the bare ligand. This significant change in the IR spectrum of $Au_{25}(SCH_2CH_2Ph)_{18}$ is not only of fundamental interest but also allows for determining *in-situ* the purity and monodispersity of the sample by FTIR spectroscopy during synthesis.

Outlook

Metal nanoclusters are very interesting materials for chemistry, physics and material science, because these clusters are an important intermediate size regime between atoms and bulk materials.

Many researchers in the last decade succeeded to prepare and isolate multiple sizes of gold clusters. In this work several silver clusters protected by different ligands, as well as gold clusters were prepared. The preparation methods of silver clusters are easier, cheaper and give higher yield than gold clusters. The stability of silver clusters in air is not as high as the one of gold clusters. However, we succeeded to prepare several stable silver clusters in air.

The following text contains some hints and several suggestions for further investigations and applications of metal monolayer protected clusters. The ideas are based on the results that were obtained within the work of this thesis and represent possible further characterization steps.

Firstly, studying the catalytic and photocatalytic activity properties of monolayer protected gold and silver nanoclusters for the synthesis of fine chemicals and perhaps as a new source of energy. There are many possible reactions that these clusters can activate, like hydrogenation or epoxidation of unsaturated olefins or unsaturated aldehydes and ketones. These clusters can catalyse these reactions in the form of a suspension in different solvents or over different supports like TiO2, Al2O3, SiO2, etc. The activity and selectivity of these very small clusters is expected to be very high. The chiral silver and gold nanoclusters have a very large potential in approaches to enantioselective catalysis reactions.

The use of chiral high performance liquid chromatography (HPLC) to enantioseparate of racemic mixtures of many size selected gold clusters protected by achiral ligands like Au25, Au55, Au102, Au144 clusters and etc., as previously employed in the case of Au38(SCH2CH2Ph)24 clusters.71 HPLC can be performed in order to test whether intrinsic chirality is an ubiquitous feature of thiolate-protected gold clusters and reveal their chiroptical properties.

The synthesis, isolation and precise determination of the composition of silver nanoclusters are still big challenges. The crystal structures of monolayer protected silver nanoclusters are still unknown, so more effort is needed to isolate single crystals of silver clusters.

The only disadvantage of silver clusters is that some of them show less stability in air. To improve the stability of these clusters the methods of encapsulation of the clusters by thin water-soluble polymer films is used.

Preparation and characterization of new metal clusters like copper, which is in the same group as silver and gold in the periodic table. We expect copper clusters will show optical and chirooptical properties similar to gold and silver clusters.

In addition, there are several major issues that remain unclear, and require much effort to understand. Issues such as what the source of the optical chirality properties of metal (Au, Ag, ets.) nanoclusters protected by chiral ligands are? What is the origin of the fluorescence properties of gold and silver nanoclusters? And the attempt to find suitable ion sources with defined matrix and laser source intensity (i.e. MALDI, ESI, etc.) connected with a mass spectrometer to measure and determine the precise molecular weight of gold and silver nanoclusters protected by water soluble ligands.

List of Abbreviations

AAS	Atomic absorption spectroscopy
APS	Ammonium persulfate
BBSH	4-(Tert-butyl)benzyl mercaptan
BSA	Bovine serum albumin
Capt	Captopril
CRDS	Cavity ring-down spectrometer
CsOAc	Cesium acetate
3D	Third dimension
CD	Circular dichroism
DFT	Density functional theory
DMSA	2,3-dimercaptosuccinic acid
DNA	Deoxyribonucleic acid
DCTB	Trans-2-[3-(4-tert-butylphenyl)-2-methyl-2-propenylidene]malononitrile
EA	Elemental analysis
ESI	ElectroSpray Ionization
Fcc	Face-centered cubic
FA	Folic acid
4-FTP	4-Fluorothiophenol
FTIR	Fourier transform infrared spectroscopy
GC-MS	Gas chromatography–mass spectrometry
HPLC	High performance liquid chromatography
HABA	4′-Hydroxyazobenzene-2-carboxylic acid

HOMO	Highest occupied molecular orbital
LDI	laser desorption ionization
L-GSH	L-glutathione
LUMO	Lowest unoccupied molecular orbital,
MALDI	Matrix-assisted laser-desorption/ionisation
MD	Marks decahedron
MPCs	Monolayer protected nanoclusters
NALC	N-acetyl-L-cysteine
Nd:YAG	Nd-doped yttrium aluminum garnet
NIR	Near-infrared
NPs	Nanoparticles
NCs	Nanoclusters
NMR	Nuclear magnetic resonance
PAGE	Polyacrylamide gel electrophoresis
p-MBA	p-Mercaptobenzoic acid
MPTS	3-(Mercaptopropyl)trimethoxysilane
2-PET	2-Phenylethylthiol
PL	Photoluminescence spectroscopy
QY	Quantum yield
QCs	Quantum clusters
SA	Sinapinic acid
SAMs	Self-assembled monolayers
SEC	Size exclusion chromatography

SP	Surface plasmon
STM	Scanning tunneling microscopy
TEM	Transmission electron microscopy
TOF-MS	Time of flight-mass spectrometer
THF	Tetrahydrofuran
TEMED	N,N,N',N' tetramethylethylenediamine
TOAB	Tetraoctylammonium Bromide
TGA	Thermogravimetric analysis
UV-vis	Ultraviolet-visible
UHV	Ultra-high vacuum
UMM	1:1 mixture of dihydroxybenzoic acid and R-cyano-4-hydroxycinnamic acid
XRD	X-ray diffraction

Acknowledgments

I would like to address my special thanks to Prof. Dr. Ulrich Heiz for giving me the chance to join his group and to work in a fascinating field of research. In addition, he is always willing to help patiently his students with their research.

I am deeply indebted to Dr. Martin Tschurl for his endless support and advice and all the friendly discussions and revisions of my papers and my Ph.D. thesis.

Special thanks to the DAAD and the Egyptian missions (German Egyptian Research Long Term Scholarship- GERLS), which have supported me during the four years to get my Ph.D. degree.

A fundamental contribution to the success of this project has been made by Prof. Dr. Thomas Bürgi for helpful discussions (university of Geneva) and by Prof. Dr. Amal Dass for MALDI-MS measurements (university of Mississippi).

Thanks to PD. Dr. Friedrich Esch for his friendly communications. He was the first one to teach me clusters science throght the “physical chemistry of nanoparticles and surface” course. My thanks also to Prof. Dr. Ulrich Boesl-von Grafenstein for his efforts to extend my DAAD scholarship yearly.

I would like to thank my colleague and friends Dr. Martin Thämer and Josef Kiermaier for their honest friendship.

I kindly acknowledge the groups of Prof. Dr. Buchner, Prof. Dr. Rieger, Prof. Dr. Gasteiger and Prof. Dr. Fässler as well as Dr. Marianne Hanzlik for using their equipments CD, FTIR, TGA, XRD and TEM, respectively. I also thank the TUM graduate school for their encouragement.

I would like to thank all the group members for the good atmosphere and all the support in major and minor issues.

Last but not least, I would like to thank my parents, my wife, my brothers, my sister and my kids for all the support over all the years, in all possible respect. This work is dedicated to them.

References

1. K-H. Meiwes-Broer, Metal Clusters at Surfaces, Structure, Quantum Properties, Physical Chemistry, Springer-Verlag Berlin Heidelberg, **2000**.
2. W. D. Knight, K. Clemenger, W. A. de Heer, W. A. Saunders, M. Y. Chou and M. L. Cohen, Phys. Rev. Lett. **1984**, 52, 2141.
3. W. D. Knight, K. Clemenger, W. A. de Heer, and W. A. Saunders, Phys. Rev. B, **1985**, 31, 2539.
4. W. D. Knight, W. A. de Heer, K. Clemenger and W. A. Saunders, Solid State Commun. **1985**, 53, 445
5. M. Kappes, R.W. Kunz, E. Schumacher Chem. Phys. Lett., **1982**, 91, 413–418.
6. A. W. Castleman, Jr. and S. N. Khanna, J. Phys. Chem. C, **2009**, 113, 2664–2675.
7. (a) D. Mendeleeff, The Principle of Chemistry, 3rd Ed. Longmans, Green and Co., London, **1905** (b) T.E. Thorpe, Scientific worthies XXVI. Dimitri Wanowitch Mendeleeff. Nature XL, **1889**,193–197.
8. S. A. Claridge, A. W. Castleman, Jr., S. N. Khanna, C. B. Murray, A. Sen and P. S. Weiss, Nano, **2009**, 3, 244–255.
9. P. Jena, S. N. Khanna and B. K. Rao, Eds.; Clusters and Nano-Assemblies; World Scientific: NJ, **2003**.
10. (a) V. Habibpour, Z. W. Wang, R. E. Palmer and U. Heiz, J. Appl. Sci. **2011**, 11, 1164. (b) S. Kunz, F. F. Schweinberger, V. Habibpour, M. Rottgen, C. Harding, M. Arenz and U. Heiz, J. Phys. Chem. C, **2010**, 114, 1651.
11. A. Kartouzian, M.Thaemer and U. Heiz, Phys. Status Solidi B, **2010**, 247, 1147.
12. M. Walter, J. Akola, O. Lopez-Acevedo, P. D. Jadzinsky, G. Calero, C. J. Ackerson, R. L. Whetten, H. Grönbeck and Hannu Häkkinen, PNAS, **2008**, 105, 9157–9162.
13. W. A. de Heer, Rev. Mod. Phys., **1993**, 65, 611.

14. S. N. Khanna and P. Jena, Phys. Rev. Lett., **1992**, 69, 1664.

15. W. A. de Heer, W. D. Knight, M. Y. Chou, M. L. Cohen, Solid State Physics, **1987**, 40, 93.

16. (a) N. D. Lang, Solid State Commun., **1969**, 7, 1047–1050. (b) N. D. Lang and W. Kohn, Phys. Rev. B, **1970**, 3, 1215–223.

17. (a) W. Ekardt, Phys. Rev. B, **1984**, 29, 1558–1564. (b) K. Clemenger, Phys. Rev. B, **1985**, 32, 1359–3162.

18. R. E. Leuchtner, A. C. Harms, A. W. Castleman, Jr., J. Chem. Phys. **1989**, 91, 2753.

19. M. Brust, M. Walker, D. Bethell, D. J. Schiffrin and R. J. Whyman, Chem. Soc., Chem. Commun., **1994**, 801.

20. M. Farrag, M. Thämer, M. Tschurl, T. Bürgi and U. Heiz, J. Phys. Chem. C, **2012**, 116, 8034−8043.

21. M. Farrag, M. Tschurl, and U. Heiz, Chem. Mater., **2013**, 25, 862-870.

22. M. Farrag, M. Tschurl, A. Dass and U. Heiz, Phys. Chem. Chem. Phys., **2013** (on line).

23. (a) G. Schmid, Chem. Rev. **1992**, 92, 1709. (b) W. W. Weare, S. M. Reed, M. G.Warner and J. E. Hutchison, J. Am. Chem. Soc., **2000**, 122, 12890.

24. (a) S. Gomez, K. Philippot, V. Colliere, B. Chaudret, F. Senocq and P. Lecante, Chem. Commun., **2000**, 1945. (b) A. Kumar, S. Mandal, P. R. Selvakannan, R. Pasricha, A. B. Mandale and M. Sastry, Langmuir, **2003**, 19, 6277.

25. R. Jin, Nanoscale, **2010**, 2, 343-362.

26. R. B. Wyrwas, M. M. Alvarez, J. T. Khoury, R. C. Price, T. G. Schaaff and R. L.Whetten, Eur. Phys. J. D, **2007**, 43, 91.

27. C. M. Aikens, J. Phys. Chem. C, **2008**, 112, 19797-19800.

28. (a) R. L.Whetten, J. T. Khoury, M. M. Alvarez, S. Murthy, I. Vezmar, Z. L.Wang, P. W. Stephens, C. L. Cleveland, W. D. Luedtke and U. Landman, Adv. Mater., **1996**, 8, 428. (b) A. C.Templeton, W. P. Wuelfing and R. W. Murray, Acc. Chem. Res., **2000**, 33, 27.

29. M. C. Daniel and D. Astruc, Chem. Rev., **2004**, 104, 293.

30. U. Kreibig and M. Vollmer, Optical Properties of Metal Clusters, Springer-Verlag: New York, **1995**.
31. S. Eustis and M. A. El-Sayed, Chem. Soc. Rev., **2006**, 35, 209–217.
32. (a) G. Mie, Ann. Phys. **1908**, 25, 377-445. (b) R. v. Gans, Ann. Phys. **1912**, 37, 881-900. (c) R. v. Gans, Ann. Phys. **1915**, 47, 270-284. (d) E. Hao, G. Schatz and J. Hupp, J. Fluoresc., **2004**, 14, 331. (e) K. L. Kelly, E. Coronado, L. L. Zhao and G. C. Schatz, J. Phys. Chem. B, **2003**, 107, 668–677.
33. C. M. Aikens, S. Li, and G. C. Schatz, J. Phys. Chem. C, **2008**, 112, 11272–11279.
34. (a) T. H. Lee and R. M. Dickson, Proc. Natl. Acad. Sci. U.S.A., **2003**, 100, 3043. (b) J. Zheng, P. R. Nicovich and R. M. Dickson, Annu. ReV. Phys. Chem., **2007**, 58, 409. (c) S. Fedrigo, W. Harbich and Buttet, J. Phys. Rev. B, **1993**, 47, 10706.
35. N. Cathcart, P. Mistry, C. Makra, B. Pietrobon, N. Coombs, M. Jelokhani-Niaraki and V. Kitaev, Langmuir, **2009**, 25,5840–5846.
36. K. Hartl, M. Nesselberger, K. J.J. Mayrhofer, S. Kunz, F. F. Schweinberger, G. Kwon, M. Hanzlik, U. Heiz and M. Arenz, Electrochimica Acta, **2010**, 56, 810–816.
37. (a) B. E. Warren, X-ray Diffraction; Constable and Company: U.K., **1990**; Chapter 13. (b) A. R. West, Solid State Chemistry and Its Applications; Wiley: New York, **1984**.
38. Z. Wu, J. Chen and R. Jin, Adv. Funct. Mater. **2011**, 21, 177–183.
39. Y. Negishi, R. Arai, Y. Niihoria and T. Tsukuda, Chem. Commun., **2011**, 47, 5693–5695.
40. M. R. Branham, A. D. Douglas, A. J. Mills, J. B. Tracy, P. S. White and R. W. Murray, Langmuir, **2006**, 22, 11376-11383.
41. (a) J. Lyklema, Fundamentals of Interface and Colloid Science, **1995**, 2. (b) D. S. Kryndushkin, I. M. Alexandrov, M.D. Ter-Avanesyan, V.V. Kushnirov, Journal of Biological Chemistry, **2003**, 278, 49636–43
42. D. A. H. Hanaor, M. Michelazzi, C. Leonelli, C.C. Sorrell, Journal of the European Ceramic Society **2012**, 32, 235–244.
43. F. Carrique, F. J. Arroyo and A. V. Delgado, Journal of Colloid and Interface Science,

2002, 252, 126–137.

44. D. L. Smisek, D. A. Hoagland, Macromolecules, **1989**, 22, 2270.
45. Y. Negishi, K. Nobusada and T. Tsukuda, J. Am. Chem. Soc., **2005**, 127, 5261-5270.
46. S. Kumar, M. D. Bolan and T. P. Bigioni, J. Am. Chem. Soc., **2010**, 132, 13141–13143.
47. C. Gautier and T. Bürgi, J. Am. Chem. Soc., **2006**, 128, 11079-11087.
48. S. Knoppe, J. Boudon, I. Dolamic, A. Dass and T. Bürgi, Anal. Chem., **2011**, 83, 5056–5061.
49. (a) T. Siebrands, M. Giersig, P. Mulvaney and C.-H. Fischer, Langmuir, **1993**, 9, 2297–2300. (b) J. P. Wilcoxon, J. E. Martin and P. Provencio, Langmuir, **2000**, 16, 9912–9920.
50. (a) H. Tsunoyama, Y. Negishi and T.Tsukuda, J. Am. Chem. Soc., **2006**, 128, 6036–6037. (b) S. Frein, J. Boudon, M. Vonlanthen, T. Scharf, J. Barber, G. Süss-Fink, T. Bürgi and R. Dechenaux, Helv. Chim. Acta, **2008**, 91, 2321–2337.
51. (a) C. Barner-Kowollik, T. Gründling, J. Falkenhagen and S. Weidner, Mass Spectrometry in Polymer Chemistry, Wiley-VCH Verlag & Co. KGaA, Boschstr. 12, 69469 Weinheim, Germany, **2012**. (b) I. Lavagnini, F. Magno, R. Seaglia and P. Traldi, Quantitative Applications of Mass Spectrometry, John Wiley & Sons Ltd, The Atrium, Southern Gate, Chichester, West Sussex PO19 8SQ, England, **2006**.
52. J. B. Fenn, M. Mann, C. K. Meng, S. F. Wong and C. M. Whitehouse, Science, **1989**, 246, 64.
53. S. A. Hofstadler and K. A. Sannes-Lowery, Nat. ReV. Drug DiscoVery, **2006**, 5, 585.
54. A. Dass, A. Stevenson, G. R. Dubay, J. B. Tracy and R. W. Murray, J. Am. Chem. Soc., **2008**, 130, 5940–5946.
55. R. Knochenmuss, Analyst, **2006**, 131, 966–986.
56. H. Qian and R. Jin, Nano Lett., **2009**, 9, 4083-4087.
57. Z. Wu, E. Lanni, W. Chen, M. E. Bier, D. Ly and R. Jin, J. Am. Chem. Soc., **2009**,131, 9.
58. J. Zheng, P. R. Nicovich, R. M. Dickson, Annu. Rev. Phys. Chem., **2007**, 58, 409.
59. (a) C. F. McFadden, P. S. Cremer and A. J. Gellman, Langmuir., **1996**, 12, 2483.

(b) M. O. Lorenzo, S. Haq, T. Bertrams, P. Murray, R. Raval, C. J. Baddeley, J. Phys. Chem. B, **1999**, 103, 10661.

60. J. D. Horvath and A. J. Gellman, J. Am. Chem. Soc. **2001**, 123, 7953.
61. G. A. Attard, J. Phys. Chem. B, **2001**, 105, 3158.
62. S. M. Barlow and R. Raval, Surf Sci, **2005**, 590, 243.
63. T. G. Schaaff, G. Knight, M. N. Shafigullin, R. F. Borkman and R. L. Whetten, J. Phys. Chem. B, **1998**, 102, 10643.
64. I. L. Garzón, J. A. Reyes-Nava, J. I. Rodríguez-Hernández, I. Sigal, M. R. Beltrán and K. Michaelian, Physical Review B, **2002**, 66, 073403.
65. I. L. Garzón, M. R. Beltrán, G. González, I. Gutíerrez-González, K. Michaelian, J. A. Reyes-Nava and J. I. Rodríguez-Hernández, Eur. Phys. J. D, **2003**, 24, 105.
66. M. R. Goldsmith, C. B. George, G. Zuber, R. Naaman, D. H. Waldeck, P. Wipf and D. N. Beratan, Phys. Chem. Chem. Phys., **2006**, 8, 63.
67. P. D. Jadzinsky, G. Calero, C. J. Ackerson, D. A. Bushnell and R. D. Kornberg, Science, **2007**, 318, 430.
68. H. Qian, W. T. Eckenhoff, Y. Zhu, T. Pintauer and R. Jin, J. Am. Chem. Soc., **2010**, 132, 8280.
69. H. Häkkinen, Nature chemistry, **2012**, 4, 443.
70. M. W. Heaven, A. Dass, P. S. White, K. M. Holt and R. W. Murray, J. Am. Chem. Soc., **2008**, 130, 3754.
71. (a) I. Dolamic, S. Knoppe, A. Dass and T. Bürgi, Nat. Commun., **2012**, 3, 798 (b) S. Knoppe, I. Dolamic, A. Dass and T. Bürgi, Angew. Chem. Int. Ed., **2012**, 51, 7589 –7591.
72. E. S. Shibu, M. A. Habeeb Muhammed, T. Tsukuda and T. Pradeep, J. Phys. Chem. C, **2008**, 112, 12168.
73. C. Chung and M. Lee, J. Electroanal. Chem., **1999**, 468, 91.
74. M. J. Hostetler, J. J. Stokes and R. W. Murray, Langmuir, **1996**, 12, 3604.
75. A. Retnakumari, S. Setua, D. Menon, P. Ravindran, H. Muhammed, T. Pradeep, S. Nair

and M. Koyakutty, Nanotechnology, **2010**, 21, 055103.

76. A. Mantion, G. Guex, A. Foelske, L. Mirolo, K. M. Fromm, M. Painsid and A. Taubert, Soft Matter, **2008**, 4, 606–617.
77. W. K. Surewicz, H. H. Mantsch and D. Chapman, Biochemistry, **1993**, 32 389–394.
78. S. Mohapatra et. al. Nanotechnology, **2007,** 18, 385102.
79. (a) T. P.Bigioni, R. L. Whetten and O. Dag, J. Phys. Chem. B, **2000**, 104, 6983. (b) Y. Negishi, Y. Takasugi, S. Sato, H. Yao, K. Kimura, T. Tsukuda, J. Am. Chem. Soc., **2004**, 126, 6518. (c) T. Huang and R. W. Murray, J. Phys. Chem. B, **2001**, 105, 12498. (d) L. A. Peyser, A. E. Vinson, A. P. Bartko, R. M. Dickson, Science, **2001**, 29, 103.
80. Z. Wu and R. Jin, Nano Lett., **2010**, 10, 2568–2573.
81. C. Zhou, C. Sun, M. Yu, Y. Qin, J. Wang, M. Kim, and J. Zheng, J. Phys. Chem. C, **2010**, 114, 7727–7732.
82. S. Link, A. Beeby, S. FitzGerald, M. A. El-Sayed, T. G. Schaaff, R. L. Whetten, J. Phys. Chem. B, **2002**, 106, 3410. (b) C. A. J. Lin, T. Y.Yang, C. H. Lee, S. H. Huang, R. A. Sperling, M. Zanella, J. K. Li, J. L. Shen, H. H.Wang, H. I.Yeh, W. J. Parak, W. H. Chang, ACS Nano, **2009**, 3, 395. (c) R. J. Zhou, M. M. Shi, X. Q. Chen, M.Wang, H. Z. Chen, Chem., Eur. J., **2009**, 15, 4944. (d) J. Zheng, C. Zhang, R. M. Dickson, Phys. Rev. Lett., **2004**, 93,077402. (e) J. Zheng, J. Petty, R. M. Dickson, J. Am. Chem. Soc., **2003**, 125, 7780. (f) J. Zheng, P. R. Nicovich, R. M. Dickson, Annu. Rev. Phys. Chem., **2007**, 58, 409.
83. R. J. Magyar, V. Mujica, M. Marquez, C. Gonzalez, Phys. Rev. B, **2007**, 75.68.
84. V. W. W.Yam, E. C. C. Cheng and K. K. Cheung, Angew. Chem., Int. Ed., **1999**, 38, 197.
85. H. Xiao, Y. X. Weng, W. T. Wong, T. C. W. Mak and C. M. Che, J. Chem. Soc., Dalton Trans., **1997**, 221.
86. R. L. White-Morris, M. M. Olmstead, F. L. Jiang, D. S. Tinti and A. L. Balch, J. Am. Chem. Soc., **2002**, 124, 2327.
87. G. Wang, R. Guo, G. Kalyuzhny, J.-P. Choi and R. W. Murray, J. Phys. Chem. B, **2006**,

110, 20282-20289.

88. T. Iwasa and K. Nobusada, J. Phys. Chem. C, **2007**, 111, 45-49. (b) K. Ikeda, Y. Kobayashi, Y. Negishi, M. Seto, T. Iwasa, K. Nobusada, T. Tsukuda and N. Kojima, J. Am. Chem. Soc., **2007**, 129, 7230-7231.
89. Y. Shichibu, Y. Negishi, T. Watanabe, N. K. Chaki, H. Kawaguchi and T. Tsukuda, J. Phys.Chem. C, **2007**, 111, 7845-7847.
90. M. W. Heaven, A. Dass, P. S. White, K. M. Holt and R. W. Murray J. Am. Chem. Soc., **2008**, 130, 3754-3755.
91. J. Akola, K. A. Kacprzak, O. L.-Acevedo, M. Walter, H. Grönbeck and H. Häkkinen J. Phys. Chem. C, **2010,** 114, 15986–15994.
92. J. B. Tracy, G. Kalyuzhny, M. C. Crowe, R. Balasubramanian, J.-P. Choi and R. W. Murray, J. Am. Chem. Soc., **2007**, 129, 6706–6707.
93. O. L.-Acevedo, H. Tsunoyama, T. Tsukuda, H. Häkkinen and C. M. Aikens, J. Am. Chem. Soc., **2010**, 132, 8210–8218.
94. N. T. Tran, D. R. Powell and L. F. Dahl, Angew. Chem., Int. Ed., **2000**, 39, 4121. (b) O. L.-Acevedo, J. Akola, R. L. Whetten, H. Grönbeck, and H. Häkkinen, J. Phys. Chem. C, **2009**, 113, 5035–5038.
95. Z. Wu, J. Suhan and R. Jin, J. Mater. Chem., **2009**, 19, 622–626.
96. H. Qian, Y. Zhu and R. Jin, Nano, **2009**, 3, 3795–3803.
97. H. Qian and R. Jin, Nano Lett., **2009**, 9, 4083-4087.
98. M. Zhu, W. T. Eckenhoff, T. Pintauer, and R. Jin, J. Phys. Chem. C, **2008**, 112, 14221-14224.
99. M. Zhu, G. Chan, H. Qianb and R. Jin, Nanoscale, **2011**, 3, 1703-1707.
100. M. A. Habeeb Muhammed, A. K. Shaw, S. K. Pal and T. Pradeep, J. Phys. Chem. C, **2008**, 112, 14324.
101. Y. Negishi, N. K. Chaki, Y. Shichibu, R. L.Whetten and T.Tsukuda, J. Am. Chem. Soc., **2007**, 129, 11322.

102. Z. Wu, C. Gayathri, R. R. Gil and R. Jin, J. Am. Chem. Soc., **2009**, 131, 6535.

103. R. L. Donkers, D. Lee and R. W. Murray, Langmuir, **2004**, 20, 1945. (b) G. Wang, R. Guo, G. Kalyuzhny, J.-P. Choi and R. W. Murray, J. Phys. Chem. B, **2006**, 110, 20282.

104. J.-P. Choi, C. A. Fields-Zinna, R. L. Stiles, R. Balasubramanian, A. D. Douglas, M. C. Crowe and R. W. Murray, J. Phys. Chem. C, **2010,** 114, 15890–15896.

105. M. A. Habeeb Muhammed and T. Pradeep, small, **2011**, 7, 204–208.

106. P. Ramasamy, S. Guha, E. S. Shibu, T. S. Sreeprasad, S. Bag, A. Banerjee and T. Pradeep, J. Mater. Chem. **2009**, 19, 8456 .

107. R. M. White, Quantum Theory of Magnetism, Springer, New York, **2007**.

108. J. Wang, J. Bai, J. Jellinek and X. C. Zeng, J. Am. Chem. Soc., **2007**, 129, 4110–4111.

109.Y. Negishi, H. Tsunoyama, M. Suzuki, N. Kawamura, M. M. Matsushita, K. Maruyama, T. Sugawara, T. Yokoyama and T. Tsukuda, J. Am. Chem.Soc., **2006**, 128, 12034–12035.

110. M. Zhu, C. M. Aikens, M. P. Hendrich, R. Gupta, H. Qian, G. C. Schatz and R. Jin, J. Am. Chem. Soc., **2009**, 131, 2490–2492.

111. W. D. Knight, K. Clemenger, W. A. de Heer, W. A. Saunders, M. Y. Chou and M. L. Cohen, Phys. Rev. Lett., **1984**, 52, 2141.

112. W. Luo, S. J. Pennycook and S. T. Pantelides, Nano Lett., **2007**, 7, 3134–3137.

113. C. A. Fields-Zinna, M. C. Crowe, A. Dass, J. E. F. Weaver and R.W. Murray, Langmuir, **2009**, 25, 7704;

114. Y. Negishi, W. Kurashige, Y. Niihori, T. Iwasa, K. Nobusada, Phys. Chem. Chem. Phys., **2010**, 12, 6219.

115. Y. Negishi, T. Iwai and M. Ide, Chem. Commun. **2010**, 46, 4713; b) C. Kumara and A. Dass, Nanoscale, **2011**, 3, 3064.

116. M. Haruta, Nature, **2005**, 437, 1098–1099.

117. A. Corma and P. Serna, Science, **2006**, 313, 332–334.

118. A. S. K. Hashmi and G. J. Hutchings, Angew. Chem., **2006**, 118, 8064–8105.

119. A. Sanchez, S. Abbet, U. Heiz, W.-D. Schneider, H. Häkkinen, R. N. Barnett and Uzi Landman, J. Phys. Chem. A, **1999**, 103, 9573-9578.
120. (a) N. L. Rosi and C. A. Mirkin, Chem. Rev., **2005**, 105, 1547. (b) A.Verma, O.Uzun, Y. H. Hu, Y. Hu, H. S. Han, N. Watson, S. L. Chen, D. J. Irvine and F. Stellacci, Nat. Mater., **2008**, 7, 588.
121. S. Sun, C. B. Murray, D. Weller, L. Folks and A. Moser, Science, **2000**, 287, 1989.
122. W. L. Barnes, A. Dereux and T. W. Ebbesen, Nature, **2003**, 424, 824.
123. S. Jansat, M. Gomez, K. Philippot, G. Muller, E. Guiu, C. Claver, S. Castillon and B. Chaudret, J. Am. Chem. Soc., **2004**, 126, 1592.
124. M. C. Daniel and D. Astruc, Chem. Rev., **2004**, 104, 293.
125. S. Kommareddy and M. Amiji, Nanomedicine: NBM, **2007**, 3, 32.
126. R. Hong, G. Han, J. M. Fernandez, B. j. Kim, N. S. Forbes and V. M. Rotello, J. Am. Chem. Soc., **2006**, 128,1078.
127. (a) A. Baiker, J. Mol. Catal. A: Chem., **1997**, 115, 473. (b) P. B. Wells and A. G. Wilkinson, Top. Catal., **1998**, 5, 39.
128. C. W Corti, R. J Holliday and D. T Thompson, Gold Bulletin, **2002**, 35, 111-117.
129. Y. Zhu, H. Qian, B. A. Drake, and R. Jin, Angew. Chem. Int. Ed., **2010**, 49, 1295 –1298.
130. M. Zhu, C. M. Aikens, F. J. Hollander, G. C. Schatz and R. Jin, J. Am. Chem. Soc., **2003**,130, 5883 – 5885.
131. M. Zhu, C. M. Aikens, M. P. Hendrich, R. Gupta, H. Qian, G. C. Schatz and R. Jin, J. Am. Chem. Soc., **2009**, 131, 2490 – 2492.
132. M. Okumura, Y. Kitagawa, K. Yamaguchi and M. Haruta, Chem. Phys. Lett., **2008**, 459, 133–136.
133. H. Tsunoyama, N. Ichikuni, H. Sakurai and T. Tsukuda, J. Am. Chem. Soc., **2009**, 131, 7086 – 7093.
134. A. Corma, M. Boronat, S. Gonzalez and F. Illas, Chem. Commun., **2007**, 3371 – 3373.
135. Y. Zhu, H. Qian, M. Zhu and R. Jin, Adv. Mater., **2010**, 22, 1915–1920.

136. O. S. Mohamed, S. A. Ahmed, M. Farrag and A. A. Abdel-Wahab, International Journal of Photoenergy, **2008**, Article ID 205358, 11 pages.

137. O. S. Mohamed, S. A. Ahmed, M. Farrag and A. A. Abdel-Wahab, J. Photochem. and Photobio. A: Chem., **2008**, 200, 209-215.

138. R. Flamini and P. Traldi, Mass Spectrometry in Grape and Chemistry, John Wiley & Sons, Inc, **2010**.

139. C. Ho, C. Lam, M. Chan, R. Cheung, L. Law, L. Lit, K. Ng, M. Suen and H. Tai, Electrospray Ionisation Mass Spectrometry: Principles and Clinical Applications, Clin Biochem Rev, **2003**.

140. J. J. Pitt, Principle and Applications of Liquid Chromatography-Mass Spectrometry in Clinical Biochemistry, Clin Biochem Rev, **2009**.

141. W. Henderson and J. S. Mcindoe, Mass Spectrometry of Inorganic and Organometallic Compounds, John Wiley & Sons Ltd, The Atrium, Southern Gate, Chichester, West Sussex PO19 8SQ, England, **2005**.

142. B. A. Mamyrin, V. I. Karataev, D. V. Shmikk and V. A. Zagulin, Sov. Phys. JETP, 1973, 37, 45.

143. N. Berova, K. Nakanishi and R. W. Moody, Circular Dichroism: Principles and Applications, John Wiley & Sons, Inc., **2000**.

144. http://en.wikipedia.org/wiki/Circular_dichroism.

145. M. L. Neidig, A. T. Wecksler, G. Schenk, T. R. Holman and E. I. Solomon, J. Am. Chem. Soc., **2007**, 129, 7531- 7537.

146. E. I. Solomon and A. B. P. Lever, Inorganic Electronic Structure and Spectroscopy, Wiley-Interscience, **2006**.

147. L. Reimer and H. Kohl, Transmission Electron Microscopy, Springer Science+Business

Media, LLC, **2008**.

148. B. B. He, Two-Dimensional X-Ray Diffraction, John Wiley & Sons, Inc, **2009.**

149. D. A. Skoog and J. J. Leary, Principles of Instrumental Analysis, Saunders College Publishing, **1992**.